Keywords

Ranque-Hilsch vortex tube, Hilsch tube, Vortex tube, Swirling flows, Energy separation, Acoustic streaming, Computational fluid dynamics, Gas liquefaction, Refrigeration techniques, Isotope separation, Uranium enrichment, Stationary wall centrifugation.

Preface

The research work described in this dissertation was carried out in the Department of Engineering, University of Cambridge, between October 1991 and August 1995. It is the result of my own work and includes nothing which is the outcome of work done in collaboration. The contents are original except where reference is made to the work of others. It has not been submitted for any other degree or qualification at any other university or institution.

Acknowledgements

So many have assisted with the production of this work, that it is impossible for me to mention them all. To all those I omit, please note that I have thanked you first!

The greatest thanks go to my supervisor Dr. J.D. Lewins, who suggested the subject of this dissertation, provided me with guidance on the many occasions that I needed it, and extended deadlines without complaint when I failed to meet them. Without his support, this work would not even have neared completion. On reflection, I am amazed that he has put up with me for so long.

Many thanks are also due to my industrial supervisor, Mr. A. J. Bull of British Nuclear Fuels plc, for his continuing concern for my progress, the many contacts he introduced me to, the comments he has made on my work, and indeed his admirably flexible attitude regarding deadlines.

Financial support for this work was provided by three bodies. The majority of the work was funded by the then Science and Engineering Research Council, now EPSRC. Essential contributions, both financial and with regard to resources, were made by BNFL. Magdalene College furnished me with a scholarship that eased the financial pains of existence as a research student.

All the Heat Laboratory technicians, Neville Coates, John Harvey, Ron Coleman and Trevor Parsons, provided valuable assistance with all my experiments. Neville assures me that the sudden replacement of the laboratory compressor on completion of my practical work was purely a co-incidence. I remain unconvinced.

Many people, greatly more experienced than me, gave help and encouragement through discussions and the offer of facilities including Dr. W. Geddes of BNFL, Dr. P. Davidson at the time of Imperial College, Prof. K. N. C. Bray and Prof. Ffowcs-Williams, both of the Engineering Department.

Thanks are also due to my friends and colleagues, including: D.S. Louch, Dr. J. Galsworthy, Dr. A. Banbury, N.E. Leadbeater, Dan Hillman, C. Farmer, D.M. Franks, Dr. P-W. Poon, Dr. Y-F. Wu, Dr. K. Lakshmisha, R. Zheng, Dr. L-L Zheng, E. Ngcobo, M.O. Allagi, P. Fanorakis, M.D. Binns, A.M. Williams, and Neil and Christina Jaques all of whom made my stay in Cambridge much more enjoyable and were always there when I needed them.

The final expression of thanks goes to my family, for their generous donations, both financial and otherwise, over the last quarter century. Ultimately they are responsible for the existence of this work.

Summary

The Ranque-Hilsch vortex tube is a device that divides a flow of compressed gas into two separate streams, one of which is warmer than the inlet gas, while the other is cooler. No external power source, other than the compressor that provides the inlet air, is employed. This dissertation investigates the seemingly paradoxical transfer of energy that must occur from the cold outlet gas to the warm outlet gas.

Rotating flows in general, and the Ranque-Hilsch vortex tube in particular, have been the subject of much study. The first objective of the dissertation is to collate the available information, and attempt to draw some preliminary conclusions as to the likely nature of the flow within the Ranque-Hilsch tube. This is a particularly important matter, as progress in understanding the tube has been inhibited by the fragmented nature of many of the works.

An experimental investigation of three Ranque-Hilsch tubes establishes some general results that characterise the thermal separation. The internal flow is examined in more detail, although practical difficulties limit the utility of the results. Measurements of the acoustical disturbances generated by an operating tube provide no evidence in support of an existing theory that attributes the energy transfer to them.

Computational fluid dynamic techniques are applied to the Ranque-Hilsch tube both to assess their potential in such calculations, and with the hope of gaining further insight into the internal flow. The fluid mechanics are dealt with by an incompressible vorticity-streamfunction solver, while the thermal solutions take some account of compressibility effects. The output of the code is adequate, but further work is required to improve its performance for use as a Ranque-Hilsch tube design tool.

In the light of the numerical and experimental results, some tentative conclusions are drawn regarding the energy transfer mechanism at work within the vortex tube. A semi-empirical model relating the thermal performance of the tube to the applied pressure ratio and the mass fraction of gas leaving through the cold exit is presented. The model employs only analytic expressions to simplify its later use in an investigation of possible applications.

The potential for use of a vortex tube in cooling applications is assessed. Particular attention is applied to gas liquefaction. It is deduced that the performance of the vortex tube must be improved for its realistic use as the sole source of cooling in an air liquefier. There is scope for the vortex tube to assist in the operation of conventional techniques, such as the Linde process, and to be the sole source of cooling for gases more easily liquefied than air.

It is confirmed that the radial mass separation effects reported by a number of workers are produced by simple centrifugation. Using this information, the potential of the Ranque-Hilsch vortex tube for use in uranium enrichment duties is studied, and found worthy of further investigation.

Contents

List of Figures

Nomenclature

Explanitory Note

This section lists most of the nomenclature used in this thesis. On occaision symbols are used without explanation or with meanings that differ from those here. In such circumstances the interpretation of the symbol is given explicity in the text, or should be obvious from the context. The same is true for symbols given more than one meaning in the tables below

Note that the convention employed for pressure is that of the Royal Society; specifically it is represented by a capital P.

Upper Case Letters

A	Area
D	Diameter (of vortex tube)
	Diffusion coefficient
$F(j\omega)$	Fourier tranform of the function $f(t)$
$K_{x_{ij}}$	Correlation coefficient
L	Length of vortex tube
	Characteristic length scale
M	Mach number
P	Static pressure
P_{atm}	Atmospheric pressure
P_x, P_y	Partial pressures of components with mole fraction x, y
P_0	Stagnation pressure
Q	Heat transfer
R	Ideal gas constant for a particular gas
$\bar{R}$	Molar (universal) gas constant (8.3143 kJ/kmol K)
R_T	Recovery factor
T	Static temperature
T_0	Stagnation temperature
T_{atm}	Atmospheric temperature
T_c	Static temperature of the cold stream
T_h	Static temperature of the hot stream
T_{jt}	Temperature drop associated with the Joule–Thomson effect
T_R	Recovery temperature
T_*	Characteristic temperature (in chapter 6)
V	Value function
W	Work (transfer)
U	Characteristic velocity

Lower Case Symbols

c	Speed of sound
c_p	Specific heat capacity at constant pressure
c_v	Specific heat capacity at constant volume
d	Orifice diameter
e	Exponential constant
f	Frequency
	Function
$f(t)$	Function of time
h	Specific static enthalpy
	Heat transfer co-efficient
h_0	Specific stagnation enthalpy
j	Square root of -1
k	Turbulence kinetic energy
m	Molar mass
$\dot{m}$	Mass flux
q	Heat flux
s	Specific entropy
r	Radial co-ordinate
r_0	Outer radius
t	Time
u	Radial Velocity
v	Swirl (circumferential) velocity
w	Axial velocity
z	Axial co-ordinate
x, y	Mole fraction

Non-Dimensional Groups

Ek	Ekman number
Gr	Grashoff number
Pr	Prandtl number
Ro	Rossby number
Re	Reynolds number
Ri	Richardson number
S	Swirl number

Bold Face Symbols - Vectors and Tensors

$\mathbf{T}$	Transformation matrix
$\mathbf{V_x}$	Variance matrix for observables

$\mathbf{V_y}$	Variance matrix for results
$\mathbf{f}$	(Body) force vector
$\mathbf{q}$	Heat flux vector
$\mathbf{v}$	Velocity vector
$\mathbf{u}$	Velocity vector relative to rotating frame
$\mathbf{x}$	Observables vector
$\mathbf{y}$	Results vector

Greek Symbols

β	Thermal expansivity
γ	Isentropic exponent c_p/c_v
Δ	Change in
δ	Inlet nozzles effective diameter
δ_{ij}	Kronecker delta
ϵ	Turbulent diffusivity, μ_e/ρ
ϵ_h	Turbulent thermal diffusivity, λ_e/ρ
θ	Circumferential co-ordinate
λ	Thermal conductivity
λ_e	Effective thermal conductivity, usually equal to the sum of the laminar and the turbulent conductivities
μ	Dynamic viscosity
μ'	Second coefficient of viscosity
μ_c	Cold mass flow fraction
μ_e	Effective viscosity, usually equal to the sum of the laminar and the turbulent viscosities
μ_h	Joule-Thomson coefficient
μ_t	Turbulent viscosity
ν	Kinematic viscosity
ρ	Density
σ_h	Turbulent Prandtl number
σ_k	Turbulent Schmidt number for turbulence kinetic energy transport
σ_ϵ	Turbulent Schmidt number for turbulent dissipation
τ_{ij}	Stress tensor
Φ	Dissipation function
ϕ	Generic variable to be solved for
χ	Wetness fraction
ψ	Streamfunction
Ω	Rotational speed (in radians / s)
ω	Angular frequency Vorticity

Subscripts

atm	Evaluated at atmospheric conditions
c	Evaluated at the cold exit to the vortex tube
cl	Evaluated at the centre-line
$cold$	Evaluated at the cold exit to the vortex tube
E	Evaluated at the node to the 'east'
e	Evaluated at the 'eastern' face
f	Value for saturated liquid under prevailing conditions
g	Value for saturated gas under prevailing conditions
hot	Evaluated at the hot exit to the vortex tube
h	Evaluated at the hot exit to the vortex tube
in	Evaluated at the (tube) inlet
$inlet$	Evaluated at the (tube) inlet
i,j	Node numbers, in computational work
max	Maximum value
N	Evaluted at the node to the 'north'
n	Evaluated at the 'northern' face
out	Evaluated at the outlet
$outlet$	Evaluated at the outlet
r_0	Evaluated at the outer radius, r_0
ref	Reference value
S	Evaluated at the node to the 'south'
s	Evaluated at the 'southern' face
$stag$	Stagnation value
t	Turbulent
W	Evaluated at the node to the 'west'
w	Evaluated at the 'western' face
$wall$	Evaluated at the wall

Superscripts

$\hat{}$	Unit vector
$\bar{}$	Time averaged
$'$	Fluctuating component
*	Non-dimensional, or normalised quantity
$<>$	Mean or expected value
$[k]$	Time level, or iteration number in computational work

Other Symbols

$\mathcal{F}$	Fourier transform of
$\mathcal{F}^{-1}$	Inverse fourier transform of

Chapter 1

Introduction

1.1 The Ranque-Hilsch Vortex Tube

The Ranque-Hilsch vortex tube is a device that separates a flow of gas into two streams simultaneously, one hotter than the inlet temperature and one cooler. Made even more remarkable by the absence of moving parts, the device was first conceived by Georges Ranque [3] in 1933 after he found evidence of a radial temperature gradient in cyclone separators. There was little interest in the vortex tube until a study by Hilsch [4] in 1946 published numerical data describing its thermal performance, along with some basic constructional details.

Figure 1.1 shows the essential features of the *counterflow* vortex tube investigated by both its progenitors. Air (or in general, the working gas) is introduced into a tube open at both ends through tangential flow inlets positioned about a quarter of the tube's length away from one end. A strongly swirling flow results and the gas proceeds along the tube; a sketch of the commonly supposed flow pattern is shown in figure 1.2. The outer regions of the flow are found to be warmer than the inlet gas, while gas towards the centre of the tube experiences cooling. An orifice positioned just 'behind' the flow inlets separates the cool central gas, which then exits the tube at the left-hand side as seen in the diagram. The warm peripheral flow leaves at the right-hand side of the tube, where a

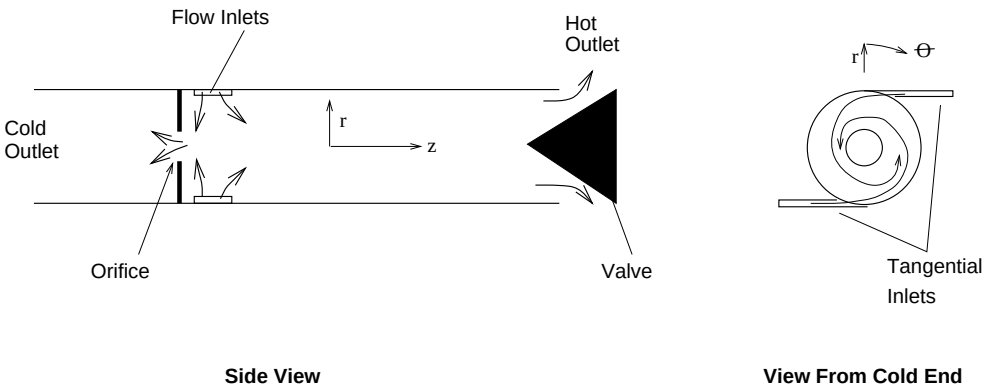

Figure 1.1: A counterflow vortex tube.

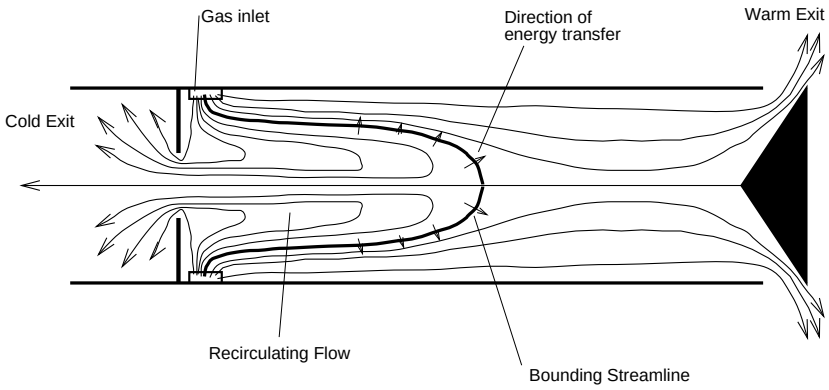

Figure 1.2: Diagrammatic sketch of the flow pattern in a counterflow tube.

.

valve is positioned to allow regulation of the relative quantities of hot and cold gas.

An alternative design for a temperature separating vortex tube, which we will term the *uniflow* variant, is shown in figure 1.3. The fundamental aspects of the device are the same as for the counterflow tube. Its distinguishing features are that the orifice and valve are combined at one end of the tube, while the other end of the tube, adjacent to the inlet nozzles, is sealed. Many investigators have suggested that uniflow tubes perform less well than equivalently proportioned counterflow designs.

It is useful at this stage to consider the magnitude of the temperature differences the vortex tube can produce. While this is discussed in some detail in the body of the thesis,

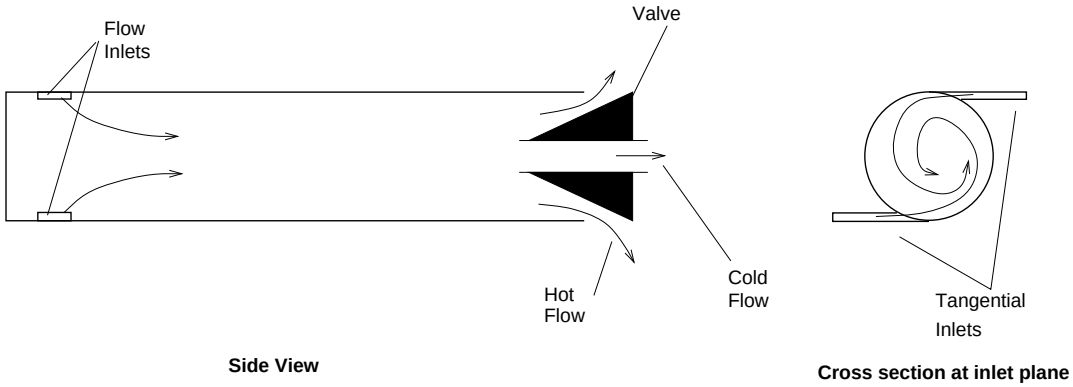

Figure 1.3: A uniflow vortex tube.

a preliminary 'feel' for the separation assists in comprehension of much of what follows. The temperature differences can be substantial. Hilsch, for example, operated a counter-flow vortex tube 12 mm in diameter on air supplied at approximately 600 kPa and 293 K, to produce a hot stream at 343 K, and a cold stream at 261 K. Hilsch also suggests that temperature differences as large as +180 K and -70 K compared to the inlet gas can be obtained from a suitably designed[1] tube driven by air at 1100 kPa. Many other workers give comparable results, although perhaps unsurprisingly, reduced inlet pressures result in smaller temperature changes. Apparatus available at Cambridge University Engineering Department for instance, delivers differences of up to -11.5 K and +8 K when run at approximately 300 kPa.

What we have in the Ranque-Hilsch tube then, is a device without moving mechanical parts, that converts a gas flow initially homogeneous in temperature, into two separate flows of differing temperatures. This is surprising. Most 'passive' energy transfer processes strive towards thermal equilibrium, producing uniformity of thermal energy. In the Ranque-Hilsch vortex tube, thermal equilibrium appears to represent an inhomogeneity of thermal energy.

It is a mistake, of course, to regard the thermodynamic system represented by the

[1]Hilsch gives few clues as to the actual design of this particular example.

vortex tube as *entirely* passive, and devoid of motion. The gas swirling through the tube at high speed is far from quiescent, and quite capable of performing some kind of work. Herein must lie the key to comprehension of the phenomenon. *How does the swirling motion of the flow in the Ranque-Hilsch vortex tube provide the impetus necessary to cause energy to accumulate in gas towards the periphery of the flow, at the expense of gas towards the centre?* Directly or indirectly, it is this question that much of this thesis will address.

Maxwell's Demon

Before leaving this introduction to the nature of the Ranque-Hilsch tube, it is worth drawing a qualified analogy with Maxwell's demon [5] [6]. Maxwell imagined an energy separator consisting of a molecule sized 'demon' controlling the trap door separating two halves of a container filled initially with a homogeneous gas. The demon is able to observe gas molecules approaching the trap door, and operates it in such a way as to collect molecules with a kinetic energy above a certain critical level in one half of the box, and those with lesser energy in the other half. Given sufficient time, the demon manages to produce a discernible temperature difference between the gas in each half of the box, seemingly in violation of the Second Law of Thermodynamics.

While the net effects of the Ranque-Hilsch vortex tube and Maxwell's demon are similar, there are a couple of notable points. Firstly, Maxwell's demon operates on a molecular, discrete basis. He identifies which molecules are already hot, and which are already cold, and takes positive action to *separate* them. There is no suggestion that the Ranque-Hilsch tube operates directly on a molecular scale, separating already hot, fast moving molecules from slower cold ones. Rather, all the discussion here will analyse the tube within the conventional fluid mechanical assumption that the working fluid can be considered as a continuum. In this sense, the effect of the Ranque-Hilsch tube is to *generate* a radial temperature (thermal energy) gradient by inducing the transfer of energy from the central region of the flow to the periphery, rather than to *separate* thermal energies by selective spatial filtering of pre-exisiting hot and cold fluid particles. Nevertheless, the

term 'separation' will frequently be used to refer to the effect of the Ranque-Hilsch tube in this thesis, as it is in the published literature. Care should be taken to bear in mind that this term is something of a misnomer. It is possible to conceive of vortex tubes operating under such low pressures that the Knudsen number is significant, and free molecule analysis becomes appropriate. These flows are outside the scope of this work, except in so far as they may exhibit behaviour similar to the continuum case.

The second point to draw from Maxwell's demon is that the thermal separation he produces is not in violation of the Second Law of Thermodynamics, when proper account is taken of the mental and physical effort the demon must expend in spotting the approaching molecules and working the trap door. Here the analogy with the Ranque-Hilsch tube is very good. As will be discussed later, when proper account is made of the work needed to operate the tube, the temperature difference it produces is entirely consistent with classical thermodynamics.

1.2 Background

Since its discovery, the Ranque-Hilsch vortex tube has been a subject of substantial investigation. In excess of a hundred papers directly addressing the device have been published over the last 50 or so years, with many more that could be considered 'relevant'. The mechanism underlying the energy transfer from the cold to the hot flow remains elusive, however. There is debate even as to the basic physics of the phenomenon. While the majority of workers suggest mechanisms based on the interactions of turbulence, compressibility and shear work (see Deissler and Perlmutter [7] for the most thorough analysis), there is a significant school of thought that cites acoustic effects as responsible (Kurosaka [8]).

One obstacle to investigations of the Ranque-Hilsch tube is the lack of any substantial published literature review since Westley [9] in 1954. An important task early in any study of the vortex tube must be to draw together the mass of literature.

1.3 Thermodynamics : The First and Second Laws

At first sight, the vortex tube may appear to represent an impossible phenomenon, violating some fundamental laws of thermodynamics. The reader should rest assured, however, that the fabric of Physics remains intact.

1.3.1 First Law Analysis

The vortex tube satisfies the First Law of Thermodynamics. Energy *is* conserved. Indeed, we can write

$$(h_0)_{inlet} = \mu_c (h_0)_{cold} + (1 - \mu_c) (h_0)_{hot} \tag{1.1}$$

where $\mu_c = \frac{\dot{m}_c}{\dot{m}_{in}}$ is the fraction of the inlet mass flow leaving through the cold exit, and h_0 represents the stagnation enthalpy. In many cases, especially with long vortex tubes, the flow velocities at the exits to the tube are small and their influence on the stagnation enthalpy may be neglected. For an ideal gas, the conservation equation may now be written

$$c_p T_0 = \mu_c c_p T_c + (1 - \mu_c) c_p T_h \tag{1.2}$$

where T_0 represents the stagnation temperature of the inlet gas, T_c the static temperature of the cold stream and T_h the static temperature of the hot stream. When rearranged with μ_c as the subject, equation (1.2) gives a convenient means of estimating the cold mass flow fraction from temperature readings alone.

For a perfect gas, with a specific heat capacity c_p independent of thermodynamic state, equation (1.2) may be simplified by cancelling the c_p from each term. With a real gas, account must be taken of the dependence of enthalpy on pressure, that, is the Joule-Thomson effect, and then equation (1.2) is invalid. A revised relationship might be written

$$T_0 = \mu_c (T_c - T_{jt}) + (1 - \mu_c) (T_h + T_{jt}) \tag{1.3}$$

where T_{jt} represents the influence of the Joule-Thomson effect. Over the range of pres-

sure changes encountered in this thesis, generally less than 670 kPa, Joule-Thomson cooling in air is relatively small at less than 2 K. Since much of the discussion deals with air, the Joule-Thomson effect will be ignored except where noted explicitly. Moreover, gases will in general be treated as perfect throughout this work and thence immune to Joule-Thomson cooling.

1.3.2 Second Law Analysis

The Clausius Statement of the Second Law of Thermodynamics[2] reads

> *It is impossible to construct a system which will operate in a cycle and transfer heat from a cooler body to a hotter body without work being done on the system by the surroundings.*

To reconcile the vortex tube with the Second Law, we have to broaden our outlook and recognise that the closed system we should consider consists of a compressor *and* a vortex tube, as shown in figure 1.4. The arrangement pictured is quasi-cyclic in as much as the outlet air has been returned to its inlet pressure, specifically, atmospheric pressure. If the two outlet streams were mixed, the resultant gas would have a uniform enthalpy equal to that of the inlet gas, assuming that the heat transfer from the compressor was sufficient to cool the newly compressed gas back to ambient temperature. Note that we assume the working gas is perfect here. Thus the open system pictured in bold could be simply converted to closed cycle operation with no effect on its performance by addition of the equipment drawn lightly. The outlet gas is mixed, passed through a heat exchanger if necessary, and returned to the compressor.

With such a scheme, the Second Law is obviously satisfied. Work is done to cause the transfer of heat from the cold gas stream to the hot stream.

[2]See, for example, Rogers and Mayhew [10].

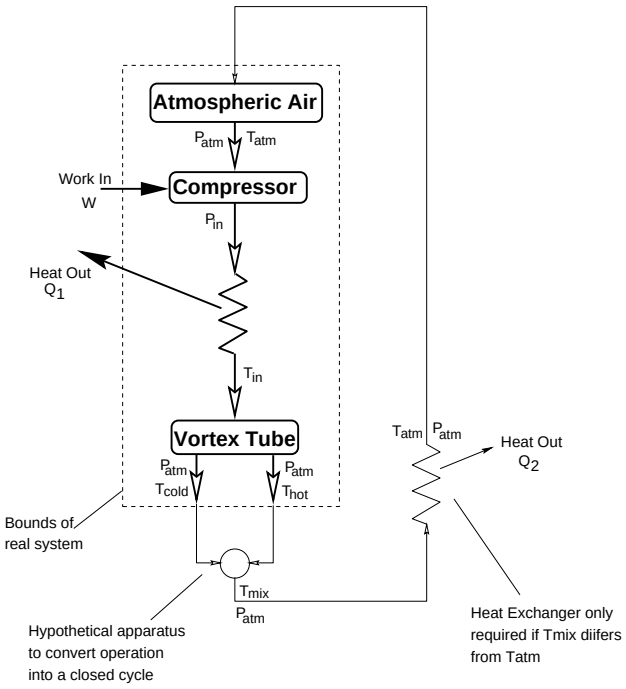

Figure 1.4: The vortex tube thermodynamic system.

1.4 Mixture (Isotopic) Separation

There are reports of detectable separation of components of differing mass within the Ranque-Hilsch tube, such that it might be possible to employ vortex tubes as mixture or isotope separators. As with the temperature separation effect, there has been considerable debate as to the mechanism responsible for this mass based separation. In this case, a 'key' into the problem is more obvious; the strongly swirling nature of the flow in the tube suggests that straightforward centrifugation is likely to be the underlying mechanism. While a couple of experimental studies have found evidence that concurs with this hypothesis, there is still plenty of scope for further analysis.

1.5 Preview of Thesis

In the next chapter, we will begin our study of the vortex tube by reviewing the substantial quantity of literature dealing with the device. After attempting to draw some preliminary conclusions from the mass of ideas discussed, we will move on to consider a series of experiments conducted with a vortex tube apparatus in chapter 3. A number of empirical observations are made from the results, and some insights into the likely mechanism of energy separation are gained.

Chapter 4 examines the development of a computer based Navier-Stokes solver that attempts to simulate flow in the Ranque-Hilsch tube. While the code developed would benefit from considerable further attention, the program reaches a level of sophistication sufficient to allow useful calculations of Ranque-Hilsch tube flows and provides some enlightenment as to the mechanism of energy transfer. The difficulties peculiar to computations of vortex tube flows and the steps taken to ensure the reliability of the code are also mentioned briefly.

In chapter 5, there is some further, more analytical, investigation of the energy transfer mechanisms highlighted by the experimental and computational work. By chapter 6 it is possible to present an empirical model to represent the performance of the vortex tube.

With chapter 7, attempts are made to employ the new-found knowledge of the Ranque-Hilsch vortex tube in the investigation of two potential applications. Attention is focussed primarily on an area that appealed to Ranque, specifically the utility of the vortex tube in gas liquefaction processes. Also presented is a brief investigation of mixture separation processes in the vortex tube, along with some deductions regarding the application of the vortex tube in uranium enrichment processes.

The last chapter draws together the information in the earlier chapters, and formulates some overall conclusions regarding the issues considered in this thesis. Suggestions for areas worthy of further study are made.

Chapter 2

Review of The Literature

2.1 Introduction

We will begin by taking a general review of the features of confined rotating flows, highlighting those aspects particularly relevant to the vortex tube. Next the review will be narrowed to studies of the Ranque-Hilsch tube specifically. The material is divided broadly into three sections considering firstly experimental, and then theoretical investigations of the thermal effects within tubes, looking lastly at studies of mixture separation. Having learned what we can, the review will be widened again, to touch upon other phenomena that might be related to the Ranque–Hilsch effect.

Efforts will be made to draw the material together, attempting to learn as much as possible about the vortex tube from existing information. In the light of this, areas ripe for research will be defined, and brief consideration given to the approach to be adopted.

2.2 Fluid Mechanics of Rotating Flows

As with many problems in fluid mechanics the basic principles and fundamental equations appear to be relatively straightforward. Unfortunately, they do not provide in themselves much insight into the problem at hand. Nevertheless they remain important, provid-

ing a basic understanding of the phenomenon under investigation. This section reviews some fundamental results in the mechanics of rotating flows, and attempts to place them in context with regard to the Ranque–Hilsch tube.

2.2.1 Governing Equations and Co-ordinate Systems

The generalised continuity, Navier-Stokes and energy equations may be written in Cartesian Tensor notation as

$$\begin{aligned} \frac{\partial \rho}{\partial t} + \nabla(\rho \mathbf{v}) &= 0 && (2.1)\\ \rho \frac{D\mathbf{v}}{Dt} &= \rho \mathbf{f} + \nabla \Pi_{ij} && (2.2)\\ \rho \frac{Dh}{Dt} &= \frac{DP}{Dt} + \frac{\partial Q}{\partial t} - \nabla \mathbf{q} + \Phi && (2.3) \end{aligned}$$

where

$$\begin{aligned} \Pi_{ij} &= -P\delta_{ij} + \tau_{ij} && (2.4)\\ \tau_{ij} &= \mu\left(\frac{\partial u_i}{\partial x_j} + \frac{\partial u_j}{\partial x_i}\right) + \delta_{ij}\mu' \frac{\partial u_k}{\partial x_k} && (2.5)\\ \mathbf{q} &= -\lambda \nabla T && (2.6) \end{aligned}$$

with $\mathbf{f}$ the body force per unit mass, $\Phi = \tau_{ij}\frac{\partial u_i}{\partial x_j}$ the dissipation function, and Q representing heat transfer with the environment.

It is both convenient and conventional in discussions of rotating flows in ducts to use cylindrical polar co-ordinates. This thesis is concerned mainly with jet driven rotating flows in cylindrical ducts, and will employ a cylindrical polar system originating from the centre of the plane co-incident with 'downstream' side of the inlet nozzles as shown in figure 2.1. In this system the continuity equation is

$$\frac{\partial \rho}{\partial t} + \frac{\partial \rho u}{\partial r} + \frac{1}{r}\frac{\partial \rho v}{\partial \theta} + \frac{\partial \rho w}{\partial z} + \frac{\rho u}{r} = 0, \qquad (2.7)$$

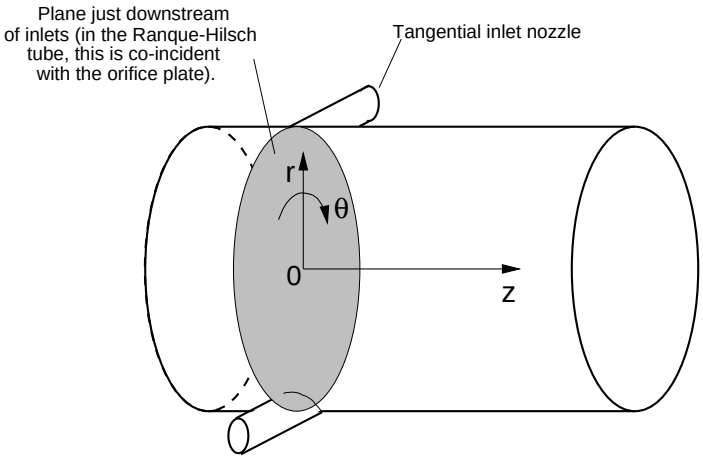

Figure 2.1: The co-ordinate system employed.

and the radial, circumferential and axial Navier-Stokes (momentum) equations are respectively, neglecting body forces

$$\begin{aligned}\rho\left(\frac{Du}{Dt}-\frac{v^2}{r}\right) &= -\frac{\partial P}{\partial r}+\frac{\partial}{\partial r}\left[\mu\left(2\frac{\partial u}{\partial r}-\frac{2}{3}\nabla\cdot\mathbf{v}\right)\right]+\frac{1}{r}\frac{\partial}{\partial\theta}\left[\mu\left(\frac{1}{r}\frac{\partial u}{\partial\theta}+\frac{\partial v}{\partial r}-\frac{v}{r}\right)\right]\\ &\quad+\frac{\partial}{\partial z}\left[\mu\left(\frac{\partial u}{\partial z}+\frac{\partial v}{\partial r}\right)\right]+\frac{2\mu}{r}\left(\frac{\partial u}{\partial r}-\frac{1}{r}\frac{\partial v}{\partial\theta}-\frac{u}{r}\right) \qquad (2.8)\end{aligned}$$

$$\begin{aligned}\rho\left(\frac{Dv}{Dt}+\frac{uv}{r}\right) &= -\frac{1}{r}\frac{\partial P}{\partial\theta}+\frac{1}{r}\frac{\partial}{\partial\theta}\left[\mu\left(\frac{2}{r}\frac{\partial v}{\partial\theta}+\frac{2u}{r}-\frac{2}{3}\nabla\cdot\mathbf{v}\right)\right]\\ &\quad+\frac{\partial}{\partial r}\left[\mu\left(\frac{1}{r}\frac{\partial u}{\partial\theta}+\frac{\partial v}{\partial r}-\frac{v}{r}\right)\right]+\frac{\partial}{\partial z}\left[\mu\left(\frac{1}{r}\frac{\partial w}{\partial\theta}+\frac{\partial v}{\partial z}\right)\right]\\ &\quad+\frac{2\mu}{r}\left(\frac{1}{r}\frac{\partial u}{\partial\theta}+\frac{\partial v}{\partial r}-\frac{v}{r}\right) \qquad (2.9)\end{aligned}$$

$$\begin{aligned}\rho\left(\frac{Dw}{Dt}\right) &= -\frac{\partial P}{\partial z}+\frac{\partial}{\partial z}\left[\mu\left(2\frac{\partial w}{\partial z}-\frac{2}{3}\nabla\cdot\mathbf{v}\right)\right]\\ &\quad+\frac{1}{r}\frac{\partial}{\partial\theta}\left[\mu\left(\frac{1}{r}\frac{\partial w}{\partial\theta}+\frac{\partial v}{\partial z}\right)\right]+\frac{\partial}{\partial r}\left[\mu\left(\frac{\partial u}{\partial z}+\frac{\partial w}{\partial r}\right)\right]\\ &\quad+\frac{\mu}{r}\left(\frac{\partial u}{\partial z}+\frac{\partial w}{\partial r}\right) \qquad (2.10)\end{aligned}$$

with dilatation

$$\nabla \mathbf{v} = \frac{\partial u}{\partial r} + \frac{1}{r}\frac{\partial v}{\partial \theta} + \frac{\partial w}{\partial z} + \frac{u}{r}. \tag{2.11}$$

The energy equation becomes

$$\frac{1}{r}\frac{\partial}{\partial r}\left(\lambda r \frac{\partial T}{\partial r}\right) + \frac{1}{r^2}\frac{\partial}{\partial \theta}\left(\lambda \frac{\partial T}{\partial \theta}\right) + \frac{\partial}{\partial z}\left(\lambda \frac{\partial T}{\partial z}\right) + \Phi = \rho \frac{Dh}{Dt} - \frac{DP}{Dt} \tag{2.12}$$

with the dissipation function,

$$\begin{aligned} \Phi &= 2\mu \left[\left(\frac{\partial u}{\partial r}\right)^2 + \left(\frac{1}{r}\frac{\partial v}{\partial \theta} + \frac{u}{r}\right)^2 + \left(\frac{\partial w}{\partial z}\right)^2 \right] \\ &\quad + 2\mu \left[\frac{1}{2}\left(\frac{\partial v}{\partial r} - \frac{v}{r} + \frac{1}{r}\frac{\partial u}{\partial \theta}\right)^2 + \frac{1}{2}\left(\frac{1}{r}\frac{\partial w}{\partial \theta} + \frac{\partial v}{\partial z}\right)^2 \right] \\ &\quad + 2\mu \left[\frac{1}{2}\left(\frac{\partial u}{\partial z} + \frac{\partial w}{\partial r}\right)^2 - \frac{1}{3}\left(\nabla \mathbf{v}\right)^2 \right] \end{aligned} \tag{2.13}$$

and the substantive derivative as

$$\frac{D}{Dt} = \frac{\partial}{\partial t} + u\frac{\partial}{\partial r} + \frac{v}{r}\frac{\partial}{\partial \theta} + w\frac{\partial}{\partial z}. \tag{2.14}$$

For an ideal gas such as air, the enthalpy is given by

$$h = c_p T \tag{2.15}$$

where c_p is a weak function of temperature over the range of interest.

In general, the full Navier-Stokes equations are not required for the solution of a problem. For the most part we will deal with statistically steady flows where

$$\frac{\partial}{\partial t} = 0. \tag{2.16}$$

Many cases allow the assumption of axisymmetry

$$\frac{\partial}{\partial \theta} = 0. \tag{2.17}$$

At times, quasi-incompressible flows will be examined, permitting considerable simplification

$$\nabla \mathbf{v} = 0. \tag{2.18}$$

2.2.2 Simple Solutions of the Swirl Equation

It is instructive to look at the solutions of simplified forms of the Navier-Stokes equations. Batchelor [11] shows that for two dimensional incompressible flow with negligible radial velocities, the momentum equations reduce to a radial component,

$$\frac{\partial P}{\partial r} = \frac{\rho v^2}{r} \tag{2.19}$$

commonly known as *simple radial equilibrium*, and a circumferential component

$$\frac{\partial v}{\partial r} = \nu \left(\frac{\partial^2 v}{\partial r^2} + \frac{1}{r}\frac{\partial v}{\partial r} - \frac{v}{r^2} \right). \tag{2.20}$$

For the case of a steady, incompressible internal flow between two rotating cylinders of radii r_1 and r_2, and angular velocities Ω_1, Ω_2 respectively the equations admit a solution of the form

$$v = \frac{1}{r}\left(\frac{\Omega_1 - \Omega_2}{r_1^{-2} - r_2^{-2}} \right) + r\left(\frac{\Omega_1 r_1^2 - \Omega_2 r_2^2}{r_1^2 - r_2^2} \right). \tag{2.21}$$

Extreme cases of this solution illustrate three commonly found rotating flows that are of considerable use in interpreting physical phenomena.

The infinitely extensive fluid surrounding a rotating cylinder has a swirl velocity distribution given by putting $r_2 \to \infty$ and $\Omega_2 = 0$ so that

$$v = \frac{r_1^2 \Omega_1}{r}. \tag{2.22}$$

This result is termed a *free vortex*, and represents an irrotational distribution requiring the exertion of a constant frictional couple on the fluid of $4\pi\mu r_1^2\Omega_1$ by each unit length of the central cylinder. Note that while the fluid viscosity does affect the couple required to sustain the motion, the motion itself is independent of the viscosity so long as $\mu > 0$.

With the opposite extreme case of the flow inside a rotating cylinder, putting $r_1 = 0$ with Ω_1 finite gives

$$v = \Omega_2 r, \tag{2.23}$$

known as a *forced* vortex. In this case we have a rigid body rotation with the tangential stresses zero at all points. The rotating cylinder does no work on the internal fluid, but it must continue to rotate at a steady speed in order to maintain the flow. Again this distribution is independent of the fluid viscosity, subject to $\mu > 0$.

Many vortex flows far more complex than those considered above, including compressible flows with low axial velocity, can be interpreted qualitatively in terms of these results. In practice, jet driven vortex flows usually exhibit a central region approximating to a forced vortex, and a periphery with a roughly free vortex distribution satisfying the no slip condition at the tube wall. Together these are termed a Rankine vortex, and a sketch of the velocity distribution is shown in figure 2.2. Experimentally determined

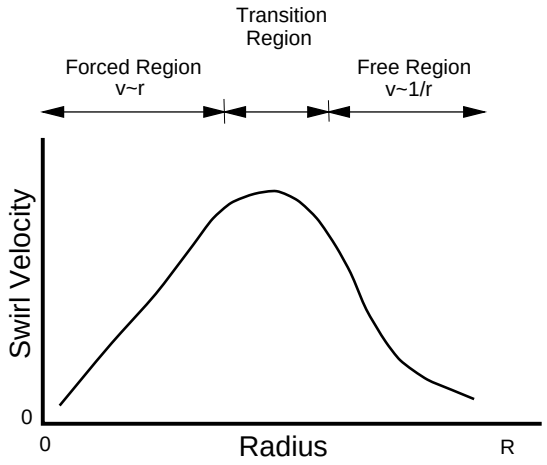

Figure 2.2: A sketch of the velocity distribution in a Rankine vortex.

flow distributions available in the literature are discussed in section 2.2.6 below.

2.2.3 Non-Dimensional Parameters : Ekman and Rossby numbers

Tritton [12] derives two non-dimensional quantities commonly employed in geophysics[1] to characterise rotating flows. We will not make substantial reference to them directly in this work, prefering to use some engineering equivalents, but they are important in understanding the wide range of literature on rotating flows.

The Rossby number Ro is defined as

$$Ro = \frac{U}{\Omega L} \tag{2.24}$$

and represents the ratio of inertial forces due to flow with a characteristic velocity U, to the effects of rotation with angular velocity Ω and characteristic length scale L. It is equivalent to the swirl number introduced in the section on dimensional analysis, 3.2.

The Ekman number Ek is defined

$$Ek = \frac{\nu}{\Omega L^2}. \tag{2.25}$$

where ν is the kinematic viscosity. Indicating the ratio of viscous to rotational forces, it is equivalent to the swirl Reynolds number more commonly employed in engineering. Both the numbers characterise the influence of rotation on the flow field and, as noted by Escudier [13], must be present in some form in any global consideration of rotating

[1]Geophysics often calls for the investigation of fluid flows in non-inertial frames of reference rotating with a constant angular velocity vector $\mathbf{\Omega}$. An example is the behaviour of winds over the rotating surface of the Earth. In such circumstances it is convenient to write the equations of motion for the fluid with respect to the rotating frame, which become with $\mathbf{u}$ as the velocity relative to the rotating frame,

$$\frac{\partial \mathbf{u}}{\partial t} + \mathbf{u}.\nabla\mathbf{u} = -\frac{1}{\rho}\nabla P - \mathbf{\Omega} \times (\mathbf{\Omega} \times \mathbf{r}) - 2\mathbf{\Omega} \times \mathbf{u} + \nu\nabla^2\mathbf{u}$$

Here $\mathbf{\Omega} \times (\mathbf{\Omega} \times \mathbf{r})$ is the *centrifugal* force and $2\mathbf{\Omega} \times \mathbf{u}$ is the *Coriolis* force. Both are fictitious forces that represent the effects of rotation. Generally, the Coriolis force is responsible for the peculiar behaviour of rotating flows. This term clearly has a scale of ΩL.

flows.

In the Ranque-Hilsch vortex tube we will find that the Ekman number is very small $Ek << 1$ over most of the flow field away from the walls. The Rossby number is typically small, but at $Ro = 0.1$, much larger than the Ekman number.

2.2.4 The Taylor-Proudman Theorem

For rotating flows with small Rossby and Ekman numbers, the equation of motion in a rotating co-ordinate system becomes

$$2\mathbf{\Omega} \times \mathbf{u} = -\frac{1}{\rho}\nabla P \tag{2.26}$$

where the pressure term P has been redefined to account for the effects of centrifugal force. Flows governed by this equation are termed *geostrophic*. Taking the curl of this equation gives for incompressible flows

$$\mathbf{\Omega}.\nabla\mathbf{u} = 0. \tag{2.27}$$

Choosing the axes such that

$$\mathbf{\Omega} = \Omega\hat{z}, \tag{2.28}$$

it is clear that

$$\frac{\partial \mathbf{u}}{\partial z} = 0. \tag{2.29}$$

This result, that there is no variation in the velocity field parallel to the axis of rotation, is known as the *Taylor–Proudman Theorem*.

As with many of the results in this section, the Taylor–Proudman Theorem is not directly applicable to the high-speed compressible flow in the Ranque-Hilsch tube. Indeed, the implication of the theorem for vortex tube type flows is that there can be no variation of the velocity field parallel to the axis of rotation, which is clearly untrue. However in the regions where there is an approximation to geostrophic flow, there does appear to

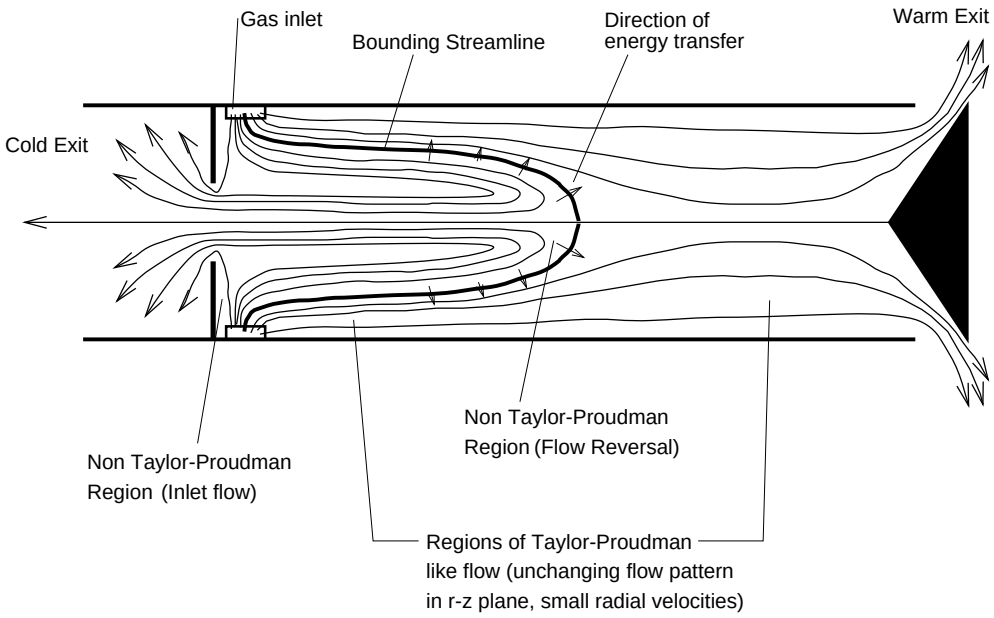

Figure 2.3: A sketch of the flow pattern in a counterflow vortex tube, based on a suggestion by Van Deemter [1].

be a definite resistance to axial changes. As an example, see figure 2.3 which shows a sketch of the flow pattern in a counterflow vortex tube based on a suggestion by Van Deemter [1]. Note how the flow pattern remains relatively unchanged along the axis as Taylor-Proudman would predict, apart from near the inlet nozzles, and the sudden flow reversal near the axis. Both these departures are attributable to viscous and compressibility effects.

2.2.5 Ekman Layers

On stationary planes perpendicular to the axis of rotation, the Ekman number becomes locally high as a 'rotating boundary layer' forms on the surface due to the action of viscosity. Such a region is known as an 'Ekman Layer', and is substantially different from 'conventional' boundary layers.

Greenspan [14] solves the Ekman layer for an infinitely extensive incompressible fluid in a rotating co-ordinate system, showing that the motion of fluid particles in the layer is

produced by a balance between viscous shear, the Coriolis force and the pressure gradient. For a *spin down* problem, which is essentially what we have at the stationary plane forming the orifice of a counterflow vortex tube, the radial pressure gradient[2] will overcome the Coriolis term and cause a net inwards flow. The direction of the flow velocity through the Ekman layer varies according to the so called *Ekman Spiral* such that the net velocity near to the wall is at 45^o to the velocity in the 'free stream'. The Ekman layer is always very thin, with a thickness $Ek^{\frac{1}{2}}$.

2.2.6 Rotating Flow in Cylindrical Ducts

Having reviewed the basic theoretical understanding of rotating flows, we will proceed by examining some of the experimentally observed features of rotating flows in cylindrical ducts. Attention will be focussed primarily on studies of jet driven rotating flows similar to that found in the Ranque-Hilsch tube, although some consideration will be given to flows induced by other techniques including vanes, and spiral tapers.

Comprehensive reviews of the behaviour of confined vortices in flow machinery are provided by Lewellen [15] and by Escudier [13].

The Steady Flow Field

The flow field in confined rotating flows has been investigated by a number of workers with a variety of techniques. A recent paper by Chang and Dhir [16] presents comprehensive results for a jet-driven air flow obtained with a hot-wire anemometer. A Rankine type vortex which exhibits an exponential decay in intensity as the flow progress along the tube and away from the inlets, is found over most of the cylindrical duct. Axial velocities are of a similar magnitude to the swirl, with a small region of reverse flow near the centre reducing in size with distance from the inlets. Radial flow is always directed inwards (towards decreasing radius) with a maximum magnitude less than one hundredth

[2]Ekman layers are usually dealt with in the rotating co-ordinate frame. Hence the use of the word pressure here strictly refers to the pressure corrected for the centrifugal force term.

of the maximum swirl velocity. The maximum radial flow always occurs near the 'knee' in the Rankine vortex profile.

Gyarmathy [17] describes optical measurements of the mass density in a high speed rotating air vortex, with a maximum Mach number exceeding 1.4. His estimates of the swirl Mach number suggest the existence of a Rankine type vortex over the majority of the flow field. He also notes a marked decrease in the static temperature of the gas near the centre of the vortex.

Flow in what they describe as a 'uniflow Ranque-Hilsch vortex tube' is examined by Holman and Moore [18]. They conclude that their swirl profiles can be adequately modelled by a relationship of the form

$$vr^n = c \tag{2.30}$$

where n and c are determined constants. This result provides a reasonable comparison with much of the inner portions of a Rankine vortex profile, until just beyond the knee. They also find that the effects of a jet driven flow can be modelled for 'engineering purposes' by an approximation that assumes the injected flow occupies an effective area that is independent of the flow rate. Thus the inlet swirl velocity just outside the nozzles could be calculated from

$$v_{in} = \frac{\dot{m}RT}{AP_{in}} \tag{2.31}$$

where $\dot{m}$ is the mass flow rate per nozzle, A is the effective area, T the inlet temperature, P_{in} is the pressure just outside the nozzle, and R is the gas constant. No attempt is made to justify this observation.

Escudier *et al.* [19] investigate the flow in a jet driven vortex tube with the inlet slit extending for the whole length, and operated on water. Employing non-intrusive techniques, they find a uniform axial velocity distribution, and a swirl velocity variation that can be closely modelled by the solution of Burgers [20],

$$v = \frac{\Gamma}{2\pi r}\left[1 - e^{\frac{\alpha r^2}{4\epsilon}}\right] \tag{2.32}$$

where Γ, α and ϵ are empirically determined constants. This expression gives a velocity distribution very similar to the Rankine distribution, and is also reminiscent of the Oseen [21, 22, 23] vortex

$$v = \frac{v_o r_o}{r}\left(1 - e^{-a(r/r_o)^2}\right) \tag{2.33}$$

where r_o is the diameter of the vortex tube and a is a constant[3]. Vatistas [24] confirms this result with measurements in an air driven cyclone chamber.

There are a large number of studies looking at the effects of particular geometries on the flow. Nejad and Ahmed [25] investigate the variation of swirl distributions through a step expansion in their containing duct. Gilham *et al.* [26] consider the self induced flow in a rotating tube with one end sealed and the other open to the atmosphere.

Turbulence

High speed rotating flows generally have high levels of turbulence. Moreover the turbulence differs from that in conventional 'straight' flows because it is anisotropic.

As well as their mean flow measurements discussed above, Chang and Dhir [16] present some turbulence measurements. The results show a clear anisotropy in the three components of the eddy viscosity calculated from the Reynolds stress components. A similar result is obtained by Kitoh [27].

Vortex Breakdown

Under certain conditions, rotating flows in ducts are seen to undergo a dramatic change as they progress along the duct. Such a change is known as a vortex breakdown and generally takes one of two forms. At moderate swirl Reynolds numbers and with low turbulence, a stable axisymmetric 'bubble' breakdown is found, as sketched in figure 2.4. With the higher Reynolds numbers and turbulence levels generally found in jet driven vortex tubes, the breakdown adopts the form of a precessing spiral, illustrated in figure

[3] In fact Oseen's solution is time dependent, so $a = 4\nu t/r_o^2$.

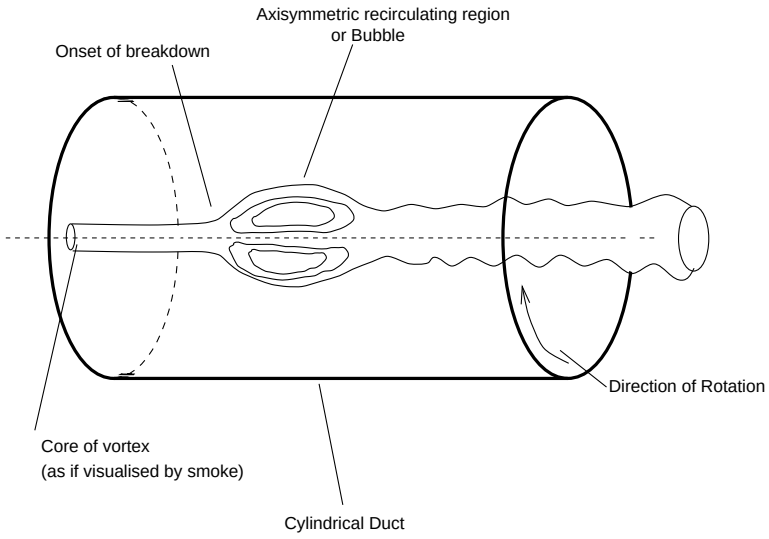

Figure 2.4: A 'bubble' breakdown.

2.5. The mean flow pattern is qualitatively indistinguishable between the two cases.

There is little agreement as to the physical processes at work in breakdowns, as shown in the varied discussions of Escudier and Keller [28, 29], and Faller and Leibovich [30, 31]. Early work by Benjamin [32] derives a generally accepted criticality condition for the flow, dependent on whether the axial flow velocity everywhere exceeds the relative phase velocity of longitudinal inertial waves travelling upstream and supported by the very rotation of the fluid. Breakdown then represents a change in the flow from super-critical, where the axial velocity exceeds the phase velocity, to a sub-critical state where the opposite is true.

Benjamin's criticality condition is very difficult to apply to practical flows. Squire [33] suggests a rule of thumb that a flow is supercritical if $v/w < 1$ at the position of maximum swirl. It will become clear later that this rule indicates that the majority of jet-driven vortex tubes have a sub-critical flow near their inlet. In a long tube however, the action of viscosity will tend to reduce the relative amount of swirl as the flow develops, perhaps to such an extent that the motion is rendered supercritical.

Breakdowns are also found where rotating flows are vented from ducts into still at-

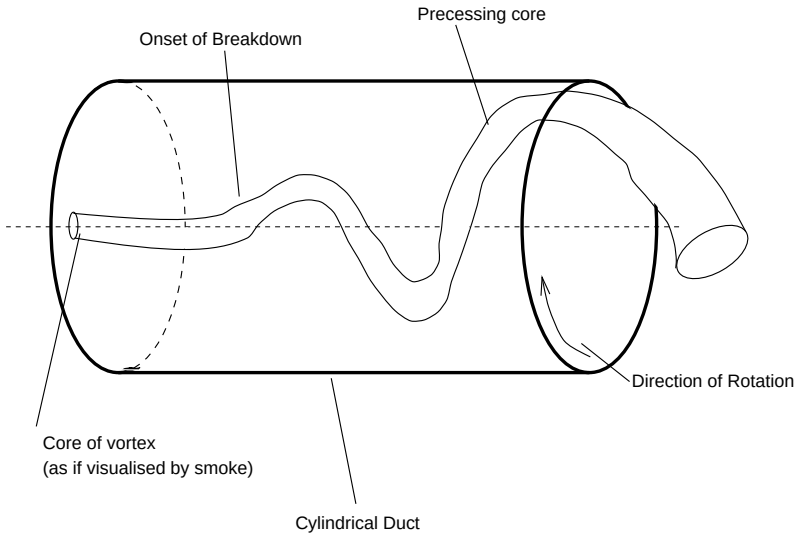

Figure 2.5: A 'spiral' breakdown.

mosphere. In these cases they are responsible for the periodic disturbances that are discussed further in section 2.2.7.

2.2.7 Periodic Disturbances in Rotating Flows

Inertial Waves

Fluids, whether incompressible or otherwise, rotating geostrophically with an angular velocity Ω can support inertial waves with angular frequencies up to 2Ω (see for example Greenspan [14] or Tritton [12]). In a rotating flow moving axially through a duct, inertial waves provide a mechanism for the upstream transmission of information where their phase velocity exceeds the axial velocity of the fluid.

The Vortex Whistle

Vonnegut [34] observed that a tone was produced by swirling flows passing from containing ducts into the still atmosphere. The sound was termed the *Vortex Whistle*. A substantial amount of work by Chanaud [35, 36] amongst others has attributed the noise

to the precession of the central region of the vortex as it enters the still air, in a manner similar to that seen with the spiral vortex breakdown.

2.2.8 Computation of Rotating Flows

General Techniques

Computation of rotating flows has been an active area of research for a number of years. Many studies are available in the literature using a variety of techniques. We will consider these after having established the nature of the equations needed to model the compressible swirling flow in the vortex tube.

In any computational study of vortex tubes, we would be interested in solving the viscous, turbulent, compressible flow equations in cylindrical co-ordinates. With recent advances in computer hardware, full three dimensional solutions of compressible flows using techniques for dealing with turbulence such as direct numerical simulation (DNS), and large eddy simulations (LES) have become possible[4]. Such methods are too complex for development here.

A minimum calculation of a vortex tube flow would constitute solution of the steady viscous compressible axisymmetric equations. Anderson [38] and Rosenzweig *et al.* [39] suggest that density changes have only a small influence on the flow pattern in the vortex tube, a fact employed by Linderstrom-Lang [40] in his analytic solution. In this case, a reasonable solution could be produced by solving the incompressible momentum equations, and then a compressible energy equation. This would also have the simplifying effect of decoupling the momentum and energy equations, influencing the choice of solution method. For this reason, much of the discussion here relates to incompressible flows.

To account for turbulence some kind of averaging procedure is required. For essen-

[4]For a discussion of the relationship between increasing computer power and the development of CFD, see Fletcher [37].

tially incompressible flows, the standard 'Reynolds decomposition' technique, writing

$$u = \bar{u} + u' \tag{2.34}$$

and then time averaging the entire equation can be applied. To avoid the appearance of third order correlations in calculations of flow with appreciable density variations, it is preferable to employ Favre averaging [41] by introducing mass weighted velocities and temperatures

$$\tilde{u} = \overline{\rho u}/\bar{\rho} \tag{2.35}$$

$$\tilde{T} = \overline{\rho T}/\bar{\rho}. \tag{2.36}$$

The dependent variables are split into average and fluctuating parts

$$u = \tilde{u} + u'' \tag{2.37}$$

$$T = \tilde{T} + T'' \tag{2.38}$$

except for the density and pressure which are decomposed in the normal way

$$\rho = \bar{\rho} + \rho' \tag{2.39}$$

$$P = \bar{P} + P'. \tag{2.40}$$

A turbulence model is used to 'close' the Reynolds stress correlations produced by the decomposition.

Turbulence Modelling

Most common turbulence models can be interpreted in terms of an eddy viscosity, whereby the Reynolds stresses are related to the mean flow quantities in such a way that the form of the governing equations remains unchanged from the laminar case. With incompress-

ible flows the relation between the modelled correlations and the mean flow quantities is often exact, in that no terms need be neglected. In compressible cases dealt with by Favre averaging, Cebeci and Smith [42] show that it is necessary to neglect some usually small terms. For such formulations, turbulence modelling is concerned with how to estimate the appropriate value of the eddy viscosity.

Deriving turbulence models for compressible flows does not present any special difficulty. Fletcher [37] states that models developed for incompressible flow can be used almost unchanged so long as the Mach number is less than five, and due account is taken of the variation of the mean density.

The effect of rotation on turbulence modelling is not so straightforward. Simple models, such as the commonly used $k-\epsilon$ model proposed by Jones and Launder [43], assume isotropic effects but as we saw earlier turbulence in rotating flows is highly anisotropic. Despite this handicap, the $k-\epsilon$ model produces creditable results, although as shown by Yang *et al.* [44], it significantly over predicts the axial decay of swirl.

A number of modifications to the standard $k-\epsilon$ model have been advanced which attempt to account for the anisotropy of the turbulence. In general these involve modifying the constants in the standard model equations by a factor dependent on the swirl. Leschziner and Rodi [45] suggest a method with reference to computing a strongly swirling axisymmetric free jet. Kim and Chung [46] derive an improvement by considering the Reynolds stress equations. In a slightly wider context, Ragsdale [47] examines the applicability of mixing length theory to turbulent vortices.

Still better results can be obtained by adopting a full Reynolds stress model (RSM). Armfield and Fletcher [48] demonstrate the accuracy of the solutions achieved in this way. Attempts to reduce the computational penalty of solving perhaps seven extra transport equations, imposed by the full Reynolds stress model in axisymmetric flow, have produced algebraic Reynolds stress models (ARSM) which replace the partial differential equations of the full implementation by algebraic expressions. The saving in time so generated more than offsets the slight inaccuracy introduced, although there can be stability problems as seen by Warfield and Lakshiminarayana [49].

Solution Techniques : Formulation and Discretisation

Many workers have employed the vorticity-streamfunction formulation for the calculation of quasi-steady strongly-swirling axisymmetric flows, taking advantage of the simplification of the momentum equations it provides in this essentially two-dimensional geometry. Despite having declined in popularity it still provides a fairly efficient and reliable method of calculating steady rotating flows. There are well known problems with respect to the implementation of certain boundary conditions, the calculation of turbulent flows, and achieving convergence where significant compressibility is present (see for example, Gosman *et al.* [50]). All these difficulties can be overcome however.

The majority of vorticity-streamfunction solutions are obtained through finite difference / finite volume discretisations, see for example Kubo and Gouldin [51]. Recently, finite element based solutions facilitating the use of unstructured grids have appeared. Elkaim *et al.* [52] use the technique to solve incompressible turbulent flow in axisymmetric geometries.

Primitive variable solution methods have become more popular in recent years, primarily thanks to their straightforward extension to three-dimensional geometries and greater suitability for flows evolving in time. While a multiplicity of solution techniques can be found, the most frequently employed is the SIMPLE algorithm, as found in the TEACH code due to Gosman *et al.* [53]. Strongly compressible flows, such as those found in gas centrifuges where peripheral densities may be many times those at the centre, demand specialised techniques as discussed by Harada [54], but are not likely to be necessary in the Ranque-Hilsch tube.

In general, primitive variable solutions employ finite differences and finite volumes as the method of discretisation. Finite element techniques present considerable obstacles in this context.

2.3 The Ranque–Hilsch Vortex Tube

2.3.1 Some Remarks on the Literature

The preceding sections have shown the scope of the field of rotating flows, and discussed its influence on our understanding of the Ranque-Hilsch tube. This section will narrow the consideration to work specifically concerning the Ranque-Hilsch vortex tube. After looking to some elementary results, attention will be focussed on experimental studies of the vortex tube. These will be considered in two groups, firstly external studies examining the performance of vortex tubes, and secondly internal studies which look at the internal flow patterns. Next, theoretical investigations of the vortex tube will be reviewed, following which numerical studies will be discussed. While works looking at the mixture separation abilities of the tube are examined, there will be no consideration of proposed applications, as this will be left until chapter 7.

It will become clear that there are almost as many approaches to understanding the Ranque-Hilsch effect as there are publications discussing it. Much of the published work, indeed, is contradictory. One of the purposes of this section is to attempt to distill, from the mass of information, a platform on which further work can be based.

2.3.2 Basic Analysis

Thermodynamics

Neglecting the flow velocities at the outlet[5], and applying the First Law of Thermodynamics to a system consisting of the compressed gas reservoir and the vortex tube, Hilsch [4] shows that the fraction of gas leaving through the cold exit μ_c is given by

$$\mu_c = \frac{T_{in} - T_h}{T_c - T_h}. \tag{2.41}$$

[5]This is a reasonable assumption for a long tube as used by Hilsch.

The specific entropy change of the fluid passing through the tube is given by

$$\Delta s = \mu_c \left(s_c - s_{in}\right) + \left(1 - \mu_c\right) \left(s_h - s_{in}\right) \tag{2.42}$$

or for an ideal gas, such as air

$$\Delta s = c_p \; ln \left(1 - \frac{\Delta T_c}{T_{in}}\right) + R \; ln \left(\frac{P_{in}}{P_c}\right). \tag{2.43}$$

Fluid Dynamics

The reservoir pressures employed by Ranque and Hilsch make it clear that the speed of swirl in the vortex tube is likely to approach sonic velocity. Indeed, from their observations high speed swirl appears necessary to obtain significant energy separation. Axial velocities will be substantial, but not as large as the swirl velocities. It might be anticipated then, that the flow would be compressible. The high swirl Reynolds number of the flow, and the rather abrupt means of gas injection would indicate the presence of high levels of turbulence as well.

Our examination of swirling duct flow has suggested that a Rankine type vortex should be anticipated in the tube. In this case the predominant pressure gradient will lie in the radial direction, providing the centripetal force for the circular motion of fluid particles, giving low pressure towards the centre and high pressure at the periphery. A secondary pressure gradient will exist between the inlet plane and the exits of the vortex tube. At the periphery of the tube this will always be positive, driving a flow axially towards the exit. Resolution of this with the radial pressure gradient imposed by the vortex, however, can result in an adverse pressure gradient near the centre-line. In the light of this, we should expect regions of recirculating flow near the centre-line of the tube.

2.3.3 Experimental Studies

Our discussion of experimentally oriented studies of the Ranque-Hilsch tube will begin with those works that examine the device from outside. After investigating the range of techniques that might be suited to an internal survey of the tube, the results of a number of experiments in the literature will be reviewed. Attention will then turn to any remaining works.

External Studies

Most external investigations of the vortex tube have consisted of essentially empirical attempts to improve its performance. A number of workers mention the effects of tapering the vortex tube, with conflicting results. Borisenko *et al.* [55] find that a conical cold tube has no effect on a counterflow tube, while a 3^o conical expansion in the hot tube gives optimal performance. Gulyaev [56] also finds that a conical expansion brings improvements, and a patent application by the Khark Aviation Institute [57] mentions expanding hot and cold tubes. Martynovskii and Alekseev [58] however, find a contracting hot tube to be preferable. Raiskii and Tunkel [59] in contrast find it impossible to better the performance of a cylindrical hot tube, noting that the majority of the energy transfer appears to occur within the first five diameters of the tube.

There is more agreement regarding other dimensions. All authors find that an efficient tube of either design must be many times longer than its diameter. Gulyaev [56] recommends a minimum length of thirteen times the diameter, and Martynovskii and Alekseev [58] get optimum performance for $40 < L/D < 50$. This is comparable to Hilsch's [4] comment that L/D should be around 50 for good temperature separation. Using the method of Evolutionary Operations, Soni and Thompson deduce $L/D > 45$. Optimum orifice diameters d mostly lie in the range $0.4 < d/D < 0.6$.

Martynovskii and Alekseev [58] make a number of notable observations with their counterflow tubes. Firstly, they cool the exterior of the hot tube, and find a consequent reduction in the temperature of the *cold* flow. Secondly, they find that allowing the cir-

cular wall of the hot tube to rotate in sympathy with the gas has no effect on the energy separation. Lastly they manage to produce an inverted temperature separation for certain small cold gas fractions, whereby the gas passing through the orifice has a higher stagnation temperature than that leaving at the valve.

Mentenin [60] examines the effect of including a flow straightener near the hot exit of the vortex tube. Paruleker [61] presents the results of his experiments with a short vortex tube, and investigates the possibility of building a 'vortex tube within a vortex tube', such that the still swirling cold efflux of one tube is fed directly into another and cooled further still. Arkharov *et al.* [62] describes a counterflow tube design supposedly gaining improved performance from the inclusion of a resonance chamber near the inlet nozzles

Techniques for Internal Studies

The vast majority of the works studying the flow internal to the vortex tube have employed intrusive techniques. While convenient, such methods are unsuited to investigations of high speed, rotating, compressible internal flows. As Reynolds [63] and others note, insertion of probes into the flow can cause substantial disruption to the flow pattern. There are a number of reasons for this. In sub-critical flows, information can be transmitted upstream through inertial waves, causing disruption to the whole pattern both ahead and behind the probe. Furthermore, the very rotation of the flow will often cause the probe to be affected by its own wake, giving inaccurate and widely fluctuating readings.

An obvious solution to these problems is to use the more modern non-intrusive measurement techniques. Unfortunately, the confined three dimensional nature of the flow can make these difficult too. Whole field approaches, such as the particle image velocimetry (P.I.V.) scheme described by Armstrong [64] and Adrian [65] amongst others, are impractical thanks firstly to difficulties in interpreting the recorded image which is distorted by the lens-like curved surface of the vortex tube, and secondly to the geometrical

constraints imposed by attempts to illuminate and photograph a confined space with limited access. Neither of the problems is insurmountable, and although their solution would provide an extremely useful measurement tool, such work is outside the scope or budget of this thesis.

Only laser-Doppler anemometry (L.D.A.), as described by Durst *et al.* [66] remains as a technique directly applicable to the vortex tube. This though represents a cumbersome method to map a whole flow field, requiring substantial setting up each time the point of measurement is moved, and is not without practical difficulties. Once again, the curved surfaces of the vortex tube do present some optical problems. Since L.D.A. requires a substantial density of seeding particles for good results, the strong rotation of the flow can preclude accurate measurement of the flow velocity towards the centre of the tube, as the particles tend to be centrifuged towards the periphery of the flow.

An alternative approach is to estimate the effect of the insertion of the probe and attempt to correct for it. A methodology for this was developed by Taylor [67] for incompressible rotating flows, which extrapolates the readings obtained by a series of geometrically similar probes of different diameters to predict that expected for a probe of zero diameter. There is some potential for application to vortex tube measurements, but it seems unlikely that the range of probe sizes required for good results can be used with the vortex tube. The analysis assumes that the inserted probes merely perturb the flow, whereas the large diameter probes would cause a dramatic change in the flow within the Ranque-Hilsch tube.

Accurate measurement of vortex tube flows is difficult. As Reynolds [63] remarks, all the data obtained by intrusive methods must be considered equally suspect.

Results of Internal Studies

Most authors investigate counterflow tubes. Hartnett and Eckert [68, 69] have a typical rig, using a 75 mm diameter Plexiglas vortex tube with 8 inlet nozzles. Internal readings are taken with intrusive probes, for excess inlet pressures ranging from 68 kPa to 136

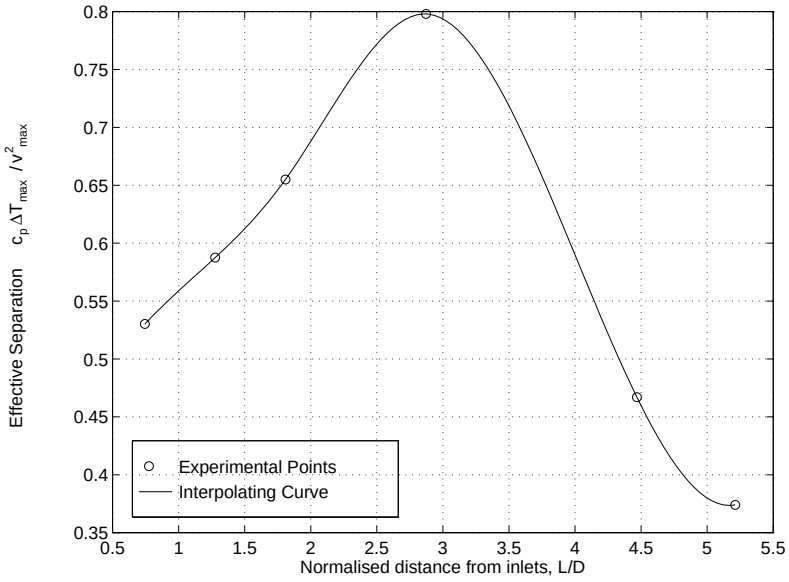

Figure 2.6: Effective energy separation as a function of axial distance from the inlet plane for Brunn's counterflow tube.

kPa. Their results show a Rankine-like vortex at all stations within their tube, and an almost linear increase in stagnation temperature with radius. There is a noticeable reduction in the stagnation temperature difference between the centre and the periphery of the tube as the flow reaches the hot exit. This though is hardly surprising, as the coldest air escapes through the orifice without travelling far down the tube, and there is evidence of heat transfer with the surroundings. Indeed, despite the partial decay of the vortex, the 'relative' separation, gauged by $c_p \Delta T_0 / v^2_{max}$, increases as the flow progresses. Some recirculation is evident near the centreline. With a 94 mm diameter Plexiglas counterflow tube, Bruun [70] obtains very similar results. Estimates of values of $c_p \Delta T / v^2_{max}$ as a function of axial distance from the inlet are plotted in figure 2.6. Further data taken by Takahama [71] in tubes with diameters ranging from 27.6 mm to 78 mm is comparable. Takahama and Soga [72] provide additional information.

A counterflow vortex tube with a divergent hot chamber is investigated by Takahama and Yokosawa [73]. The results were not markedly different from tubes of conventional

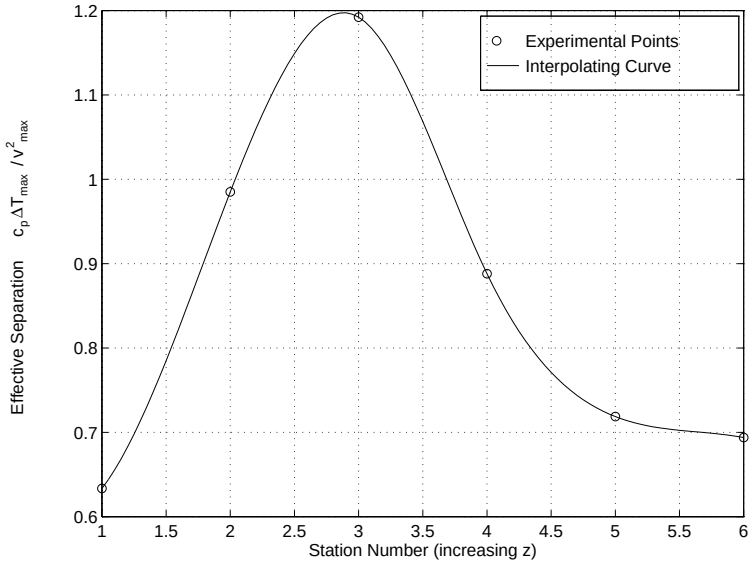

Figure 2.7: Effective energy separation as a function of axial distance from the inlet plane for Lay's uniflow tube. Note that Lay does not give details of the axial position of his stations, although they are at an approximately equal spacing. Larger station numbers are further from the inlets.

design, although the swirl was found to decay less rapidly.

Lay [74] examines flow in a uniflow tube operated at reservoir pressures between 68 kPa and 238 kPa. All the profiles within the tube are comparable to those found in counterflow tubes. Once again, there is some evidence of an axial development of the energy separation. A plot of the value of the effective energy separation parameter $c_p \Delta T_0 / v^2_{max}$ as a function of station number is shown in figure 2.7.

Effect of Fluids other than Air

A vortex tube operated on steam gives performance characteristics qualitatively similar to those that would be obtained with air. Experiments by Starostin and Itkin [75] show that for substantial separations, say 70 K between the hot and cold streams, a much larger inlet reservoir pressure is necessary than with air. Work by Takahama *et al.* [76] establishes that the Ranque-Hilsch effect diminishes as the wetness fraction of the steam

increases.

Gaseous hydrocarbons also exhibit the Ranque-Hilsch effect. Williams [77] expands methane through a counterflow vortex tube, obtaining performance characteristics very similar to those of air. Collins and Lovelace [78] examine the effect of the vortex tube on two phase propane. As with steam, they find that performance declines for wetness fractions greater than 0.2.

High pressure water is introduced into a commercially (Vortec Corp. [79]) available counterflow Ranque-Hilsch tube by Balmer [80]. He shows there there is no thermodynamic reason why energy separation in liquids should not occur, and finds experimental evidence of a radial temperature gradient at very high inlet pressures. No net cooling is found though, and the energy separation seems attributable to viscous effects.

2.3.4 Theoretical Studies

Early workers, including Hilsch [4], attributed the energy separation in the vortex tube to a change in the swirl velocity profile from a free vortex near the inlet nozzles to a forced vortex further along the tube. Viscous dissipation was envisaged as producing the final radial temperature separation. While such a transformation would indeed represent an energy transfer from the centre of the flow to the periphery as shown by Kassner and Koernschild [81], it seems extremely unlikely that it is in fact the mechanism responsible for the behaviour of the Ranque-Hilsch tube. For one thing, none of the experimental studies of vortex tubes have found any evidence of a free vortex near the inlet. For another, there does not seem to be any physical process that could be responsible for such an effect. Kurosaka's [8] acoustic streaming comes close, but does not envision the axial development assumed by others.

Many detailed analytic investigations of the Ranque-Hilsch tube have been published in the last half century, although there has not been any significant advance since 1982. The rest of our discussion will be limited to these more recent publications, as many of them cover similar ground to their predecessors such as Fulton [82], Scheper [83],

Scheller and Brown [84].

Deissler and Perlmutter consider a planar, axially symmetric compressible vortex. Employing a turbulent diffusivity ϵ, they produce an analytic solution of the swirl equation

$$\rho u \frac{\partial v}{\partial r} + \frac{\rho u v}{r} = \rho \epsilon \left(\frac{\partial^2 v}{\partial r^2} + \frac{1}{r} \frac{\partial v}{\partial r} - \frac{v^2}{r} \right) \tag{2.44}$$

by specifying an axial velocity distribution and using continuity to deduce a compatible radial flow profile. The result gives Rankine like profiles qualitatively comparable to those obtained experimentally. Using an energy equation modified to account for the expansion and contraction of eddies within the radial pressure gradient produces stagnation temperature curves broadly comparable with the results of Hartnett and Eckert [68]. A similar, less complete, analysis is given by Van Deemter [1] who reaches the same conclusions.

Hinze [85] also cites the behaviour of eddies in the radial pressure gradient as involved in the energy separation. Say that the relationship between the mean radial temperature and pressure distributions is other than what might be termed *adiabatic*, given for an ideal gas by

$$\frac{T}{T_1} = \left(\frac{P}{P_1} \right)^{\frac{\gamma - 1}{\gamma}} . \tag{2.45}$$

Assuming that the turbulent motion of the air particles is approximately adiabatic, then their expansion or contraction in the radial pressure gradient will cause them to adopt a temperature different to that of their surroundings. Once the fluid particle reaches its destination, then it will come into thermal equilibrium with its surroundings, resulting in net heat flux. The implications of this mechanism are considered further in chapter 5.

Sibulkin [86] includes axial variations in his solution by replacing variations in z with a variation in time t. By assuming the Mach number to be much less than unity throughout the flow field, the Navier-Stokes equations are decoupled from the energy equation, as the gas density no longer depends on temperature. This allows calculation of velocity profiles at points along the axis of a vortex tube (i.e. with increasing time) using numer-

ical methods previously developed by Sibulkin [87, 88]. An initial velocity profile is required to represent the behaviour of the gas at the tangential inlets. Sibulkin assumes that the inflowing gas occupies an annulus of the same height as the inlet nozzles, while the gas at the 'core' remains undisturbed. Performance curves for the behaviour of a vortex tube with cold gas fraction are estimated by integrating the energy equation for a fluid element travelling along the centre-line of a counterflow tube. Comparison of the results with some experimental data appears favourable, and Sibulkin concludes that the Ranque-Hilsch effect is due to the differential expansion of the core and peripheral gas as it travels axially up the tube from the inlet, and to thermal conduction from the quiescent core to the high speed periphery.

Linderstrom-Lang [40] presents a incompressible, axisymmetric potential solution of the Navier-Stokes equations, based on a method developed by Lewellen [89]. An order of magnitude analysis reduces the turbulent energy equation to a balance between four terms, namely axial and radial convection by the mean flow, turbulent conduction radially, and a turbulent dissipation term. The radial conduction term is evaluated with a thermal eddy viscosity and accounts for the effect of the radial pressure gradient. An eddy viscosity is also used to model the dissipation. A parameter study based on his results deduces that the Energy number, the cold mass flow fraction, the turbulent Reynolds number and the 'amount' of radial flow in the overall flow pattern are all strong influences on the energy separation. The results stand comparison with experiment.

Linderstrom-Lang also explores a heat-exchanger analogy for vortex tube operation, originally proposed by Scheper [83]. Considering the work of Cohen [90] in the field of isotopic enrichment, a value function to represent the effect of the tube on the gas passing through it is derived.

In a comprehensive general discussion of Ranque–Hilsch tubes, Gulayev [91] reviews a number of works. Using a semi-empirical theory of the vortex tube, he deduces that turbulent heat transfer between the parallel streams of flow is responsible for the effect.

A radical departure from 'conventional' theories is offered by Kurosaka [8] who proposes acoustic streaming as the mechanism of energy separation. A perturbation ana-

lysis suggests that acoustic energy generated by the vortex whistle could be deposited at the periphery of the flow, thereby transforming a base Rankine vortex into a forced vortex. Detailed discussion will be presented with some experiments in chapter 3.

Lay [74, 92] gives a flow-field solution by superposing independent potential type calculations of the axial and swirl velocity fields. No solution for the temperature field is provided, although Lay suggests that there is evidence of a transformation in the swirl velocity profile from a free to forced vortex.

2.3.5 Computational Fluid Dynamics Studies

It is surprising perhaps that there has been only one published attempt to simulate the Ranque-Hilsch vortex tube using numerical techniques. Kahlil *et al.* [93] give detailed results for a calculation of the flow field within a counterflow vortex tube similar to that employed by Bruun [70]. Using the SIMPLE finite volume method developed by Gosman *et al.* [53], and the $k - \epsilon$ turbulence model, the estimated flow compares well with experiment. Curiously, no mention is made of any attempt to calculate the temperature field within the tube.

2.3.6 Mixture Separation – Centrifugation Effects

The swirling flow within the vortex tube provides a mechanical separation effect that can be used to filter solid particles from a gas flow or alter the isotopic composition of gaseous mixtures. A number of authors have investigated the potential of the Ranque-Hilsch tube in this context, including Stone and Love [94], Elser and Hoch [95], Baker and Rothkamp [96], and Torochesnikov and Koval [97] amongst others. As with the thermal effect, there has been little agreement regarding the physical mechanism of the mixture separation.

A comprehensive work by Linderstrom-Lang [98] investigates the oxygen concentration of air leaving the hot and cold exits of a modified vortex tube. Measurements show a discernible, although small, difference in concentration between the two streams. In

general, the hot outer flow is found to be enriched in oxygen, the heavier component of the air[6], although at low flow rates through the cold exit the separation is reversed. Linderstrom-Lang deduces that there is no direct connection between the energy and isotopic separations, the former being attributable entirely to centrifugation. Certain peculiarities in the internal flow patterns proposed account for the reversal of the separation.

Marshall [99] passes a number of different gases through a vortex tube based on the design of Linderstrom-Lang. The results tend to confirm that centrifugation is the primary mechanism of separation, and reveal an optimum inlet Reynolds number for maximum separative effect. Schlenker [100] describes a vortex tube isotope separator that has its performance improved with the aid of a beam of discrete frequency electro-magnetic waves directed its the centre-line to excite the required component.

Also of note in this context is the gaseous fission rocket concept. Developed theoretically during the late 1950's and 1960's, this proposed containing a cloud of heavy fissionable material within a jet driven vortex tube, while allowing a hydrogen propellant to pass through and escape out of a narrow central orifice at one end. The propellant would be heated by the fissioning material and leave at sufficiently high velocity so as to provide a substantial thrust. The fissionable material would be centrifuged towards the periphery of the vortex tube, and thence unable to escape. Keyes [101] for example, presents experiments studying the radial concentration of a heavy hydrocarbon suspended in helium when passed through a vortex tube, finding substantial separation. Kerrebrock and Meghreblian [102] give an analysis of the likely flow pattern, assuming that the flow remains laminar. This is extended to a turbulent case by Rosenzweig *et al.* [103].

[6]For the purposes of this discussion, assume that air is a binary mixture of nitrogen and oxygen.

2.4 Other Relevant Phenomena

There are a number of poorly understood energy separation phenomena that are worth considering partly for completeness and partly for comparison with the Ranque-Hilsch effect. A review of such phenomena in general, is provided by Eckert [104], who considers energy separation in boundary layers, impinging jets, and resonance tubes. Reynolds [105] discusses energy separation in an aerodynamic context.

2.4.1 The Eckert-Weise Effect

The Eckert-Weise effect refers to the cooling found in the wake of a bluff body obstructing a flow of appreciable Mach number. Kurosaka *et al.* [106] investigate the energy separation found in the von Karman vortex street behind a cylinder with its axis at right angles to an air flow. Their conclusion that the separation is caused by the action of the shed vortices in the positive pressure gradient from the centre of the wake to the free stream is notable for its similarity to certain explanations advanced for the vortex tube.

2.4.2 Temperature Anomalies in Stars

It is known in astrophysics that the exterior layers of certain stars are hotter than simple heat transfer models would predict. The majority of the body's heat is produced through fusion near the centre of the star, and naively one would anticipate a gradual reduction in temperature with radial distance from the centre. In practice a temperature minimum is found within the exterior layers, beyond which exists a limited region where temperature increases with radius. This temperature distribution is notable thanks to its apparent similarity to the Ranque-Hilsch effect. The work of Mullan and Cheng [107] amongst many others has suggested that this energy transfer can be attributed to acoustic streaming.

2.5 Discussion

2.5.1 On the Nature of the Ranque-Hilsch Effect

A number of deductions as to the nature of the Ranque-Hilsch effect can be drawn from our review of the literature. We will attempt to bring together the information from the literature survey, without referring to the specific results or theories:

1. Energy separation is related directly to the swirl. The greater the swirl, the greater the energy separation.
2. The energy separation shows evidence of axial development in the region near the inlet. In other words the separation increases as the flow progresses axially, at least along the first few diameter lengths. Interpretation of data is difficult however, as the swirl decays with axial distance and as noted above, the energy separation potential depends directly on the level of swirl. Gauging the 'effective' separation by the ratio of the maximum temperature difference to the maximum swirl velocity provided a reasonably clear picture of the development.
3. Pre-existing energy separations appear to be supported by swirl, at temperature differences greater than those which the swirl could itself generate. Towards the exits of the tubes, the swirl decays substantially, but the energy separation does not decrease in proportion.
4. There is considerable dispute as to the nature of the swirl velocity profiles in the vortex tube. Early workers suggest the presence of a free vortex. Experimental evidence from a number of environments does not support this, reporting Rankine vortex and forced vortex-like patterns. Reports that the effects of jet driven vortex flows can be modelled by considering the inlet flow as confined to a peripheral band, combined with Batchelor's result for flows inside a rotating cylinder would appear to support the existence of Rankine

vortices.

5. The axial flow pattern in both types of vortex tube can be interpreted qualitatively with reference to the Taylor-Proudman theorem. Regions of recirculation near the centre-line can be accounted for by virtue of the adverse pressure gradient found there, and posses a qualitative similarity with vortex breakdown.

6. Comparison of the results of feeding compressible gases and essentially incompressible liquids through vortex tubes indicate that compressibility is not essential for the appearance of an energy separation. Its presence is essential for there to be substantial cooling, and aids separation generally. This conclusion also agrees with the results of operating vortex tubes on two-phase substances, where performance declines with increasing wetness fraction.

7. There are high levels of turbulence in all jet driven vortex flows. Clearly turbulence must have some influence on the energy separation, but we cannot draw any conclusions regarding its importance. A number of mechanisms by which turbulent transport in a strong pressure gradient could produce an energy separation have been advanced.

8. Periodic disturbances are supported by rotating flows in the form of inertial waves. There is considerable experimental evidence for their existence in geometries similar to the Ranque-Hilsch tube. There are reports of such disturbances, in the form of the vortex whistle, with regard to the vortex tube although their source has not been determined. A mechanism citing periodic disturbances as responsible for the Ranque-Hilsch effect has been advanced.

9. Analytic studies have suggested that viscous effects can at least contribute to any energy separation.

10. It has been suggested that the physical separation of substances with different atomic masses in the vortex tube is not directly connected with energy separation, excluding the fact that both require swirl.

2.5.2 The Comparison of Temperature Distributions from Uniflow and Counterflow tubes

As both the uniflow and counterflow tubes exhibit the Ranque-Hilsch effect it would be useful to determine how to compare radial temperature distributions from tubes of each type with similar geometries. Since the axial flow velocities within the tubes are reported to be much smaller than the swirl velocities, it is unlikely that they have a great effect on the radial temperature distribution. It would be reasonable in this light to compare temperature distributions where the flow patterns in the tubes are similar, in other words in the region from the inlet nozzles up to the sudden reversal of the central flow in the counterflow tube. Beyond this point, near to the control valve, the radial profiles are not comparable as the cold central gas has been 'syphoned' off in the counterflow tube.

This suggestion is compatible with one observation. Comparison of the effective separation curves for counterflow (figure 2.6) and uniflow tubes (figure 2.7) shows that the effective separation in the counterflow tube declines much faster as the valve is approached. This is because the central cold flow has been removed ion the counterflow case. In the section near the inlet nozzles, the two tubes give a similar axial development of separation.

2.6 Implications for Investigations of the Ranque-Hilsch Vortex Tube

Our survey of the vortex tube has highlighted four areas worthy of further attention. Particularly useful would be a series of experiments with the objectives of confirming certain existing results, obtaining data for later use in an empirical model and comparison with any theory, and further investigation of the mechanism underlying the energy separation, in particular the swirl velocity profiles and the nature of any periodic disturbances in the flow.

Secondly there is plenty of potential for the application of CFD techniques to the vortex tube. A program that gave results even with only a qualitative similarity to experimental values would be extremely useful, both to provide insight for this project, and as a design tool for the future.

It is unlikely that any analytic model of the vortex tube can hope to achieve an agreement with reality that is better then qualitative. There is scope, however, for analytical investigations of possible mechanisms of energy transfer, and of factors which might influence the Ranque-Hilsch effect. This will be our third objective, which we will supplement by attempting to produce an empirical model of vortex tube performance.

Completion of the above should provide sufficient knowledge to allow the final objective to be tackled, specifically a pilot study of potential applications for Ranque-Hilsch tubes. Ranque's interest in the vortex tube was motivated partly by its potential application to gas liquefaction, and we shall look at this in some detail. Further consideration will also be given to the utility of the vortex tube in isotope separation.

2.7 Closure

In this chapter we have reviewed current knowledge regarding the Ranque-Hilsch vortex tube. Efforts have been made to encapsulate its important features, and areas likely to benefit from further attention have been identified.

Chapter 3

Preliminary Investigations and Experiments

3.1 Opening Remarks

In this chapter some of the more important features of the vortex tube highlighted by the literature survey will be investigated further. We will start by conducting a thought experiment to establish which features of a vortex tube might influence its performance, and then perform dimensional analysis on the results. While useful in that it provides us with a set of non-dimensional parameters with which to describe vortex tubes, it turns out to be a difficult path.

Next we will consider a set of experiments conducted to shed some light on the flow in vortex tubes, and in the process examine in depth a few of the ideas touched on earlier. The work was performed using an existing set of vortex tubes, and the section begins by discussing their more important features. Some initial experiments serve merely to characterise the tubes, and examine the validity of earlier works. They are worthy of consideration, however, as they bring out many remarkable features of vortex tubes. Careful analysis is made of the errors inherent in most of this work, partly to provide a clear impression of the limitations of the techniques employed, and partly to serve as an example

to future workers in the field.

Towards the end of the chapter, the possible influence of acoustic streaming in the Ranque-Hilsch tube is examined in some depth. After drawing conclusions from the available evidence, the results of a number of experiments investigating acoustical disturbances in the CUED tubes are presented.

3.2 Dimensional Analysis

3.2.1 Background

The vortex tube and Ranque-Hilsch effect constitute a complex situation. Frequently, in such circumstances, the technique of dimensional analysis is employed in an attempt to set the direction of any further work.

Stephan [108] performed an approximate analysis for geometrically similar counterflow tubes, yielding,

$$\frac{\Delta T_c}{(\Delta T_c)_{max}} = f(\mu_c). \tag{3.1}$$

where ΔT_c is the cold tube temperature drop, $(\Delta T_c)_{max}$ is the maximum value of ΔT_c as the fraction of gas leaving through the cold port μ_c, is varied across its range of $(0, 1)$, while all other parameters are held constant. As is shown in section 3.4.4, this result is well born out in practice.

Westley [109] attempted empirically to optimise counterflow vortex tube performance by varying parameters according to the non-dimensional relationship

$$\frac{\Delta T_c}{T_{in}} = f\left(R,\ \frac{P_{in}}{P_c},\ \frac{d_c}{D},\ \frac{d_{in}}{D}\right). \tag{3.2}$$

with T_{in} representing the inlet (static) temperature of the gas, P_{in} the inlet (static) pressure, P_c the static pressure in the cold outlet, d_c the diameter of the orifice, D the inner diameter of the main vortex tube and d_{in} the effective diameter of the inlet nozzles, defined as the diameter of a circle with the same area as the inlet nozzles. R represents the set-

ting of the control valve at the hot exit, calculated by dividing the distance the valve has been withdrawn from the tube by its maximum extent of travel, and may be thought of as a non-linear function of the cold exit mass flow proportion, μ_c.

Unfortunately, neither of these results is easy to extend directly. In the light of this a fresh approach, based on the earlier parts of Stephan's work, was adopted.

3.2.2 Analysis

Consider a counterflow vortex tube. The factors that might be expected to influence its performance are listed, with their symbols and dimensions in table 3.1. Note that the size of the cold outlet tube is omitted for two reasons; firstly a number of experiments have observed that its length has a negligible effect on the flow in the remainder of the tube, and secondly, its neglect renders the analysis immediately applicable to uniflow type vortex tubes, by substituting the diameter of the cold outlet nozzle in the control valve for that of the orifice diameter in the counterflow tube.

It is worth pointing out that not all the parameters listed are *completely* uncorrelated. In particular, the cold mass flow fraction μ_c, will be a function primarily of the orifice diameter d_c, the effective diameter of the hot exit d_h, the overall dimensions of the tube L,D, and the static pressures at both outlets, P_c, P_h. It is however, useful to consider the cold mass flow fraction as an independent variable since (i) in many cases one would expect it to be a fairly weak function of the other parameters and (ii) it provides a useful 'flow-oriented' parameter, especially in geometrically similar tubes. This redundancy must be considered when performing the dimensional analysis. It would not be sensible to maintain both d_h and μ_c when examining, for example, otherwise[1] geometrically similar tubes operated under identical sets of inlet and outlet conditions over a range of

[1]The word 'otherwise' is used advisedly here, since strictly, the tubes are not geometrically similar unless d_h^* is the same in each case. However, it is conventional in vortex tube analysis to ignore this fact, see, as an example, Stephan [110, 108] or Wesley [9, 109, 111]. This is also convenient, moreover, as it is useful to model the dependence of performance on d_h^* or μ_c. See the following text for some elaboration.

Variable Name	Symbol	Dimensions
Geometrical Parameters		
(Hot) Tube length	L	L
Tube internal diameter	D	L
Inlet nozzle effective diameter	δ	L
Orifice diameter	d_c	L
Effective diameter of hot flow exit restriction (i.e. of the area between the tube wall and the valve)	d_h	L
Mass Flows		
Mass fraction of flow leaving through cold exit	μ_c	1
Overall mass flow rate	$\dot{m}$	MT^{-1}
Reservoir Conditions		
Inlet (reservoir) pressure	P_{in}	$ML^{-1}T^{-2}$
Inlet (reservoir) temperature	T_{in}	Θ
Gas density at tube inlet	ρ_{in}	ML^{-3}
Gas Properties		
Gas viscosity	μ	$ML^{-1}T^{-1}$
Gas thermal conductivity	λ	$MLT^{-3}\Theta^{-1}$
Heat capacity of gas at constant pressure	c_p	$L^2T^{-2}\Theta^{-1}$
Gas isentropic exponent	γ	1
Gas coefficient of thermal expansivity	β	Θ^{-1}
Mole fraction of gas component i in any mixture, at the inlet	$(X_i)_{in}$	1
Internal Flow Parameters		
Static pressure at cold exit	P_c	$ML^{-1}T^{-2}$
Static pressure at hot exit	P_h	$ML^{-1}T^{-2}$
Swirl (azimuthal) velocity at tube inlet	v_o	LT^{-1}
Co-ordinates		
Co-ordinates in 3 dimensions	r,θ,z	L
Other Factors (Not considered here)		
Tube material		
Internal roughness		
Gas molecular mass		

Table 3.1: Independent variables influencing the flow in counterflow vortex tubes. The dimensions should be interpreted according to the conventional scheme, viz.: M represents dimensions of mass; L, those of length; T, of time and Θ, of temperature.

values of d_h and μ_c, as, on the basis of the above,

$$\mu_c = f_1\left(d_c^*,\ L^*,\ D^*,\ P_c^*,\ P_h^*,\ d_h^*\right) \tag{3.3}$$

where * denotes a non-dimensional quantity, with d_c^*, L^*, D^*, P_c^*, and P_h^* invariant between the tubes, leaving,

$$\mu_c = f_1\left(d_h^*\right) \tag{3.4}$$

as intuition tells us to expect. In this case the two parameters are perfectly correlated, and one should be dropped. A similar argument could be advanced regarding the relationship between the inlet swirl velocity v_o and P_{in}, δ, $\dot{m}$ when any two of v_o^*, P_{in}^*, δ^*, $\dot{m}^*$ are held constant.

Table 3.2 lists some potentially interesting parameters of vortex tube performance, which could be considered as functions of the independent variables given in table 3.1. Of necessity, this list is merely a subset of the possible parameters.

The dependent variables are divided into two types. As their name suggests, the field variables are those which vary over the entire vortex tube, being functions of the spatial co-ordinates. Integrated variables are those which refer to a specific value, and are consequently not spatially dependent. The spatial co-ordinates should not be included in analysis of these integral quantities.

Assume that the pressures outside the flow exits are equal, that is $P_c = P_h$, as is always the case in practice. Performing the most general dimensional analysis under this constraint, with the parameters listed, one obtains

$$N.\ D.\ V.\ = f\left\{\begin{array}{c} L/D,\ \delta/D,\ d_c/D,\ d_h/D, \\ S,\ Re,\ E,\ P_{in}/\rho_{in}v_0^2,\ P_c/\rho_{in}v_0^2,\ \mu_c \\ \gamma,\ Pr,\ \beta T_{in},\ (X_i)_{in} \\ r/D,\ \theta,\ z/D \end{array}\right\} \tag{3.5}$$

where 'N.D.V.' refers to the non-dimensional dependent variables listed in table 3.3 and

Variable Name	Symbol	Dimensions
Field Variables		
Velocities in 3 Dimensions	u,v,w	LT^{-1}
Pressure	P	$ML^{-1}T^{-2}$
Temperature	T	Θ
Density	ρ	ML^{-3}
Component concentrations	x_i	1
Integrated Properties		
Cold outlet temperature	T_c	Θ
Hot outlet temperature	T_h	Θ

Table 3.2: Some potentially interesting parameters of vortex tube performance, dependent on the independent variables listed in table 3.1.

Description	Symbol	Composition
Normalised cold temperature drop	$\Delta T_c/T_{in}$	$(T_c - T_{in})/T_{in}$
Normalised hot temperature rise	$\Delta T_h/T_{in}$	$(T_h - T_{in})/T_{in}$
Normalised velocities	u/v_o, v/v_o, w/v_o	
Normalised pressure	$P/\rho_{in}v_o^2$	
Normalised temperature	T/T_{in}	
Normalised density	ρ/ρ_{in}	

Table 3.3: Non-dimensional dependent variables.

Swirl Reynolds number	$Re = \frac{\rho_{in} v_0 D}{\mu}$
Swirl number	$S = \frac{\rho_{in} v_0 D^2}{\dot{m}}$
Prandtl number	$Pr = \frac{\mu c_p}{\lambda}$
Energy number	$E = \frac{c_p T_{in}}{v_0^2}$.

If geometric similarity is assumed, the expression becomes

$$N.\,D.\,V. = f\left\{\begin{array}{c} S,\ Re,\ E,\ P_{in}/\rho_{in}v_0^2,\ P_c/\rho_{in}v_0^2,\ \mu_c \\ \gamma,\ Pr,\ \beta T_{in},\ (X_i)_{in} \\ r/D,\ \theta,\ z/D \end{array}\right\} \tag{3.6}$$

and if only a single, particular gas is used, then for the integrated properties,

$$N.\,D.\,V. = f\left\{ S,\ Re,\ E,\ P_{in}/\rho_{in}v_0^2,\ P_c/\rho_{in}v_0^2,\ \mu_c \right\}. \tag{3.7}$$

Equation (3.7) is the simplest non-dimensional relationship of useful generality that we can write to describe vortex tube behaviour. With seven independent variables, it is too complex to be of much direct use.

The large number of independent variables in expression (3.7) is a result of uncertainties in the performance of the inlet nozzles and gas supply to the tube. Nozzle and supply design has been characterised only by the effective diameter parameter δ, and it is clear that there could be a large number of arrangements satisfying this criterion. Even limiting any study to tubes with geometrically similar nozzles would not provide a solution, since differences in the behaviour of the gas supply system would cause some of the parameters, especially E and $P_{in}/\rho_{in}v_0^2$, to vary.

These difficulties can be overcome if consideration is further limited to only a single tube, with a particular supply arrangement, connected to a compressed gas source with an invariant reservoir temperature T_{in}. There will be, then, a unique relationship between P_{in}, P_c, and v_0, so our non-dimensional relationship can be reduced to

$$N.\,D.\,V. = f\left\{P_{in}/P_c,\ \mu_c\right\} \tag{3.8}$$

Thus only two parameters are required to characterise a particular vortex tube installation. Dealing with a number of nominally geometrically similar installations is a much more difficult problem, although we might expect equation (3.8) to apply as an approximation if the difference in tube diameters was small[2] and they were powered by the same supply.

[2]No attempt will be made to define 'small'.

3.3 The CUED Vortex Tubes

Three vortex tubes were used for the experiments, as shown in figure 3.1. They were originally designed by Walker [112], according to the principles set out by Soni and Thompson [113]. Two are made from brass, having internal diameters of 26 mm and 18 mm, and the third from transparent Perspex, with an internal diameter of 24 mm. Table 3.4 gives details of their dimensions in conjunction with figure 3.2.

Tube	Material	Hot Tube Length	Cold Tube Length	Internal Diameter	Nozzle Diameter	No. Of Nozzles
A	Brass	1300 mm	250 mm	26 mm	6 mm	2
B	Brass	900 mm	250 mm	18 mm	4 mm	2
C	Perspex	1300 mm	250 mm	24 mm	6 mm	2

Table 3.4: Pertinent dimensions of the CUED vortex tubes.

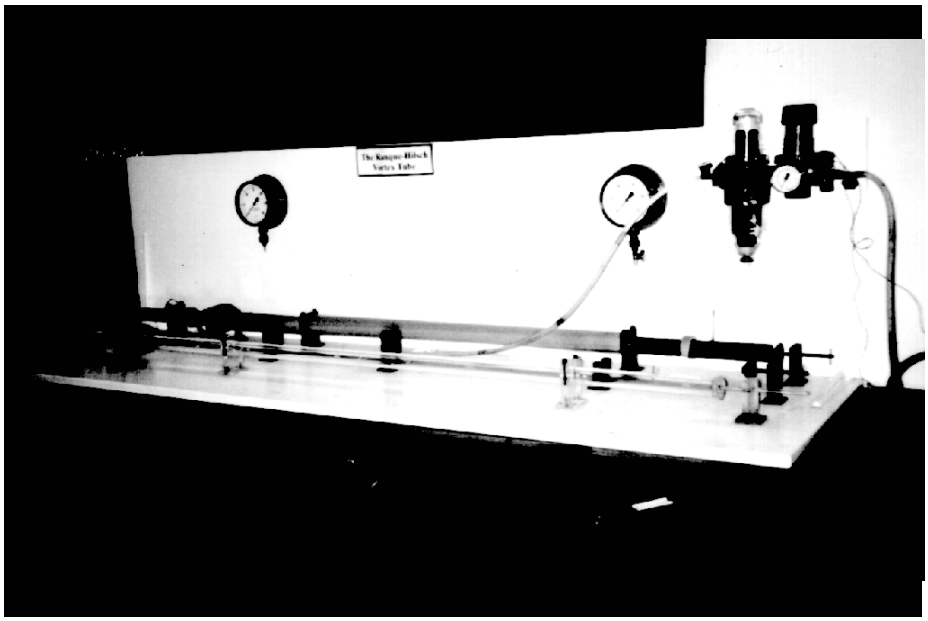

Figure 3.1: Photograph of the vortex tube apparatus. The plastic tube (C) and the 26 mm diameter brass tube (A) are visible. Tube B has been removed for clarity.

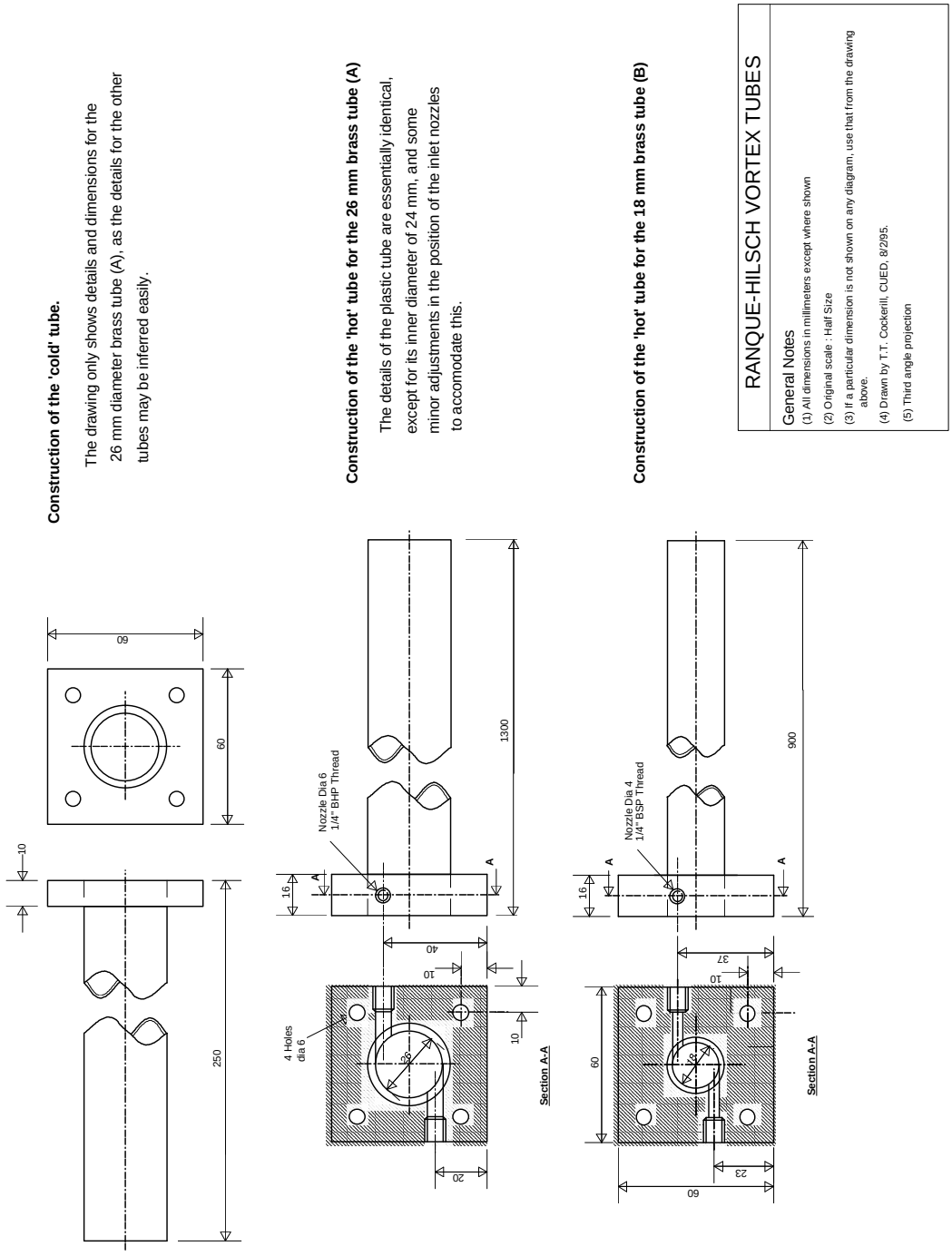

Figure 3.2: Drawing of the CUED vortex tubes.

The orifice in each tube may be varied by inserting a Perspex plate, drilled out to any desired diameter, into a slot separating the hot and cold tubes. By inserting a solid plate, a tube can be run in the uniflow configuration, although in this case, there is no way of separating the hot and cold streams. With the counterflow setup, the relative amounts of hot and cold gas can be controlled using the simple conical valve arrangement near the hot exit.

All the tubes are equipped with two tangential inlet nozzles, slightly displaced from the orifice plate. It is quite possible however to run a tube on a single nozzle by only connecting the gas supply to a single inlet port, and closing off the unused opening with a clamp. Air is supplied from the laboratory compressor, via a filter and an adjustable pressure regulator, together giving a maximum achievable inlet stagnation pressure at the tube of around 690 kPa.

A number of holes of approximately 3 mm diameter are drilled at points along each tube. These allow measurement probes to traverse the radius of the tube at various stations along the axis.

3.4 Basic Measurements

3.4.1 Background

In order to characterise the vortex tubes, and verify the findings of earlier workers, some relatively straightforward measurements were made. The data also gives a 'feel' for the nature of the vortex tube.

Three aspects were investigated. Firstly, the basic performance characteristics of the tube were assessed, secondly the dependence of the outlet temperatures on the cold mass fraction, and lastly how the temperature of the tube wall varies with axial distance from the orifice.

3.4.2 Description of Equipment

For these simple experiments, all temperatures were measured using a type K thermocouple. A digital readout was provided by a Comark type 6110 microprocessor thermometer.

With the brass tubes, estimates of the outlet gas temperatures were obtained by fastening the thermocouple to the outer tube wall, near to the outlet, with 'blu-tak'. It was assumed that the wall temperature was representative of the gas temperature. This is not too bad an assumption, for flows near the outlet ports. The high conductivity of brass and the thinness of the wall makes the temperature difference between the inside and the outside of the tube small[3]. Additionally the flow is well mixed near the outlets, giving a fairly uniform temperature profile across the radius.

With a plastic tube, a technique based on conduction is not viable. Gas temperature readings here were taken by placing the thermocouple just within a measurement hole, and sealing with 'blu-tak'. As with the conduction technique, this is far from accurate, but has the advantage of being quick.

Mass flow measurements were not taken explicitly. Instead the cold mass fraction was estimated from the energy conservation equation, viz:

$$\mu_c = \frac{\Delta T_h}{\Delta T_h + \Delta T_c} \tag{3.9}$$

The inlet flow ('reservoir') temperature, used in the calculation of the ΔT values, was obtained from a thermocouple introduced into the supply pipe. As the flow velocity there is low, the static and stagnation temperatures are essentially identical. Where required, numerical values for mass flow rates were estimated from density, velocity and pressure information. Any other equipment employed is described in the appropriate sections.

[3] A quantitative assessment of the error due to this assumption is given in appendix A.

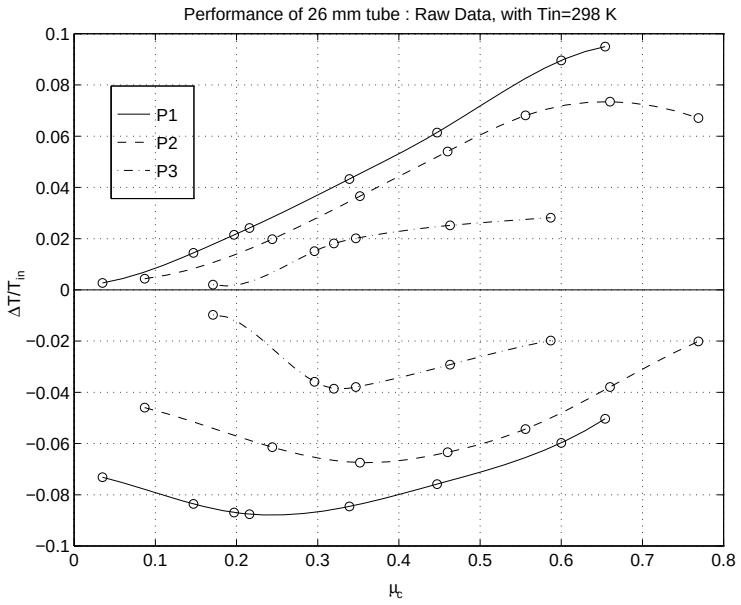

Figure 3.3: Raw performance data for the 26 mm tube with a 7 mm diameter orifice. The circles represent data points, and the lines are interpolating splines. The data were taken at pressure ratios : P1: $P_{in}/P_c = 6.82$, P2: $P_{in}/P_c = 5.12$, P3: $P_{in}/P_c = 3.41$, with the upper curves representing the hot flow, and the lower curves, the cold. The pressure at the cold outlet in each case was atmospheric.

3.4.3 Essential Characteristics

Basic performance

Figure 3.3 shows the variation in energy separation performance for the 26 mm tube as a function of the cold fraction μ_c, and the inlet pressure P_{in}. The data shows the characteristic form reported by Hilsch [4] and others, with the hot curves rising from zero $\Delta T/T_{in}$ at $\mu_c = 0$ towards a finite value at $\mu_c = 1$, and the cold curves starting from a finite value at $\mu_c = 0$, reaching a maximum near $\mu_c = 0.3$ and then falling towards zero at $\mu_c = 1$. Investigations of the other tubes produced similar families of curves. At any reservoir pressure and cold fraction, the 18 mm diameter tube gave an increased separation compared to the 26 mm tube, while the 24 mm tube exhibited a lesser performance.

Comments on tube operation

Perhaps the most obvious feature of the tubes was the amount of noise they produced in operation. The hiss of the escaping air was usually so loud that it was advisable to wear ear defenders. A strange whistle-like noise was just audible under the majority of flow conditions, but it was far from a pure tone, and its source was difficult to determine by ear.

When run at a very high cold fraction, near $\mu_c = 1$, all the tubes exhibited an unexplained instability, producing a brief spitting noise at irregular intervals of approximately one second. As the tubes gave very little energy separation under such conditions, it was concluded that the phenomenon was most likely unconnected with the Ranque-Hilsch effect, and not investigated further.

When the tubes were operated near their optimum, the energy separation was quite striking. Both the hot and cold outlets would be painful to touch for any extended period, and atmospheric water vapour would condense onto the cold outlet pipe.

Flow visualisation

Flow visualisation was attempted in order obtain a general impression of the flow within the tube. Initial efforts injecting vapourised oil were unsuccessful, as the droplets were 'centrifuged' on to the outer wall, where they quickly merged to form a flow of liquid. Seeding the flow with 'glitter' proved much more successful. The results were recorded on video tape, and examined using a high quality video player with a digital frame buffer. Hard copy of the interesting frames was obtained with a video printer. Unfortunately it was not possible to resolve details of the flow, such as the nature of any vortex breakdown, using this technique. The motion was too quick to be recorded in detail on a standard video, and the particles too large to react to rapid changes in the flow direction.

Figure 3.4 shows a flow visualisation result obtained using the Perspex tube with a 10 mm diameter orifice, operating at a reservoir pressure of 276 kPa ($P_{in}/P_c = 2.7$) and producing a small temperature separation. The particle streaklines clearly show the

Figure 3.4: The results of the flow visualisation. The top photograph is a control picture, with no particles introduced into the flow. Compare the middle picture, which clearly shows streaklines. In both cases, the field of view shows an 80 mm length in the hot tube of installation C, between $z^* = 0.105$ and $z^* = 0.166$. The lower picture is of a length of the hot tube of installation C between $z^* = 0.074$ and $z^* = 0.124$ that gives a particularly clear impression of the nature of the flow. In all cases the axial flow is from left to right.

spiralling nature of the flow. Measuring the angle to the tube axis of their central portions, and employing the geometry of figure 3.5 gives an estimate of the ratio of the swirl and axial velocities. At the left hand side of the picture (the 'upstream' end)

$$\frac{v}{w} = 1.767, \tag{3.10}$$

whereas at the right hand hand side the swirl has decayed slightly since

$$\frac{v}{w} = 1.585. \tag{3.11}$$

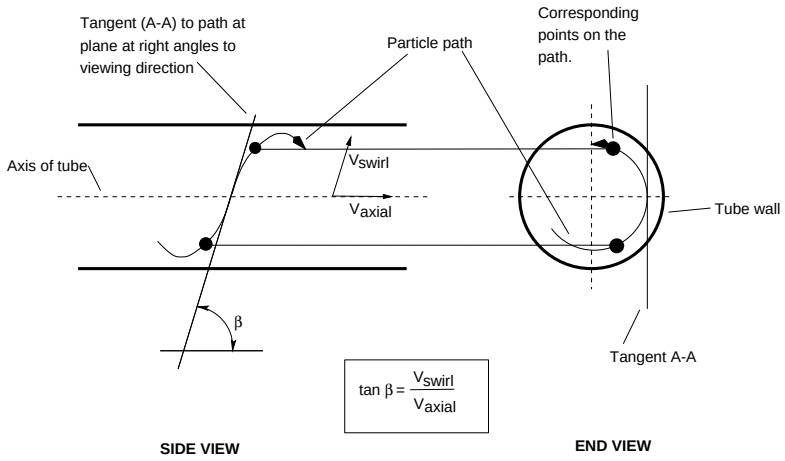

Figure 3.5: The geometry employed to estimate the flow direction from the streakline results.

3.4.4 Performance and Cold Mass Fraction.

In order to test Stephan's approximate similarity relationship, equation (3.1), the dependence of the cold temperature drop, ΔT_c as a function of the cold mass flow fraction, μ_c was investigated for the 26 mm and 18 mm diameter vortex tubes. Readings were taken over a range of the the available inlet pressures.

Figure 3.6 shows the normalised data for the 26 mm tube, with a 7 mm diameter ori-

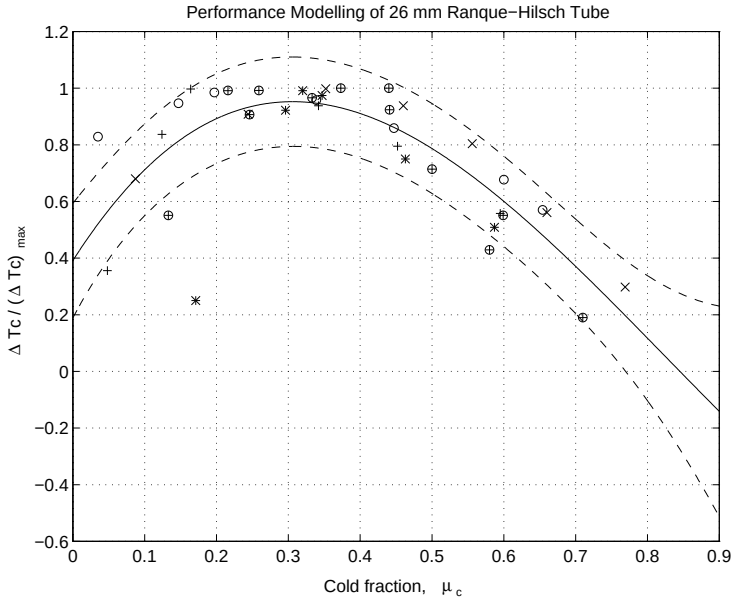

Figure 3.6: The 'performance' of the 26 mm diameter vortex tube as a function of the cold outlet mass flow fraction. Each set of points represents data obtained at one inlet pressure, the solid line is the mean fit, and the dotted lines represent bounds containing at least fifty percent of the data points.

fice. Following Stephan, and fitting a cubic yields,

$$\frac{\Delta T_c}{(\Delta T_c)_{max}} = 3.23\mu_c^3 - 7.97\mu_c^2 + 3.97\mu_c + 0.39. \tag{3.12}$$

Normalised data for two geometrically similar situations, the 18 mm tube with a 5 mm orifice and the 26 mm tube with a 7.5 mm orifice, is shown in figure 3.7. A cubic fit gives,

$$\frac{\Delta T_c}{(\Delta T_c)_{max}} = 3.34\mu_c^3 - 6.97\mu_c^2 + 3.07\mu_c + 0.57. \tag{3.13}$$

While it is clear that Stephan's work is essentially correct, the analysis raises a number of issues. Foremost is the nature of the curve to be fitted through the data. The choice of a cubic function is entirely arbitrary, and in this case, not completely satisfactory, as discussed in chapter 6, where an improved formulation is developed.

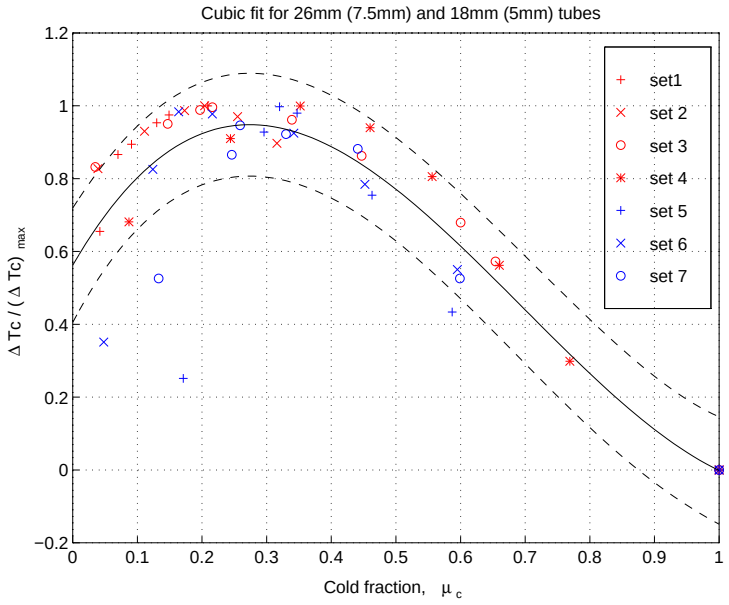

Figure 3.7: The 'performance' of the 18 mm and 26 mm diameter vortex tubes in geometrically similar configurations, as a function of the cold outlet mass flow fraction. The points represent measured data, the solid line is the mean fit, and the dotted lines represent bounds containing at least fifty percent of the data points. The data sets are annotated as follows: set 1 - 18 mm tube, $P_{in}/P_c = 6.89$, 1 inlet nozzle; set 2 - 18 mm tube, $P_{in}/P_c = 6.89$, 2 nozzles; set 3 - 26 mm, $P_{in}/P_c = 6.89$, 1 nozzle; set 4 - 26 mm, $P_{in}/P_c = 5.17$, 1 nozzle; set 5 - 26 mm, $P_{in}/P_c = 3.45$, 1 nozzle; set 6 - 26 mm, $P_{in}/P_c = 6.89$, 2 nozzles; set 7 - 26 mm, $P_{in}/P_c = 5.17$, 2 nozzles. Atmospheric pressure (P_c) was approximately 100 kPa in each case.

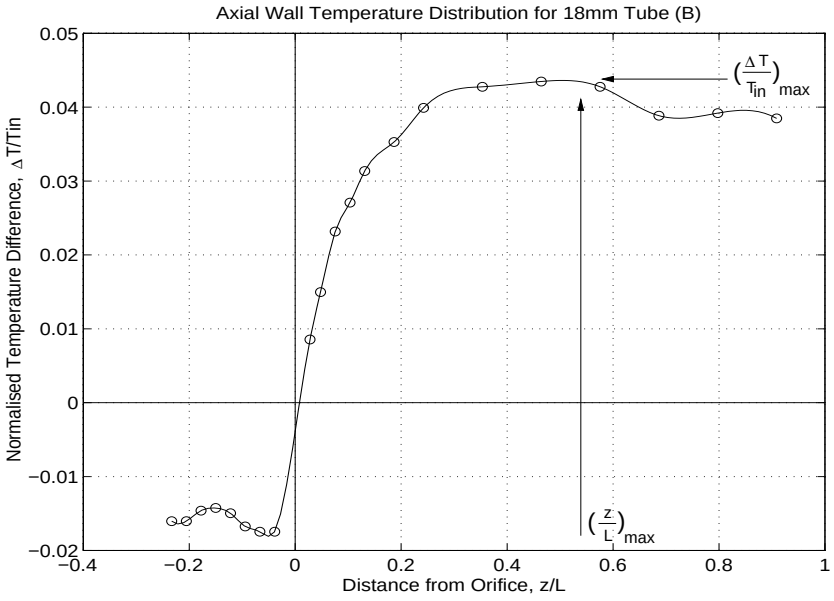

Figure 3.8: Variation of the temperature of the cylindrical wall with distance from the orifice, for the 18 mm tube. The circles represent measured data, while the solid line is an interpolating spline.

A secondary problem is the fairly wide spread of the data, even when taken in a single tube (figure 3.6). The dimensionless model only provides only an approximate result, although it might be hoped that a sound basis for the fitted function would bring some improvement.

3.4.5 Axial Wall Temperature Variations

Figure 3.8 shows a typical result for the variation of the temperature of the cylindrical wall with distance from the orifice. Note firstly the decline in temperature of the hot tube between $z^* = 0.5$ and $z^* = 1$. This would appear to be due to heat transfer from the tube to the environment, and suggests that there is little energy separation advantage to be gained from the portion of the hot tube beyond $z^* = 0.5$.

In the cold tube, minimum temperature is achieved just beyond the orifice. Heat transfer with the environment would appear, again, to be responsible for the small in-

crease in temperature of the cold flow as it approaches the outlet.

Re-normalising a number of such curves by dividing $\Delta T/T_0$ by its maximum value $(\Delta T/T_0)_{max}$ and the axial co-ordinates z^* by the value z^*_{max}, determined as marked on figure 3.8 collapses them to nearly the same line over the range $0 < z < z_{max}$. The relationship can be modelled empirically by an expression of the form

$$\Delta T^* = 1 - e^{a+bz^*} \tag{3.14}$$

Reduced data from tubes A and B is shown in figure 3.9, along with the fitted expression

$$\Delta T^* = 1 - e^{0.0565-4.33z^*} \tag{3.15}$$

which shows at least a working correspondence.

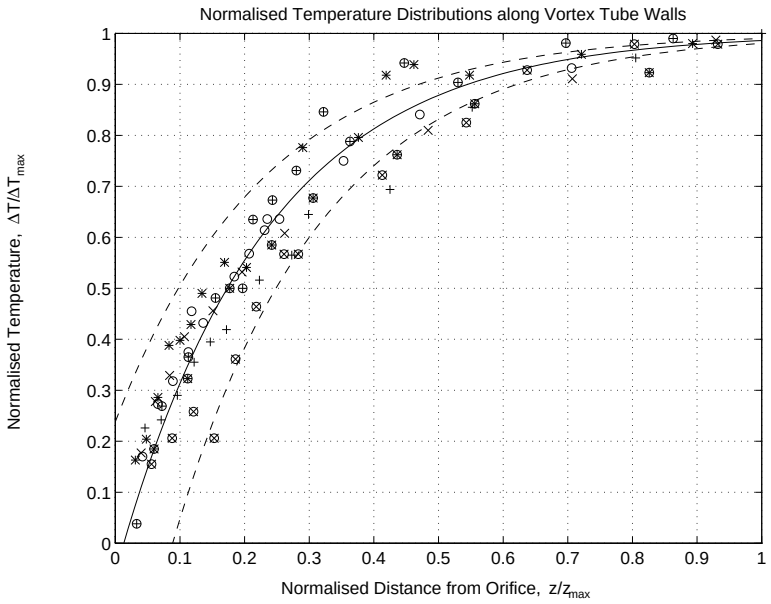

Figure 3.9: Normalised cylindrical wall temperature axial distributions for the 18 mm and 26 mm vortex tubes. The solid line represents the fitted relationship, and the dotted lines error bounds that should contain at least 50 percent of the points.

3.5 Flow Field Mapping

3.5.1 Background

The flow field internal to vortex tubes has been examined by a number of workers including Lay [74], Sibulkin [86], and Takahama [71]. All comprehensive investigations have been performed using intrusive techniques, which are poorly suited to high speed rotating flows.

Without access to non-intrusive instruments, there seems little point in undertaking a detailed investigation of the flow inside the CUED tubes. A cursory examination is useful however, allowing confirmation of earlier findings, providing data for later comparison with numerical results, and precipitating the development of a comprehensive methodology for error analysis in such experiments, that might prove valuable to later workers with better equipment.

Prior to the main experimental work described in this section, some preliminary investigations of the velocity fields were made using a technique that only requires measurement of the stagnation pressure and the flow direction. This technique is discussed in appendix E.

3.5.2 Description of Equipment

Stagnation temperature, stagnation pressure and static pressure were measured at points in the vortex tubes with 'home made' cylindrical probes of a conventional design, such as that detailed by Ower and Pankhurst [114] and Benedict [115]. Flow direction was determined by rotating the stagnation pressure probe until it gave a maximum reading, and noting the angle between the axis of the vortex tube and the direction faced by the probe hole. The other two probes were rotated to face the local flow before readings were taken. A simple traverse arrangement was used to move the probes across the tube radius.

The probes were calibrated in the flow through a duct driven by a suction fan at its

outlet. This had the advantage of making the stagnation pressure and temperature within the duct approximately equal to atmospheric pressure and temperature respectively. Both the effects of probe inclination to the flow, and variation of the flow speed were investigated[4]. Any systematic error was accounted for, and estimates of the magnitude of the random error were used to calculate the overall uncertainty, in the next section.

3.5.3 Analysis of Errors

Calculation

From the readings of local stagnation pressure P_0, static pressure P, recovery temperature T_R, and flow angle to the azimuthal directions, the flow field was estimated according to the standard compressible flow relations (see for example Leipmann and Roshko [116]):

$$M = \sqrt{\frac{2}{\gamma-1}\left\{\left(\frac{P_0}{P}\right)^{\frac{\gamma-1}{\gamma}}-1\right\}} \tag{3.16}$$

$$T_0 = \frac{\left\{1+\frac{\gamma-1}{2}M^2\right\}T_R}{1-R_T+\left\{1+\frac{\gamma-1}{2}M^2\right\}R_T} \tag{3.17}$$

$$T = \frac{T_0}{1+\frac{\gamma-1}{2}M^2} \tag{3.18}$$

$$V^2 = M^2\gamma RT \tag{3.19}$$

where M is the local Mach number, T the static temperature, V^2 the square of the magnitude of the local velocity vector, and R_T the recovery factor of the stagnation temperature probe. Any other flow field properties can be easily evaluated from these basic terms.

[4]Some details of the calibration procedure are given in appendix B.

Error evaluation

A matrix technique was employed, wherein all relationships between an observables vector, $\mathbf{x}$, and results vector, $\mathbf{y}$, are reduced to the linear form

$$\mathbf{y} = \mathbf{T}.\mathbf{x}, \tag{3.20}$$

where $\mathbf{T}$ is a transformation matrix. The law of propagation of errors then implies

$$\mathbf{V_y} = \mathbf{T}\mathbf{V_x}\mathbf{T}^T \tag{3.21}$$

with $\mathbf{V_x}$ being the variance matrix for the observables, and $\mathbf{V_y}$ for the results. Each variance matrix takes the form

$$\mathbf{V_x} = \begin{bmatrix} \sigma_{x_1}^2 K_{x11} & \sigma_{x_1}\sigma_{x_2} K_{x12} & \sigma_{x_1}\sigma_{x_3} K_{x13} & \dots \\ \sigma_{x_2}\sigma_{x_1} K_{x21} & \sigma_{x_2}^2 K_{x22} & \sigma_{x_2}\sigma_{x_3} K_{x31} & \dots \\ \sigma_{x_3}\sigma_{x_3} K_{x31} & \sigma_{x_3}\sigma_{x_2} K_{x32} & \sigma_{x_3}^2 K_{x33} & \dots \\ . & . & . & \end{bmatrix} \tag{3.22}$$

where σ_{xi} is the absolute error in the i^{th} component of vector x, and $K_{x_{ij}}$ is the correlation between the errors in the i^{th} and j^{th} components of x.

If, as in this case, the mapping between the results and observables is non-linear, then it may be linearised for small changes in the observables δx, such as those due to errors, by writing it in the form

$$\mathbf{y} = \mathbf{y}|_{x=a} + \sum_{i=1}^{i=n} \left(\frac{\partial \mathbf{y}}{\partial x_i} \right)_{x=a} \delta x_i \tag{3.23}$$

assuming that x has n components. This yields a transformation

$$\mathbf{T} = \begin{bmatrix} \frac{\partial y_1}{\partial x_1} & \frac{\partial y_1}{\partial x_2} & \frac{\partial y_1}{\partial x_3} & \dots \\ \frac{\partial y_2}{\partial x_1} & \frac{\partial y_2}{\partial x_2} & \frac{\partial y_2}{\partial x_3} & \dots \\ . & . & . & . \end{bmatrix}. \tag{3.24}$$

As an illustrative example, the observables matrix for the stagnation temperature relationship (3.17) above, is

$$\mathbf{x}_{T_0} = \begin{bmatrix} M \\ T_R \\ R_T \end{bmatrix}. \tag{3.25}$$

For the results matrix, we obtain

$$\mathbf{y}_{T_0} = [T_0]\,. \tag{3.26}$$

The transformation matrix is given by

$$\mathbf{T} = \begin{bmatrix} \frac{\partial T_0}{\partial M} & \frac{\partial T_0}{\partial T_R} & \frac{\partial T_o}{\partial R_T} \end{bmatrix} \tag{3.27}$$

with

$$\frac{\partial T_0}{\partial M} = \frac{T_R\,(\gamma-1)\,M - \left(1+\frac{\gamma-1}{2}M^2\right) T_R R_T\,(\gamma-1)\,M}{1+\frac{R_T(\gamma-1)}{2}M^2} \tag{3.28}$$

$$\frac{\partial T_0}{\partial R_T} = \frac{(-T_R)\left(1+\frac{\gamma+1}{2}M^2\right)\frac{\gamma-1}{2}M^2}{\left(1+\frac{\gamma-1}{2}M^2 R_T\right)^2} \tag{3.29}$$

and

$$\frac{\partial T_0}{\partial T_R} = \frac{1+\frac{\gamma-1}{2}M^2}{1+\frac{\gamma-1}{2}M^2 R_T}. \tag{3.30}$$

3.5.4 Results

Experimental results will be presented for the flow in tube A in the counterflow configuration only. Values for other counterflow tubes were comparable. Flow in the uniflow configuration differs qualitatively only in that there is no region of reversed flow near the inlet plane, where the gas leaves through the cold exit.

Figures 3.10, 3.12, 3.11 and 3.13 respectively show typical stagnation and static temperature, and stagnation and static pressure fields over a radial plane through the centreline of the tube. In each of the diagrams the upper axis shows the normalised value of the

parameter, and the lower axis the normalised error calculated as detailed in the previous section. In each case the tangential inlet nozzles and the orifice plate were positioned at an axial distance of 0 m. Note that the full length of the tube is not shown in the diagrams. The hot tube extends axially to 1300 mm, but under the particular conditions used there was little variation of the flow parameters outside the region shown. Similarly the cold tube is 250 mm long, but there was little axial variation beyond 40 mm from the inlet, and essentially none once 200 mm was reached

The gaps in the colour-maps represent regions of the tube where it was not possible to get reliable readings. Problems were experienced particularly near the centre-line of the tube, where it was found that the probe had a large effect on the flow, making readings difficult. Alignment of the probes with the overall flow direction sometimes proved impossible within 2 mm of the centre-line, as the flow velocities were too small to produce a visible change in reading when the probe was rotated. Similar problems were experienced in the periphery of cold tube when close to the orifice. The weak flow here prevented determination of its direction, although it was possible to get values for both pressures and the temperature.

Measurements were also unreliable near to the inlet plane. Turbulence levels were very high there, producing widely fluctuating readings, that made probe alignment impossible. The lack of values from the inlet plane prohibits non-dimensionalisation of the data in the manner described at the beginning of the chapter. An alternative scheme was adopted wherein the stagnation and static temperatures were normalised by subtracting the reservoir temperature of the gas, and then dividing by the maximum resulting stagnation temperature value, that is

$$T^* = \frac{T - T_{in}}{max\,(T_0 - T_{in})}. \tag{3.31}$$

A similar procedure was used to derive a normalised pressure value with respect to atmospheric pressure, P_{atm},

$$P^* = \frac{P - P_{in}}{max\,(P_0 - P_{atm})}. \tag{3.32}$$

The absolute uncertainty values were normalised by dividing by the $max\,(T_0 - T_{in})$, or the $max\,(P_0 - P)$ as appropriate. Axial and radial distances have not been normalised, as retaining the true values provides a better feel for the size of the gradients within the tube.

Figures 3.14 and 3.15 show radial profiles of swirl and axial velocity at stations spaced along axis the of the tube. As with the pressure and temperature results, the upper diagram gives the results, while the lower diagram presents details of the uncertainty in the values. The values are normalised by the maximum swirl velocity that was measured in the tube[5]. Again, difficulty in aligning the probes near to the centre-line of the tube means that values cannot be calculated across a whole radius.

Interpretation of the stagnation temperature field, figure 3.10, is complicated by the absence of readings near the centre-line, and the fairly large errors in the readings. There does seem to be evidence of an axially developing radial energy gradient in the first 0.3 m or so of the hot tube. Certainly the outer gas appears to be gaining energy as it passes down the axis, and by implication the central gas must be losing energy. The axial velocity profiles show that this 0.3 m long region contains the central reversed flow that leaves through the orifice to become the cold flow. The result is not inconsistent with a hypothesis that the energy separation develops as the the gas passes along the tube.

Beyond an axial distance of 0.4 m, the radial stagnation temperature distribution becomes relatively uniform. It is notable from figure 3.14 that the swirl velocity has decayed substantially by this point. This marks the end of the Ranque-Hilsch separation.

As the gas proceeds further along the tube, towards the hot exit, the stagnation temperature rises. The static temperature beyond 0.4 m shows a similar pattern. This would suggest that heat transfer from the environment was responsible. In this particular configuration the inlet gas was relatively cool, such that the hot stream produced had a temperature below ambient. As the hot arm of the brass vortex tube was uninsulated during the experiment, heat transfer from outside would be a likely explanation.

[5]Note that this is not the same as the maximum swirl velocity within the tube. The fact that measurements near the inlet plane were unsuccessful mean that the true maximum swirl velocity is unknown.

Figure 3.10: The stagnation temperature field in tube A with a 7.5 mm orifice, operated at pressure ratio of $P_{in}/P_c = 2.4$. The upper diagram shows the normalised stagnation temperature, the lower gives the normalised estimated uncertainty field.

Figure 3.11: The stagnation pressure field in tube A with a 7.5 mm orifice, operated at a reservoir pressure of $P_{in}/P_c = 2.4$. The upper diagram shows the normalised stagnation pressure, the lower gives the normalised estimated uncertainty field.

Figure 3.12: The static temperature field in tube A with a 7.5 mm orifice, operated at pressure ratio of $P_{in}/P_c = 2.4$. The upper diagram shows the normalised static temperature, the lower gives the normalised estimated uncertainty field.

Figure 3.13: The static pressure field in tube A with a 7.5 mm orifice, operated at a reservoir pressure of $P_{in}/P_c = 2.4$. The upper diagram shows the normalised static pressure, the lower gives the normalised estimated uncertainty field.

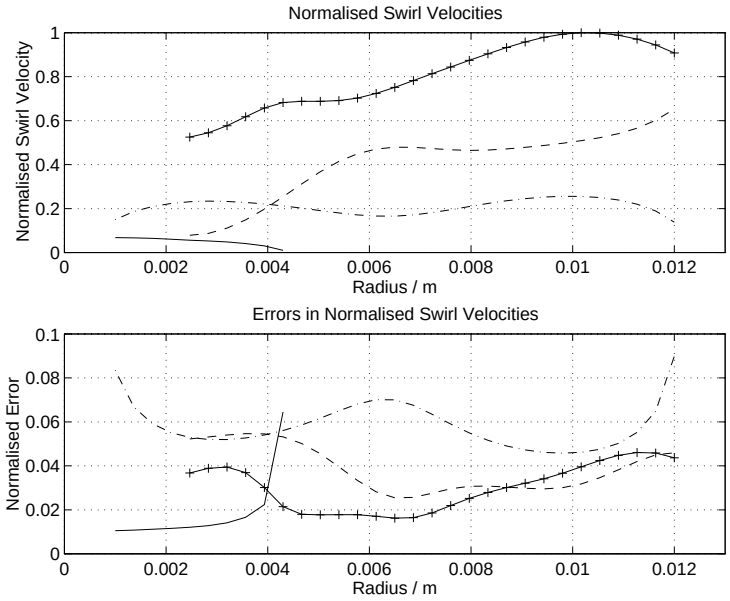

Figure 3.14: Swirl velocity profiles in tube A with a 7.5 mm orifice, operated at a reservoir pressure of $P_{in}/P_c = 2.4$. The upper diagram shows the normalised swirl velocities, the lower gives the normalised estimated uncertainty field. The solid line with symbols represents data obtained at an axial distance of 0.05 m, the dashed line at 0.2 m, the chained line at 0.6 m, and the solid line at -0.04 m.

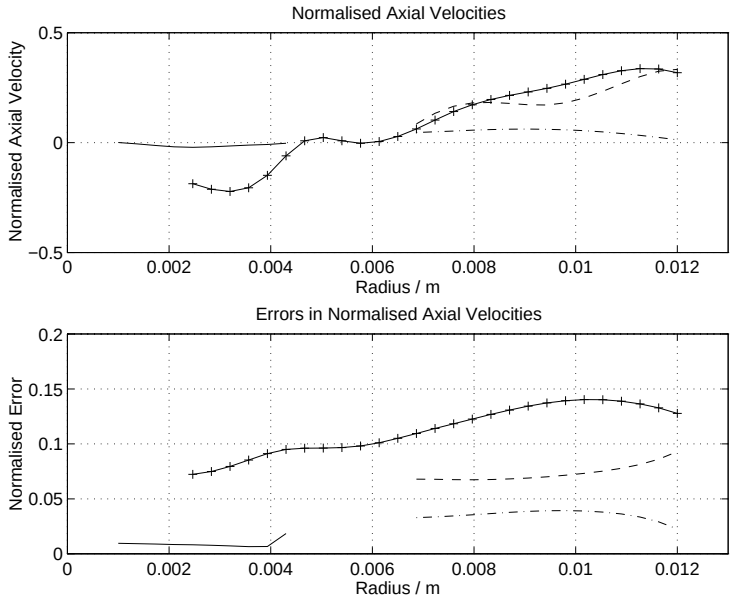

Figure 3.15: Axial velocity profiles in tube A with a 7.5 mm orifice, operated at a reservoir pressure of $P_{in}/P_c = 2.4$. The upper diagram shows the normalised axial velocities, the lower gives the normalised estimated uncertainty field. The solid line with symbols represents data obtained at an axial distance of 0.05 m, the dashed line at 0.2 m, the chained line at 0.6 m, and the solid line at -0.04 m.

The swirl velocity profiles, figure 3.14 clearly show that the swirl velocity decays as the gas travels along the tube. Near to the inlet plane, there is good evidence consistent with the existence of a forced vortex. At an axial distance of 0.2 m the profile is still comparable to a forced vortex, but maximum velocity has reduced by more than one-third. By 0.6 m, the maximum velocity is greatly reduced, and the profile has become nearly flat. It is notable that swirl velocities in the cold tube appear to be small.

3.6 Acoustical Measurements

3.6.1 Background

Acoustic Streaming in Vortex Tubes

Kurosaka [8] attributes the energy separation in the vortex tube to acoustic streaming caused by the vortex whistle. Assuming the flow to be at steady state and using an order of magnitude argument, Kurosaka divides the flow radially into layers. Working radially inwards he identifies three regions illustrated by figure 3.16, (a) a steady boundary layer adjacent to the wall, (b) a middle layer, stretching from the inner edge of the steady boundary layer to the inner edge of the unsteady boundary layer, and, (c) an inviscid core.

By solving the Navier-Stokes and energy equations in the middle layer and inviscid core, using the method of matched asymptotic expansions after Van Dyke [117], Kurosaka produces an expression for the magnitude of the streaming velocity at the inner edge (i.e. adjacent to the inviscid core) of the middle layer $\bar{v''}$ in terms of the angular frequency of the applied disturbance. Modelling a vortex tube flow as a Rankine vortex,

$$\begin{aligned} v_o(r) &= \Omega r \quad (0 < r < r^*) \\ v_o(r) &= \Gamma / r \quad (r^* < r < r_o) \end{aligned} \tag{3.33}$$

where Γ is the circulation at r^*, the interface radius between the forced and free vortex

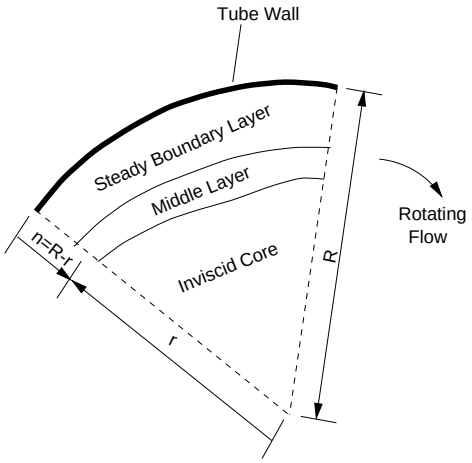

Figure 3.16: The layers identified by Kurosaka.

components, Kurosaka derives a relationship between the swirl Ω and the expected angular frequency of disturbances generated by the vortex whistle ω,

$$\omega = \pm(|m| - 1 + \lambda^{-2|m|})\frac{\Gamma}{r^{*2}}, \tag{3.34}$$

where m is the circumferential wavenumber of the disturbance and $\lambda = r_o/r^*$. This, combined with the expression for the streaming velocity, shows that the magnitude of the streaming at the boundary between the middle layer and the inviscid core is given by

$$\bar{v''}(|n| \to \infty) = \frac{\tilde{v_e}^2 \zeta}{\Gamma / r_o} \tag{3.35}$$

with

$$\zeta = \frac{3}{4}\frac{|m|}{(|m| - 1 + \lambda^{-2|m|})\lambda^2 - |m|} \tag{3.36}$$

where n is the radial co-ordinate measured inwards from the tube wall[6], and $\tilde{v_e}$ is the magnitude of the steady swirl velocity at the interface between the middle layer and the the core. As expression (3.35) implies that $\bar{v''}(|n| \to \infty) > 0$ at all times, any streaming

[6]In this context, $|n| \to \infty$ should be interpreted in the expansion matching sense of 'as the middle layer merges into the inviscid core.'

must be in the same direction as the mean flow.

When $m = 1$, ζ, and hence expression (3.35) become singular. Kurosaka concludes that should acoustic waves of the angular frequency predicted when $m = 1$ in equation (3.34) be present, then substantial streaming is likely. Since any streaming will always be in the direction of the mean flow, it will tend to supplement that flow. The Rankine vortex would tend to be deformed, with an excess of angular momentum building up at its periphery. Considerations elsewhere show that such a conversion would tend to cause an energy separation of the form found in the vortex tube.

To investigate his theory, Kurosaka measured the acoustic output of a modified, commercial vortex tube, operating in the uniflow form. He obtained a series of spectra similar to that shown in figure 3.17, with peaks at discrete frequencies, clearly showing harmonics.

By drilling out the sides of the tube, and installing tuned acoustic suppressors, Kurosaka attempted to attenuate the disturbances at a particular inlet pressure. By gradually increasing the inlet pressure, he observed the energy separation of his tube develop in the normal way, until the pressure was such that acoustic disturbances are attenuated, yielding spectra such as that in figure 3.18. At this point there was a fairly substantial drop in the separation performance.

It is clear that there must be some relationship between Kurosaka's acoustic attenuators and the reduction in performance of his tube. The general validity of the acoustic streaming explanation is questionable however. Escudier [13] notes that Hilsch [4] and Westley [9, 109, 111] make no mention of a whistling sound, and suggests that the main effect of installing acoustic suppressors would be to change the basic flow structure from that of a slightly asymmetric precessing vortex core (giving a spiral breakdown[7]) to a symmetric annular flow (giving a bubble breakdown), with a consequent loss in discrete frequency excitation. In a long tube, such a change in the flow might not have a dramatic effect on the overall outcome. However, with a short[8] tube such as Kurosaka's, it would

[7]The phenomenon of vortex breakdown is discussed in chapter 2.

[8]Kurosaka's tube had a length to diameter ratio of about 3.1. Compare this with Hilsch's shortest tube,

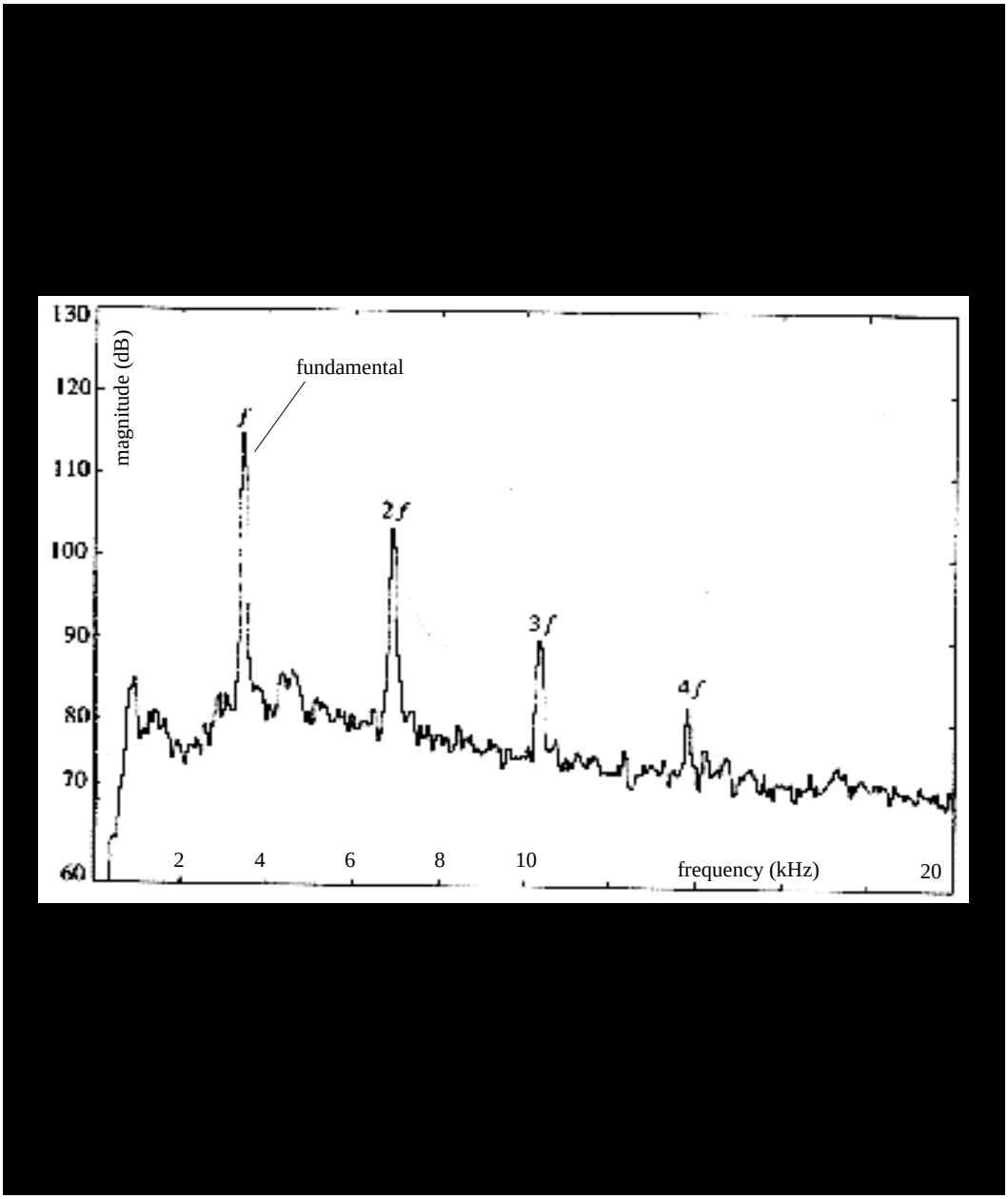

Figure 3.17: The spectral density of the acoustic signal obtained by Kurosaka from a uni-flow vortex tube of length 41.9 mm, and internal diameter 17.5 mm, operated on air at an inlet gauge pressure of 1.02 x (atmospheric), or approximately 100 kPa (gauge). *Taken from reference [8] .*

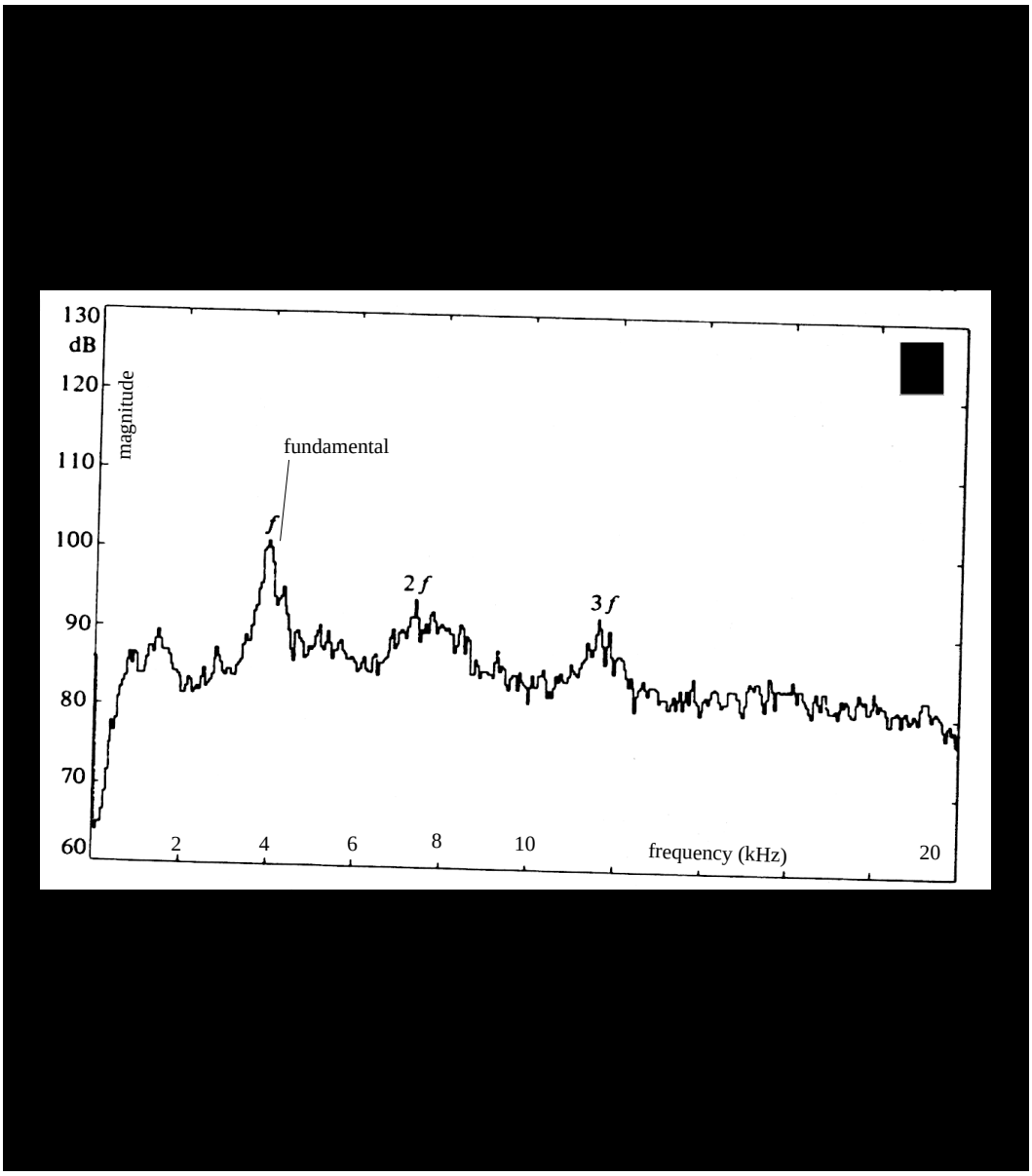

Figure 3.18: The spectral density of the acoustic signal obtained by Kurosaka from a uni-flow vortex tube of length 41.9 mm, and internal diameter 17.5 mm, operated on air at an inlet gauge pressure of 1.02 x (atmospheric) [i.e. approximately 100 kPa (gauge)], when fitted with tuned acoustic suppressors. *Taken from reference [8].*

dominate the flow. The breakdown bubble would most likely fill the tube, severely reducing any energy separation, as well as destroying the acoustical output.

There are further reasons to question the acoustic streaming explanation. Perhaps the greatest is the experimental evidence that points to a development of the energy separation as the flow progresses along the axis of the vortex tube. Although they use counterflow tubes[9] Wesley [109], for example finds an optimum length/diameter (L/D) ratio much greater than unity, while Soni and Thompson [113] achieve maximum efficiency at $L/D > 45$. If there were no improvement in the energy separation along the axis, in other words if the mechanism was a planar phenomenon then we would expect the optimum L/D to be small. The previous section presented clear evidence of a gradual development, as does Reynolds[10] [63]. While the stagnation temperature along the axis increases with distance from the inlet, the radial stagnation temperature gradient becomes steeper. In contrast, acoustic streaming would provide a relatively planar effect, independent of the tube length.

A second difficulty is the behaviour of the energy separation in Kurosaka's tube as the pressure, and hence whistling frequency, are increased beyond that at which the acoustic suppressors operate. Figure 3.19 shows that the decline in performance and acoustic output at the absorbed frequency is dramatic. When the pressure is increased further, there is no evidence of a sudden resumption of performance, as might be expected with a resonance phenomenon. Indeed the pressure increases to 250 kPa, nearly 2.5 times that at which the acoustics suppressors came into operation, before the previous maximum is attained, supporting Escudier's supposition of a fundamental change in the flow regime to a 'less efficient' state precipitated by the presence of the acoustic suppressors.

A further anomaly may be seen in comparison with the work of McDuffie [118], who also measures the sound output from a vortex tube, of a similar diameter to Kurosaka. He finds no evidence of the frequencies detected by Kurosaka, although he does identify

which had a ratio of 17. The CUED tubes have $L/D = 50$.

[9]The relationship between the interpretation of data from counter and uniflow tubes is discussed in the previous chapter.

[10]Reynolds investigates a counterflow tube.

an unexplained ultrasonic peak near 31 kHz when his tube is configured for optimum performance.

Application to the CUED vortex tubes

To investigate the acoustic influences in the CUED vortex tubes, a number of sound recordings were made at various points around the three tubes, and their frequency spectra analysed. Measurements were taken at a number of inlet pressures across the available range, and at conditions which did and did not promote significant energy separation.

The frequency-swirl relationship, equation (3.34), shows that the fundamental frequency produced by the vortex whistle is given by

$$f_1 = \frac{V(r^*)\, r^*}{2\pi r_o^2}. \tag{3.37}$$

To estimate the maximum value of $V(r^*)\, r^*$, and hence the maximum expected fundamental frequency, consider the inlet plane of tube A. Assume that the free vortex part of the Rankine vortex is very small here, and that the gas enters the tube at the speed of sound. This gives $r^* \approx 0.013$ mm and $V(r^*)\, r^* \approx 330$ m/s, giving $f_1 \approx 4.04$ kHz. Kurosaka finds three substantial peaks in his spectra. Further assuming that the CUED tubes produce similar spectra, we ideally need to be able to examine spectral components up to 12 kHz. However, the flow mapping experiments did not produce any evidence of swirling faster than 250 m/s, which would reduce the maximum likely frequency to just over 9 kHz.

The apparatus assembled to investigate the possible existence of such acoustic streaming is described in the next section.

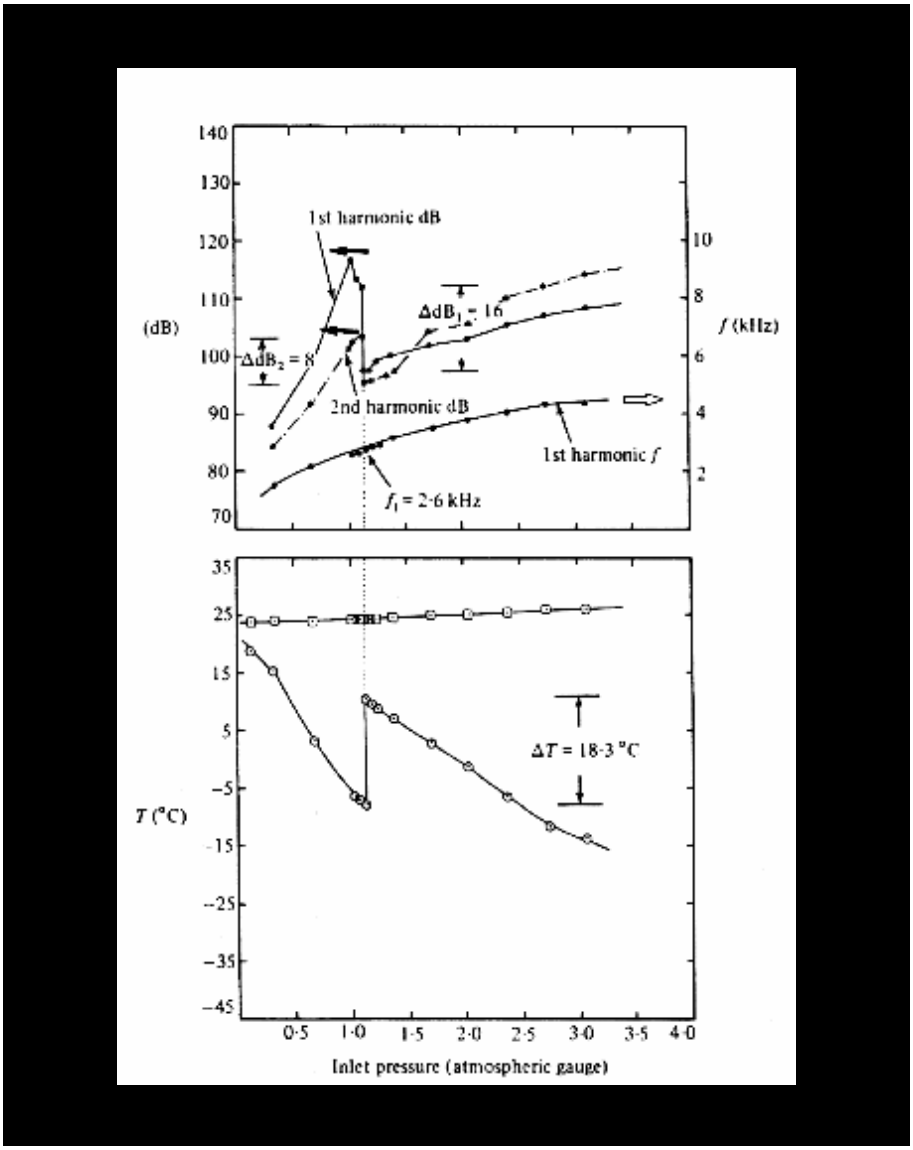

Figure 3.19: Graph illustrating the behaviour of the energy separation, and the acoustical output from Kurosaka's tube as the excitation (whistling) frequency is increased, first to that absorbed by the acoustic suppressors, and then beyond. In the top figure, the upper curves show the variation of the magnitudes of the first and second harmonics with the inlet pressure. The lower curve illustrates the dependence of the frequency of the first harmonic on the inlet pressure. Turning to the bottom figure, the upper curve shows the inlet temperature at each inlet pressure, whereas the lower curve displays the measured temperature at the centre of the inlet plane. *Taken from reference [8].*

3.6.2 Description of Equipment

Sound generated by the vortex tubes was recorded digitally, using a microphone connected to the audio input port of an Apple Macintosh Classic II computer. The Classic II machine incorporates an eight bit analogue to digital (A-D) converter designed specifically for audio uses, and supporting sampling frequencies up to 22.05 kHz. Using the 'Soundbuilder' software [119] , sound samples could be saved to disk in Microsoft Wave (.wav) format and exported to other systems for later analysis. In particular the numerical package 'Matlab' running on an HP-700 Unix workstation was used for signal processing.

Analysis in the previous section suggested that noise with significant spectral components up to 10 kHz should be expected from the CUED vortex tubes. The sampling theorem[11] then requires a minimum sampling rate of 20 kHz to avoid aliasing. Since the Macintosh can only operate at a discrete number of sampling rates, the recordings were made at the only rate exceeding 20 kHz, namely 22.05 kHz. No attempt was made to band-limit the signal recorded, through filtering, but the shape of the resultant power spectra, such as that shown in figure 3.21, and in particular their rapid decline towards the Nyquist frequency[12], suggests the results are competent.

For the majority of readings, the level of noise was such that it was necessary to reduce the voltage produced by the microphone to avoid swamping the A-D converter. This was achieved with a simple voltage divider circuit giving a voltage attenuation of 10:1. Tests with a tuning fork indicated that the circuit had little effect on the phase of the recorded signal.

[11]The Sampling Theorem states that for a digital recording of a signal to be useful (and unique), the sampling rate f_s used to record the signal must be at least twice that of the highest frequency spectral component of that signal (see for example, Gabel and Roberts [120]). If the sampling rate is insufficient, the spectral components of frequencies higher than the *Nyquist critical frequency*, $f_c = f_s/2$ are folded (aliased) back into the the range $(-f_c, f_c)$, as is shown by Press, Teukolsky, *et al.* [121].

[12]Since aliased spectral components are folded back into the spectrum, an incompetently sampled (i.e. aliased) signal will have a Fourier transform that tends to a finite value as the Nyquist frequency is approached. The spectrum of a competently sampled signal will tend to a low value at the Nyquist frequency. Press, Teukolsky, *et al.* [121] suggest that this fact forms a useful rule of thumb for checking sampled signals.

In ideal circumstances, acoustic measurements should be taken in an anechoic chamber. This was not possible in this case. Instead the sound recordings were made in a very noisy environment, indeed in the same laboratory as the compressor, and so are likely to be contaminated with extraneous noises. Fortunately, the microphone was highly directional, and in the main only picked up sounds from its immediate environment. Additionally the attenuation device described above made it possible to move the microphone close to the tube, reducing any contamination still further. Aural inspection of the recordings is unable to detect the extraneous sound.

Nevertheless recordings of the compressor alone were taken, and their spectral content compared to that of the tube noise samples. Attempts were made to subtract the two signals to reduce the magnitudes of the compressor components in the spectra. Using the linear properties of Fourier transforms

$$F_{tube}(j\omega) = F_{total}(j\omega) - F_{compr}(j\omega) \tag{3.38}$$

and then taking the inverse transform of the result

$$f_{tube}(t) = \mathcal{F}^{-1}\{F_{tube}(j\omega)\} \tag{3.39}$$

we can generate a signal, $f_{tube}(t)$ that represents the acoustical disturbances produced by the tube alone.

Before performing the subtraction (equation 3.38), it was necessary to match the phase and magnitude of the two signals. As the compressor signals showed a distinct, characteristic, peak near 86 Hz, (figure 3.20) this was used as a reference for scaling the magnitude and fixing the phase of the compressor signal. The magnitude of the peak in the Fourier transform of each signal was compared, and the compressor signal scaled to give equal magnitudes. In addition the phase of all the components in the compressor signal was advanced or retarded as necessary to make the signals in phase at the 90 Hz peak. For some signals the subtraction technique was unsuccessful. This would seem

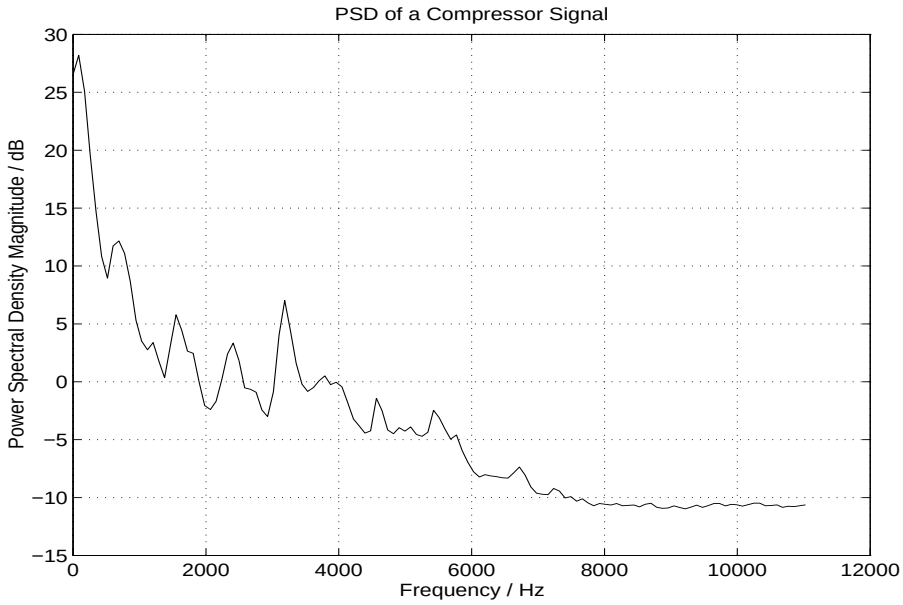

Figure 3.20: Power spectral density of a compressor signal.

to be due to the fact that relatively small variations in the positioning of the microphone made substantial differences to the recorded compressor signal, in some cases too large for the simple technique described to cope with. In these cases the 'noise' was eliminated 'manually' by comparing the traces.

3.6.3 Results

Samples were taken at various points around all three of the tubes, operating over the range of possible conditions. A typical set of results, obtained with the 26 mm tube operated in a counterflow configuration with a 7.5 mm diameter orifice at an inlet pressure of approximately 300 kPa ($P_{in}/P_c = 2.97$), will be presented as representative.

Figure 3.21 shows the power spectral density (PSD) of the signal recorded near the valve. There are no obvious peaks, and the result is in marked contrast to those of Kurosaka. The relatively flat profile was characteristic of all the recordings taken near the valve, and the relatively high frequency content in the band between 3000 Hz and 6000

Hz would appear to be due to the 'hissing' of the air as it impacts on the angled sides of the conical valve insert.

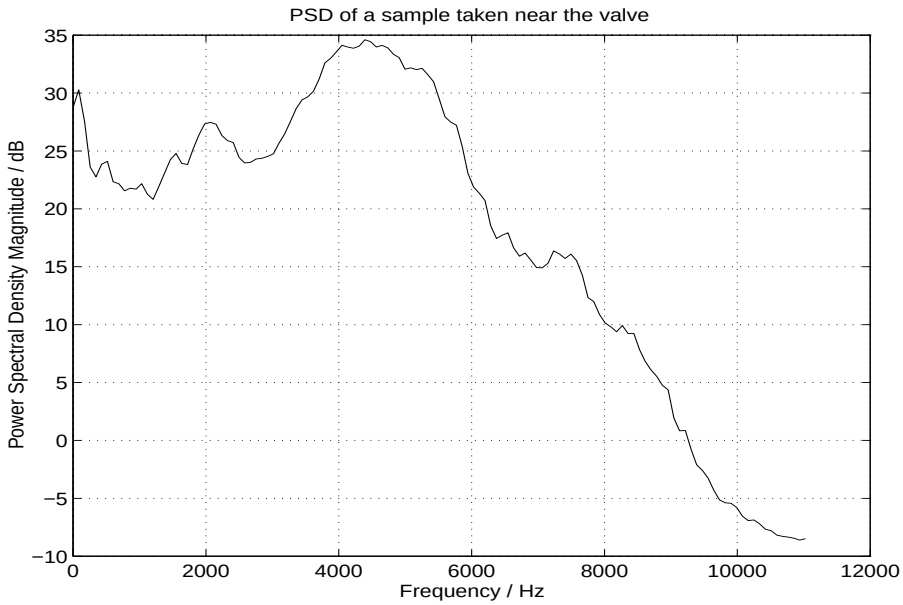

Figure 3.21: The power spectral density of the acoustic disturbances in the 26 mm tube, measured near the valve.

Spectral densities of the signals obtained near the inlet nozzles and near the cold outlets are shown in figures 3.22 and 3.23 respectively. Again, they are both substantially different from Kurosaka's results. One curious feature observable in both is their marked 'peakiness'. Considering figure 3.23, the first peak visible is at approximately 344 Hz, with the next one at 1033 Hz, then 1636 Hz and so on giving a repeating pattern of first a 698 Hz jump followed by a 603 Hz jump. The pattern was always most marked in signals taken at the cold exit, and for the most part did not vary significantly either with operating conditions, or indeed with the tube in use. There was no evidence of the peaks if the tube was run in a uniflow setup, or if the orifice was removed completely.

It would appear from this evidence that the peaks are due to longitudinal oscillations in the cold tube of each of the rigs caused by blowing over the orifice plate, and are entirely unrelated to any possible acoustic streaming. Three facts support this conclusion.

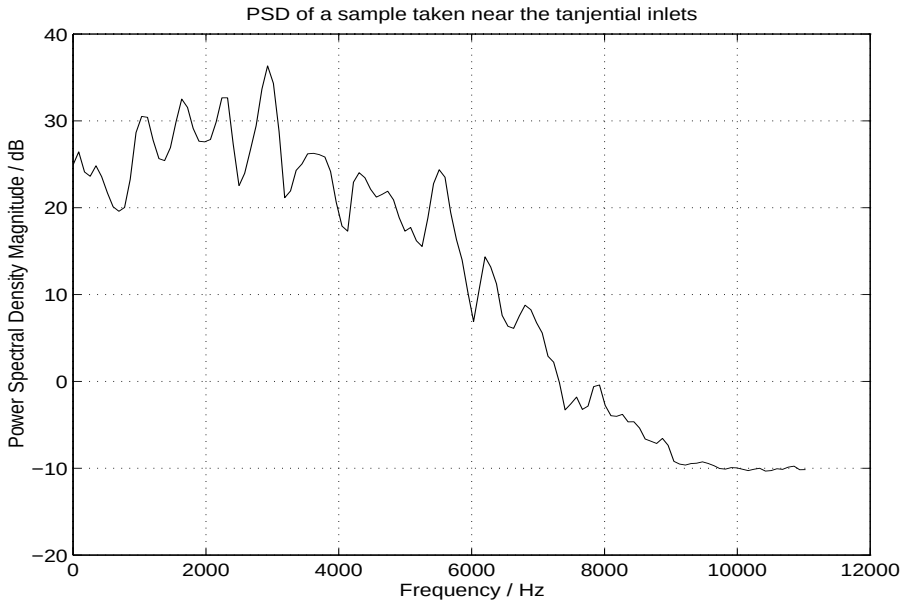

Figure 3.22: The power spectral density of the acoustic disturbances in the 26 mm tube, measured near the inlet nozzles.

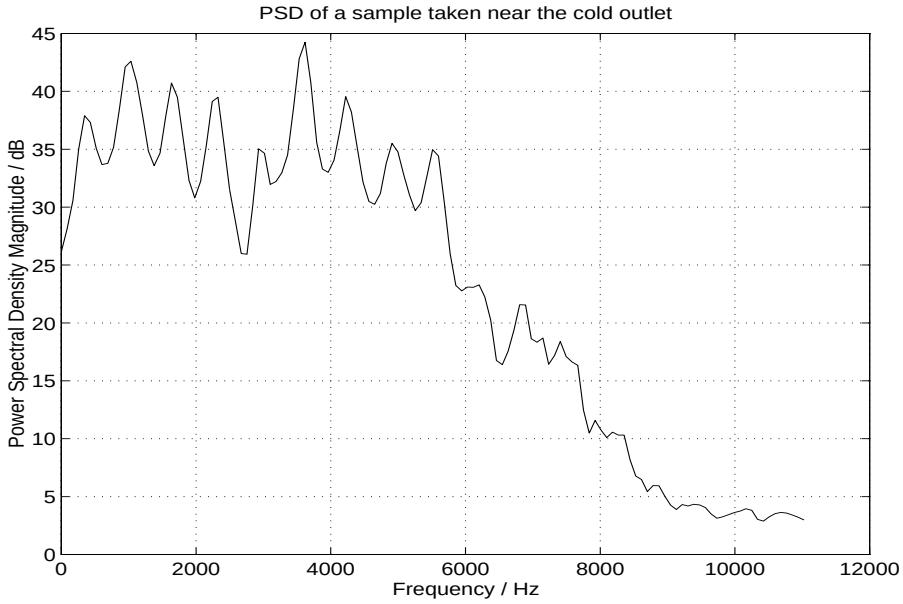

Figure 3.23: The power spectral density of the acoustic disturbances in the 26 mm tube, measured near the cold outlet.

Firstly, that the peaks are most visible in recordings taken near the cold exit; secondly that they were not visible in uniflow configurations or when the orifice was removed; and thirdly the approximately 1:3:5:7... relationship of the frequencies, which would be expected from longitudinal vibrations in a pipe effectively sealed at one end. For each rig the cold tube was 250 mm long. This equates to a fundamental frequency of longitudinal vibrations of approximately 340 Hz, corresponding well with the first frequency quoted above. The variations in step between the detected harmonics would appear to be due to the limited resolution of the algorithm used in calculating the spectral density, since the average separation is 650 Hz, nearly twice 344 Hz, as would be anticipated.

If the tubes were run without any orifice plate present at all, and with the hot valve shut tightly, such as to encourage the vortex to propagate down the cold tube, then there was a significant change in the acoustic output, aside from that mentioned already. A loud whistle became audible, and this showed up clearly in the spectra. Figure 3.24 shows a result obtained from a recording near the cold exit of the 26 mm tube operating without an orifice plate at an inlet pressure of 276 kPa ($P_{in}/P_c = 2.73$). The first part of the spectrum, magnified in figure 3.25 shows an acoustic disturbance reminiscent of Kurosaka's result, with the three peaks at approximately 400 Hz, 800Hz and 1200 Hz appearing to be a fundamental with two harmonics.

Recordings taken at other points around the tube did not show such clear peaks, indicating that the source of the disturbances was indeed near the cold outlet. Slowly inserting a solid plastic rod of 8 mm diameter for a distance 30 mm or more into the cold exit and such that it was parallel to and coincident with the major axis of the tube, eliminated the whistle and spectral peaks. If the rod was inserted in a similar orientation, but towards the periphery of the tube, little effect on the noise was observed. This would tend to locate the source of the noise even more precisely, to the behaviour of the central region of the vortex as it leaves the tube. In contrast to Kurosaka's observations, probes inserted radially into the tube had little influence on the disturbances.

The swirl distribution near the cold exit was measured using the intrusive probes described earlier in the chapter. Limits on the values are shown by the upper and lower

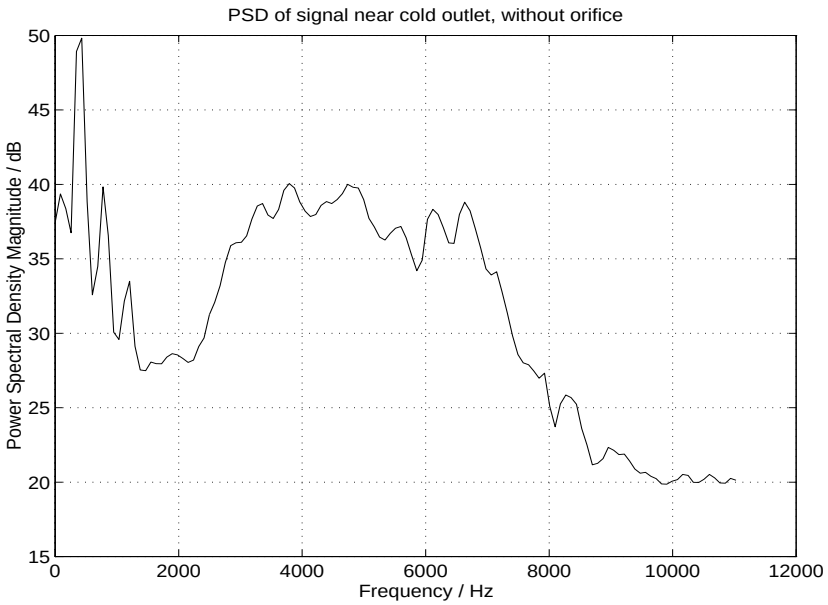

Figure 3.24: The power spectral density of the acoustic disturbances in the 26 mm tube run without an orifice plate, measured near the cold outlet.

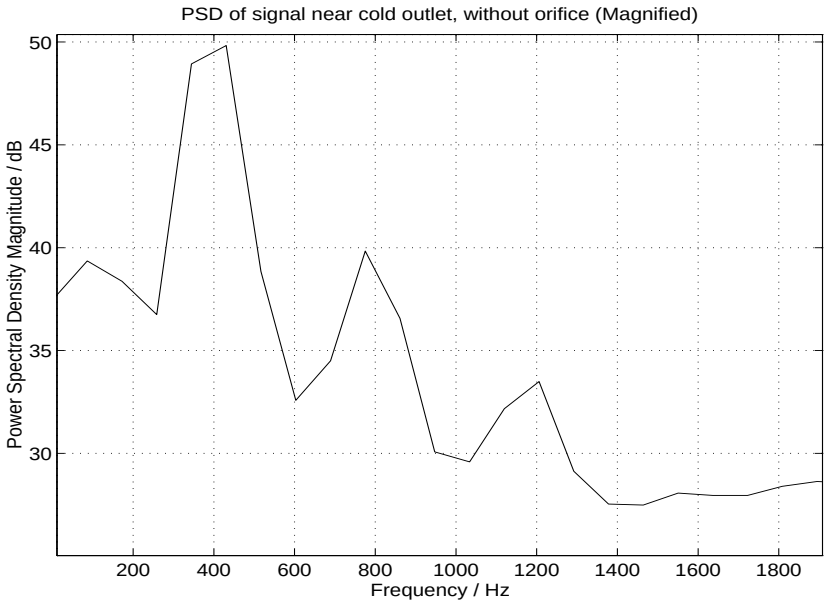

Figure 3.25: Close up of the power spectral density of the acoustic disturbances in the 26 mm tube run without an orifice plate, measured near the cold outlet, for frequencies up to 2 kHz.

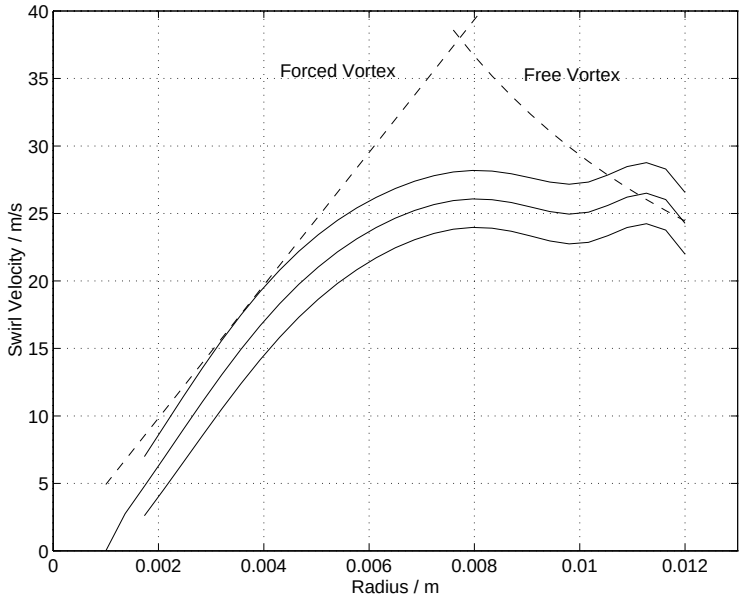

Figure 3.26: The swirl velocity distribution near the outlet of the cold tube. The upper and lower solid lines show the limits on the velocity distribution, accounting for estimated uncertainties, while the middle line gives the mean value. The dashed line illustrates an attempt to model the upper limit on the velocity as a Rankine vortex.

solid lines in figure 3.26. In order to calculate the disturbance frequency associated with the distributions, it is necessary to approximate them as a Rankine vortex.

As the frequency-swirl relationship only applies to inviscid flow, the approximation will be limited to swirl values lying outside the boundary layer on the cylindrical wall. The extent of the boundary layer is very difficult to identify, but the sudden decline in swirl velocity beyond a radius of 0.011 m suggests that the boundary layer starts here. This radius will be used as the effective radius of the tube in the frequency estimation, that is it will be assumed $r_o = 0.011$ m.

The dashed line in figure 3.26 shows the Rankine vortex approximation to the upper limit on the swirl distribution, which has parameters

$$\omega = 4.9292 \times 10^3 \tag{3.40}$$

$$\Gamma = 0.2933 \tag{3.41}$$

$$r^* = 0.0077 \tag{3.42}$$

$$r_o = 0.011. \tag{3.43}$$

The values were arrived at by a trial and error process, employing a few guidelines. Firstly the forced vortex line is tangential to the forced vortex part of the distribution. Secondly, Γ for the free vortex approximation was calculated by taking a representative point on the measured line, near to the boundary layer. The interface radius r^* was estimated as the intersection of the free and forced approximations. Values were also estimated for the lower limit on the swirl distribution.

Applying the frequency-swirl relationship, equation (3.34) to the Rankine vortex approximations predicts a fundamental frequency lying in the range 323 Hz $< f <$ 385 Hz. This partly overlaps with the measured frequency, which the spectral density plot shows to lie in the range 350 Hz $< f <$ 420 Hz. That the two results overlap quite well further confirms that the pure tone is caused by the interaction of the vortex with the still atmosphere at the cold exit. Increasing the inlet pressure of the gas supplied to the tube, and

thence the swirling velocity, produced a rise in the whistle frequency, again as would be expected from a vortex whistle.

Such results would seem to confirm Escudier's hypothesis regarding Kurosaka's experiment. In the normal uniflow and counterflow configurations, when the vortex is forced to travel down the long ($L/D = 50$) hot tube, no particular evidence of acoustical disturbances was found even though a significant temperature separation was evident. When the orifice plate was removed entirely, with the vortex traversing only the much shorter cold tube ($L/D = 10$), organised periodic disturbances, emanating from the central region of the exit to the cold tube and similar to those observed by Kurosaka, were found. The appearance of the disturbances must be directly related to the distance the vortex travels before leaving the tube, and is mostly due to the precessing of the vortex core as the strongly swirling flow enters the still atmosphere. When the vortex only travels the distance of the short cold tube it is still strong enough to produce acoustic disturbances as it enters the still atmosphere. After travelling the much longer length of the hot tube though, viscous dissipation has reduced the strength of the vortex to the extent that acoustical effects cannot be detected. Whatever their cause though, it seems safe to conclude Kurosaka's spinning waves were related only to the shortness of his apparatus, and not directly to the energy separation he found.

3.7 Discussion

3.7.1 Scope

We have considered information useful for two distinct, but related objectives regarding the vortex tube. The earlier sections of the chapter, namely the dimensional analysis along with the two similarity relationships, constitute what could be termed an 'external' investigation. Their results may help perhaps with attempts to model the behaviour of Ranque-Hilsch tubes. In contrast the later sections presenting the mapping of the flow and the acoustical measurements provide a more 'internal' picture of the tube, perhaps

providing a key into the mechanism underlying the energy separation. This section attempts not only to amplify the distinct conclusions we can draw from the work, but also to go some way towards reconciling those conclusions with each other.

3.7.2 External Measurements

Stephan's result raises a number of points. His original expression (3.1) can be re-written,

$$\Delta T_c^* = \frac{(\Delta T_c)_{max}}{T_{in}} \times f(\mu_c). \tag{3.44}$$

Comparing this to the results of the dimensional analysis for a single tube run on a single gas at a constant reservoir temperature

$$\Delta T_c^* = f\left(\frac{P_{in}}{P_c}, \mu_c\right) \tag{3.45}$$

suggests that for that single tube, by writing

$$\frac{(\Delta T_c)_{max}}{T_{in}} = f_1\left(\frac{P_{in}}{P_c}\right) \tag{3.46}$$

we can separate the variables to yield

$$\Delta T_c^* = f_1\left(\frac{P_{in}}{P_c}\right) \times f_2(\mu_c). \tag{3.47}$$

In this expression $f_1 = \Delta T_c^*$ could be interpreted as representing the separative power of the vortex tube, characteristic of the maximum temperature difference that can be obtained under any particular circumstances. Similarly f_2 would represent how that separative power was used to produce differing amounts of hot and cold gas. It would seem reasonable to extend this result to the other integrated variables. This idea is developed further in chapter 6.

Stephan's result was found to apply for a number of geometrically similar tubes, whereas

the conclusion of the dimensional analysis was restricted to a single tube. Their reconciliation, however, suggests that the result of the dimensional analysis would also model well a range of geometrically similar tubes. Consequently, the independent parameters that were rendered invariant when specialising the dimensional analysis from a general result for geometrically similar installations, to a single tube, cannot have a strong influence on the performance of geometrically similar tubes.

3.7.3 Internal Measurements

The detailed investigations of the flow patterns have produced results consistent with the findings of others. One particular feature to draw from the work are the clear regions where there is axial development of the energy separation. Whatever causes the radially outwards energy transfer in the vortex tube needs time to do its work, and theories suggesting an instant process should be considered very carefully in this light.

Momentarily casting aside the acoustical investigations, the applicability of acoustic streaming to vortex tube energy separation seems debatable. The proposed mechanism allows little scope for any re-enforcement of the energy separation as the flow progresses axially along the tube. Considering the evidence together, it would seem reasonable to deduce that acoustic streaming does not play a major part in producing the Ranque-Hilsch effect. To rule out acoustic effects in the vortex tube altogether would be rash though, as their influence in more general rotating flows is well known. It is safe to conclude that acoustic streaming by the vortex whistle is not responsible for the Ranque-Hilsch effect, although organised disturbances could somehow affect the velocity distribution in the tube in such a way as to encourage it.

3.8 Closure

This chapter began by considering the physical variables that might be expected to affect the performance of vortex tubes. From these, a set of dimensionless quantities was de-

rived. Further examination suggested that the operating point of any particular vortex tube could be characterised by two variables, P_{in}/P_c and μ_c, which would also serve to characterise approximately any set of geometrically similar vortex tubes.

Examination of the dependence of vortex tube performance on μ_c over a range of pressures confirmed that the two parameter model was plausible, and further suggested that the correct form of function to model the behaviour was a product between independent functions of each parameter alone.

A series of experiments to investigate the internal flow pattern in the vortex tubes yielded results for the most part consistent with preceding work. Flow visualisation provided a general impression of the flow, and allowed an estimation of flow velocities within the tube. Mapping of the flow field with intrusive probes produced a more detailed picture of the flow, complete with a thorough analysis of the inaccuracies of the procedures employed.

The possibility of an acoustic streaming mechanism being responsible for the energy flux in the vortex tube, as suggested by Kurosaka [8], was considered in some detail. An experimental study identified a number of acoustic disturbances in the tubes, but ruled out acoustic streaming as a major influence in the Ranque-Hilsch effect. The results were consistent with the interpretation advanced by Escudier [13].

With the results detailed in this chapter, experimental work on the vortex tube has been taken about as far as is possible with the available equipment. Foundations have been laid for the following, more theoretical, examinations of the vortex tube.

Chapter 4

Computation of Ranque-Hilsch Tube Type Flows

4.1 Objectives

Preceding chapters have highlighted some significant features of flows in Ranque-Hilsch tubes. Internal investigations have shown the basic nature of the flow, but their scope is severely limited by the disruption intrusive probes bring. Some external acoustic measurements have suggested that the direct influence of acoustical disturbances on the flow is small.

One curious observation from the literature survey was the dearth of numerical studies directed at the vortex tube. In the light of the difficulties of experimental study, computer based investigation would seem an attractive approach. Having said that, the energy separation in the vortex tube is a complex phenomenon, and any numerical solution that attempts to predict it will require a fair degree of sophistication even to obtain a qualitatively valid result.

To develop such a model represents a considerable effort. For reasons of practicality, the remit here was reduced to consideration of a basic qualitatively useful model that could be employed to investigate some of the important features of the Ranque-Hilsch

tube. In this capacity the focus was on computing the flow pattern accurately. Calculations of the temperature field were added when results for the flow were satisfactory.

The chapter begins by discussing the simplifications and assumptions that limit the physical model underlying the code. Next, the steps taken to account for the effects of turbulence are presented, after which the numerical method employed is described. A number of benchmark cases were run using the code to verify its correct functioning, and the results of these test runs are discussed briefly. Towards the end of the chapter, the attempts to simulate Ranque-Hilsch tube flows are described, and some conclusions drawn from the outcome.

4.2 Physical Modelling

4.2.1 Assumptions and Simplifications

The scope of the numerical model was reduced through a number of assumptions:

Steady-State

The model only aims to calculate steady-state solutions. This permits the time dependent terms in the Navier-Stokes equations to be abandoned. It also increases the range of solution techniques available, as there is no need for intermediate solutions obtained on the way to convergence to satisfy the Navier-Stokes equations.

Axisymmetry

Development of a full three-dimensional solver is outside the scope of this work. Code was developed in cylindrical co-ordinates, assuming axi-symmetry about the centre-line of the vortex tube. This is a significant limitation, as it is unlikely that the flow is axi-symmetric in reality, but has the advantage of allowing the solution of three velocity scalars, while only requiring the complexity associated with a two-dimensional solution.

Compressibility

Provision was made in the code for non-uniform density calculations. The density itself could be estimated using the equation of state with the calculated pressure and temperature values.

Compressible calculations should be limited to cases that might be described as 'flow with appreciable change of density', where the character of the equations remains elliptic. Fortunately such conditions exist within the vortex tube under an axisymmetric approximation, where the density variations are caused predominantly by the effects of swirl, rather than velocity and pressure variations in the 'main' axial and radial flow directions. Problems might be anticipated with more general compressible flows, where the axial and radial velocity fields are more strongly coupled with the density.

In practice, compressible calculations were found to be very time consuming, and so, many runs were performed under an incompressible assumption. Again, this represents a further level of approximation to real vortex tube flows. While the effect on the flow pattern is comparatively small, the lack of compressibility and its associated expansion work, removes any possibility of cooling.

One compromise that was found useful was to calculate the flow pattern using an assumption of incompressibility, but to allow density variations in the energy equation. The pressure used to calculate the density was taken directly from the result of the incompressible calculation. A similar approximation was employed in an analytical study by Linderstrom-Lang [40].

Turbulence

Flow in the vortex tube is turbulent. The steady state assumption, and practical considerations dictate that a turbulence model must be employed to represent its effects.

Domain limitations

The flow in the inlet plane, near the tangential nozzles is very complex. No attempt will be made to simulate this region. Inlet conditions will be limited to the radial induction of a swirling flow through an annular slit.

4.2.2 The Vorticity-Streamfunction Formulation

Comments

Primitive variable numerical solutions of the Navier-Stokes equations require careful specification in order to avoid difficulties caused by the pressure solution. Many methods have been developed to overcome such problems, see Patankar [122] for one example, but the solution of strongly swirling jet driven flows still represent a difficult situation. In many ways the assumption of axial symmetry aggravates the problem, as the major velocity component, the swirl velocity, responsible for the peculiar features of the flow, including most of the pressure variations, is reduced almost to the capacity of a convected property albeit one with a direct coupling to the axial and radial velocities.

In an attempt to avoid the difficulties that primitive variable solutions can experience, it was decided to adopt the so-called vorticity-streamfunction formulation of the radial and axial Navier-Stokes equations which eliminates explicit pressure terms from the equations solved. An additional advantage, in an axisymmetric case, is a reduction in the number of variables that must be solved, from three (axial and radial velocities, and pressure) to two (vorticity and streamfunction).

The vorticity-streamfunction formulation offers problems of its own, however. Firstly, the variables solved are a level of abstraction removed from the velocity and pressures with which one is familiar. To recover the more easily understood quantities a substantial amount of post-processing is required. Secondly the specification of boundary conditions is made more difficult, again by the need to couch them in terms of the vorticity and streamfunction. Lastly, to keep the complexity of the equations within reasonable

bounds, the choice of turbulence model, if required, is limited to one which can be incorporated in the governing equations without altering their form from the laminar case.

The analysis presented in this section draws heavily on the work of Gosman *et al.* [50], although a number of changes have been incorporated to specialise the solution the vortex tube. Note that the analysis is general in that it allows scope for density fluctuations, whereas the majority of vorticity-streamfunction calculations cited in the literature are limited to incompressible flow.

Derivation

Define the vorticity in cylindrical co-ordinates[1]

$$\omega = \frac{\partial u}{\partial z} - \frac{\partial w}{\partial r} \tag{4.1}$$

and the streamfunction ψ such that

$$\rho w = \frac{1}{r}\frac{\partial \psi}{\partial r} \tag{4.2}$$

$$\rho u = -\frac{1}{r}\frac{\partial \psi}{\partial z}. \tag{4.3}$$

The continuity, radial momentum and axial momentum equations may be reformulated in terms of these two quantities in such a way that pressure does not explicitly appear. For turbulent flows it is necessary to perform the analysis with the equations already time averaged, and to assume that closure is achieved with a stress transport model that relates the turbulence correlations to gradients of the mean quantities in such a way that the form of the equations is unchanged from that in laminar flow, if the effects of the turbulence are represented by an eddy viscosity.

Analysis begins by cross-differentiating the axial and radial momentum equations,

[1]The analysis in this chapter will be presented in cylindrical co-ordinates. The original derivation for the vorticity and stream function equations was performed in generalised orthogonal co-ordinates, after Gosman [50]. This allows the solution of vorticity-streamfunction problems in Cartesian co-ordinates, which is useful when verifying the code.

and then subtracting one from the other to eliminate the pressure term. A considerable quantity of algebra is required to introduce the streamfunction and vorticity, giving the vorticity equation

$$\frac{1}{r}\left\{\frac{\partial}{\partial z}\left(\frac{\omega}{r}\frac{\partial\psi}{\partial r}\right)-\frac{\partial}{\partial r}\left(\frac{\omega}{r}\frac{\partial\psi}{\partial z}\right)\right\}+\frac{1}{r}\left\{\frac{\partial}{\partial r}\left(\frac{w^2+u^2}{2}\right)\frac{\partial\rho}{\partial z}-\frac{\partial}{\partial z}\left(\frac{w^2+u^2}{2}\right)\frac{\partial\rho}{\partial r}\right\}-\frac{1}{r^2}\frac{\partial}{\partial z}\left(\rho v^2\right)=\mathcal{S}, \tag{4.4}$$

where $\mathcal{S}$ incorporates all terms that involve viscosity and might be considered to represent the effects of shear work on the vorticity. We can write this term as[2]

$$\mathcal{S}=\frac{1}{r^2}\nabla.\left\{r^2\nabla\left(\frac{\mu_e\omega}{r}\right)\right\}+S_{\partial\mu_e}, \tag{4.5}$$

with

$$\begin{aligned}S_{\partial\mu_e} &= \frac{2}{r}\left[-\frac{\partial w}{\partial z}\frac{\partial^2\mu_e}{\partial r\partial z}+\frac{\partial w}{\partial r}\frac{\partial^2\mu_e}{\partial z^2}-\frac{\partial u}{\partial z}\frac{\partial^2\mu_e}{\partial r^2}+\frac{\partial u}{\partial r}\frac{\partial^2\mu_e}{\partial z\partial r}+\frac{\partial}{\partial r}\left(\frac{\partial w}{\partial z}+\frac{1}{r}\frac{\partial\left(ru\right)}{\partial r}\right)\frac{\partial\mu_e}{\partial z}\right]\\ &\quad+\frac{2}{r}\left[-\frac{\partial}{\partial z}\left(\frac{\partial w}{\partial z}+\frac{1}{r}\frac{\partial\left(ru\right)}{\partial r}\right)\frac{\partial\mu_e}{\partial r}\right].\end{aligned} \tag{4.6}$$

Note that the velocity terms have not been eliminated entirely from the left-hand side of equation (4.4). There are three reasons for this. Firstly the introduction of vorticity squared terms that would result from their removal would complicate the numerical solution. Secondly the remaining terms vanish in incompressible calculations, and for compressible flows can be quite adequately incorporated as a source term, evaluated using the velocity and density values from the previous sweep of the domain. The velocity terms incorporated in $\mathcal{S}$ can also be adequately evaluated as a source term using the previous solution approximation.

For convenience when discussing the iterative solver in the later parts of the chapter,

[2] μ_e in this expression is the effective viscosity and is described in section 4.3.1.

all the equations in this section will be written in a common format as follows

$$A\left\{\frac{\partial}{\partial z}\left(\phi\frac{\partial\psi}{\partial r}\right)-\frac{\partial}{\partial r}\left(\phi\frac{\partial\psi}{\partial z}\right)\right\}-\frac{\partial}{\partial z}\left\{Br\frac{\partial\left(C\phi\right)}{\partial z}\right\}-\frac{\partial}{\partial r}\left\{Br\frac{\partial\left(C\phi\right)}{\partial r}\right\}+rD=0. \quad (4.7)$$

In general the first term in the equation will have convective properties, the second and third terms will be diffusive in nature, and the final term is a source. With this formulation, the vorticity equation becomes

$$\begin{aligned} r^2\left\{\frac{\partial}{\partial z}\left(\frac{\omega}{r}\frac{\partial\psi}{\partial r}\right)-\frac{\partial}{\partial r}\left(\frac{\omega}{r}\frac{\partial\psi}{\partial z}\right)\right\}-\frac{\partial}{\partial z}\left\{r^2.r.\frac{\partial\left(\mu_e\frac{\omega}{r}\right)}{\partial z}\right\}-\frac{\partial}{\partial r}\left\{r^2.r.\frac{\partial\left(\mu_e\frac{\omega}{r}\right)}{\partial r}\right\} \\ +r\left\{-\frac{\partial\left(\rho v^2\right)}{\partial z}-r\left[\frac{\partial}{\partial z}\left(\frac{w^2+u^2}{2}\right)\frac{\partial\rho}{\partial r}-\frac{\partial}{\partial r}\left(\frac{w^2+u^2}{2}\right)\frac{\partial\rho}{\partial z}\right]-r^2S_{\partial\mu_e}\right\} &= 0 \end{aligned} \quad (4.8)$$

where the variable solved for is ω/r.

The streamfunction equation is derived from the continuity equation by replacing the products of density and velocity using the definitions of the streamfunction given above. The resulting equation has no diffusive terms and may be written in the standard format as

$$-\frac{\partial}{\partial z}\left\{\frac{1}{\rho r^2}r\frac{\partial\psi}{\partial z}\right\}-\frac{\partial}{\partial r}\left\{\frac{1}{\rho r^2}r\frac{\partial\psi}{\partial r}\right\}-r\left(\frac{\omega}{r}\right)=0. \quad (4.9)$$

Equations (4.8) and (4.9) represent the heart of the solver.

4.2.3 The Swirl Equation

Applying the assumption of axisymmetry to the momentum equation in the circumferential direction produces considerable simplification. Elimination of the axial and radial velocities by substituting the streamfunction expressions, and writing the result in the the standard form of equation (4.7) gives

$$\frac{\partial}{\partial z}\left(v\frac{\partial\psi}{\partial r}\right)-\frac{\partial}{\partial r}\left(rv\frac{\partial\psi}{\partial z}\right)-\frac{\partial}{\partial z}\left(\mu_e r^2.r.\frac{\partial\left(\frac{rv}{r^2}\right)}{\partial z}\right)-\frac{\partial}{\partial r}\left(\mu_e r^2.r.\frac{\partial\left(\frac{rv}{r^2}\right)}{\partial r}\right)=0, \quad (4.10)$$

to solve for rv.

4.2.4 The Energy Equation

Under the assumptions outlined earlier, and accounting for the contribution of the turbulent kinetic energy to the total energy budget, the equation for the transport of stagnation enthalpy h_0 written in the standard form is

$$\begin{aligned}\left[\frac{\partial}{\partial z}\left(h_0\frac{\partial\psi}{\partial r}\right)-\frac{\partial}{\partial r}\left(h_0\frac{\partial\psi}{\partial z}\right)\right]-\left[\frac{\partial}{\partial z}\left(\frac{\mu_e}{\sigma_h}.r.\frac{\partial h_0}{\partial z}\right)+\frac{\partial}{\partial r}\left(\frac{\mu_e}{\sigma_h}.r.\frac{\partial h_0}{\partial z}\right)\right]\\ -\frac{\partial}{\partial z}\left(\mu_e r\left\{\left(1-\frac{1}{\sigma_h}\frac{\partial\left(\mathbf{v}^2/2\right)}{\partial z}\right)+\left(\frac{1}{\sigma_k}-\frac{1}{\sigma_h}\right)\frac{\partial k}{\partial z}\right\}\right)\\ -\frac{\partial}{\partial r}\left(\mu_e r\left\{\left(1-\frac{1}{\sigma_h}\frac{\partial\left(\mathbf{v}^2/2\right)}{\partial r}\right)+\left(\frac{1}{\sigma_k}-\frac{1}{\sigma_h}\right)\frac{\partial k}{\partial z}\right\}\right)\\ -\frac{\partial}{\partial z}\left(r\mu_e\Phi_r\right)-\frac{\partial}{\partial r}\left(r\mu_e\Phi_z\right) = 0. \quad (4.11)\end{aligned}$$

The functions, Φ_r and Φ_z are given by

$$\Phi_r = \frac{\partial}{\partial r}\left(\frac{u^2}{2}\right)-\frac{2}{3}u\left(\frac{\partial w}{\partial z}+\frac{1}{r}\frac{\partial\left(ru\right)}{\partial r}\right)+w\frac{\partial u}{\partial z}-\frac{v^2}{r}, \quad (4.12)$$

$$\Phi_z = \frac{\partial}{\partial z}\left(\frac{w^2}{2}\right)-\frac{2}{3}w\left(\frac{\partial w}{\partial z}+\frac{1}{r}\frac{\partial\left(ru\right)}{\partial r}\right)+u\frac{\partial w}{\partial r}. \quad (4.13)$$

The transport coefficient σ_h is the turbulent Prandtl number for enthalpy transport, or as we are dealing with perfect gases, temperature diffusion. By definition we have

$$\sigma_h = \frac{\mu_e c_p}{\lambda_e} \quad (4.14)$$

with λ_e the effective thermal conductivity of the gas. Clearly in the laminar case λ_e is equal to the molecular conductivity of the gas. A similar role is played in the transport of the turbulent kinetic energy by σ_k.

4.3 Turbulence Modelling

4.3.1 Necessity

It has been established that the flow within the vortex tube is turbulent. To account for this, we are attempting to solve the time averaged Navier-Stokes equations. In order to provide closure for the fluctuating components a certain amount of empiricism is required in the form of a turbulence model. The reader will recall that our adoption of a vorticity-streamfunction formulation essentially limits our choice to stress transport models that do not alter the basic form of the equations to be solved. In this context the problem reduces to one of how to calculate the turbulent part μ_t of the expression for the effective viscosity

$$\mu_e = \mu_t + \mu \tag{4.15}$$

which replaces the 'pure' laminar value, μ in the Navier-Stokes equations.

This section briefly describes the two-equation $k-\epsilon$ model incorporated into the code, and considers some of the modifications that can be made to better model turbulence in swirling flow.

4.3.2 The Two-Equation Model

The two equation model, as developed by Launder and Jones [43], solves transport equations over the entire flow field for two properties that can be used to characterise the turbulence at any point, specifically the turbulent kinetic energy k and the turbulent dissipation rate ϵ. Values for the turbulent viscosity can be estimated from

$$\mu_t = C_\mu \rho \frac{k^2}{\epsilon}, \tag{4.16}$$

where C_μ is an empirical constant.

Adopting the standard format of presentation, the transport equations solved in cyl-

indrical co-ordinates are

$$\left\{\frac{\partial}{\partial z}\left(k\frac{\partial\psi}{\partial r}\right)-\frac{\partial}{\partial r}\left(k\frac{\partial\psi}{\partial z}\right)\right\}-\frac{\partial}{\partial z}\left(\frac{r\mu_t}{\sigma_k}\frac{\partial k}{\partial z}\right)-\frac{\partial}{\partial r}\left(\frac{r\mu_t}{\sigma_k}\frac{\partial k}{\partial r}\right)+r\left(\rho\epsilon-P_s\right) = 0 \tag{4.17}$$

$$\left\{\frac{\partial}{\partial z}\left(\epsilon\frac{\partial\psi}{\partial r}\right)-\frac{\partial}{\partial r}\left(\epsilon\frac{\partial\psi}{\partial z}\right)\right\}-\frac{\partial}{\partial z}\left(r\frac{\mu_t}{\sigma_\epsilon}\frac{\partial\epsilon}{\partial z}\right)-\frac{\partial}{\partial r}\left(r\frac{\mu_t}{\sigma_\epsilon}\frac{\partial\epsilon}{\partial r}\right)-r\left(C_1\frac{\epsilon}{k}P_s-C_2\frac{\rho\epsilon^2}{k}\right) = 0. \tag{4.18}$$

The production of turbulent kinetic energy is given by

$$P_s=\mu_t\left\{2\left[\left(\frac{\partial w}{\partial z}\right)^2+\left(\frac{\partial u}{\partial r}\right)^2+\left(\frac{u}{r}\right)^2\right]+\left(\frac{\partial w}{\partial r}+\frac{\partial u}{\partial z}\right)^2+\left(\frac{\partial v}{\partial z}\right)^2+\left[r\frac{\partial}{\partial r}\left(\frac{v}{r}\right)\right]^2\right\} \tag{4.19}$$

Conventionally (see Jones and Launder [43]) the empirical model constants are taken to be as shown in table 4.1.

C_μ	σ_K	σ_ϵ	C_1	C_2
0.09	0.9	1.22	1.44	1.92

Table 4.1: The empirical constants used in the standard $k-\epsilon$ turbulence model.

4.3.3 Modifications of the Two-Equation Model

The effects of anisotropic turbulence in rotating flows cannot be accommodated directly by the two-equation model. A number of modifications to the model have been suggested in order to improve its performance in strongly swirling flows. Some calculations discussed in this thesis were accomplished using the modification suggested by Launder *et al.* [123], based on a Richardson number correction to the turbulence energy dissipation equation.

In this context the turbulent Richardson number is defined

$$Ri_t = \frac{k^2}{\epsilon^2}\frac{v}{r^2}\frac{\partial (rv)}{\partial r}. \tag{4.20}$$

The constant C_2 in the turbulence dissipation equation (4.18) is replaced by $C_2\ (1 - C_C Ri_t)$ where a series of numerical experiments by Launder have suggested that $C_C = 0.2$.

4.4 Numerical Technique for Through-Flow Calculations

4.4.1 The Nature of the Computational Problem

To solve numerically the continuum equations developed above, it is first necessary to convert them into a set of simultaneous algebraic difference equations. The first part of this section describes the method employed to achieve this, and discusses its limitations.

The second aspect to the numerical solution is the choice of procedure employed to satisfy the algebraic equations. A relatively simple, explicit successive relaxation method was chosen, updating each variable in turn, and then returning to the first.

Towards the end of the section the mechanism utilised to obtain the more intuitive pressure and velocity from the vorticity and streamfunction distributions is related.

4.4.2 Discretisation

A composite finite volume / finite difference method was used for the discretisation of the equations. The analysis follows the 'Tank and Tube' approach documented in a number of publications (Gosman [50]), and will only be outlined here.

The general form of the differential equations, equation (4.7) is to be integrated over the control volume[3] shown in figure 4.1. We need to evaluate the relationship

[3]The diagram shows an area, representing a view of a cross section taken through and parallel to the axis of symmetry. The analysis will be presented for a body of revolution produced by rotating the area shown through one radian about the axis of symmetry.

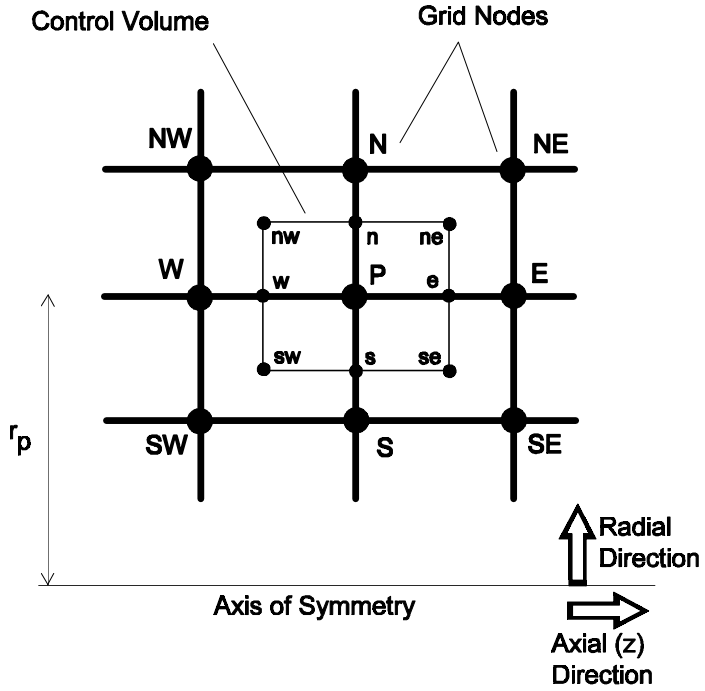

Figure 4.1: The finite control volume in cylindrical co-ordinates.

$$\int_{r_n}^{r_s}\int_{z_w}^{z_e} A\left\{\frac{\partial}{\partial z}\left(\phi\frac{\partial\psi}{\partial r}\right)-\frac{\partial}{\partial r}\left(\phi\frac{\partial\psi}{\partial z}\right)\right\}\,dr\,dz$$
$$-\int_{r_n}^{r_s}\int_{z_w}^{z_e}\left\{\frac{\partial}{\partial z}\left(Br\frac{\partial(C\phi)}{\partial z}\right)+\frac{\partial}{\partial r}\left(Br\frac{\partial(C\phi)}{\partial r}\right)\right\}\,dr\,dz$$
$$+\int_{r_n}^{r_s}\int_{z_w}^{z_e} rD\,dr\,dz \;=\; 0. \qquad (4.21)$$

If A is constant, then one integration may be performed directly on all terms except the last. Examination of the equations shows that A is unity for all variables except the vorticity ω/r, where it is r^2. For the vorticity, and any similar case, A will be replaced by a constant 'average' value, to be denoted A_P. The square of the value of the radius at the centre of the cell, r_P^2 will be employed here. This difficulty resolved, performing the

integration gives

$$A_P \left[\int_{r_s}^{r_n} \left\{ \phi_e \left(\frac{\partial \psi}{\partial r} \right)_e - \phi_w \left(\frac{\partial \psi}{\partial r} \right)_w \right\} dr - \int_{z_w}^{z_e} \left\{ \phi_n \left(\frac{\partial \psi}{\partial r} \right)_n - \phi_s \left(\frac{\partial \psi}{\partial r} \right)_s \right\} dz \right]$$
$$- \int_{r_n}^{r_s} \left\{ (Br)_e \left(\frac{\partial (C\phi)}{\partial z} \right)_e - (Br)_w \left(\frac{\partial (C\phi)}{\partial z} \right)_w \right\} dr$$
$$- \int_{z_e}^{z_w} \left\{ (Br)_n \left(\frac{\partial (C\phi)}{\partial z} \right)_n - (Br)_s \left(\frac{\partial (C\phi)}{\partial z} \right)_s \right\} dz$$
$$+ \int_{r_s}^{r_n} \int_{z_w}^{z_e} rD \, dz \, dr = 0. \tag{4.22}$$

Convective Terms

Each of the convective terms in equation (4.22) has a similar form. Only one will be considered here,

$$I = A_P \int_{r_s}^{r_n} \phi_e \left(\frac{\partial \psi}{\partial r} \right)_e dr, \tag{4.23}$$

the extension to other terms being straightforward. An average for the value of ϕ_e over the range of integration can be defined

$$\bar{\phi}_e = \frac{\int_{r_n}^{r_s} \phi_e \left(\frac{\partial \psi}{\partial r} \right)_e dr}{\int_{r_n}^{r_s} \left(\frac{\partial \psi}{\partial r} \right)_e dr}. \tag{4.24}$$

If ψ and ϕ are well behaved, and can be approximated as linear over the range of integration, then an approximate expression for the integral could be formulated

$$I = A_P \bar{\phi}_e \left(\psi_{ne} - \psi_{se} \right) \tag{4.25}$$

with the subscripts ne and se referring to values at the appropriate corners of the domain.

To proceed, two further assumptions will be made. Firstly, the value of ϕ inside the

control volume is uniform, and adopts the value associated with the continuum solution at node P; in other words the value of ϕ within the control volume is that at its centre ϕ_P. Secondly that $\bar{\phi}_e$ takes on the value of ϕ associated with the fluid *upstream* of the e-face of the control volume. This is equivalent to upwind finite differencing, and thence the integral becomes

$$I = A_P \left[\phi_E \left\{ \frac{(\psi_{ne} - \psi_{se}) - \mid \psi_{ne} - \psi_{se} \mid}{2} \right\} + \phi_P \left\{ \frac{(\psi_{ne} - \psi_{se}) + \mid \psi_{ne} - \psi_{se} \mid}{2} \right\} \right]. \quad (4.26)$$

The final assumption in the discretisation will be that ϕ_{se} and ϕ_{ne} can be approximated as the average of the ψ values at the surrounding nodes, that is

$$\psi_{se} = \frac{\psi_{SE} + \psi_E + \psi_P + \psi_S}{4}. \quad (4.27)$$

Diffusive Terms

The diffusive terms in equation (4.22) all take the form of

$$I = \int_{r_s}^{r_n} [Br]_e \left[\frac{\partial}{\partial z} (C\phi) \right]_e dr. \quad (4.28)$$

For this integration, assume that *locally* to the cell, B, and $C\phi$ vary linearly with z. Thus approximate relations may be written

$$r_e = \frac{r_E + r_P}{2}, \quad (4.29)$$

$$B_e = \frac{B_E + B_P}{2}, \quad (4.30)$$

$$\left[\frac{\partial (C\phi)}{\partial z} \right]_e = \frac{C_E\phi_E - C_P\phi_P}{z_E - z_P}. \quad (4.31)$$

The integral may be approximated as

$$I = \frac{B_E + B_P}{2} \times \frac{r_E + r_P}{2} \times \frac{C_E\phi_E - C_P\phi_P}{z_E - z_P} \times \frac{r_N - r_S}{2}, \quad (4.32)$$

and similarly for the other terms.

Source Term

Consider the source term in the partially integrated equation (4.22)

$$Source = \int_{r_s}^{r_n} \int_{z_w}^{z_e} rD \; dz \; dr. \tag{4.33}$$

To perform this integration, it will be assumed that D is constant over the whole of the control volume. The integral is then equivalent to the value of D, multiplied by the volume of the control volume, i.e.

$$Source \approx D.Vol, \tag{4.34}$$

where for an angle of one radian around the axis of symmetry

$$Vol \approx r_P \left(\frac{z_E - z_W}{2}\right) \left(\frac{r_N - r_S}{2}\right). \tag{4.35}$$

If, as if often the case, D takes the form of a differential expression, it can be discretised using central differences.

Special formulation near the centre-line

Particular care must be taken with the discretisation procedure near the axis of symmetry, where r is small. For those $C\phi$ that are dependent on negative powers of r, serious numerical problems can occur. A case in point is the solution of the swirl equation, which has $C = 1/r^2$ and $\phi = vr$, giving $C\phi = v/r$.

In general, it is required to impose a symmetry boundary condition at the centre-line. The easiest approach for the swirl equation is to formulate the boundary condition in terms of $C\phi = v/r$ which being the angular velocity tends to a finite value at the axis. The discretisation at the next node out radially is adapted to use this value directly. Thus, for nodes adjacent to the centreline, a special discretisation is employed for the southerly

diffusive term,

$$\int_{z_w}^{z_e} \left[Br.r. \frac{\partial \left(\frac{1}{r^2} rv\right)}{\partial r} \right]_s dz. \tag{4.36}$$

The differential is written

$$\frac{\partial \left(\frac{1}{r^2} rv\right)}{\partial r} = \frac{\frac{1}{r_P^2} (rv)_P - \left(\frac{v}{r}\right)_{centreline}}{r_P}, \tag{4.37}$$

with the $\left(\frac{v}{r}\right)_{centreline}$ term carried all the way though into the final expression for $(rv)_P$.

Final stage

When the discretisation of all the terms is complete, the integral expressions in the governing equation are replaced by their algebraic equivalents. The result is re-arranged to make the value of ϕ at the central node, ϕ_P, the subject of the expression, giving the general form

$$\phi_P = C_E \phi_E + C_W \phi_W + C_N \phi_N + C_S \phi_S + D. \tag{4.38}$$

Such an equation exists for the value of each of the variables ϕ at each node within the domain.

4.4.3 Gauss-Siedel Iteration

A straightforward Gauss-Siedel relaxation technique was employed to solve the simultaneous algebraic equations (4.38) for each dependent variable ϕ. Details of the order of the solution are given in section 4.5.

4.4.4 Velocity Calculations

Axial and radial velocities were calculated directly from the streamfunction and streamfunction values using finite difference approximations to

$$w = \frac{1}{\rho r}\frac{\partial \psi}{\partial r}, \tag{4.39}$$

$$u = -\frac{1}{\rho r}\frac{\partial \psi}{\partial z}. \tag{4.40}$$

4.4.5 Pressure Calculations

Pressure values were estimated by simple line integration of the velocity and density fields. The integral was first performed along the centre-line of the domain, starting from a point of known pressure. The radial variation of the pressure field was estimated by integrating outwards from the centre-line.

4.5 Code Implementation

4.5.1 Outline

A flow diagram illustrating the overall solution procedure is shown in figure 4.2. After initialisation of the variables with their starting values, the boundary conditions for the problem are established. The calculation begins with a sweep updating the vorticity solution, followed by the streamfunction, and then the swirl velocity. Next the velocity field is estimated for use in the following calculations. Using this information, the temperature field is calculated. With a turbulent computation, the turbulence model is then called to estimate the new turbulent viscosity. If required the pressure can calculated by direct integration of the velocity fields. For a compressible flow, this stage is essential to allow the density field to be updated, but for an incompressible fluid it is more efficient to delay all pressure calculations until the vorticity and streamfunction have both converged.

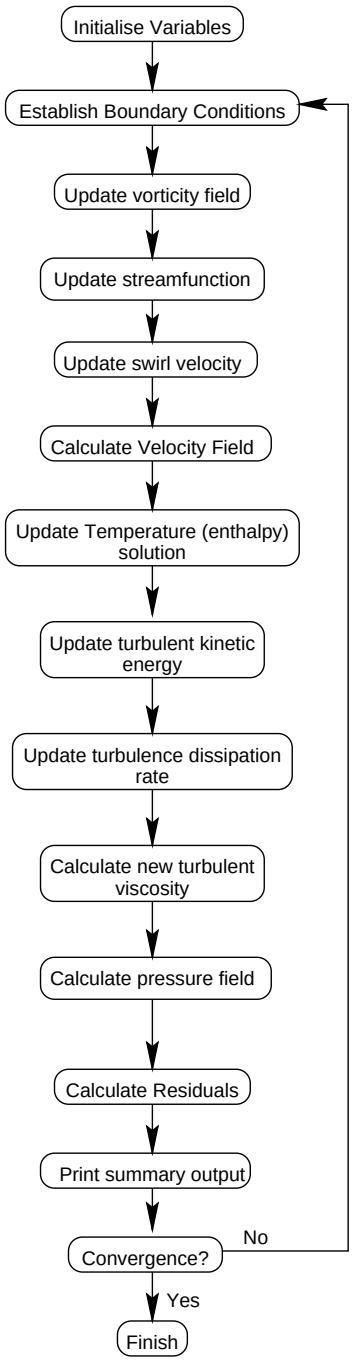

Figure 4.2: Flow diagram for the vorticity-streamfunction code.

4.5.2 Stability

The stability characteristics of explicit vorticity-streamfunction based numerical methods mean that care has to be taken with the solution. In cases with substantial swirl, generally a swirl number in excess of unity, heavy under-relaxation was required to prevent divergence with a consequent increase in the solution time. Use of a red-black ordering technique (Press *et al.* [124]) provided a modest increase in the speed of convergence.

Adaptive Relaxation Parameter Technique

The stability of the solution process was slightly improved by the adoption of a simple procedure that attempted to adjust the degree of relaxation applied to the variables, depending on the recent history of the computations.

Relaxation on all the variables solved was implemented as

$$\phi^{[k+1]} = (1 - R_\phi)\,\phi^{[k]} + R_\phi \phi^* \tag{4.41}$$

where $R|\phi$ is the relaxation coefficient, $\phi^{[k+1]}$ is the value of the variable after the $(k+1)$th sweep of the grid, $\phi^{[k]}$ is the old value of the variable and ϕ^* is the value produced by the Gauss-Siedel solver. With the adaptive technique, the size of R_ϕ was calculated as a function of the residual from the previous two sweeps according to the following algorithm. If the residual had decreased at the last sweep, the relaxation coefficient was multiplied by a small factor, typically 1.002. If the residual had increased, the relaxation factor was divided by factor larger than that used for multiplication, typically 1.01. Relaxation factors were calculated independently for each variable.

Generally the adaptive technique in general did little to speed up the overall time to convergence required by the code. Although no quantitative tests were carried out, in most cases the time penalty imposed by evaluating a new relaxation coefficient after each sweep of the grid more than offsets the savings provided by the efforts of the routine to keep the coefficient as high as possible.

The greatest advantage of the technique was in cases that proved to have poor stability properties, and in particular computations with large swirl. These computations appeared to be only marginally stable at first, but after a number of iterations would 'settle down', and begin to converge well. The adaptive technique allowed the use of very small relaxation coefficients in the early stages of such calculations, but would increase the coefficients as the values started to converge. This gave three advantages, by promoting stability in the early stages of computation, reducing unnecessary delays due to over cautious relaxation in the later stages, and reducing the need for experimentation to find suitable coefficients for each case.

No attempt was made to optimise the adaptive technique, and considerable improvements could be made. The routine, as described above, errs on the side of caution. It is particularly prone to sudden, isolated increases in residuals that have previously shown good convergence characteristics, and then continue to do so.

4.5.3 Convergence Criterion

The convergence of solutions given by the code was determined by means of the value of the residual evaluated according to the criterion

$$\frac{max\left(\phi^{[k+1]} - \phi^{[k]}\right)}{max\left(\phi^{[k+1]}\right)} < \epsilon. \tag{4.42}$$

In general ϵ was taken as 5×10^{-5}. Any other values are given in the text.

4.6 Verification of the Through-Flow Code

4.6.1 Overview

In order to verify the correct functioning of the code a number of benchmark calculations were performed. This section reviews the results of some of the test calculations, with

the objective of assuring the reader as to the validity of the vortex tube simulations that follow. More details concerning the computations can be found in appendix C.

4.6.2 Driven Cavity Laminar Benchmark

To test the basic function of the vorticity-streamfunction solver, the flow pattern in a driven cavity was calculated. The code was operated in its Cartesian mode under laminar conditions.

The driven cavity problem is a commonly used benchmark, and there are many solutions available in the literature. A typical domain is shown in figure 4.3. Results pro-

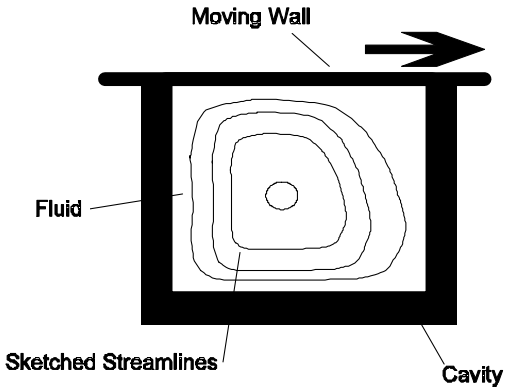

Figure 4.3: Outline of the driven cavity problem.

duced by the solver stood comparison with the computations of Gosman [50].

Verification of grid independence was achieved by calculating the same problem with grids ranging from 21x21 to 91x91 nodes. Comparison of the solutions showed a reasonable correspondence. The differences that were visible could be attributed to the change in numerical viscosity resulting from the different grid spacings.

4.6.3 Rotating Pipe-Flow Laminar Benchmark

Assessment of the vorticity-streamfunction formulation in cylindrical co-ordinates, and of solutions of the swirl equation was accomplished by computing the laminar axisym-

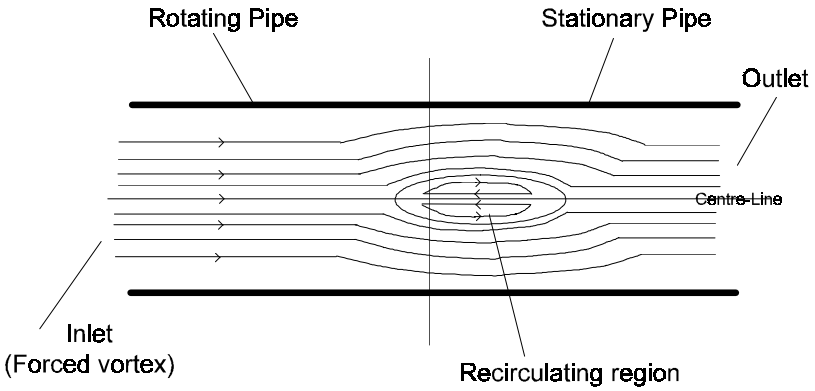

Figure 4.4: The computational domain used to verify the performance of the vorticity-streamfunction solver in cylindrical co-ordinates with swirl.

metric flow field in a pipe, the upstream portion of which rotates, while the downstream portion is stationary as shown by figure 4.4. Such a problem was investigated in detail by Silvester *et al.* [2] who suggests that the size of the recirculation region arising from the step change in the angular velocity of the pipe provides a good measure of the validity of any solution. The vorticity-streamfunction solver gave results that had a fair quantitative similarity to those of Silvester, and a good qualitative similarity.

Recirculating flow fields provide a good test of the conservation characteristics of any code. Evaluating the calculated axial mass flow rate along the length of the pipe showed very good mass conservation characteristics over most of the field. The highest errors could be found in the regions of highest recirculation. At no point did the error exceed two percent of the overall flow rate, even on the coarsest 31x31 grid.

4.6.4 Turbulent Pipe-Flow Benchmark

To test the two-equation $k-\epsilon$ solver, a number of solutions for the turbulent non-swirling axisymmetric flow in a pipe were calculated and compared to analytic results by Nikuradse (see Schlicting [125]). The velocity profiles at all points in the solution showed an excellent correspondence with the benchmark.

4.6.5 Verification of the Energy Equation

No attempt has been made to quantitatively verify the temperature field solutions provided by the energy equation. All the solutions obtained with the code have been physically plausible.

4.7 Vortex Tube Computations

4.7.1 Overview

The vorticity-streamfunction code was used to calculate a number of Ranque-Hilsch tube flows. This section begins by outlining the boundary conditions employed in the computations, and then presents some of the results obtained with a discussion of their significance.

4.7.2 Boundary Conditions

Geometrical Constraints, and the Streamfunction

A number of geometrical arrangements were investigated to obtain a flow comparable to that found in the vortex tube. The most successful designs for the uniflow and counterflow tubes are shown in figures 4.5 and 4.6 respectively. As noted earlier, the difficult to model inlet nozzles have been replaced with an annular slit, through which a swirling flow is introduced at a mass flow rate comparable to that in real tubes.

In the vorticity-streamfunction formulation, solid boundaries are inserted by forcing the streamfunction to adopt a constant, pre-specified value along the desired line. With counterflow simulations, this has the side effect that the cold mass flow fraction μ_c must be chosen *a priori*.

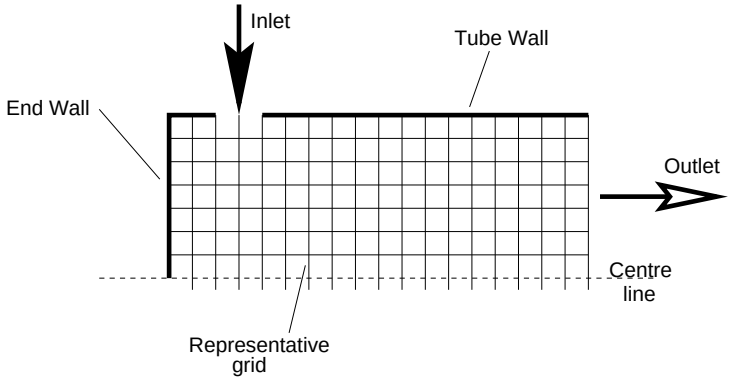

Figure 4.5: The geometry employed for uniflow calculations.

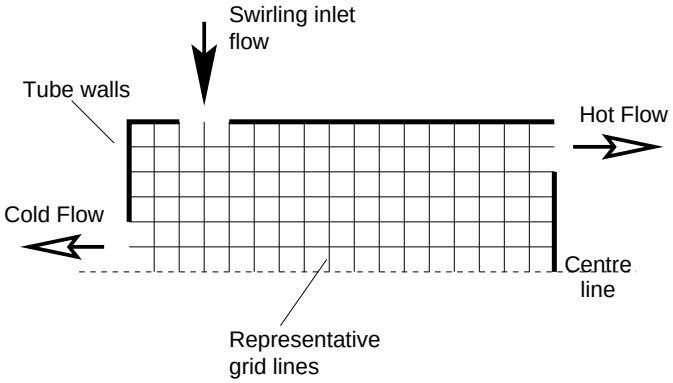

Figure 4.6: The geometry employed for counterflow calculations.

Velocity and Vorticity

No-slip conditions are imposed at all solid boundaries. For the swirl velocity, this condition is easily implemented by setting the swirl velocity on the walls to zero. With the axial and radial velocities however, it is more complicated as the conditions have to be formulated in terms of the vorticity and the streamfunction.

A first-order boundary condition will be derived for the general case of a variable density flow, adjacent to a solid wall extending in the z-direction and moving with a velocity w_{wall} parallel to the axis of the tube. The vorticity at the wall ω_w will be calculated in terms of the streamfunction at the wall ψ_w and the streamfunction at a point adjacent to the wall ψ_p. Typically this is the condition applied at the circumferential wall of the vortex tube. Derivation of an expression for the vorticity at a wall extending in the radial direction is analogous.

Differentiating the relationship between the streamfunction and the axial velocity,

$$w = \frac{1}{\rho r}\frac{\partial \psi}{\partial r}, \tag{4.43}$$

gives adjacent to the wall

$$\left(\frac{\partial w}{\partial r}\right)_w = \left\{\frac{1}{\rho r}\frac{\partial^2 \psi}{\partial r^2} - \left(\frac{1}{r^2} + \frac{1}{\rho^2}\frac{\partial \rho}{\partial r}\frac{1}{r}\right)\frac{\partial \psi}{\partial r}\right\}_w . \tag{4.44}$$

At the wall, the normal velocity $u_w = 0$, and so the vorticity equation becomes

$$\omega_w = -\left(\frac{\partial w}{\partial r}\right)_w , \tag{4.45}$$

as given by the negation of expression (4.44). Applying expression (4.43) at the wall, gives

$$\left(\frac{\partial \psi}{\partial r}\right)_w = (\rho r w)_w , \tag{4.46}$$

where $w_w = w_{wall}$ from the no-slip condition. Expanding ψ in a Taylor series about its

value at the wall shows also

$$\left(\frac{\partial^2\psi}{\partial r^2}\right)_w = \frac{2\left(\psi_p - \psi_w\right)}{\left(r_p - r_w\right)^2} - \frac{2\left(\rho r w\right)_w}{r_p - r_w}. \tag{4.47}$$

Combining these results, the first-order expression for the vorticity on the circumferential wall is

$$\omega_w = \frac{2\left(\psi_{w-1} - \psi_w\right)}{\left(\rho r\right)_w \left(r_p - r_w\right)^2} - w_{wall}\left(\frac{1}{\rho}\frac{\partial\rho}{\partial r} + \frac{1}{r_w} + \frac{2\rho r_w}{r_p - r_w}\right) \tag{4.48}$$

Where necessary, the density gradient term can be evaluated as a one-sided difference at the wall, but in most cases it can be ignored. Where the wall velocity is zero, the term vanishes. In other cases the density gradient close to the wall is likely to be small.

Thermal Conditions

The external walls of the tube were assumed to adopt at the temperature of the inlet gas.

Centre-Line

The centre-line of the tube represents a symmetry axis. Zero gradient Neumman boundary conditions are imposed on all variables here.

Outlet conditions

It is assumed that the flow is fully developed where it leaves the tube. Zero gradient or constant gradient Neumman boundary conditions are imposed on all variables. In general a zero gradient condition was preferable, as the extra 'freedom' permitted by constant gradient conditions could lead to instability. Care has to be taken that the length of the domain is sufficient to ensure that there is no recirculation near the outlet.

The particular choice of boundary condition at the outlet of the uniflow geometry had very little effect on the upstream flow. A similar observation was made regarding the boundary conditions for the warm outlet of the counterflow tube.

Conditions imposed at the cold outlet of the counterflow tube were found to be more important, the constant gradient condition appearing to be preferable. The assumption that the flow is fully developed on leaving the tube is poor here.

Turbulence Conditions

The specification of boundary conditions for the turbulence quantities k and ϵ in a strongly rotating flow is problematic. It is well known that the standard $k-\epsilon$ equations are inaccurate close to a solid wall, even under 'straightforward' non-swirling flow. Two approaches are commonly employed to overcome this difficulty. Perhaps the most satisfactory is that adopted by Elkaim [52], who uses a mildly reformulated low Reynolds number turbulence model close to the wall. An alternative is to abandon the turbulence model altogether at a node close to the wall, and use a 'law of the wall' expression to estimate turbulent effects there, as performed by Armfield *et al.* [48].

Close to the wall the mixing length of the turbulence can be evaluated using

$$l = \kappa r^* \left(1 - e^{-\frac{r^+}{A}}\right) \tag{4.49}$$

where $r^* = r_o - r$, $r^+ = \frac{r^*\sqrt{\tau_w/\rho}}{\nu_t}$, and A is the Van Driest damping constant, usually taken as 26. The wall shear stress is evaluated as

$$\tau_w = \sqrt{\tau_{wz}^2 + \tau_{w\theta}^2}. \tag{4.50}$$

The turbulent viscosity at a point close to the wall can be evaluated from

$$\mu_t = \rho l^2 \left\{ \left(\frac{\partial u}{\partial r}\right)^2 + \left(\frac{\partial w}{\partial r} - \frac{w}{r}\right)^2 \right\}^{\frac{1}{2}} \tag{4.51}$$

and the turbulent kinetic energy and dissipation rate from

$$k = \frac{\nu_t^2}{l^2 C_\mu^{\frac{1}{2}}} \tag{4.52}$$

and

$$\epsilon = \frac{C_\mu^{\frac{3}{4}} k^{\frac{3}{2}}}{l}. \tag{4.53}$$

Equation (4.49) is only valid in the approximate range $30 < r^+ < 100$. To ensure that the boundary values are evaluated at a point in this range, the routine searches inwards from the cylindrical wall for the first node which lies within the specified range. Values of k and ϵ are evaluated there using the procedure above, and the node becomes the boundary node for the subsequent solutions of the k and ϵ equations. Any points between the determined boundary node and the cylindrical wall are assumed to lie within the laminar sublayer of the boundary layer.

The calculations presented were performed either with a law of the wall condition, or without any special treatment, by solving the standard $k - \epsilon$ equations right up to the wall where $k = 0$ and $\epsilon = 0$. Qualitative differences between the two flows were not great.

4.7.3 Inlet Conditions

Vorticity and Streamfunction

The inlet flow through the annular slit was assumed to enter the tube with a uniform radial velocity, and no axial velocity. Conditions consistent with this require zero vorticity, and a streamfunction that varies linearly with the axial co-ordinate across the length of the slit, calculated by integrating relation (4.3) assuming a constant known inlet density and radial inlet velocity.

Swirl Velocity

The inlet flow was assumed to have uniform swirl velocity, right up to edges of the inlet 'slot'.

Turbulence

It was assumed that the turbulent kinetic energy of the inlet flow was a certain percentage of the overall kinetic energy. The expression used to provide a reasonable value for the inlet turbulence was

$$k = a\left(\bar{u}^2 + \bar{v}^2\right), \tag{4.54}$$

evaluated using the velocity of the inlet flow. The value of a was taken as 0.03, following the practice of Elkaim *et al.* [52]. Numerical values for the dissipation in the inlet flow were calculated from

$$\epsilon = C_d \frac{k^{\frac{2}{3}}}{bD}, \tag{4.55}$$

where C_d is the same quantity as employed in the turbulence model, D is the diameter of the tube, and the constant b is 0.005. Again this value was taken from Elkaim [52].

4.7.4 Grid Considerations

The majority of the computations were performed on a grid of 43x43 nodes, as this was found to provide a good compromise between precision and computational effort. Nodes were concentrated radially near to the cylindrical wall of the tube in order to resolve the steep gradients found there, and near to the inlet. Figure 4.7 shows a typical grid.

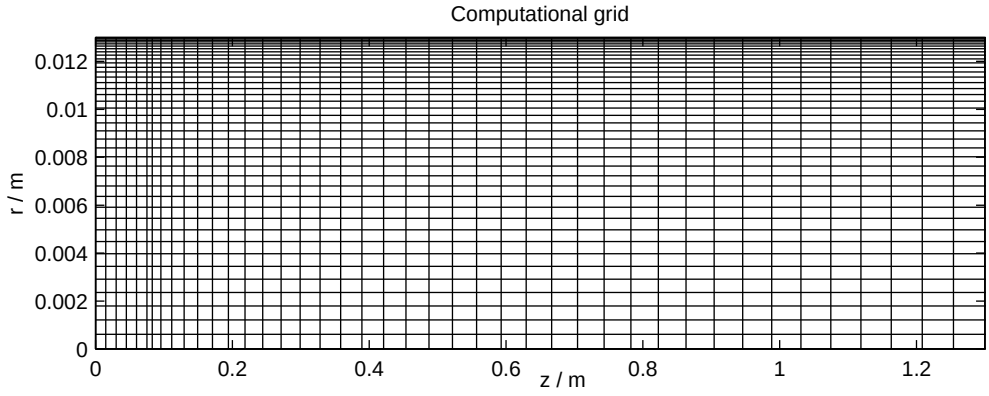

Figure 4.7: The computational grid.

4.8 Results for Uniflow Tubes

Control Experiment

As a 'control' experiment, the flow field in a uniflow tube without any swirl was estimated. Tube dimensions were set to be the same as those for the 26 mm diameter CUED tube investigated in chapter 3, and the working fluid was assumed to be air. The outcome is shown in figure 4.8. The flow pattern is much as expected, and produces no significant evidence of energy separation.

Results

Figure 4.9 shows the result of a calculation for the uniflow tube with an inlet swirl number[4] of 10.4. The flow pattern in a real vortex tube is captured quite well, with an approximately forced vortex formed at the inlet, which decays substantially by the outlet. There is evidence of a small region of recirculation near to the axis, just along from the inlet.

This particular calculation assumed a turbulent Prandtl number of one. While there is some evidence of an energy (stagnation temperature) separation just along from the inlets, it is not great, and decays quickly. At $z = 0.083$ m a stagnation temperature differ-

[4] At the inlet nodes the radial velocity was 4 m/s and the swirl velocity was approximately 300 m/s.

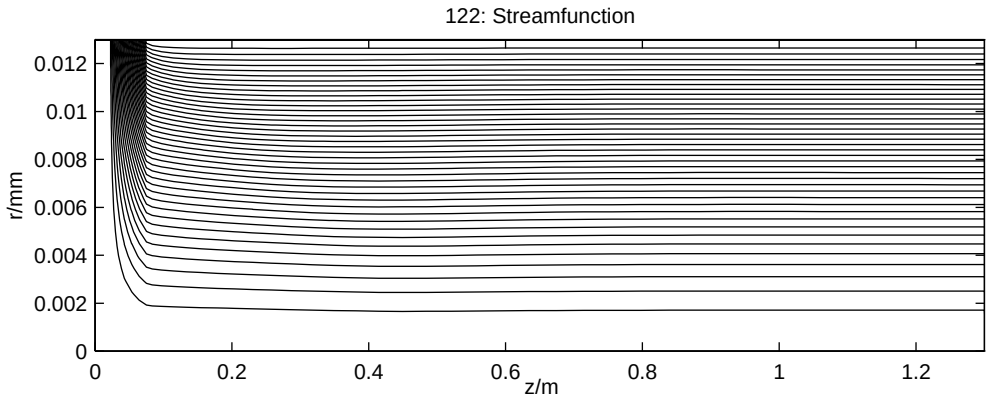

Figure 4.8: Uniflow tube flow calculation, with no swirl. The top diagram shows the streamline pattern, the middle diagram shows the axial velocity variation and the bottom diagram gives the temperature distribution. The radial inlet was positioned between nodes 3 and 8.

ence of more than 10 K between inner and outer regions of the flow is visible, but near the exit $z = 1.16$ m, it has disappeared.

Reducing the Prandtl number to 0.2 (see figure 4.10), thereby increasing the turbulent thermal diffusivity, produces some increase in the energy separation. Increasing the Prandtl number to 5 reduces the separation.

The Richardson Number Correction

Figure 4.11 compares two swirl velocity profiles some distance along a uniflow tube, computed under the same conditions as the preceding results, but one with the Richardson number correction to the turbulence model disabled. The result without the correction shows a quicker decay of the swirl as was expected from the discussion in section 4.3.3, thanks to the increased turbulent viscosity it predicts.

4.9 Results for Counterflow Tubes

Results for the counterflow tubes show similar overall features to the uniflow calculations. As can be seen from figure 4.12 the recirculating region near the cold flow outlet orifice is caught quite well, although it appears to be shorter than might have been anticipated.

4.10 Discussion

The computations give results for the fluid mechanics that qualitatively compare very well with the experiments of chapter 3 and the literature. The swirl profiles confirm the existence of an approximately forced vortex in the inlet regions. Also notable is the decay through turbulent and viscous dissipation into a Rankine vortex further down the tube. Axial velocity variations are predicted well too, with recirculation close to the centre-line near to the inlets, and in general a much faster flow towards the periphery throughout

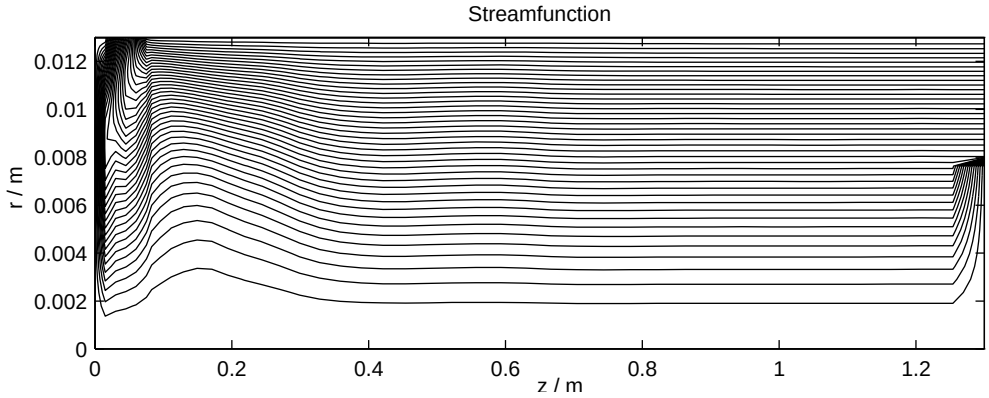

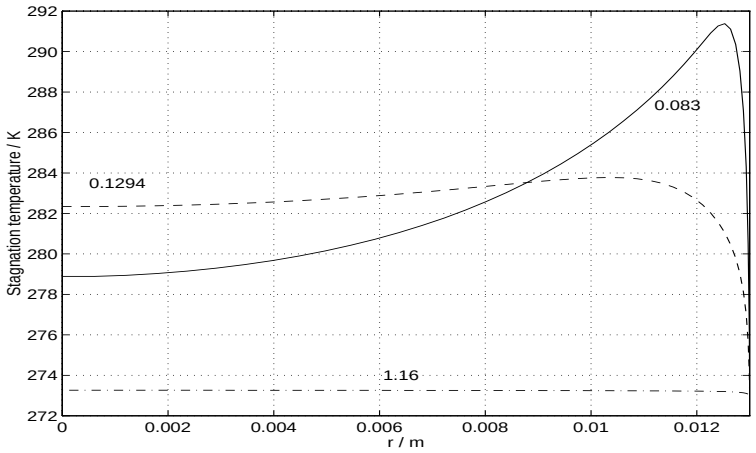

Figure 4.9: Uniflow tube calculation with an inlet swirl number of 10.4, and unity turbulent Prandtl number. The upper diagram shows the streamline pattern, the middle diagram shows the swirl distribution, and the lower diagram gives stagnation temperature distributions across radii at the axial positions noted by each curve. The radial inlet was positioned between nodes 2 and 6.

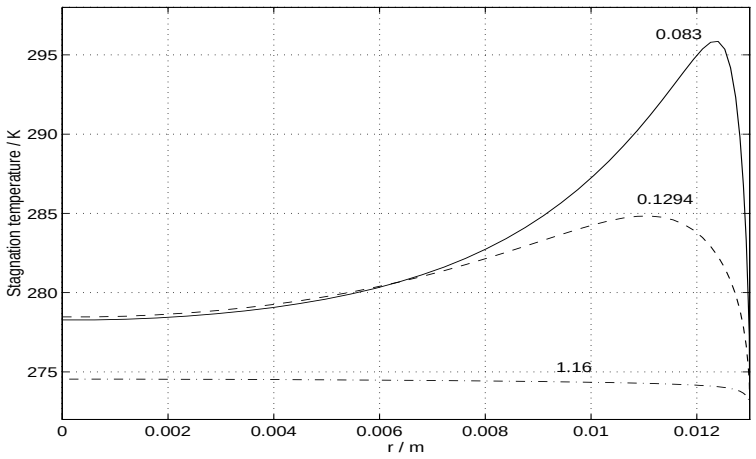

Figure 4.10: Uniflow tube calculation with an inlet swirl number of 10.4, and a turbulent Prandtl number of 0.2. The upper diagram gives the static temperature distribution, and the lower gives the stagnation temperature distributions across radii at the axial positions noted by each curve.

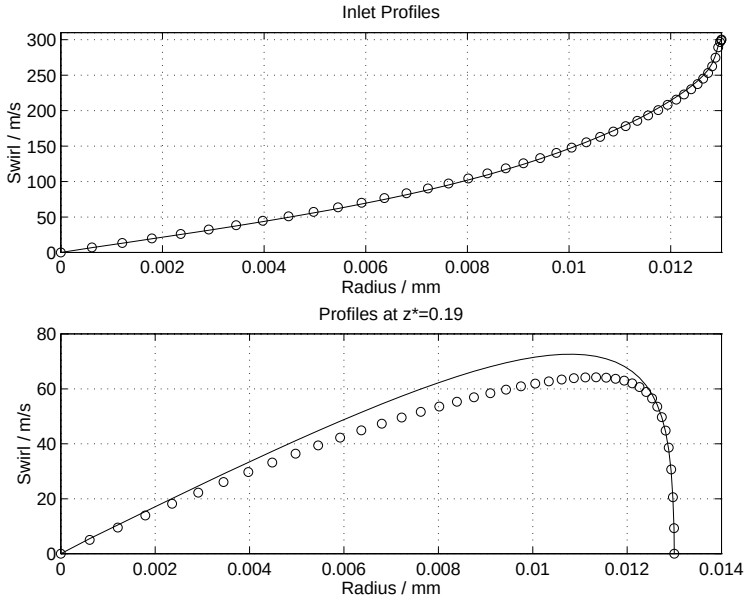

Figure 4.11: The effect of the Richardson number correction.The upper graph compares the swirl velocity profiles at the inlet (the circles represent the solution without the Richardson number correction, the solid line with it). Comparison of swirl velocity profiles at a normalised axial position of 0.19 (lower diagram) shows the increased decay without the correction.

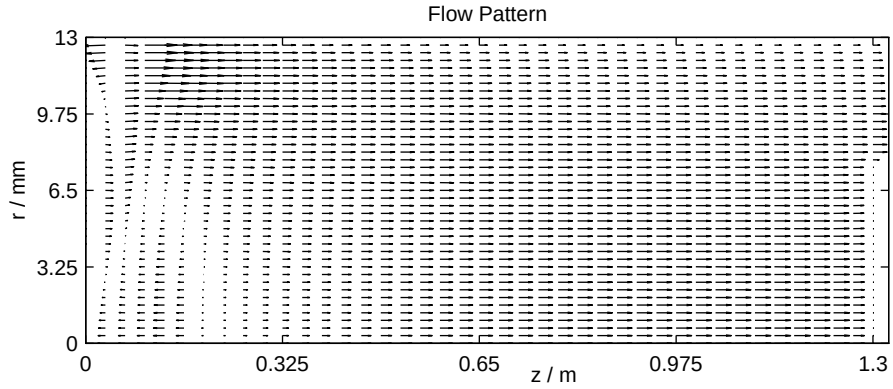

Figure 4.12: Counterflow tube calculation with an inlet swirl number of 10.4, and a cold fraction of $\mu_c = 0.4$. The upper diagram shows the flow pattern, the middle diagram shows the swirl distribution, and the lower diagram gives static temperature distributions.

most of the tube.

The energy and temperature separations are not captured well. Indeed, the solutions predict that the central flow initially becomes warmer than the periphery. Despite this, some insight into the phenomenon is possible, especially from the effect of the turbulent Prandtl number on the temperature field. A low turbulent Prandtl number represents a high thermal diffusivity in comparison to the momentum diffusivity. This appears to encourage the formation of an energy separation. A high Prandtl number by comparison seems to reduce the potential for the formation of an energy separation.

In the two uniflow cases presented, the flow patterns and hence the kinetic energy distributions are essentially identical. The temperature fields differ however, with the low Prandtl number (high thermal diffusivity) result exhibiting a cooler central flow than that with unity Prandtl number. The increased energy separation in the low Prandtl number case appears to be due to the fact that the increased thermal diffusivity encourages thermal conduction, producing a more uniform radial temperature distribution. In other words the difference in the radial energy separation between the two cases appears to be due almost entirely to the differences in the radial temperature distribution, which in turn is caused by the differing turbulent conductivities.

Formation of a forced vortex in the simulated vortex tube is subtly different to that in a real tube. With the simulated tube, the inlet flow already has a substantial kinetic energy. The production of the forced vortex then involves a slowing of the gas that moves towards the central regions, tending to convert kinetic energy to heat[5], while the gas at the periphery carries on swirling at close to the inlet velocity and temperature . Thus the central flow would tend to become warmer. In a real vortex tube, the gas in the inlet nozzles could be thought of as stationary until it enters the tube. Formation of a forced vortex then involves acceleration of the peripheral gas, tending to cool it, while the central gas remains near to the inlet temperature.

The net effect of the two processes is similar. In the absence of energy transfer through

[5]This discussion employs a simple adiabatic energy equation, $h_o = h + v^2/2$.

the fluid, they both tend to produce a cool gas at the periphery, and a warmer one near the centre. For the simulated vortex tube, this influence can be seen clearly, and subsequent radial conduction produces an energy separation. The better the conduction, the better the maximum separation. With a real vortex tube however, the influence cannot be seen directly. At no point is there evidence of the central gas being warmer than the periphery. We must tentatively conclude that the radial energy transfer mechanisms in the real tube are so good as to transfer thermal energy from the centre to the periphery before there is any detectable temperature gradient.

It seems that thermal conduction processes are important in the formation of any radial energy separation in the vortex tube. Production of a substantial separation requires a much greater radial transport of thermal energy than that predicted by the vorticity streamfunction code. For a real tube, in view of the experimental evidence for an energy separation that develops as the gas moves axially, it seems likely that the transport may be against the temperature gradient. The next chapter investigates mechanisms through which this transport could occur.

4.11 Closing Remarks

A relatively simple computational fluid dynamics technique has been employed to solve the flow in a Ranque-Hilsch vortex tube. The considerable assumptions made during the development of the code limit its utility, but it is able to produce solutions for the flow that are at least qualitatively similar to those found in practice. Less success was achieved in simulating the energy separation effect, although some insight into the Ranque-Hilsch phenomenon was obtained.

Chapter 5

Mechanisms of Energy Transfer

5.1 Introduction

Having completed our detailed examinations of the vortex tube, we will attempt to draw some conclusions regarding the energy transfer processes at work within the device. The study will begin by considering the information collected in the preceding chapters, and comparing the importance of various factors. Analysis of the axisymmetric energy equation assists in the interpretation of the data, and reveals some of the physical processes that might underlie the energy transfer.

5.2 Review

5.2.1 The Ranque-Hilsch Phenomenon

Two aspects to the Ranque-Hilsch phenomenon can be distinguished. Firstly there is a radial energy separation in the form of a stagnation temperature that increases from the centre of the tube to the periphery. Secondly, there is a static temperature separation with the peripheral gas warmer than the central gas.

Of the two manifestations, the stagnation temperature separation is the more interesting. To some extent the static temperature gradient results from the 'dissipation' of the

velocity component of the stagnation temperature variation. As an example, the variation of the temperature of the cylindrical wall of the tube with axial distance from the orifice can probably be attributed in a large part to the frictional dissipation of the swirl velocity in the outer regions of the gas.

While the axial development of the radial static temperature profile can be explained in terms of a pre-existing stagnation temperature separation, there are still many matters to be addressed. The over-riding question is how the stagnation energy separation occurs in the first place. There are other features to be accounted for though, in particular the apparent increase in stagnation temperature separation in regions of high swirl which requires energy transfer against the temperature gradient, and how a radial static temperature separation is maintained along a significant length of the tube, despite the effects of turbulent conduction which would be expected to produce a uniform distribution.

5.2.2 The Evidence

On the basis of the previous chapters, flow in the vortex tube could be characterised as follows. The tangential injection of compressed gas produces a turbulent, fast rotating flow in the inlet region that is comparable to a forced vortex. The vortex decays along the length of the tube, such that the swirl velocity at the end far from the injectors, near the valve, is very much slower than at the inlet.

As the gas progresses along the axis of the tube and away from the entry region, there do not appear to be any dramatic changes in the flow pattern. Gas that moves to the centre when it enters the tube remains at the centre, and similarly gas that is initially at the periphery does not move substantially inwards. The only exception to this is for a counterflow tube, where some of the gas near the centre-line undergoes a sudden reversal of direction, reminiscent of a bubble breakdown, and flows back towards the inlet region to leave through the orifice. In all cases though, the gas that leaves through the central 'cold' exit is gas that has been nearer the centre throughout its passage in the tube

whereas gas leaving through the outer 'warm' exit is taken from the periphery.

Energy transfer from the inner gas to the outer gas occurs in the regions of high swirl near the inlet nozzles, producing the thermal separation associated with the vortex tube. Acoustic streaming does not appear to play a significant role in the energy transfer.

Undoubtedly the most important feature of the flow is the approximately forced vortex in the inlet region. This vortex essentially 'drives' the whole vortex tube, establishing the pressure gradients that are responsible for the axial and radial flow patterns. It somehow provides the mechanism by which the potential energy of the compressed inlet gas is converted into an energy separation.

The very formation of a forced vortex at the inlet plane can itself account for some of the energy separation. Firstly, the peripheral gas has a much larger kinetic energy than the central gas. Secondly, were the inlet flow adiabatic, the static temperature would decline with increasing radius as a greater portion of the reservoir enthalpy is taken up by the swirl velocity. This would tend to promote a radially outwards conduction of heat as the gas passed down the vortex tube, re-enforcing the energy separation.

Attributing any part of the Ranque-Hilsch effect directly to the formation of a forced vortex in the inlet region could be considered merely a reformulation of the original question concerning the origin of the energy separation, to one addressing the mechanism by which the forced vortex itself is formed. The flow in the inlet region is very difficult to analyse, making it hard to draw conclusions regarding the formation of the forced vortex. It was seen in chapter 2 that a body of fluid subjected to an external torque will form a forced vortex. A comparable situation appears to exist at the vortex tube inlet, with the tangentially injected gas exerting an external torque on the gas already within the tube.

Given that there is axial development of the energy separation, the forced vortex itself cannot be wholly responsible for the Ranque-Hilsch effect. As the flow progresses along the vortex tube, there must be additional energy transfer from the central gas to the peripheral gas. Furthermore, it is necessary to consider how the energy separation 'survives' the regions of relatively low swirl near to the tube exit in a uniflow tube, producing hot and cold streams.

5.3 The Energy Equation

It is useful to return now to the energy equation (2.12) and elaborate on the significance of some of the modes of energy transfer that its terms represent. Assuming axisymmetry the equation may be written

$$\frac{1}{r}\frac{\partial}{\partial r}\left(\lambda r\frac{\partial T}{\partial r}\right)+\frac{\partial}{\partial z}\left(\lambda\frac{\partial T}{\partial z}\right)+\Phi=\rho\left(u\frac{\partial h}{\partial r}+w\frac{\partial h}{\partial z}\right)-\left(u\frac{\partial P}{\partial r}+w\frac{\partial P}{\partial z}\right) \tag{5.1}$$

with the dissipation function

$$\Phi=2\mu\left\{\left(\frac{\partial u}{\partial r}\right)^2+\left(\frac{u}{r}\right)^2+\left(\frac{\partial w}{\partial z}\right)^2+\frac{1}{2}\left(\frac{\partial v}{\partial r}-\frac{v}{r}\right)^2+\frac{1}{2}\left(\frac{\partial v}{\partial z}\right)^2+\frac{1}{2}\left(\frac{\partial u}{\partial z}+\frac{\partial w}{\partial r}\right)^2-\frac{1}{3}\left(\nabla\mathbf{v}\right)^2\right\}. \tag{5.2}$$

Attention will be confined to the 'main body' of the vortex tube, that is away from the inlet region. Analysis will begin by accounting for the effects of turbulence, and considering the sizes of some of the terms.

The energy equation may be Reynolds averaged in the conventional manner by splitting each variable into a constant and a fluctuating component. It is quite reasonable to neglect the influence of molecular heat conduction in this context, which will be overwhelmed by the effects of the turbulence. Following Hinze [85] in his analysis of the vortex tube, fluctuations in the density and the pressure will be considered negligible. This is mostly a matter of expediency, although there is some physical justification. All analysis so far has suggested that the density of the gas within the vortex tube does not vary greatly in comparison to the temperature and velocity fields so it might be anticipated that density fluctuations would not have a dominating effect on the energy fluxes within the tube. The pressure fluctuations are likely to be substantial, but it will be shown later that the terms containing pressure gradients are small compared to some of the others, and again, the pressure fluctuations are not likely to be dominant.

Proceeding with the Reynolds averaging, one obtains,

$$\bar{\rho}c_p\bar{u}\frac{\partial\bar{T}}{\partial r}+\bar{\rho}c_p\bar{w}\frac{\partial\bar{T}}{\partial z}=-\frac{\partial}{\partial z}\left(\bar{\rho}c_p\overline{T'w'}\right)-\frac{\partial}{\partial r}\left(\bar{\rho}c_p\overline{T'u'}\right)+\bar{u}\frac{\partial\bar{P}}{\partial r}+\bar{w}\frac{\partial\bar{P}}{\partial z}+\bar{\Phi}+\bar{\Phi}' \qquad (5.3)$$

where $\bar{\Phi}$ represents the mean dissipation and $\bar{\Phi}'$ represents the time averaged fluctuating dissipation terms. The resulting terms will be considered in more detail, although analysis will necessarily be limited by our poor knowledge of the nature of the fluctuations within the tube. For most of the remainder of this chapter, the bars over averaged values of single variables will be dropped. Terms without dashes or over bars should be assumed to be steady components.

5.3.1 Terms in the Energy Equation

The flow in the vortex tube is highly turbulent. This has been indicated by the large swirl Reynolds number of the flow, the results of the experimental work, the numerical experiments and the work of others. We start to consider the influence that the turbulent fluctuations have have on the energy transfer within the vortex tube by looking further at groups of terms in the energy equation.

Dissipation

It will be assumed that the turbulent dissipation function can be accommodated through an eddy viscosity model, that is

$$\left(\bar{\Phi}+\Phi'\right)=\rho\epsilon\cdot\bar{\Phi}. \qquad (5.4)$$

The nature and magnitude of the eddy viscosity will be considered later.

Some of the terms in the dissipation function are likely to be small compared to others, and therefore can be ignored. Evidence so far has suggested that radial velocities within the body of the tube are small. While the validity of this conclusion is assessed below, it is probably reasonable already to suggest that the radial velocity does not make

a significant contribution to the dissipation. Furthermore, it has also been observed that velocity gradients in the radial direction are much larger than those in the axial direction. In this light the latter may be ignored. As the mean density variations within the flow are also quite small, the divergence term is not likely to have a great influence either, leaving as an approximation for the dissipation function

$$\bar{\Phi} + \Phi' = \rho\epsilon \left\{ \left(\frac{\partial v}{\partial r} - \frac{v}{r} \right)^2 + \left(\frac{\partial w}{\partial r} \right)^2 \right\}. \tag{5.5}$$

Mean Convection

The mean convection terms are likely to be fairly small, compared to the dissipation function. While radial temperature gradients are substantial, the small radial velocities will limit its magnitude.

It might be anticipated that the mean convection in the axial direction would also be small. Two factors make conclusions difficult to draw regarding this term though. Firstly, the axial velocity is not negligible. Secondly, it is the only term allowing any axial development of the temperature field, which we have seen to be significant.

Turbulent Convection

While turbulent convection axially is likely to be overwhelmed by the mean convection, the same cannot be said for the radial direction. Hinze [85] shows that the radial turbulent convection term in a turbulent strongly swirling compressible flow should be replaced by the expression

$$-\frac{1}{r}\frac{\partial}{\partial r} \left\{ \rho c_p \epsilon_h r \left(\frac{\partial T}{\partial r} - \frac{\gamma - 1}{\gamma} \frac{T}{P} \frac{\partial P}{\partial r} \right) \right\} \tag{5.6}$$

where ϵ_h is the eddy diffusivity for the transport of heat. The mathematical proof is involved; however the same expression can be conveniently derived by employing a mixing length model (see for example Deissler and Perlmutter [7]). The main points of the

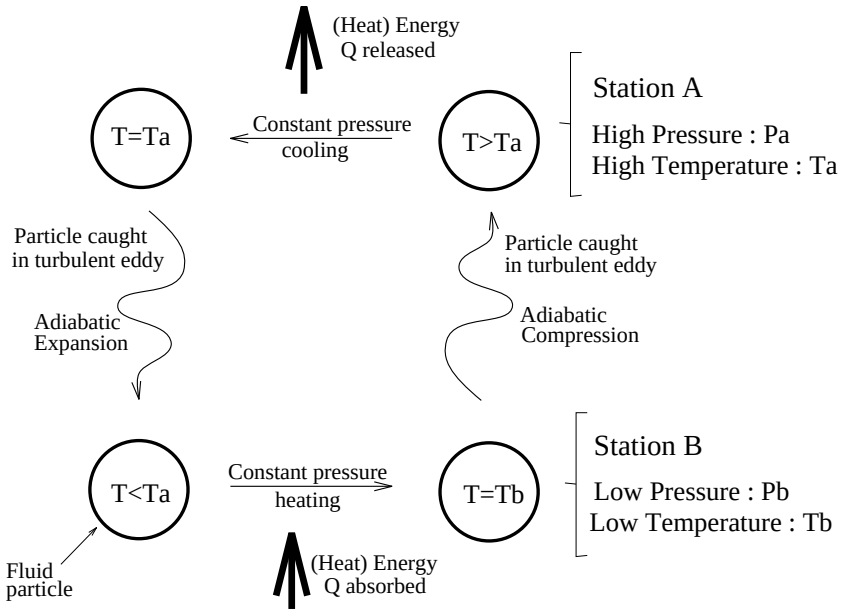

Figure 5.1: The motion of a fluid particle caught in an eddy, through the radial temperature and pressure gradients. Station A represents a position towards the periphery of the vortex tube, and station B towards the centre.

analysis will be presented.

Consider an eddy moving radially from an inner station B to an outer station A, as shown in figure 5.1. Assume the eddy moves isentropically[1], without exchanging heat with the intermediate fluid. When the fluid particle arrives at station A, it displaces an mass of fluid equal to itself. If the displaced fluid was in thermal equilibrium with the surrounds, it would have a temperature T_a. Thus, if the arriving particle has temperature T'_a the net heat transported to station A by the eddy is $(mass\ of\ eddy) \times c_p\,(T'_a - T_a)$. The heat flux from station B to station A is therefore

$$q_t = c_p \cdot \rho \cdot f \cdot (T'_a - T_a) \tag{5.7}$$

[1]This is a large assumption, and is unlikely to be completely true. However it is no more arbitrary than the conventional assumptions of mixing length models, and may be justified on the basis that the scale of the motions is small, and the fluctuations are rapid. Deissler and Perlmuter [7] mention that certain meteorological experiments support the assumption, but fail to provide any details. There is at least some evidence that the motion of the fluid eddies could be considered as adiabatic, again from work by Deissler [126].

where f represents the volume of eddies per second passing from station B to station A, and it is assumed that the density of the fluid particle does not change significantly.

Let l be the radial distance between the two stations, ΔT_f the difference in the average fluid temperature and ΔT_e the change in the eddy temperature, in which case

$$q_t = -c_p \cdot \rho \cdot f \cdot l \cdot \left(\frac{\Delta T_f}{l} - \frac{\Delta T_e}{l} \right). \tag{5.8}$$

Assuming that l is small, this may be written

$$q_t = -c_p \cdot \rho \cdot f \cdot l \cdot \left(\frac{dT}{dr} - \frac{dT_e}{dr} \right). \tag{5.9}$$

For the isentropic eddy motion

$$T_e = constant \times P^{\frac{\gamma-1}{\gamma}} \tag{5.10}$$

and thence

$$\frac{dT_e}{dr} = \frac{1}{\rho c_p} \frac{dP}{dr} = \frac{\gamma - 1}{\gamma} \frac{T}{P} \frac{dP}{dr}. \tag{5.11}$$

The turbulent heat flux becomes

$$q_t = -c_p \rho \cdot f \cdot l \cdot \left(\frac{dT}{dr} - \frac{1}{\rho c_p} \frac{dP}{dr} \right). \tag{5.12}$$

or

$$q_t = -c_p \rho \cdot \epsilon_h \cdot \left(\frac{dT}{dr} - \frac{1}{\rho c_p} \frac{dP}{dr} \right). \tag{5.13}$$

replacing lf by the eddy diffusivity ϵ_h. The radial turbulent convection term can be approximated by this expression, that is

$$\frac{\partial}{\partial r} \left(\rho c_p \overline{T'u'} \right) = \frac{\partial q_t}{\partial r}. \tag{5.14}$$

It is worth noting, as did Schultz-Grunow [127], that if we imagine the same fluid

particle continually being sent back and forth between stations A and B, then it is subjected to a cyclic thermodynamic process. The particle acquires heat at low pressure, and delivers heat at high pressure, in a process analogous to conventional refrigeration cycles.

5.4 Application to Data

The assumptions and simplifications of the preceding section require stronger foundations. To this end, they will be tested against experimental evidence. The terms remaining in the energy equation will then be compared to each other, with the objective of producing a minimalistic representation of the energy transfer processes likely to be at work in the vortex tube.

5.4.1 Magnitude of Radial Velocity – Departures from Simple Radial Equilibrium

It is convenient to assume that the radial velocities within the vortex tube are small compared to those in the axial and tangential directions. This assumption has been already been employed in some of the analysis so far[2]. If the radial velocities are indeed negligible, then the radial momentum equation reduces to expression (2.19), that is

$$\frac{\partial P}{\partial r} = \frac{\rho v^2}{r}. \tag{5.15}$$

Thus examining the value of $\frac{\partial P}{\partial r} - \frac{\rho v^2}{r}$ for the experimental data should provide an indication of the validity of simple radial equilibrium in the vortex tube.

Figure 5.2 shows the value of the test parameter as a function of radius at three stations in the 26 mm diameter vortex tube. The calculations were performed numerically

[2]See also appendix E for a further discussion of the validity of simple radial equilibrium within the vortex tube.

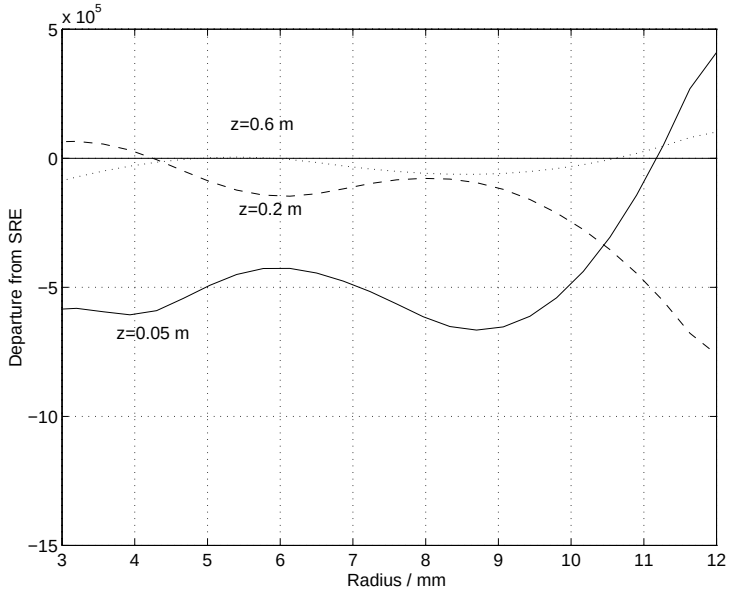

Figure 5.2: The magnitude of the departure from simple radial equilibrium at stations in the 26 mm diameter vortex tube.

using the data presented in chapter 3. Conformance to simple radial equilibrium is quite good at the two downstream stations, $z = 0.2$ m and $z = 0.6$ m, but relatively poor near to the inlet region at $z = 0.05$ m. The departure from equilibrium near the inlet region is probably due to the disturbance caused by the intrusive probes used for measurements, especially since the disturbances will be most significant in the fast flows found in such areas.

The magnitude of the radial velocity at the first station in the 26 mm tube was calculated from the radial momentum equation by

$$\rho u \frac{du}{dr} = \frac{\rho v^2}{r} - \frac{dP}{dr} \tag{5.16}$$

and integrating such that

$$u^2 = 2 \int_{r_1}^{r_2} \left(\frac{v^2}{r} - \frac{1}{\rho} \frac{dP}{dr} \right) dr. \tag{5.17}$$

The result of a numerical calculation is given by figure 5.3. Velocity values are plotted

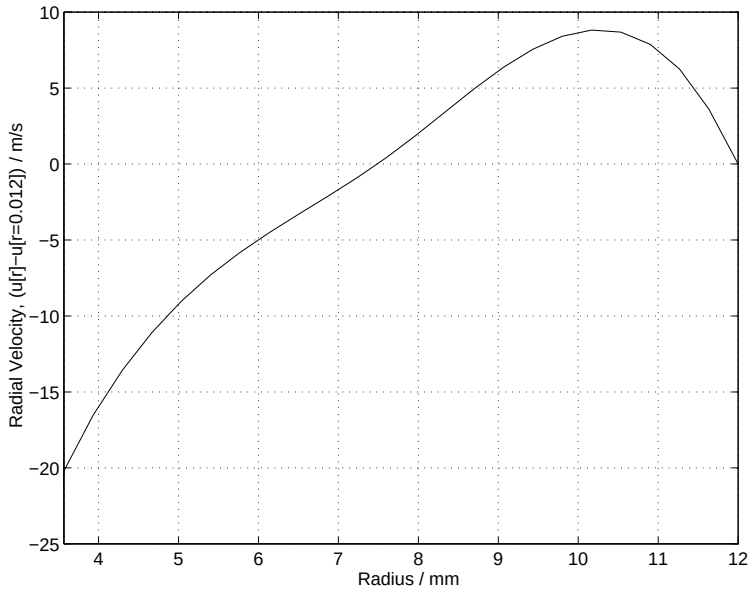

Figure 5.3: The magnitude of the radial velocity relative to that at a radius of 0.012 m, at $z = 0.05$ m in the 26 mm diameter vortex tube.

relative to the radial velocity at a radius of 12 mm, as reliable values could not be taken right up to the wall to provide an absolute reference of zero radial velocity. As this is very close to the wall, however, the values shown are representative of the absolute radial velocity. The estimated radial velocity is relatively small compared to the swirl and axial velocities beyond a radius of approximately 5 mm. In the centre of the tube it is more significant, and simple radial equilibrium will not be a good approximation there.

5.4.2 Terms in the Dissipation Function

To investigate the assumptions outlined regarding the dissipation function, values of $\left(\frac{\partial v}{\partial r} - \frac{v}{r}\right)^2$, $\left(\frac{\partial w}{\partial r}\right)^2$, $\left(\frac{\partial w}{\partial z}\right)^2$, and $\left(\frac{\partial v}{\partial z}\right)^2$ were estimated from the experimental data for the 26 mm diameter vortex tube, at axial stations in the hot tube. No account was taken of terms involving the radial velocity, on the basis that they are small and poorly known.

Figure 5.4 shows the calculated values as a function of radius, at a distance of 0.05 m from the inlet nozzles. Only two of the terms investigated were significant, $\left(\frac{\partial v}{\partial r} - \frac{v}{r}\right)^2$,

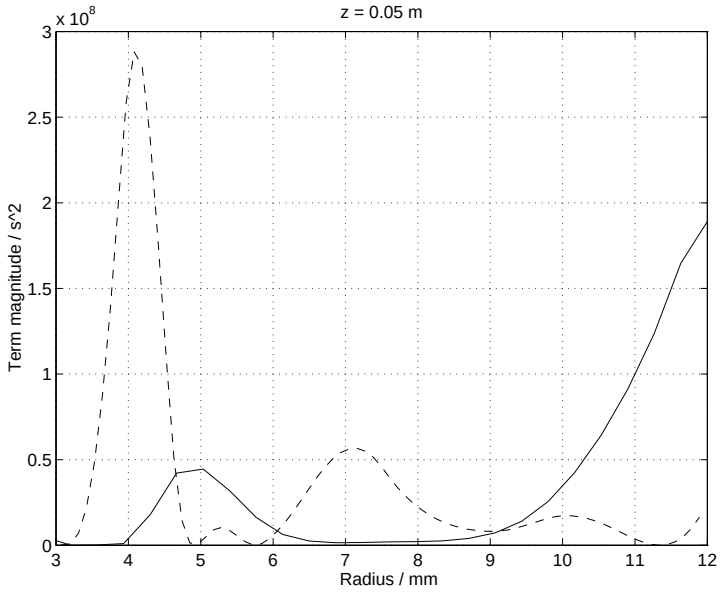

Figure 5.4: Terms in the dissipation function at $z = 0.05$ m, in the 26 mm diameter vortex tube. The solid line represents the contribution of the swirl velocity term $\left(\frac{\partial v}{\partial r} - \frac{v}{r}\right)^2$, the dashed line that of $\left(\frac{\partial w}{\partial r}\right)^2$. Other terms were too small to produce distinguishable lines on the graph.

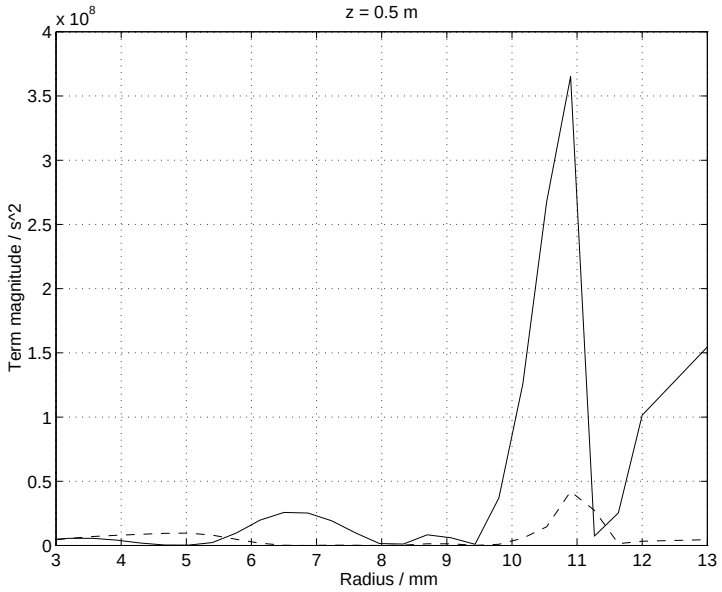

Figure 5.5: Terms in the dissipation function at $z = 0.5$ m, in the 26 mm diameter vortex tube. The significance of the lines is as for figure 5.4.

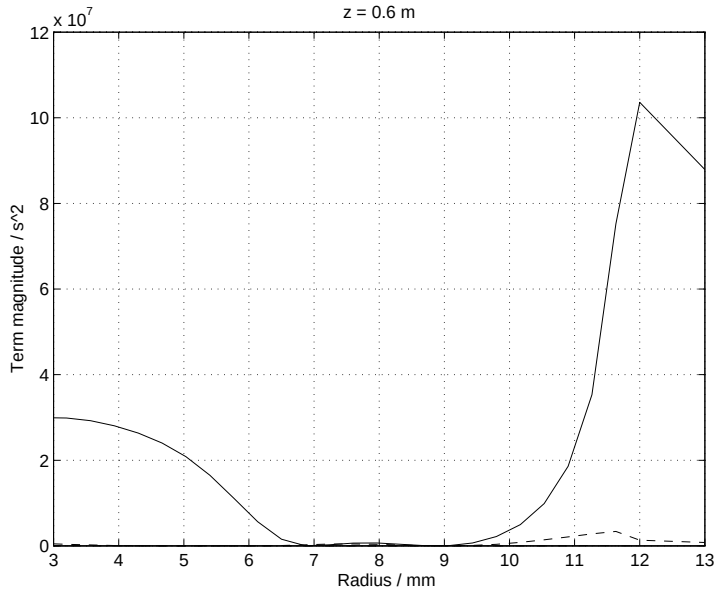

Figure 5.6: Terms in the dissipation function at $z = 0.6$ m, in the 26 mm diameter vortex tube. The significance of the lines is as for figure 5.4.

$\left(\frac{\partial w}{\partial r}\right)^2$, the others producing values too small to be distinguished on the graph.

Values calculated much further along the tube, at distances of 500 mm and 600 mm from the inlets are shown in figures 5.5 and 5.6 respectively. Over the vast majority of these regions, the swirl, $\left(\frac{\partial v}{\partial r} - \frac{v}{r}\right)^2$ term is by far the largest.

The tentative conclusions regarding the dissipation function are confirmed. The dissipation of the swirl velocity is the dominant term over much of the vortex tube, although near to the inlet nozzles the axial velocity is also important.

5.4.3 The Influence of Turbulent Convection

If the turbulent convection process represented by expression (5.6) is to contribute positively to the radial energy separation then it is important that

$$\frac{1}{\rho c_p}\frac{dP}{dr} - \frac{dT}{dr} > 0. \tag{5.18}$$

Figure 5.7 gives the values of $\frac{1}{\rho c_p}\frac{dP}{dr} - \frac{dT}{dr}$ at three stations in the hot tube of the 26 mm diameter apparatus. The greatest potential for outwards radial transport is found at the station nearest the inlets, and declines as the gas proceeds along the tube towards the hot exit. This is not unexpected, since the turbulent convection mechanism is essentially a non-equilibrium phenomenon, and is dependent on the strong swirling of the flow to provide a radial pressure gradient. Towards the warm exit of the tube the swirl has substantially decayed, and additionally the transport mechanisms have had plenty of opportunity to bring the temperature and pressure fields into equilibrium.

The variation of the potential for radially outwards thermal transfer perhaps also helps to explain the axial development of the energy separation. Near the inlets, there is plenty of potential for outwards energy transfer from the central regions of the flow by turbulent convection. This would explain the initial re-enforcement of the energy separation found close to the inlets. Quite quickly though, and in the case of the 26 mm diameter tube within the first 200 mm of axial distance, this potential is drastically re-

duced and the outwards energy transfer effectively ceases. Yet the effect of the pressure gradient is not entirely eliminated, as figure 5.7 shows little evidence of any inwards directed energy transfer beyond 200 mm either. It would seem reasonable to surmise that the pressure gradient is still sufficiently large to limit any turbulent transport of energy down the temperature gradient, even though it no longer actively re-enforces the energy separation.

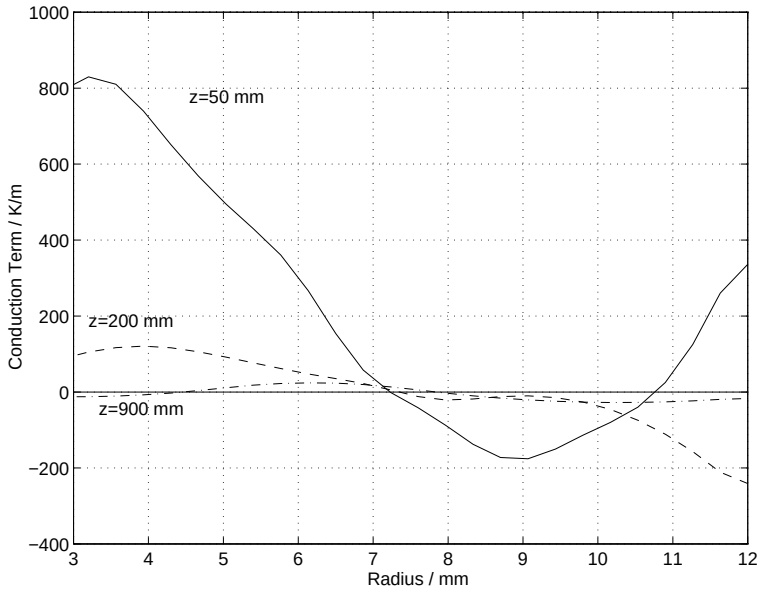

Figure 5.7: The potential for turbulent heat conduction radially outwards at three stations in the 26 mm diameter vortex tube. Positive values indicate energy transfer directed outwards, negative values correspond to inwards turbulent conduction.

5.4.4 Magnitudes of Terms in the Energy Equation

Having simplified the groups of terms in the energy equation, it is useful to compare the relative significance of the remaining quantities at various points in the flow.

Figures 5.8, 5.9 and 5.10 give values of the quantities representing turbulent radial convection, $\frac{\partial}{\partial r}\left[r\rho\epsilon_h c_p\left(\frac{\partial T}{\partial r}-\frac{1}{\rho c_p}\frac{\partial P}{\partial r}\right)\right]$, dissipation of the swirl velocity, $r\rho\epsilon\left(\frac{\partial v}{\partial r}-\frac{v}{r}\right)^2$, axial convection by the mean flow, $r\rho c_p w\frac{\partial T}{\partial z}$ and work done against the pressure gradient by

the axial flow $rw\frac{\partial P}{\partial z}$, as a function of the radius, estimated from the experimental data in chapter 3. Terms involving the radial velocity were ignored.

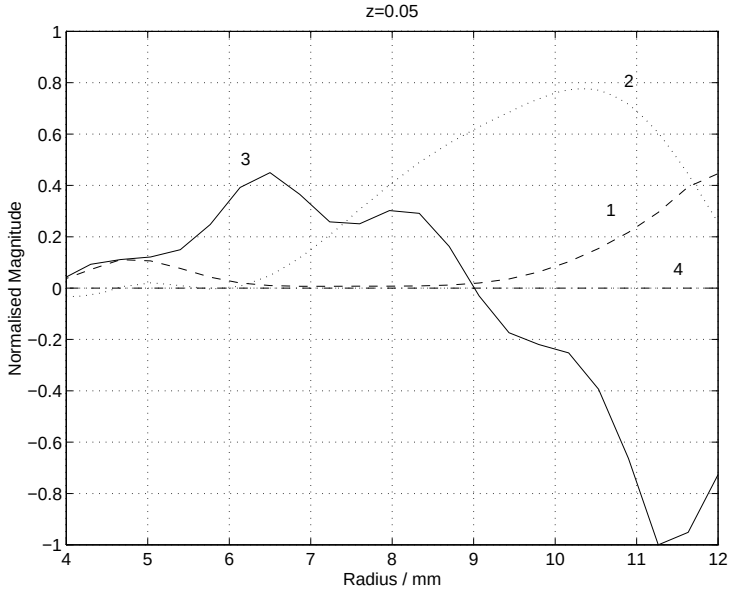

Figure 5.8: Terms in the energy equation at $z = 0.05$ m. The dashed line, labelled 1, represents the reduced dissipation function, the dotted line labelled 2 represents the effects of axial convection, the solid line, 3, represents the effects of radial turbulent heat transport, and the fourth chained line is the axial pressure work term.

One difficulty in evaluating the terms concerns the appropriate values for the turbulent mass and thermal diffusion co-efficients, ϵ and ϵ_h, although only approximate values are necessary for the purposes of comparison. It was assumed that the two values were identical[3] and approximately equal to 100 times the molecular viscosity divided by the local density. This value is fairly arbitrary, but is representative of the figure associated with high speed rotating flows, see for example Keyes [101].

The first figure gives the values for the 26 mm device at an axial station in the hot tube, 50 mm away from the inlet nozzles. It is clear that the axial pressure gradient term, rep-

[3]This arbitrary assumption is made by many authors. The justification is that the turbulent transport process is similar in both cases. In other words, the same fluid particles are responsible for the momentum and the thermal transport.

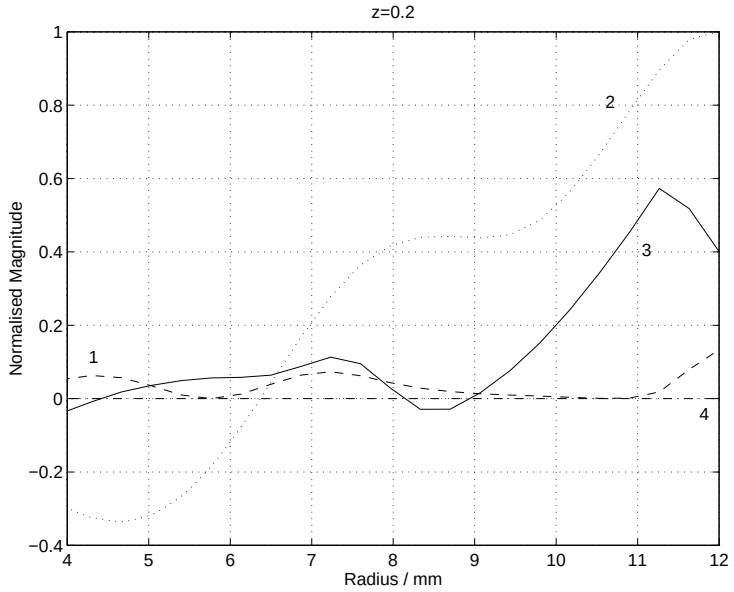

Figure 5.9: Terms in the energy equation at $z = 0.2$ m.The dashed line, labelled 1, represents the reduced dissipation function, the dotted line labelled 2 represents the effects of axial convection, the solid line, 3, represents the effects of radial turbulent heat transport, and the fourth chained line is the axial pressure work term.

resented by the chained line can have very little influence on the resulting temperature distributions, and can be ignored. The other three terms all have regions where they are significant, however.

Results at an axial station 200 mm away from the inlet nozzles are given in the second figure. It is notable that the radial turbulent conduction term (line 3) is less significant here than in the last diagram, presumably because the swirl has decayed significantly.

The third diagram gives values of the terms at a station 600 mm away from the inlet nozzles, well beyond the region in which the energy separation was seen to develop. Here, the radial turbulent conduction term has declined even more, such that the energy and temperature distributions are dominated by axial convection and by dissipation.

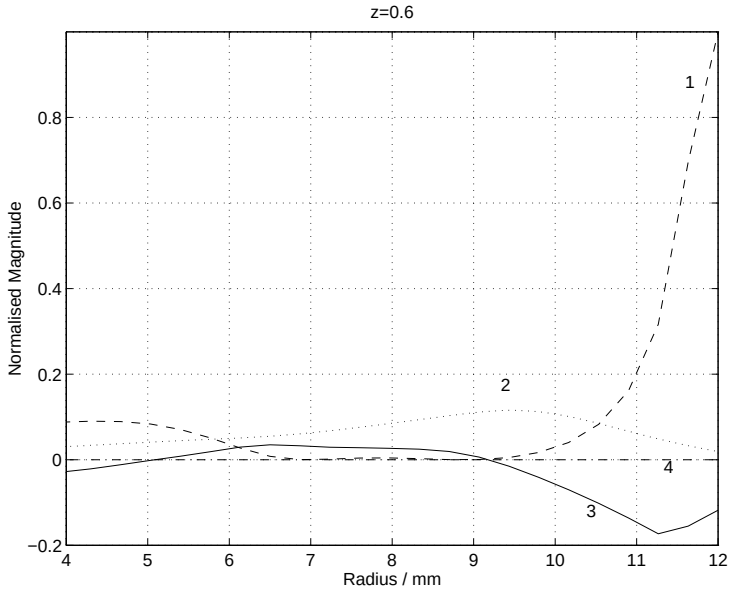

Figure 5.10: Terms in the Energy equation at $z = 0.6$ m.The dashed line, labelled 1, represents the reduced dissipation function, the dotted line labelled 2 represents the effects of axial convection, the solid line, 3, represents the effects of radial turbulent heat transport, and the fourth chained line is the axial pressure work term.

Conclusions Regarding the Energy Equation

The analysis has suggested that three energy transport processes are likely to be important in understanding the behaviour of the Ranque-Hilsch energy separation within the main body of the vortex tube: axial convection by the mean flow, turbulent convection in the radial direction, and dissipation of kinetic energy. It is also likely that radial convection by the mean flow is important near to the centre-line of the vortex tube, but this will be ignored partly thanks to a lack of information prohibiting its quantification and partly because it is not likely to have a dominant effect[4].

In the next section, an energy transport equation composed of these processes alone will be examined in some detail. Before embarking on this investigation, however, it is

[4]In any case the effects of mean radial convection could be accounted for by an increased or decreased turbulent convection term.

worthwhile discussing qualitatively the emerging picture of the energy transport processes within the body of the vortex tube.

The reduced energy equation for the body of the vortex tube, where there is minimal motion in the radial direction could be written as

$$w\frac{\partial T}{\partial z} = \frac{1}{r\rho c_p}\frac{\partial}{\partial r}\left[\rho c_p \epsilon_h r\left(\frac{\partial T}{\partial r} - \frac{1}{\rho c_p}\frac{\partial P}{\partial r}\right)\right] + \frac{\epsilon}{c_p}\Phi + \frac{w}{\rho c_p}\frac{\partial P}{\partial z} \tag{5.19}$$

In a uniflow tube where the axial velocity w is essentially always positive, then the sign of the axial temperature gradient is always the same as that of the right hand side. Cooling at the centre as the flow progresses along the tube requires that $\frac{\partial T}{\partial z}$ is negative and hence that $\frac{1}{\rho c_p}\frac{\partial P}{\partial r}$ increases faster radially than $\frac{\partial T}{\partial r}$, and that the radial turbulent convection term is the largest. Similarly, any energy transfer to the periphery requires that $\frac{\partial T}{\partial r}$ increases more rapidly than $\frac{1}{\rho c_p}\frac{\partial P}{\partial r}$ so that $\frac{\partial T}{\partial z}$ is positive there. While the dissipation term contributes to any heating effect, it does not represent an energy transfer, but merely the transformation of any kinetic energy separation into a thermal separation.

For a counterflow tube matters are similar, except in the reversed flow central region where any additional cooling as the cold gas approaches the orifice means that $\frac{\partial T}{\partial z}$ must be positive. As the axial velocity is negative here, the right hand side must also be negative to permit cooling, again requiring that $\frac{1}{\rho c_p}\frac{\partial P}{\partial r}$ increases more rapidly than $\frac{\partial T}{\partial r}$.

The analysis suggests that a strong radial pressure gradient is necessary to produce cooling of the central gas, and additional energy transfer to the peripheral gas as the flow proceeds along the vortex tube. This corresponds well with experimental observations. Firstly the outwards energy transfer is seen to be confined to a region extending a short distance axially from the inlets. This region possess the strongest vortices and would be the most conducive to energy transfer. Secondly the energy transfer is found to increase with greater vortex strength, and this could be attributed to the consequent increase in radial pressure gradient. Lastly the counterflow type tube is generally found to be more effective than the uniflow variety. This would be because the central cold flow in the counterflow tube passes through the regions with the highest radial pressure gradients

twice; once just after inlet as it proceeds initially towards the valve, and once after the flow reversal as it approaches the orifice.

5.5 Analysis

Having examined the magnitude of the terms in the energy equation and identified those which appear to be important for the Ranque-Hilsch phenomenon, numerical solutions of certain reduced forms of the energy equation will be presented. As with the majority of the chapter, the analysis here will only discuss the processes within the 'body' of the flow, and spend little time on the difficult inlet region.

5.5.1 Turbulent Conduction Process – Radial Terms Only

The most straightforward, but still useful, simplification of the energy equation is that obtained by considering only the turbulent radial conduction terms and the reduced dissipation function, that is

$$\frac{1}{r}\frac{d}{dr}\left[r\left\{\rho c_p \epsilon_h \left(\frac{dT}{dr} - \frac{1}{\rho c_p}\frac{dP}{dr}\right)\right\}\right] + \rho\epsilon\left(\frac{dv}{dr} - \frac{v}{r}\right)^2 = 0. \tag{5.20}$$

As there are no axial terms in this equation, investigation of axial effects is prohibited. Hinze [85] obtained such a relation, and then made the reasonable assumption of simple radial equilibrium

$$\frac{dP}{dr} = \frac{\rho v^2}{r}, \tag{5.21}$$

to give an expression that relates the temperature distribution to the swirl velocity and turbulence characteristics only,

$$\frac{1}{r}\frac{d}{dr}\left[r\left\{\rho c_p \epsilon_h \left(\frac{dT}{dr} - \frac{1}{c_p}\frac{v^2}{r}\right)\right\}\right] + \rho\epsilon\left(\frac{dv}{dr} - \frac{v}{r}\right)^2 = 0. \tag{5.22}$$

Numerical Method

Equation (5.22) can be solved for a temperature distribution given prescribed swirl velocity and density variations. This was done numerically for several experimentally determined velocity profiles.

The differential terms were discretised using central differences, over a set of finite nodes spaced radially at positions r_i and the result re-arranged to give an expression for T_{i+1} as a function of the values at the preceding node, i. Distances between the nodes were much smaller then the spacings between the experimental values. To provide compatibility, the experimental values were interpolated to give values at the computational nodes by fitting a spline through the data.

Integrating from the centre outwards provides a first solution for the temperature distribution. The radial pressure distribution was calculated by numerically integrating the simple radial equilibrium expression, and the result used with the equation of state for a perfect gas to estimate the density. A second estimate for the temperature distribution was calculated with the new values, and the process iterated until convergence.

Only one boundary condition is required for each of the temperature and pressure distributions, and in both cases they were enforced at the centre. For the pressure, this was specified as atmospheric. The temperature at the centre of the vortex was determined using energy conservation between the inlet to the tube and the particular axial position under consideration, that is

$$\dot{m}_{in} h_{0,in} = 2\pi \int_0^{r_0} (r h_0 \rho w) \; dr. \tag{5.23}$$

where h_0 is the stagnation enthalpy. For any set of stagnation enthalpy values, say h_0^*, one could write

$$h_0^* = h_0 + \Delta h \tag{5.24}$$

where Δh represents the constant correction necessary to h_0^* in order for the distribution to satisfy the energy conservation relation (5.23). Substituting in the energy conservation

relation gives

$$\Delta h = \frac{2\pi}{\dot{m}_{in}} \int_0^{r_0} (h_0^* r \rho w) \; dr - h_{0,in}. \tag{5.25}$$

which can then be used to calculate h_0 from h_0^*. From the resulting value of h_0 at the centre of the tube, the corresponding static enthalpy and temperature at the centre my be calculated. This value was used as the boundary condition for the next iteration. The axial velocity distribution $w(r)$ was taken from experimental values. This procedure was applied for both uniflow and counterflow calculations, although in the latter case it provides an inaccurate central value since the mass flow through the hot tube is not constant at all stations along the axis.

Results

Calculations were performed for a number of values of ϵ_h/ϵ. Solutions for the velocity measurements of Lay [74, 92] at two stations in a uniflow tube, given by the lines in figures 5.11 and 5.12, can be compared to his results for the stagnation temperature distribution given by the circles. The former figure applies to data taken near to the tangential inlets and shows that for values of ϵ_h/ϵ near to unity the solution models the measured stagnation temperature quite well. Data taken near the valve was used for the latter figure, and again the comparison between solution and experiment is quite good for ϵ_h/ϵ close to one.

Evaluation of the solution procedure for a counterflow tube was made using the data of chapter 3. In view of the inaccuracy of the central thermal boundary condition in this case, it is not reasonable to expect the values obtained from calculations to compare directly with experimental values. The temperature distributions have been normalised therefore, as the best that can be hoped for is some similarity in the form of the variations.

Figure 5.13 compares the stagnation temperature solutions obtained using the velocity distribution close to the inlet nozzles with the experimentally determined variation. Similar data nearer to the valve is given in figure 5.14. In both cases, the form of the functions compares quite well with experiment in the outer regions of the tube, but is

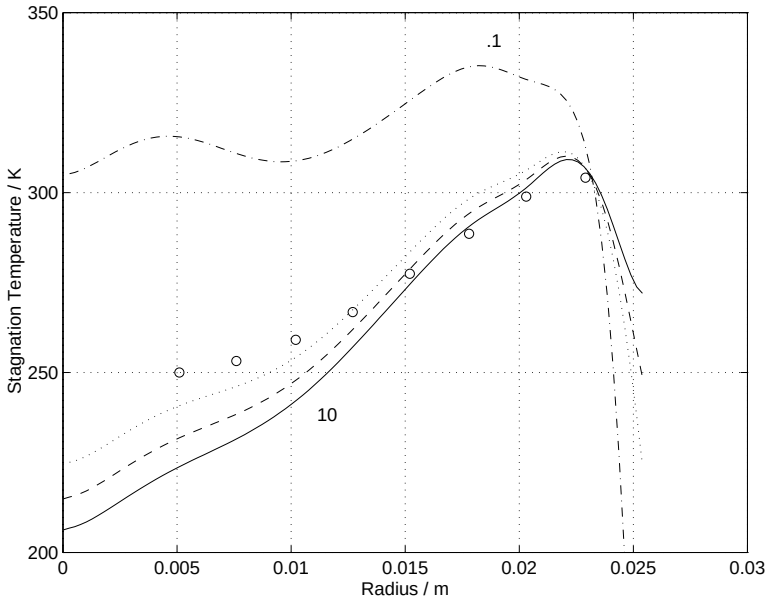

Figure 5.11: Comparison of solutions and experimental values for Lay's data, table 2 station 1. The solid line gives the calculated variation of the stagnation temperature with radius for value of ϵ_h/ϵ equal to 10, the dashed line for 1, the dotted line for 0.5, and the chained line for 0.1. Experimentally determined values of the stagnation temperature are shown as circles.

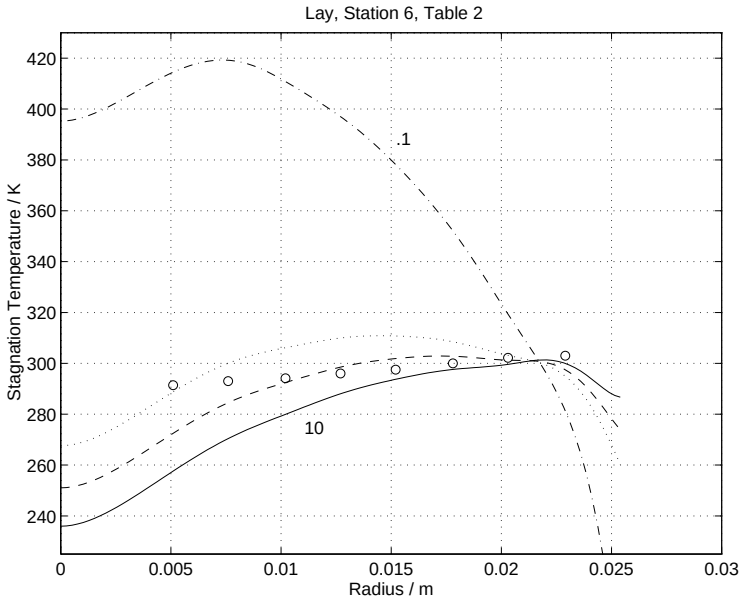

Figure 5.12: Comparison of solutions and experimental values for Lay's Data, table 2 station 6. The solid line gives the calculated variation of the stagnation temperature with radius for value of ϵ_h/ϵ equal to 10, the dashed line for 1, the dotted line for 0.5, and the chained line for 0.1. Experimentally determined values of the stagnation temperature are shown as circles.

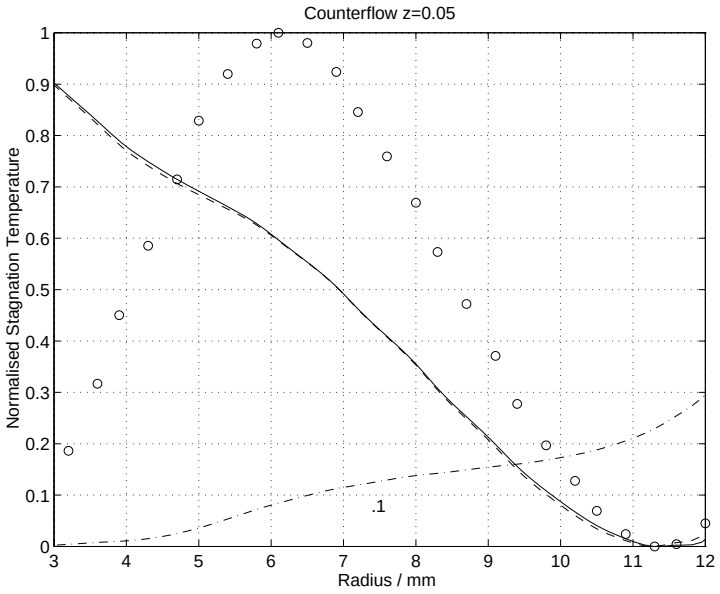

Figure 5.13: Comparison of solutions experimental values for counterflow data, $z = 0.05$ m. The solid line gives results for $\epsilon_h/\epsilon = 10$, the dashed line for $\epsilon_h/\epsilon = 2$, and the chained line for $\epsilon_h/\epsilon = 0.1$. Experimentally determined values are shown as circles.

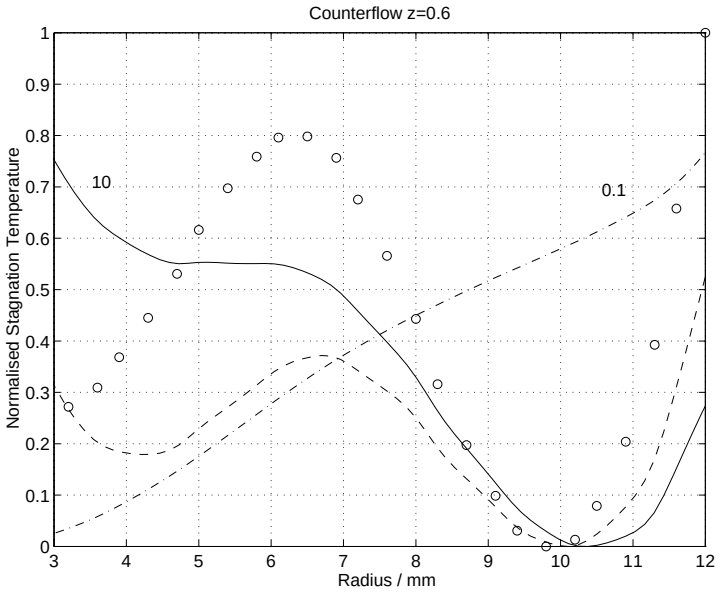

Figure 5.14: Comparison of solutions and experimental values for counterflow data, $z =$ 0.6 m. The solid line gives results for $\epsilon_h/\epsilon = 10$, the dashed line for ϵ_h/ϵ =2, and the chained line for $\epsilon_h/\epsilon = 0.1$. Experimentally determined values are shown as circles.

much less satisfactory near the centre. Two reasons might be advanced to explain this departure: firstly the inadequacy of the central boundary condition on temperature in the counterflow case, and secondly that axial and indeed radial mean convection are likely to be most significant nearer the centre where the axial and radial velocities approach the magnitude of the swirl velocity.

Conclusions

A balance between dissipation and radial turbulent convection models the energy separation in the body of the vortex tube quite well, for experimentally determined velocity distributions. The calculated energy distributions depend on the ratio of the thermal turbulent transport coefficient ϵ_h to the momentum turbulent transport coefficient ϵ. Good agreement between experimental and calculated energy distributions is obtained for $\epsilon_h/\epsilon \sim 1$, which would be anticipated on the grounds that similar transport processes are responsible for the thermal and momentum effects.

5.5.2 The Turbulent Conduction Process - Radial and Axial Terms

Including the axial terms in the energy equation gives

$$\frac{1}{r}\frac{\partial}{\partial r}\left[r\left\{\rho c_p \epsilon_h \left(\frac{\partial T}{\partial r} - \frac{1}{c_p}\frac{v^2}{r}\right)\right\}\right] + \rho\epsilon\left(\frac{\partial v}{\partial r} - \frac{v}{r}\right)^2 - \rho w c_p \frac{\partial T}{\partial z} + w\frac{\partial P}{\partial z} = 0. \qquad (5.26)$$

The effect of the axial terms on the axial development of the energy separation was investigated numerically using this equation.

Numerical Method

For the evaluation of the effect of the axial terms, a very simple model of the fluid mechanics of the vortex tube was used. Swirl velocities along the tube were calculated from

an axisymmetric swirl equation derived by neglecting radial velocity and axial diffusion

$$\rho w \frac{\partial v}{\partial z} = \frac{\partial}{\partial r}\left[\mu\left(\frac{\partial v}{\partial r} - \frac{v}{r}\right)\right]. \tag{5.27}$$

It was assumed that the axial velocity was always directed in the positive axial direction, as might be the case in a uniflow tube, enabling the use of a parabolic solution technique. As a further simplification the axial velocity distribution across the radius was assumed to be invariant as the flow proceeded along the tube. Finite difference discretisation of the swirl equation, where i represents node numbers in the axial direction and j in the radial direction gives

$$v_{i+1,j} = v_{i,j} + \frac{z_{i+1} - z_i}{\rho_{i,j} r_{i,j}^2 w_{i,j}^2} \cdot \frac{\left[\mu r^2 \left(\frac{\partial v}{\partial r} - \frac{v}{r}\right)\right]_{i,j+\frac{1}{2}} - \left[\mu r^2 \left(\frac{\partial v}{\partial r} - \frac{v}{r}\right)\right]_{i,j-\frac{1}{2}}}{r_{i,j+\frac{1}{2}} - r_{i,j-\frac{1}{2}}} \tag{5.28}$$

with

$$\left(\frac{\partial v}{\partial r}\right)_{i,j+\frac{1}{2}} = \frac{v_{i,j+1} - v_{i,j}}{r_{i,j+1} - ri, j} \tag{5.29}$$

$$r_{i,j+\frac{1}{2}} = \frac{1}{2}\left(r_{i,j+1} + r_{i,j}\right) \tag{5.30}$$

$$\left(\mu r^2\right)_{i,j+\frac{1}{2}} = \frac{1}{2}\left[\left(\mu r^2\right)_{i,j+1} + \left(\mu r^2\right)_{i,j}\right] \tag{5.31}$$

and similarly for $j - \frac{1}{2}$, with

$$r_{i,j-\frac{1}{2}} = \frac{1}{2}\left(r_{i,j-1} + r_{i,j}\right) \tag{5.32}$$

and so on.

Having obtained a first estimate for the radial distribution of swirl velocity at an axial position, values for the static pressure across the radius were obtained by numerically integrating the simple radial equilibrium expression. In discretised form, this expression

is

$$P_{i+1,j+1} = P_{i+1,j} + (r_{i+1,j+1} - r_{i+1,j}) \frac{\rho_{i+1,j} v_{i+1,j}^2}{r_{i+1,j}}. \tag{5.33}$$

A first approximation for the density was obtained by using values from the previous axial node, that is $\rho_{i,j}$.

Next, the radial temperature distribution was obtained by solving equation (5.26) elliptically. Finite difference discretisation gives

$$T_{i+1,j} = \frac{A}{B} \tag{5.34}$$

where

$$\begin{aligned} A \;=\; & \left(\epsilon_h r \cdot \frac{v^2}{r}\right)_{i+1,j+\frac{1}{2}} - \left(\epsilon_h r \cdot \frac{v^2}{r}\right)_{i+1,j-\frac{1}{2}} - \frac{c_p \left(r\rho\epsilon_h\right)_{i+1,j+\frac{1}{2}} T_{i+1,j+1}}{r_{i+1,j+1} - r_j} \\ & - \frac{c_p \left(r\rho\epsilon_h\right)_{i+1,j-\frac{1}{2}} T_{i+1,j-1}}{r_{i+1,j} - r_{i+1,j-1}} + \frac{\Delta r \;\; (r\rho w)_{i+1,j} \, c_p T_{i,j}}{\Delta z} \\ & + \Delta r \left[(r\Phi)_{i+1,j} + \left(rw \frac{\partial P}{\partial z} \right)_{i+\frac{1}{2},j} \right] \end{aligned} \tag{5.35}$$

with

$$\Phi_{i+1,j} = (\rho\epsilon)_{i+1,j} \left(\frac{v_{i+1,j+\frac{1}{2}} - v_{i+1,j-\frac{1}{2}}}{r_{i+1,j+\frac{1}{2}} - r_{i+1,j-\frac{1}{2}}} - \left(\frac{v}{r}\right)_{i+1,j} \right)^2 \tag{5.36}$$

$$\left(rw \frac{\partial P}{\partial z} \right)_{i+\frac{1}{2},j} = (rw)_{i,j} \frac{P_{i+1,j} - P_{i,j}}{z_{i+1,j} - z_{i,j}} \tag{5.37}$$

$$\Delta r = r_{i+1,j+\frac{1}{2}} - r_{i+1,j-\frac{1}{2}} \tag{5.38}$$

$$\Delta z = z_{i+1,j} - z_{i,j} \tag{5.39}$$

and

$$B = -\frac{\left(r\rho c_p \epsilon_h\right)_{i+1,j+\frac{1}{2}}}{r_{i+1,j+1} - r_{i+1,j}} - \frac{\left(r\rho c_p \epsilon_h\right)_{i+1,j-\frac{1}{2}}}{r_{i+1,j} - r_{i+1,j-1}} + \frac{\Delta r \;\; (r\rho w)_{i+1,j} \, c_p}{\Delta z}. \tag{5.40}$$

The newly calculated pressure and temperature values at $i+1$ were then used to provide a better estimation of the density $\rho_{i+1,j}$, using the equation of state for an ideal gas. After

this new estimates of velocity pressure and temperature, still at axial position $i+1$ were calculated using the new density values, and the process repeated until a reasonable degree of convergence had been obtained. The solution then advances to the next axial position $i+2$, and iterates to convergence there.

Results

A solution was calculated for a 0.013 m radius uniflow tube operated on air. The computation started with a forced vortex of angular velocity 26 000 rad/s upstream, and a uniform radial temperature distribution of 298 K. The axial velocity distribution specified increased linearly from 10 m/s at the centre of the tube to 40 m/s at the periphery, as shown in figure 5.15. It was assumed that the pressure at the centre of the tube remained constant at the atmospheric value (101325 Pa), and that the temperature of the gas immediately adjacent to the outer wall of the tube was constant at 298 K. A zero gradient boundary condition was employed at the centre of the tube for the temperature calculation. The turbulent diffusivities ϵ and ϵ_h were taken to be 100 times the laminar value. Calculations were performed on a regularly spaced grid of 31 points radially and 1000 points axially over a distance of 1 m.

In a calculation as simplified as this it is unrealistic to expect any more than a qualitative comparison between experimental and numerical results. Comparisons will be drawn with both the results of Lay taken in a uniflow tube as discussed earlier, and with the experimental data from a 0.013 m diameter counterflow tube described in chapter 3. Figure 5.16 shows the computed variation of the stagnation temperature along the axis of the tube at four radial positions. There is clear evidence of a reduction in stagnation enthalpy near the centre of the tube, and a rise towards the periphery over the first 0.2 m of axial length. It is interesting that this distance is comparable to the length of the region over which the energy separation was found to grow in the experimental study of the counterflow tube. Details of the development of the radial stagnation temperature profiles in this region are given in figure 5.17, and over the remainder of the tube in

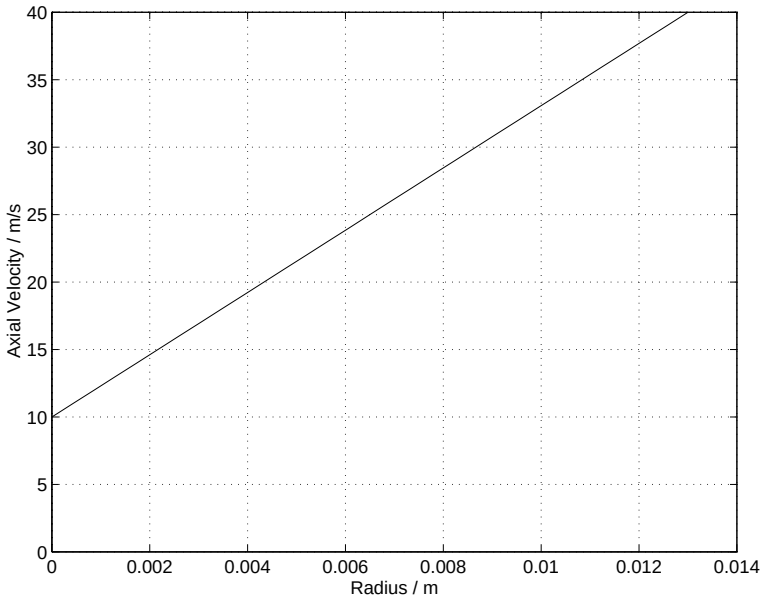

Figure 5.15: The axial velocity profile.

figure 5.18.

By a distance of 0.5 m from the upstream end, the stagnation temperature difference between the inner and outer regions of the flow has declined substantially, so that there is little between them. It is notable from figure 5.19 that the swirl velocity has decayed greatly by this point, such the maximum circumferential velocity is less than half that at the upstream end, reducing the influence of the pressure gradient in producing energy transport up the radial temperature gradient.

At the downstream end of the simulated tube, near $z = 1$ m, the stagnation temperature separation appears to have been reversed with the outer regions having the lowest energy. This is unrealistic, and can be attributed to the inadequacies of the calculation. Since the swirl velocity has decayed so greatly by this point, any stagnation temperature separation is attributable primarily to a differences in the static temperature. This can be seen by comparing the curves for the axial variation of the static temperature, figure 5.20, with those for the stagnation temperature. Near to an axial distance of 1 m, the two plots are very similar.

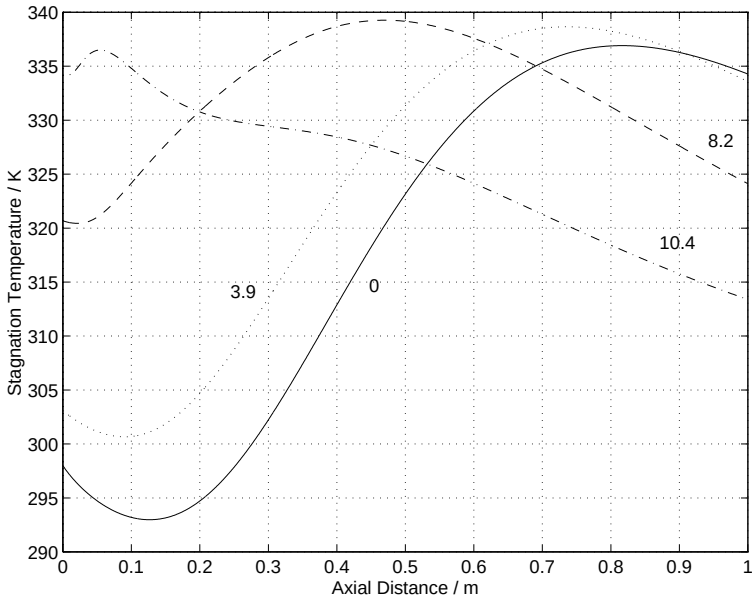

Figure 5.16: Axial variation of the stagnation temperature at four radial positions, calculated from the reduced energy equation including axial terms. The solid line gives values for the centre of the tube, that is zero radius, the dotted line for a radius of 3.9 mm, the dashed line for 8.2 mm, and the chained line for 10.4 mm.

The calculation has assumed that gas adjacent to the wall of the vortex tube has remained at a constant 298 K, a value substantially below the static temperature of most of the gas in the body of the tube in this downstream region. It has also assumed that turbulence levels are constant throughout the tube such that the significance of turbulent thermal conduction due to radial temperature gradients is the same over the whole domain.

The cooling of the outer region in the simulated tube is due to turbulent thermal convection of energy out of the solution domain, through the constant temperature wall which effectively acts as a heat sink. Looking at the temperature profiles across the radius (figures 5.21 and 5.22) makes this clear, as the negative temperature gradient near to the wall is consistent with conduction through it.

A reversal of the energy separation like this is not found in a real tube for a number of reasons. Firstly, the tube wall experiences considerable heating such that gas in

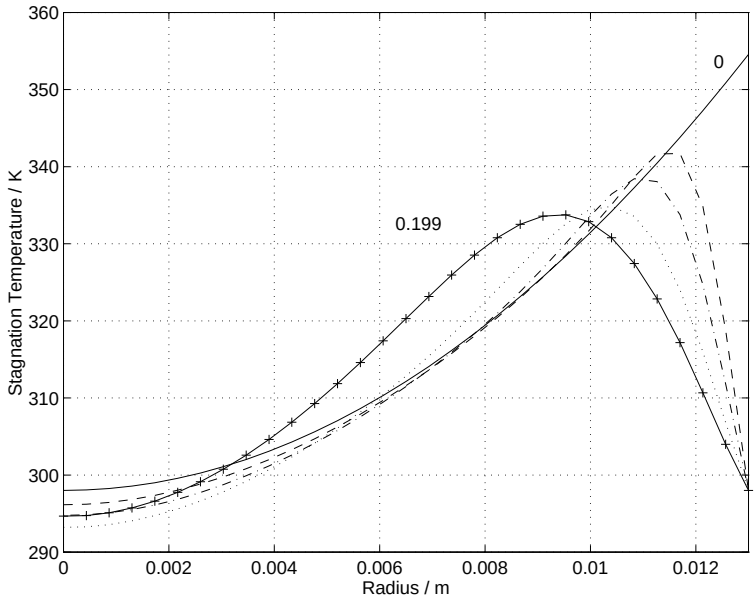

Figure 5.17: Stagnation temperature profiles at stations close to the inlet, calculated from the reduced energy equation including axial terms. The solid line gives the initial stagnation temperature distribution at $z = 0$, the dashed line at $z = 24$ mm, the chained line at $z = 49$ mm, the dotted line at $z = 99$ mm and the solid line with symbols at $z = 199$ mm.

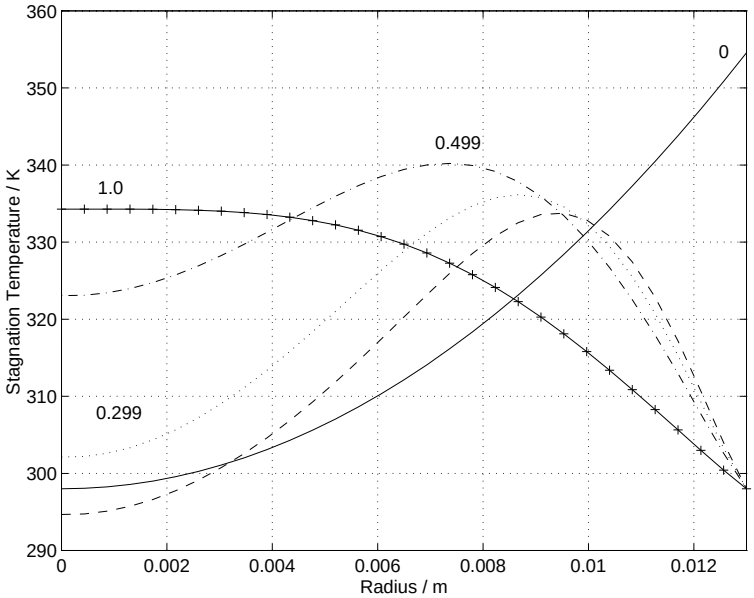

Figure 5.18: Stagnation temperature profiles at stations spaced along the axis, calculated from the reduced energy equation including axial terms. The solid line gives the stagnation temperature distribution at $z = 0$, the dashed line at 0.199 m, the dotted line at 0.299 m, the chained line at 0.499 m, and the solid line with symbols at 1 m.

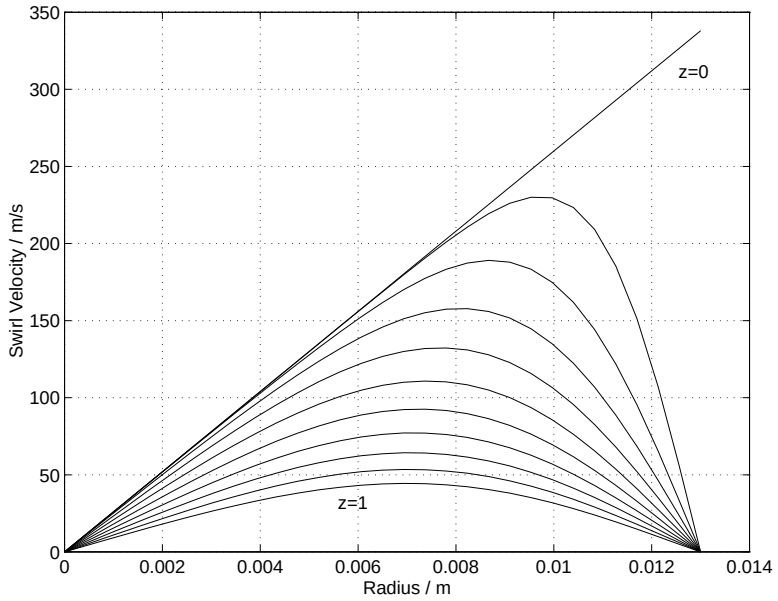

Figure 5.19: Swirl velocity profiles at stations along the tube axis, calculated using the simplified method. The curves are plotted for axial stations 0.1 m apart, with the top curve giving the distribution at the upstream end $z = 0$ m, and the lowest curve at the downstream end $z = 1$ m.

contact with it is much warmer than ambient temperature, as assumed by the calculation. Secondly the conduction occurs in a region of relatively low swirl, and thence, relatively low turbulence. As the calculation has assumed uniform turbulence over the whole domain, it over-exaggerates the turbulence in the downstream, low swirl, region. Both these factors mean that conduction of heat out through the wall of the vortex tube has a much smaller influence on the temperature distributions in a real tube than the calculations suggest. In fact most vortex tubes retain a cooler region at the centre all along their length.

Deductions

The solutions obtained to the energy equation including axial terms indicate that axial convection by the mean flow influences the heat transfer within the tube in such a way so as to cause the energy separation to develop as the flow progresses along the tube.

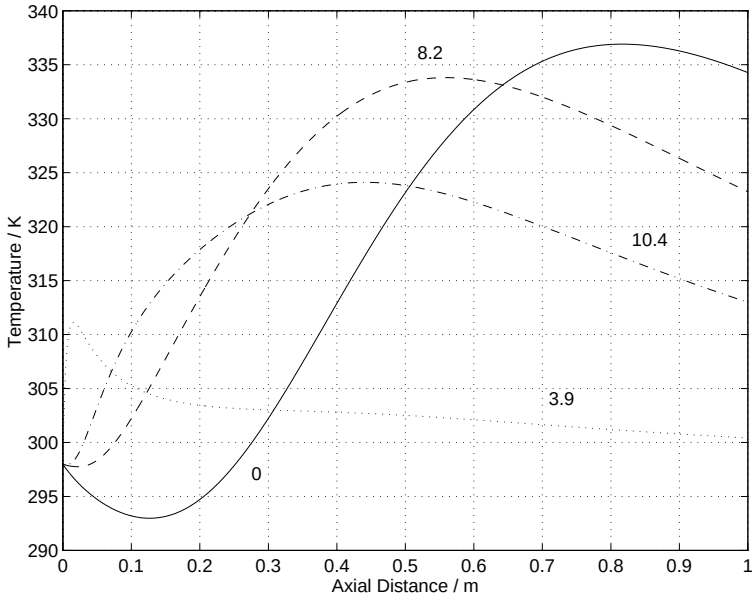

Figure 5.20: Axial variation of the static temperature at four radial positions, calculated from the reduced energy equation including axial terms. The solid line gives values for the centre of the tube, zero radius, the dotted line for a radius of 3.9 mm, the dashed line for 8.2 mm, and the chained line for 10.4 mm.

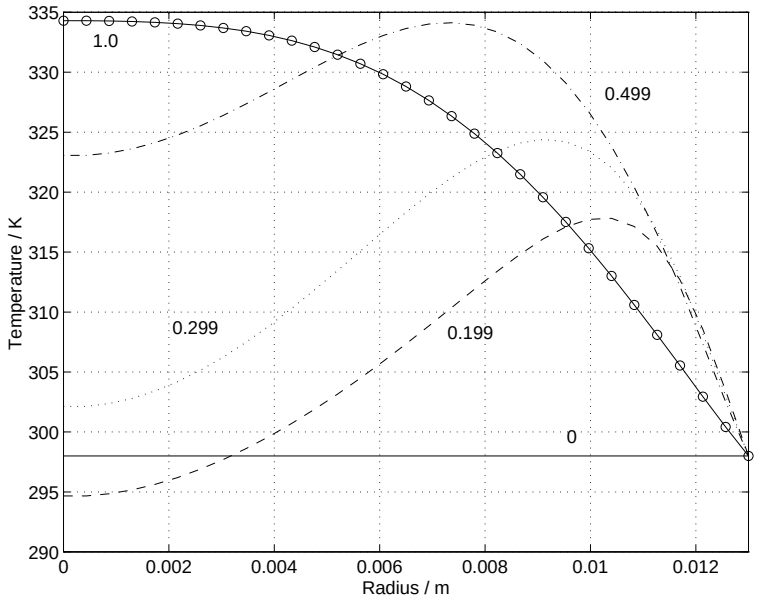

Figure 5.21: Static temperature profiles at stations spaced along the axis, calculated from the reduced energy equation including axial terms. The solid curve gives the distribution at the upstream end, $z = 0$ m, the dashed line at 0.199 m, the dotted line at 0.299 m, the chained line at 0.499 m, and the solid line with circles at 1 m.

The region of development is small in relation to the overall length of the tube, but is sufficiently large that maximum separation is found a substantial distance away from the inlet to the tube. This agrees well, at least qualitatively, with the other information within the chapter.

5.6 Conclusions

The energy separation found in the Ranque-Hilsch tube can be accounted for by two phenomena. Firstly, the formation of an approximately forced vortex near the tangential inlets to the tube initially provides a kinetic energy separation, the peripheral gas having a much higher velocity than that near the centre. Secondly, the strong radial pressure gradient produced by the forced vortex enables turbulent fluctuations to transport thermal energy radially outwards and re-enforce the existing energy separation until the

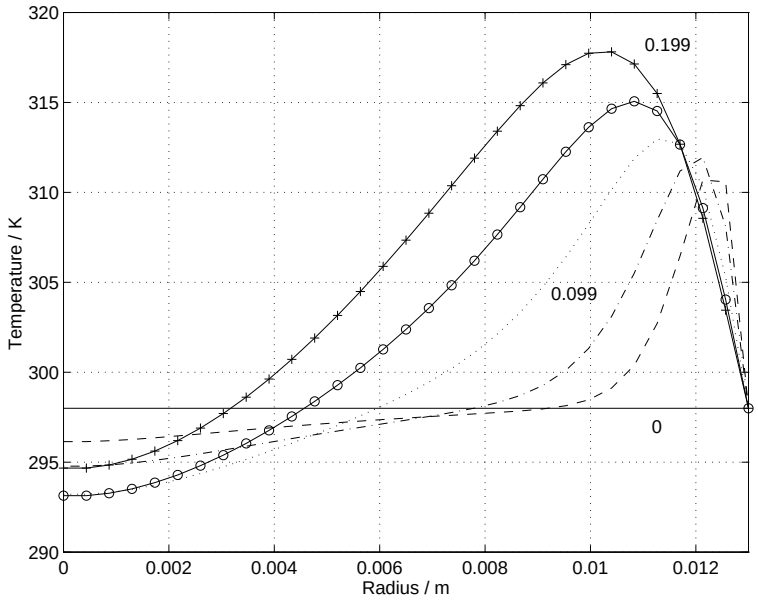

Figure 5.22: Static temperature profiles close to the inlet, calculated from the reduced energy equation including axial terms. The solid curve gives the distribution at the upstream end, $z = 0$ m, the dashed line at 0.024 m, the chained line at 0.049 m, the dotted line at 0.099 m, the solid line with circles at 0.149 m, and the solid line with pluses at 0.199 m.

thermal and pressure gradients have come into equilibrium.

The effects of the two processes are modified by axial convection and by viscous dissipation of the kinetic energy of the flow to produce the characteristic distributions found within the vortex tube. Axial convection extends the turbulent thermal transport process over a significant length of the tube, and is responsible for the observed axial development of the energy separation. Viscous dissipation converts the kinetic energy separation into a thermal separation, and serves to produce a temperature rise in both the hot and cold streams as their kinetic energy is reduced.

The energy separation is maintained by the flow so long as the swirl is strong enough to provide a substantial radial pressure gradient to help offset the effects of turbulent conduction. As the swirl decays, for example towards the end on a uniflow tube, the energy separation declines.

Such an explanation is consistent with many observed features of vortex tubes, essentially attributing the existence of a radial stagnation enthalpy gradient to the formation of a forced vortex, and the cooling of the central flow below the inlet temperature to a turbulent transport process that depends on the compressibility of the fluid. In particular it would explain why a vortex tube operated on high pressure water produces an energy separation, but with no net cooling of the central flow (Balmer [80]).

Chapter 6

A Model of Ranque-Hilsch Tube Performance

6.1 Introduction

In this chapter, a semi-empirical model of the performance of a vortex tube will be developed, based on the insights of the previous chapters. The intention is to produce a set of analytical expressions relating the temperature separation produced by a vortex tube to as many independent variables as possible.

6.2 A Model of Ranque-Hilsch Tube Performance

We wish to relate the performance of a vortex tube to as many independent variables as are necessary, and in particular the inlet pressure, the inlet temperature and the cold mass flow fraction. Dimensional analysis has shown that for any particular vortex tube installation, the functional relationship for the performance as measured by the temperature difference between the inlet stream and the cold stream reduces to

$$\frac{\Delta T_c}{T_{inlet}} = f\left(\frac{P_{inlet}}{P_{outlet}},\ \mu_c\right). \tag{6.1}$$

The results of Stephan [110] confirmed the validity of this relationship, but gave no insight regarding the form of the expressions that should be employed. Empirical curve fitting was the only means of producing an analytical relation.

Information presented in the preceding chapters will be employed in order to derive some approximate expressions that can be used to model vortex tube performance, proceeding in the manner of the scale analysis advocated by Bejan [128]. One thing that has been clear throughout this work though, is the difficulty of quantitively predicting the Ranque-Hilsch energy separation; some empiricism will be necessary in any model.

6.3 Assumptions

On the basis of the work so far, the following assumptions will be made about flow in the vortex tube:

The swirl is the most important feature of the flow

The dominant feature of flow in the vortex tube is the swirling flow near the inlet plane. This swirl drives the whole of the flow in the tube and is responsible for its peculiar features, including the energy separation. The swirl itself is driven by the potential energy of the compressed air fed into the tube.

A forced vortex is formed near the inlet plane

The swirl velocity profile near the inlet plane is approximately that of a forced vortex, and can be very roughly represented by

$$v = \Omega r. \tag{6.2}$$

Simple Radial Equilibrium

Radial velocities near the inlet plane are small, such that the flow can be modelled approximately by the simple radial equilibrium expression

$$\frac{\partial P}{\partial r} = \frac{\rho v^2}{r}. \tag{6.3}$$

This cannot be true very close to the inlet nozzles, but will be nearly the case a short distance away from them.

The axial velocity and swirl velocity fields can be decoupled

The axial and swirl velocity fields can be decoupled in that while the axial velocity field is influenced by the swirl, and indeed under the assumptions above is driven by it, any changes in the axial velocity field do not substantially affect the swirl. One implication of this is that changes in the cold mass flow fraction only affect the axial velocity field and do not influence the swirl near the inlets at all. In view of the close coupling of the swirl field and the overall pressure drop across the tube, the cold mass flow fraction will not have any affect on the ratio P_{inlet}/P_{outlet}, nor will it affect the 'separation potential' of the vortex tube[1].

For an 'ideal' uniflow vortex tube with a purely geometrical means of separating the hold and cold flows, as shown in figure 6.1, this assumption will be true. In most practical vortex tubes, the assumption will be only approximately correct. With all the vortex tubes considered up to this point, the cold mass flow fraction has been controlled by using a valve at the hot outlet to affect the pressures internal to the tube. Closing the valve, to increase the cold mass flow fraction raises the internal pressure somewhat, slightly reducing the expansion undergone by the inlet gas as it enters and reducing the magnitude of the swirl.

[1]The concept of separation potential will be discussed later in the chapter.

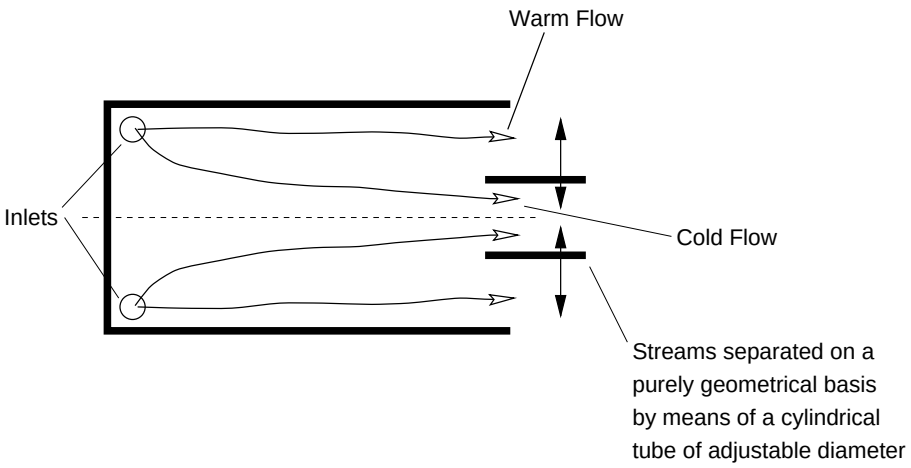

Figure 6.1: An 'ideal' vortex tube.

The static temperature does not vary greatly across the inlet plane

It will be assumed that the radial variation of the static temperature near the inlet plane is not sufficient to have a large effect on the density. The model will only account for the influence of temperature on the flow by considering that its effect at the inlet plane can be characterised by a single value, equivalent to the mass averaged temperature across the plane. Later, this single value will be related to the inlet temperature of the gas.

The density will of course vary across the radius, but the assumption implies that this is due mostly to the effects of pressure rather than temperature. Despite the radially increasing static temperature at the inlet plane, the density increases radially also thanks to the large pressure gradient.

That a significant proportion of the energy separation develops as the flow progresses along the vortex tube is important in making this assumption workable. If the whole of the energy separation was manifest in the static temperature distribution near the inlet then the density distribution would be significantly altered.

6.4 Limitations

The model will be subject to two rather more arbitrary restrictions, in addition to the rational assumptions.

The energy transfer mechanism

The model will mostly be independent of the mechanism of heat transfer, since empiricism will be used to estimate the magnitude of the energy separation. Some of the assumptions might be invalidated, however, were an acoustic mechanism similar to that proposed by Kurosaka responsible, since this would imply that the majority of the energy transfer occured near the inlet plane. It would also cast doubt on the assumption that we can characterise the flow by the strength of the forced vortex found near the inlet.

Applicability of the model

As with the result of the dimensional analysis, equation (6.1), the form of the functions derived in the model will not vary from vortex tube to vortex tube irrespective of any geometric similarity. In this sense the model has a general applicability.

The empirically determined values, however, will depend strongly on the particular vortex tube under investigation. It would be anticipated that geometrically similar vortex tubes have empirical constants that are related, but little account will be taken of this, as there is insufficient evidence to test the hypothesis. Instead, each vortex tube must be characterised individually. In this capacity the model is specific to particular vortex tubes.

6.5 Reformulation

All modelling attempts so far have been constructed in terms of the the cold temperature drop ΔT_c. It is convenient to develop any model in terms of a reduced heat transfer per

heat capacity flux defined

$$q = \mu_c \, \Delta T_c = \frac{Q}{\dot{m} c_p} \tag{6.4}$$

where Q represents the rate of energy transfer from the cold stream to the warm stream. This notation has the particular advantage that q remains finite at zero cold gas mass flow fraction, $\mu_c = 0$, whereas the temperature drop ΔT_c is undefined.

Adopting the assumption that the swirl and radial flows can be partially decoupled, equation (6.1) can be written

$$q = T_{inlet} \cdot f_1 \left(\frac{P_{inlet}}{P_{outlet}} \right) \cdot f_2 \left(\mu_c \right). \tag{6.5}$$

The significance of this expression is that the pressure ratio P_{inlet}/P_{outlet} provides the energy separation potential, whereas μ_c influences to what extent that potential is exploited.

For the moment the influence of the pressure ratio will be neglected, and we will write

$$q = q_{max} \cdot f_2 \left(\mu_c \right), \tag{6.6}$$

with q_{max} representing the maximum magnitude of the reduced heat transfer over the range $0 \leq \mu_c \leq 1$. This is entirely compatible with Stephan's work, and we will proceed by improving his result for the dependence of the heat transfer on the value of μ_c.

6.6 The Influence of the Cold Mass Flow Fraction

Constraints on the form of $f_2 \left(\mu_c \right)$

An expression to represent the effect of the cold mass flow fraction μ_c on the reduced heat transfer q is required. It is immediately clear that any function to fulfil this role must be continuous, monotonic, and have a maximum value of one. The function must also have a minimum value of zero, which is only achieved when there is no flow separation, that

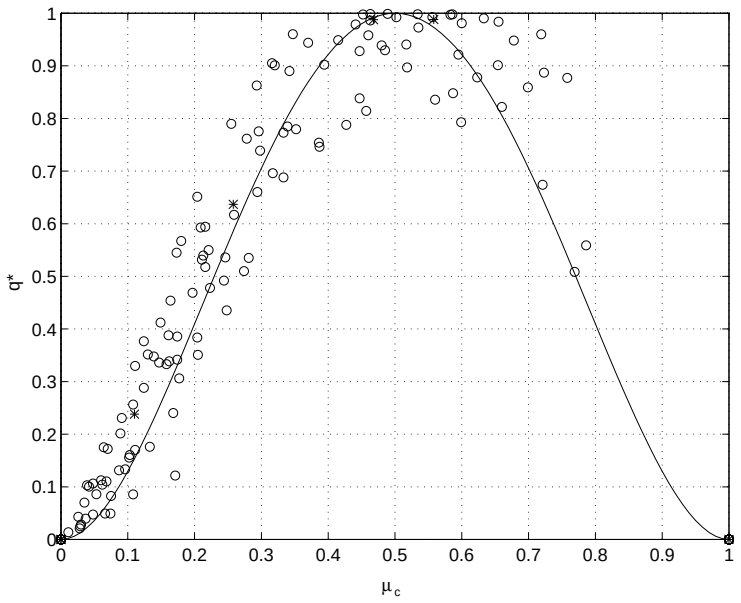

Figure 6.2: The quartic relation and the data it models, plotted as the normalised heat transfer, q^* against the cold gas fraction μ_c. The circles represent data taken in the CUED vortex tubes under 18 distinct conditions.

is when $\mu_c = 0, 1$.

It would be anticipated that the function would rise smoothly from zero gradient at the extremities. Empirical observation also suggests that the maximum value should occur near $\mu_c = 0.5$. This is not surprising if it is assumed, as suggested in the previous chapter, that the maximum energy separation possible under any set of conditions is limited by the maximum sustainable temperature difference between the hot and cold flows. When $\mu_c = 0.5$ both streams offer the same heat capacity flux and exhibit a minimum overall temperature difference for any given heat exchange between the two.

Realisation

The simplest analytic form which meets the requirements is a quartic in μ_c,

$$q^* = \frac{q}{q_{max}} = 16\left(\mu_c^2 - 2\mu_c^3 + \mu_c^4\right), \tag{6.7}$$

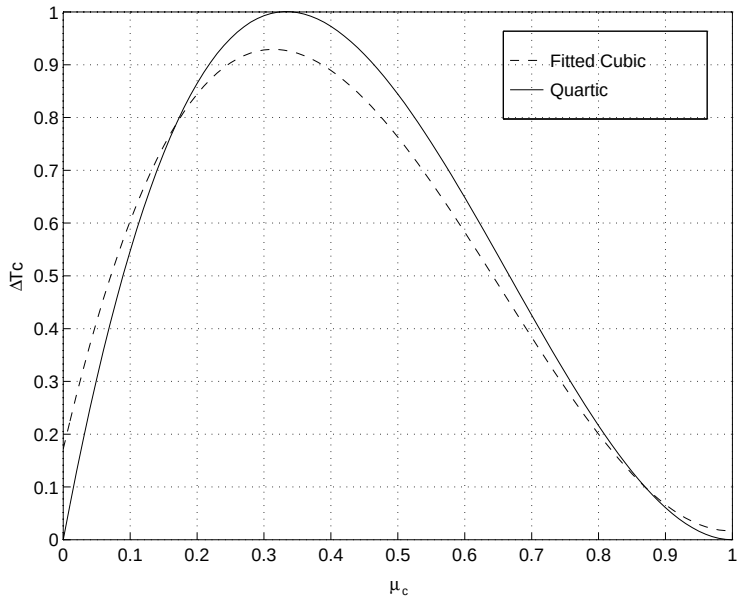

Figure 6.3: Comparison between the quartic relation plotted as ΔT_c against μ_c and Stephan's result. The solid line shows the new function, the dotted line shows a fitted cubic.

although this has the disadvantage of enforcing symmetry about $\mu_c = 0.5$. Figure 6.2 shows equation (6.7) along with a considerable number of data points taken from a number of vortex tubes operating at a wide variety of conditions. The comparison is quite good, and note also that no empirical fitting is required at this stage.

While there is room for improvement in the function, the correlation between the quartic and the data points appears to be better than that with an arbitrary cubic with constants determined by a least squares method. Comparison between the two functions is made in figure 6.3. An additional advantage of the new function is that it can represent data taken from a wide variety of tubes under different conditions, whereas an arbitrary function tends to be more specific to a particular tube.

6.7 The Influence of the Pressure Ratio

To assess the influence of pressure ratio on the value of the heat transfer q, we investigate how the 'separation potential' q_{max} might depend on pressure.

The assumption that the whole phenomenon can be characterised by the forced vortex formed near the inlet plane is very important here. Analysis begins with the 'simple radial equilibrium' expression (6.3), combined with the swirl velocity distribution in a forced vortex, relation (6.2) and the assumption that radial variations of the static temperature across the inlet plane are unimportant. Combining with the equation of state for an ideal gas and integrating radially outwards from the centre produces

$$\int_{P_{cl}}^{P} \frac{dP'}{P'} = \int_{0}^{r} \frac{\Omega^2 r'}{RT} dr' \tag{6.8}$$

where P_{cl} is the static pressure at the centre of the vortex tube.

It will be assumed that T may be replaced by some characteristic value T_* that is constant with respect to r. Performing the integration gives

$$\frac{P_{r_0}}{P_{cl}} = \exp\left(\frac{\Omega^2 r^2}{2RT_*}\right). \tag{6.9}$$

Near to the centre-line of the tube, the pressure is close to the value at the tube outlets, $P_{cl} \approx P_{outlet}$. This follows from the assumption that the most important feature of the flow is the swirl near the inlet, and that it is responsible for the major part of any pressure variations. The swirl velocity near the centre of the tube is very small, and thus it would be anticipated that the pressure there was dominated by other influences, and in particular linked with the axial velocity field. Since the axial velocity is generally fairly small, the pressure changes associated with it are relatively insignificant, and there is little pressure change along the axis of the vortex tube. The static pressure near the centre of the tube will be very close to that at the tube exit, therefore. This is especially the case in a counterflow tube, where an exit is positioned very close to the inlets.

Now consider relationship (6.9) applied near to the cylindrical wall of the vortex tube, where $r = r_0$ and $P = P_{r_0}$, in a region close to the tangential inlet nozzles. The pressure here will be closely related to the inlet pressure of the gas supplied to the tube, although the exact relationship will be complicated and heavily dependent both on the design of the inlet nozzles and the dynamics of the process by which the inlet gas mixes with the rotating vortex.

Some insight into the interdependence of the two quantities can be obtained from an approximate analysis. The relationship between the static pressure and the stagnation pressure at $r = r_0$ is the standard isentropic expression

$$\frac{P_{r_0}}{P_{stag}} = \left(1 + \frac{\gamma - 1}{2} M^2\right)^{\frac{\gamma}{1-\gamma}} . \tag{6.10}$$

As the radial and axial velocities are neglected in this analysis, the local Mach number is $M = \Omega r_0 / c$, where c is the local sound speed. Since a constant static temperature has been assumed across the vortex, an approximate expression for the sound speed is $c = \sqrt{\gamma R T_*}$. Eliminating Ωr_0 by rearranging equation (6.9), and then substituting for M gives

$$\frac{P_{stag}}{P_{cl}} = \frac{P_{r_0}}{P_{cl}} \cdot \left(1 + \frac{\gamma - 1}{\gamma}\, ln\left(\frac{P_{r_0}}{P_{cl}}\right)\right)^{\frac{\gamma}{\gamma-1}} . \tag{6.11}$$

The local stagnation pressure P_{stag} at the periphery of the vortex will be substantially less than the inlet (reservoir) pressure thanks to the lossy nature of the mixing process between the inlet flow and the gas already within the tube. Such losses are particularly difficult to model, but here we will assume that the loss is related to the difference between the inlet pressure and the local static pressure such that

$$P_{stag} = P_{inlet} - \beta \left(P_{inlet} - P_{r_0}\right) \tag{6.12}$$

where β is a loss coefficient, and thence the relationship between the inlet pressure and

the peripheral static pressure becomes

$$\frac{P_{inlet}}{P_{cl}} = \frac{P_{r_0}}{P_{cl}} \cdot \left\{ \left[1 + \frac{\gamma - 1}{\gamma} \, ln \left(\frac{P_{r_0}}{P_{cl}} \right) \right]^{\frac{\gamma}{\gamma - 1}} - \beta \right\} \cdot \frac{1}{1 - \beta}. \tag{6.13}$$

Generally, the inlet swirl velocity in the vortex tube is limited to approximately $M = 1$, dependent on the design of the nozzles. This seems sensible on physical grounds unless the nozzle has been specifically designed as a converging-diverging device. Ahlborn *et al.* [129] also suggest that the Mach number in the vortex tube is generally less than unity, on the basis of a number of experimental measurements.

In this case, the maximum value of the ratio P_{r_0}/P_{cl}, is limited to the value obtained when the inlet velocity is equal the speed of sound, that is $\Omega r_0 = c$. Thus for air at least using (6.9)

$$\left(\frac{P_{r_0}}{P_{cl}} \right)_{max} = e^{\frac{\gamma}{2}} \approx 2.01, \tag{6.14}$$

and interest should be concentrated on the behaviour of relationship (6.13) over the range $1 < \frac{P_{r_0}}{P_{cl}} < 2.01$, as illustrated in figure 6.4 for a range of values of the loss coefficient β from say 0 to 0.9. The curves are sufficiently flat that the relationship between P_{r_0} and P_{inlet} could be reasonably modelled as linear for the approximate purposes of this analysis.

We will write $P_{r_0} \sim P_{inlet}$, which will be a rough approximation[2] until the inlet nozzles begin to choke. At this point P_{r_0} would remain relatively constant, but in general vortex tubes operated at pressure ratios sufficiently large to produce choking will not be considered. Expression (6.9) now becomes

$$\frac{P_{inlet}}{P_{outlet}} \sim \exp \frac{\Omega^2 r_0^2}{2RT_*} \tag{6.15}$$

relating the pressure ratio applied across the tube to the strength of the forced vortex

[2]The symbol $\sim$ is used here in the sense of 'varies with'. That is the quantity on the left hand side of the expression varies with the quantity on the right hand in a way that could be very roughly approximated as linear. The quantities would also be expected to have similar magnitudes.

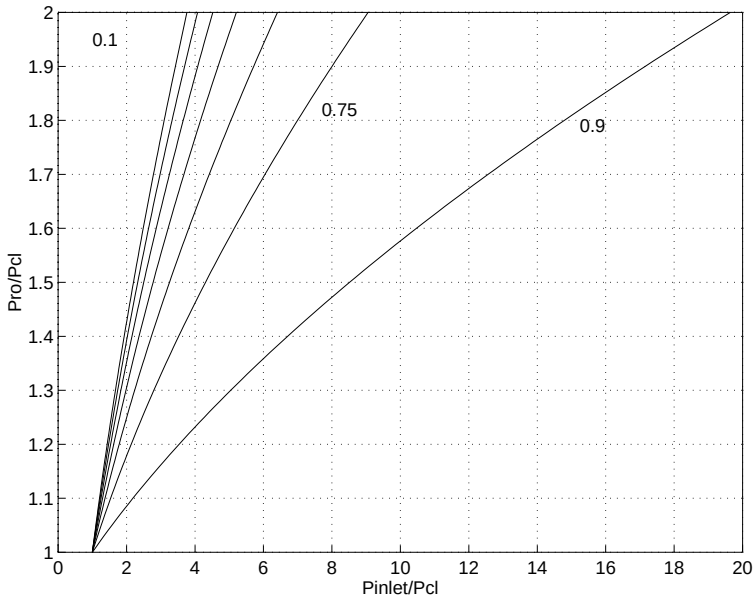

Figure 6.4: The dependence of the pressure at $r = r_0$ on the inlet stagnation pressure. The curves represent a range of values of β from 0.1 to 0.9. The figures adjacent to the curves give particular values.

formed near the inlets.

One of the initial assumptions was that the swirl, as characterised by the angular velocity of the forced vortex formed near the inlet plane, is directly responsible for the energy separation. As such, it is directly connected with the 'separation potential' of the vortex tube represented by q_{max}. The actual relationship between the separation potential and the initial vortex is complex. From dimensional considerations we shall write $q_{max} \sim \Omega^2/2$ on the basis that both quantities represent an energy (flux) per heat capacity flux, $\dot{m}c_p$.

Re-arranging equation (6.15), our expression for the influence of the applied pressure ratio on the separation potential is

$$q_{max} \sim \frac{RT_*}{r_0^2}\ ln\left(\frac{P_{inlet}}{P_{outlet}}\right). \tag{6.16}$$

Clearly this is far from an exact relationship; however it would be hoped that it repres-

ents the form of the dependence.

Empiricism is necessary to deduce a numerical value for q_{max} from the pressure ratio. Write the previous expression as an equality

$$q_{max} = k \cdot \frac{T_{inlet}}{T_{ref}} \cdot ln\left(\frac{P_{inlet}}{P_{outlet}}\right) \tag{6.17}$$

where k is a constant that represents how well the potential of the pressure difference is converted into a temperature separation, evaluated at inlet temperature T_{ref} for a particular tube. The arbitrary inlet plane temperature T_* has been replaced by the inlet (reservoir) temperature of the gas T_{inlet}. Under the assumptions here, the two can be related by means of energy conservation. Neglecting the effects of the axial velocity distribution in the tube and taking T_* as the mass averaged temperature across the radius gives

$$T_* = T_{inlet} - \frac{\Omega^2 r_0^2}{2c_p} \cdot \frac{r_0^2 e^{r_0^2} - e^{r_0^2} + 1}{e^{r_0^2} - 1}. \tag{6.18}$$

Substituting for $\Omega^2 r_0^2$ using equation (6.9) applied at $r = r_0$, the relation is

$$T_* = \frac{T_{inlet}}{1 + \frac{\gamma-1}{\gamma} ln\left(\frac{P_{r_0}}{P_{cl}}\right) f\left(r_0^2\right)} \tag{6.19}$$

where

$$f\left(r_0^2\right) = \frac{r_0^2 e^{r_0^2} - e^{r_0^2} + 1}{r_0^2\left(e^{r_0^2} - 1\right)}. \tag{6.20}$$

As figure 6.5 shows, the pressure ratio P_{r_0}/P_{cl} has a significant, but fairly small influence on the value of T_*/T_{inlet}. While it would be fairly straightforward to model the effect of the pressure ratio on T_*/T_{inlet} using a scheme of the form

$$\frac{T_*}{T_{inlet}} = 1 - (constant)\, ln\left(\frac{P_{r_0}}{P_{cl}}\right), \tag{6.21}$$

in view of its fairly small influence, which is in any case only large when the tube approaches choking, the intentionally vague definition of T_*, and the considerable approx-

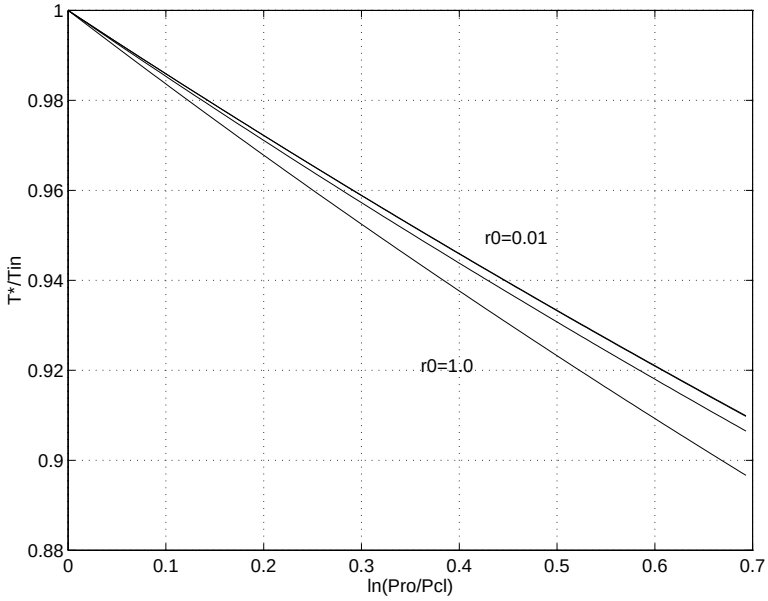

Figure 6.5: The dependence of T_*/T_{inlet} on the pressure ratio P_{r_0}/P_{cl} over the range of interest from 1 to 2 and the tube radius r_0. The upper line was calculated for $r_0 = 0.01$ m, the lower $r_0 = 1$ m and the intermediate line for 0.1 m.

imations already made, the simple approximation

$$T_* \sim T_{inlet} \tag{6.22}$$

will not introduce great errors. This also provides consistency with expression (6.5).

The 'tube constant' k is determined by plotting values of q_{max} against $ln\left(\frac{P_{inlet}}{P_{outlet}}\right)$, and calculating the gradient of the best fitting straight line. This has been done for six tubes in figure 6.6, where the fit of the straight lines is generally quite good.

The relationship is only valid so long as the inlet nozzles remain unchoked. If choking occurs, then in general the value of q_{max} will no longer be influenced by further increases in the applied pressure ratio. As noted already, supersonic flow does not appear to exist within the body of conventional vortex tubes, and hence any increase in reservoir pressure beyond that required for choking cannot influence the flow within the tube. If supersonic flow is achieved within the nozzles, it must be returned to a subsonic flow by

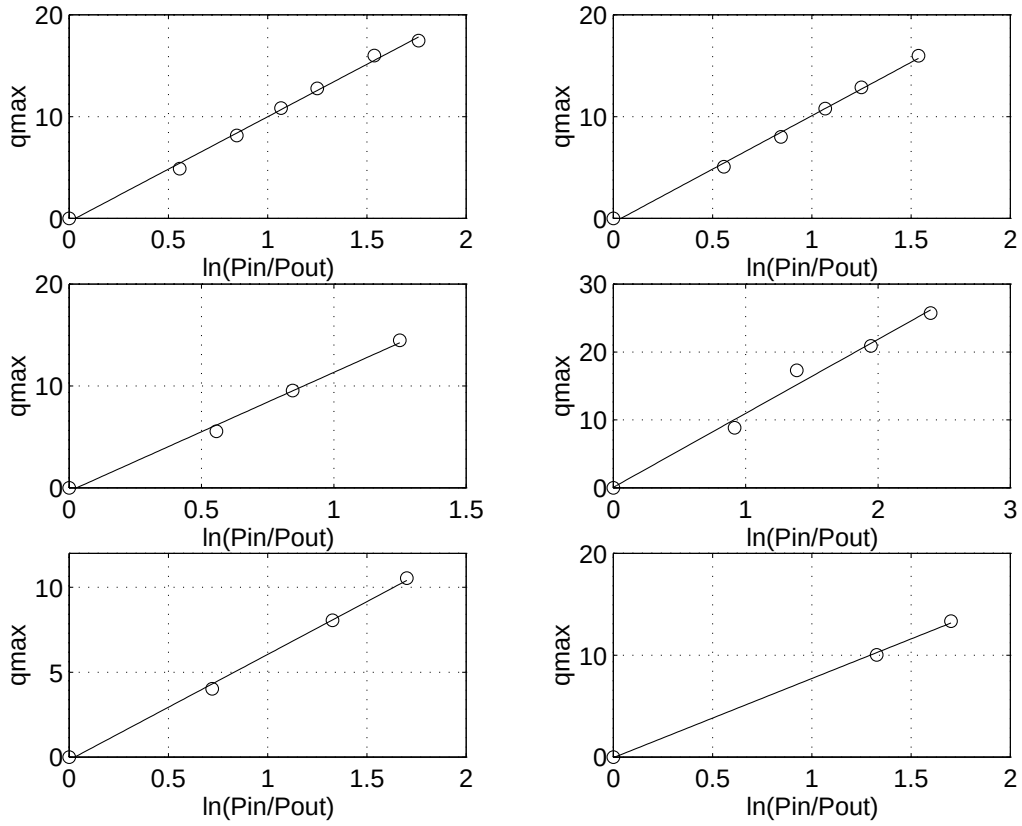

Figure 6.6: Evaluation of the tube constant for six tubes, with the solid line representing the fitted line, and the circles the raw data points. The data employed was sourced as follows, starting from the top left and then moving across in sequence : (1) Stephan's [108] 17.6 mm diameter tube operated on air, (2) Stephan's tube operated on oxygen, (3) Stephan's tube operated on helium, (4) Hilsch's [4] 8.2 mm diameter tube with 2.6 mm diameter orifice as portrayed in his figure 2, (5) 26 mm diameter CUED tube operated on a single nozzle with a 7.5 mm orifice, (6) 18 mm diameter CUED tube operated on two nozzles with a 7 mm diameter orifice.

the action of irreversible processes either within the nozzle itself, or as part of the mechanism by which the inlet flow mixes with gas already in the vortex tube.

It would be possible to include the choking process explicitly within the model by allowing k to be a function of the applied pressure ratio, and fitting a more complex expression to the data points of figure 6.6. This, however, has the disadvantage of blurring the interpretation of k as a figure of merit for a vortex tube. In any case it is wasteful to operate a vortex tube such that the nozzles are choked. It would be more effective to divide the separation potential between two unchoked tubes connected in series. Modelling of the performance near to choking is not important, therefore. The onset of choking may as well be considered as a 'cut off' pressure ratio, beyond which a tube should not be operated.

By comparison of equations (6.16) and (6.17)

$$\frac{k}{T_{ref}} \sim \frac{R}{r_0^2}, \tag{6.23}$$

suggesting that tube constants of otherwise similar tubes should be inversely proportional to the square of their radii. The data presented in figure 6.6 has not been taken from similar tubes, so comparison is difficult. Examination at least shows that the smallest diameter tube, that employed by Hilsch, has the largest tube constant, whereas the largest tube, the 26 mm diameter CUED tube has the smallest constant.

6.8 The Final Relationship

As long as the tube is not choked, the semi-empirical model of vortex tube performance can be summarised with the two equations

$$q_{max} = k \cdot \frac{T_{inlet}}{T_{ref}} \cdot ln\left(\frac{P_{inlet}}{P_{outlet}}\right) \tag{6.24}$$

$$q = q_{max} \cdot 16\left(\mu_c^2 - 2\mu_c^2 + \mu_c^4\right) \tag{6.25}$$

where $q = \mu_c \Delta T_c$ and $q_{max} = max\,(\mu_c \Delta T_c)$. The 'tube constant' k is an empirically determined value that constitutes an order of merit figure for a particular vortex tube installation, representing how effectively a vortex tube utilises the separation potential of compressed air supplied to it. If choking does occur then the performance as represented by q_{max} may be considered as constant with respect to pressure ratio, keeping the value attained when choking occured.

6.9 Departures from Ideality

6.9.1 Departures from the Form of $f_2\,(\mu_c)$

For some data available in the literature, the variation of q with μ_c slightly departs from the analytic form of $f_2\,(\mu_c)$ suggested above. The discrepancies are most obvious in, for example, Hilsch's data at low pressure ratios, with the maximum value occuring between $\mu_c = 0.5$ and $\mu_c = 0.6$. No such anomalies are visible in data from the CUED tubes.

Two facts might account for the differences between the approximate analytic function and some of the data. The CUED tubes were well insulated from their surroundings and produced relatively small temperature differences. As such they were not prone to external heat transfer. Hilsch's tubes by contrast, produced large temperature differences, and do not appear to have been insulated.

At low cold mass flow fractions, there are relatively small quantities of very cold gas gas leaving through the cold exit. Under these conditions, the cold flow would be particularly susceptible to external heat transfer while travelling through the cold tube, which would tend to reduce the measured cold temperature drop ΔT_c and hence the estimated heat transfer q. This would 'skew' the curve of q against μ_c, moving the peak in the direction of increasing μ_c.

At high values of cold mass flow fraction, say $\mu_c > 0.7$, gas from the outer regions of the vortex would be included within the cold flow. Gas near to the periphery of the vortex, since it is above ambient temperature, would be subject to some external cooling.

This would tend to reduce the measured values of ΔT_c and q at high values of μ_c, skewing the curve peak further still towards increased μ_c.

Thus it might be expected that Hilsch's poorly insulated tubes would produce curves with peaks at higher values of μ_c than the well insulated CUED tubes. This does indeed seem to be the case.

A second fact explaining discrepancies in general might be the interdependency of μ_c and the separation potential found in real tubes. The analysis has assumed that the thermal separation effect is directly related to the strength of the inlet swirl, which is in turn dependent on the overall pressure ratio P_{inlet}/P_{outlet}. In fact, the swirl strength will depend on the ratio of the inlet pressure to some 'internal pressure' near the inlet plane, which will be termed P_t. No attempt will be made to evaluate P_t, but note that it essentially represents the pressure required to drive the swirling gas axially along the vortex tube.

Most vortex tubes, employing a valve to regulate the relative amounts of hot and cold flow, effectively vary the cold mass flow fraction by using the valve to vary the internal pressure P_t. There will a weak relationship between the thermal separation potential of the apparatus and the cold mass flow fraction μ_c, although its nature is very difficult to predict.

It would be possible to accommodate such non-ideal behaviour with a more complex function for $f_c(\mu_c)$. A number were tried, including higher order polynomials, and Gaussian functions. None gave a noticeably better fit than the quartic, and all lost its attractive features of generality and good analytic behaviour.

6.9.2 Non-Conformance to Variation of Performance with Pressure Ratio

In general the dependence of vortex tube performance on the pressure ratio P_{in}/P_{out} follows the anticipated form very well. Care must be taken, however, in specification of the inlet pressure where there might be losses between the reservoir/air supply and the in-

lets to the tube. If the losses are substantial, then the inlet pressure should be measured close to the inlet nozzles.

For the CUED vortex tubes, the pressure in the receiving tank of the compressor was taken to represent the inlet pressure for some measurements. For certain configurations, the results did not correspond well with the expected form. The dependence of q_{max} on $ln\left(P_{inlet}/P_{outlet}\right)$ appeared linear, but the fitted line did not pass through the origin. It was found that subtracting a constant value from the reservoir pressure, that is writing $P_{inlet} = P_{reservoir} - constant$, restored the relationship to that expected.

Interestingly, the constant value was the same from case to case, and approximately equal to the difference between the reservoir pressure, and the reading of a pressure gauge incorporated in the supply very close to the inlets. It was deduced therefore that pressure losses in the supply were responsible for the departure from the expected behaviour.

Chapter 7

Applications of the Ranque-Hilsch Tube

7.1 Overview

The Ranque-Hilsch vortex tube has certain intrinsic features that make it attractive for industrial applications. Particularly enticing are its high reliability thanks to the absence of any moving parts, and its inherent safety as a result of there being no requirement for external power in the form of electricity or flames. These features suggest potential for employment in safety-critical environments or in situations where maintenance is difficult. As pointed out by Bull [130], process equipment in nuclear reactors often has to meet both criteria simultaneously.

This chapter considers the potential of the vortex tube to perform thermal tasks and physical separations. In a study of this size it is practical neither to design specific applications in detail nor to provide a comprehensive review of areas likely to benefit from the vortex tube. Instead, after a brief consideration of the wider potential, attention will be focussed on two aspects. Firstly schemes to liquefy gases using vortex tubes will be examined. Secondly, there will be some consideration of the isotopic separation produced by the tube, and its potential compared to existing techniques in the nuclear industry.

7.2 Simple Heating and Cooling Applications

7.2.1 Thermal Capabilities

Thermal Power

Any thermal application of the vortex tube will be influenced primarily by the heating and cooling power available from the device. Estimating the mass flow rate for the 18 mm diameter CUED vortex tube gives a rate of energy transfer from the cold stream to the hot stream at around 300 watts. This power level is available simultaneously both in the cold stream to cool a heat sink at ambient temperature, and in the hot stream to warm a heat sink at ambient temperature. Commercially available vortex tubes from the Vortec Corp. [79] have thermal powers cited as ranging from 2.9 watts to 1764 watts.

Refrigeration Performance

Performance of simple refrigeration plant is usually characterised by means of the Coefficient of Performance (C.O.P.) defined for the cyclic work-absorbing device of figure 7.1 as

$$COP = \frac{Q_A}{W}. \tag{7.1}$$

To evaluate the vortex tube as a refrigerator in this manner, it is necessary to devise a quasi-cyclic system to analyse, such as that shown in figure 7.2.

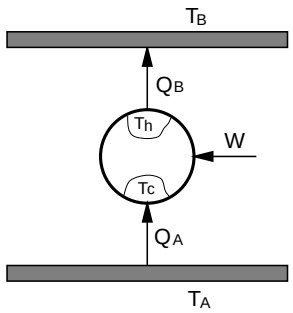

Figure 7.1: A cyclic work absorbing device.

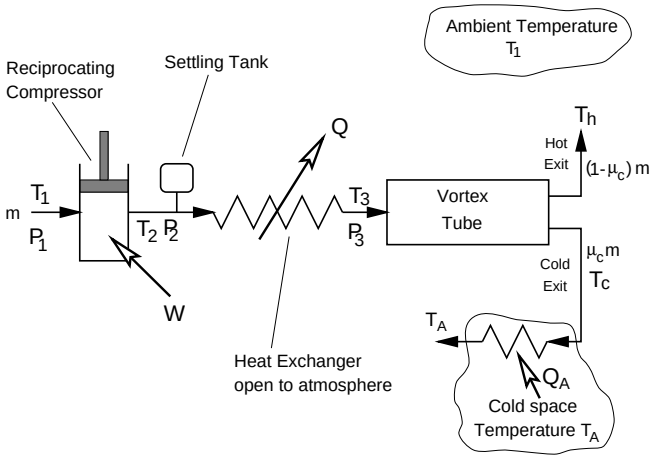

Figure 7.2: Quasi-cyclic vortex tube refrigeration plant.

Assuming the isentropic efficiency of the compressor to be η_{is}, and that the plant operates on a perfect gas with constant pressure heat capacity c_p, the work input to the system is

$$W = \dot{m} c_p \left\{ \frac{T_1}{\eta_{is}} \left[\left(\frac{P_2}{P_1} \right)^{\frac{\gamma-1}{\gamma}} - 1 \right] \right\}. \tag{7.2}$$

If the cold space has temperature T_A, the heat absorbed by the plant is

$$Q_A = \mu_c \dot{m} c_p \left(T_A - T_C \right) = \mu_c \dot{m} c_p \left(T_A - [T_1 - \Delta T_c] \right). \tag{7.3}$$

Neglecting the pressure drop across the heat-exchanger and assuming $T_3 = T_1$, gives

$$COP = \frac{\mu_c \left(\Delta T_c - [T_1 - T_A] \right)}{\frac{T_1}{\eta_{is}} \left[\left(\frac{P_2}{P_1} \right)^{\frac{\gamma-1}{\gamma}} - 1 \right]}. \tag{7.4}$$

Inserting some typical values for a domestic refrigerator, say $\eta_{is} = 0.7$, $T_A = 278$ K, taking the ambient temperature to be equal to that of the hot space such that $T_1 = T_B = 293$ K, specifying the operating point of the vortex tube as $\Delta T_c = 35$ K, $\mu_c = 0.7$, $P_2/P_1 = 3.5$, and assuming an air operated plant with $\gamma = 1.4$, gives $COP = 0.08$. Comparing this to the ideal COP of 18.5 achieved by a reversed Carnot Cycle machine under the same

conditions shows just how poorly the vortex tube performs as a refrigerator. While the performance of the scheme could be improved through careful selection of the working fluid, it is unlikely that performance levels associated with conventional processes could even be approached.

7.2.2 Applications

The thermal separation provided by the vortex tube finds ready application where there are modest heating or cooling requirements. Although the efficiency of the device is poor compared to conventional techniques[1], its low capital cost can offset this. It is particularly useful where there is a ready supply of compressed gas, as in these circumstances the heating or cooling required can be obtained almost for free. Suggestions have included correcting for the aerodynamic heating experienced by thermometers in high speed aircraft (Vonnegut, [131]), cooling sensitive materials undergoing machining operations (Vortec Corp. [79]), cooling experiments in laboratories dealing with explosive chemicals (Bruno, [132]), use in conjunction with thermocouples to improve the performance of a Peltier refrigerator (Landecker [133]) and temperature control of divers' air supplies (Baz *et al.* [134]), manned underwater habitats (Baz *et al.* [135]) and hyperbaric chambers (Baz *et al.* [136]).

7.3 Gas Liquefaction

7.3.1 Principles of Liquefaction

The fundamental principle underlying all gas liquefaction techniques is to extract heat from the gas in such a way as to bring its thermodynamic state into the saturation region of the enthalpy-entropy plane (Mollier diagram). For gases with comparatively high boiling points, such as the alkane series of hydrocarbons, the heat removal can be ac-

[1] A typical refrigerator has a C.O.P around 3.

complished by a cascade of conventional refrigeration circuits. Other gases with boiling points lying below that of methane[2], in what we will term the cryogenic range after Haywood [137], are conventionally liquefied through the cooling induced by some form of expansion process originating at high pressure.

As noted already, the Ranque-Hilsch tube makes a poor substitute for a conventional refrigerator, and is unlikely to perform well in liquefaction plant based around such schemes. Attention will be focussed, therefore, on the application of the vortex tube as an expansion engine in plant of the cryogenic design. Quantitative results will be presented on the assumption that air is the working fluid, although the qualitative conclusions will apply to any gas including those that liquefy outside the cryogenic range.

The simplest cryogenic plant is the Linde process shown schematically in figure 7.3. A reciprocating compressor produces a driving pressure of perhaps 20 MPa. The com-

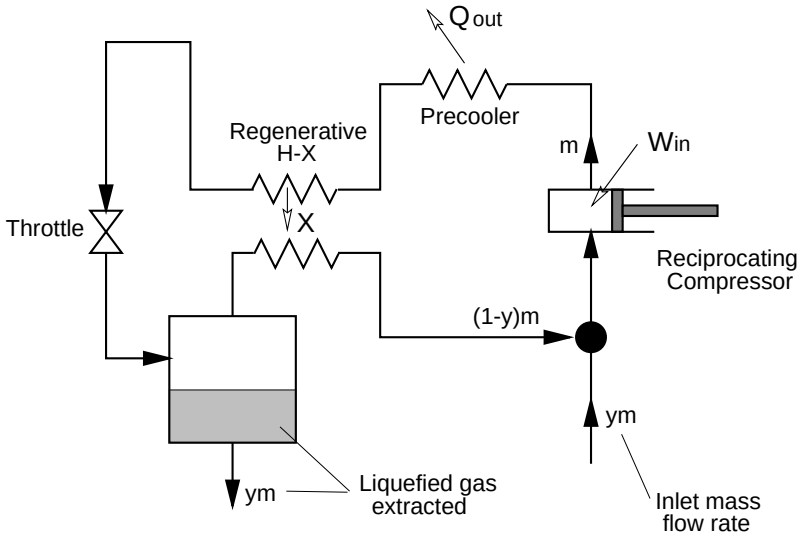

Figure 7.3: Schematic of the Linde process.

pressed gas is cooled to near ambient temperature in the pre-cooler, and then passes through a regenerative heat exchanger which separates the high and low temperature

[2]110 K at atmospheric pressure.

regions of the plant. On reaching the throttle the gas expands and undergoes a temperature change by virtue of its departure from ideal behaviour, as represented by the isenthalpic Joule-Thomson coefficient

$$\mu_h = \left(\frac{\partial T}{\partial P}\right)_h . \tag{7.5}$$

The Joule-Thomson coefficient is a function of temperature and pressure, and must be positive for a drop in temperature to occur here. Under usual conditions this requirement is satisfied by air. Matters are different for helium and hydrogen plant, where the gas must be pre-cooled by an external refrigerator before liquefaction through throttle expansion is possible.

More sophisticated liquefaction schemes are represented by the Claude and Heylandt processes which seek to improve the expansion cooling process. Partially replacing the throttle expansion with a preceding resisted expansion increases the temperature drop by removing energy in the form of work from the gas. As an added bonus that work can be put to some use, such as helping to drive the compressor.

7.3.2 Liquefaction in the Vortex Tube

The simplest application of the vortex tube to gas liquefaction would be as a supplement to the throttle cooling of the Linde process, as suggested in figure 7.4. Effectively the vortex tube would then be employed as an expansion engine extracting work from the gas, much as in the Claude and Heylandt processes. Unlike those processes however, the work would be done by one portion of the flow on the other portion, the work receiving portion being subsequently separated off.

Inclusion of a vortex tube in the Linde process could have a number of advantages. Most notable is that all gases would effectively have an 'artificially enhanced' isenthalpic Joule-Thomson coefficient. Expansion would automatically give a cooling effect, and thence any pre-cooling system would be rendered unnecessary. This saving would have

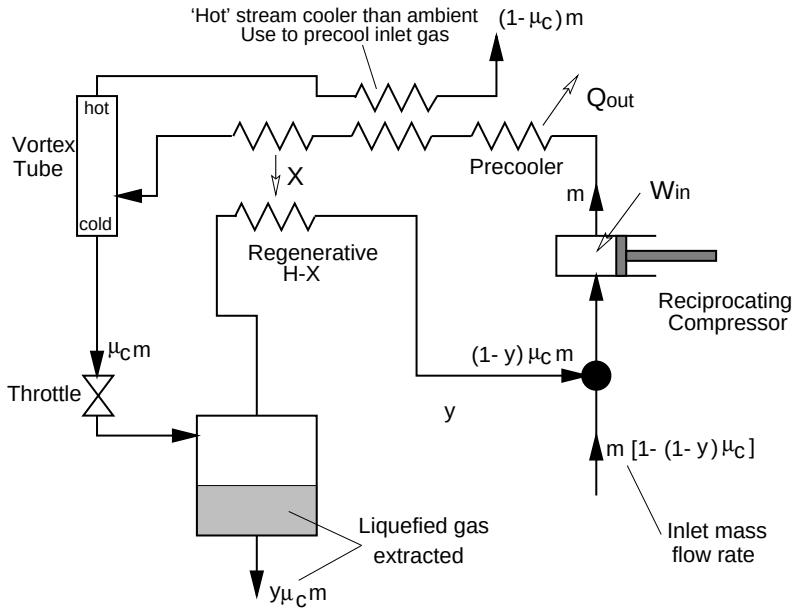

Figure 7.4: Linde-type gas liquefaction process incorporating a vortex tube.

to be offset against the reduction in yield produced by venting off a substantial proportion of the inlet flow.

It is quite possible that the throttle could be entirely replaced by a vortex tube. In the Claude and Heylandt processes, care has to be taken to avoid condensation within the expansion engine, and the final cooling stage is always a throttle. Such precautions are not necessary with the vortex tube, which can quite happily cool saturated gases. That gas liquefaction is possible in Ranque-Hilsch tubes has been demonstrated by Fin'ko [138] who operated a counterflow vortex tube on air pre-cooled with liquid nitrogen. His experiments found liquid air running from the cold outlet, although the two-phase nature of the flow seemed to degrade performance.

Reference to the empirical model developed in the last chapter shows that the thermal separation performance of the vortex tube varies as the logarithm of the applied pressure ratio. Thus, a greater temperature difference can be obtained from a given pressure difference by expanding the gas through a large number of vortex tubes rather then a single tube, although at the expense of a reduced outlet mass flow rate. While in prac-

tice there would be a limit to the process, as a certain minimum pressure ratio is required to produce the flow regimes that provide useful separation, at the kind of pressure differences typically employed in liquefaction plant expanding the gas through a series of many vortex tubes would give a cooler outlet flow than 'blowing' the pressure available on a single expansion.

With such a vortex tube cascade the yield of the plant, measured as a proportion of the inlet mass flow rate would be drastically reduced. It should be noted though, that many of the 'hot streams' leaving the lower tubes in the cascade would be cooler than the ambient temperature and could perhaps be 'recycled' in an attempt to improve the yield. Careful analysis is necessary to determine the practicality of any such scheme, and the next section presents performance calculations of three possible arrangements.

7.4 Vortex Tube Cascades for Liquefaction

7.4.1 General Principles

Modelling the Vortex Tube

For the purposes of this pilot study, the characteristics of vortex tube performance can be estimated well enough by the empirical model developed in the previous chapter. No account was taken there of the degradation of separation performance found in two phase flows. Scant data makes an empirical analysis impractical, so we will assume here that temperature separation performance declines linearly to zero as the inlet wetness fraction, χ, approaches unity so that the specific heat transfer is given by

$$q = q_{max} \cdot f_2(\mu_c) \cdot (1 - \chi). \tag{7.6}$$

In gas liquefaction calculations it is more convenient to measure the heat removed from the cooled gas rather than the temperature change. The model will be reformulated in terms of the specific enthalpy change experienced by a perfect gas passing from the

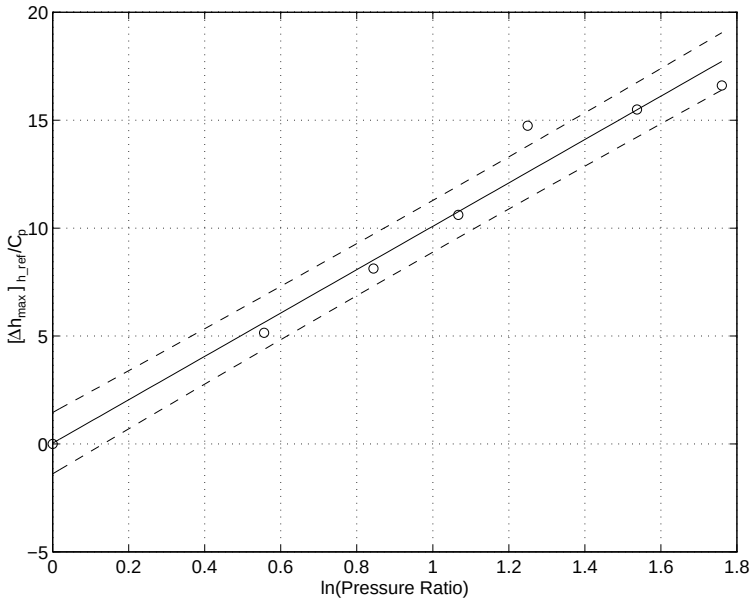

Figure 7.5: Evaluation of the characteristic tube constant k for Stephan's [110] tube operated on air. The raw data are shown as circles, the mean fitted line in solid, and 50 percent error bounds as solid lines.

inlet to the cold outlet by writing

$$\Delta h_c = \frac{Q}{\mu_c \dot{m}} = \frac{c_p q}{\mu_c} \tag{7.7}$$

with Q representing the overall energy transfer between the two streams and $\dot{m}$ the inlet mass flow rate.

Thus the model employed can be written as

$$\Delta h_c = \Phi h_{in} \left(1 - \chi\right) \tag{7.8}$$

where

$$\Phi = \frac{f_2\left(\mu_c\right)}{\mu_c} \cdot \frac{k}{T_{ref}} \cdot ln\left(\frac{P_{inlet}}{P_{outlet}}\right). \tag{7.9}$$

with $f_2(\mu_c)$ as defined in the previous chapter, and k a constant characteristic of the vortex tube.

The calculations that follow will assume a vortex tube with performance characteristics similar to that investigated by Stephan [110], which has a tube constant $k = 10.05$ for air. The fitted straight line and raw data used to obtain this value are shown in figure 7.5. Since the the data shows evidence of the inlet flow becoming choked for pressure ratios greater than 5, the energy separation performance will be assumed to saturate for such pressure ratios.

Modelling Assumptions

Analysis will be confined to cascades consisting of arrays of identical vortex tubes. All the tubes will be assumed to operate at the same cold mass flow fraction, and with the same inlet mass flow rate. In the two cascades where the overall mass flow rate declines as the gas passes 'down' the cascade this latter assumption could be met by a tree arrangement as shown in figure 7.6. Thus the first stage of cooling would involve many

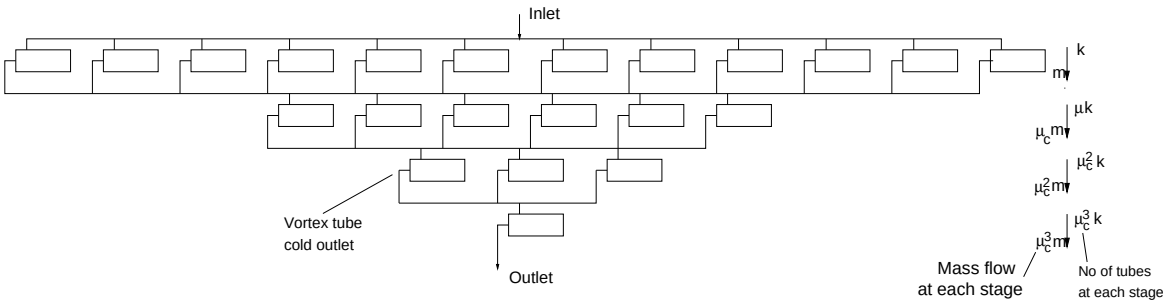

Figure 7.6: The shape of a vortex tube cascade.

vortex tubes operating in parallel, whereas the final stage would employ only a single tube.

Under these circumstances all the tubes in the cascade would operate at identical pressure ratios. Given the assumed similarity of all the flows in the tubes, we would expect the inlet swirl Mach numbers M_{sw} to be identical. The outline model of tube performance based on a forced vortex discussed in section 6.7 shows, with equation (6.15),

that

$$\frac{P_{inlet}}{P_{outlet}} \sim \exp \frac{\Omega^2 r_o^2}{2RT_*}. \tag{7.10}$$

Noting that Ωr_0 is the inlet swirl velocity, and subject to the limitations of section 6.7 the sonic velocity at inlet is $c = \sqrt{\gamma RT_*}$ then

$$\frac{P_{in}}{P_{out}} \sim e^{M_{sw}^2 \gamma} \tag{7.11}$$

confirming the consistency of pressure ratio.

Certain cascades will incorporate heat exchangers. Modelling will assume unity effectiveness[3], and neglect the pressure drop required to force the gas through them.

Methodology

All possible cascades can be considered globally to have an inlet flow, a desired outlet flow and a number of waste outlet flows as illustrated by figure 7.7. The overall mass and enthalpy flux balances are respectively

$$\dot{m}_{in} = \sum_i \dot{m}_{waste,i} + \dot{m}_{out} \tag{7.12}$$

$$\dot{m}_{in} h_{in} = \sum_i \dot{m}_{waste,i} h_{waste,i} + \dot{m}_{out} h_{out}. \tag{7.13}$$

In cascades without recycling these relations combined with the vortex tube model are sufficient to solve the cascade. With recycling, the overall balances must be solved simultaneously with balances written for each stage. The particular method of solution depends on the cascade, but in general it is possible to derive a recurrence relationship between the conditions at adjacent stages and thence solve the overall balances.

[3]The effectiveness of a heat exchanger is defined as the ratio of the actual heat transfer achieved between the streams, to the maximum possible heat transfer.

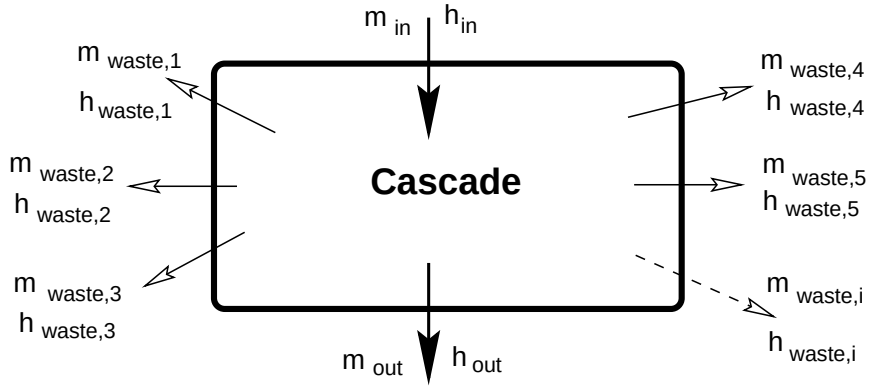

Figure 7.7: Enthalpy and mass fluxes entering and leaving a cascade.

Optimisation Criterion

We are interested in the performance of the cascades as gas liquefiers. The outlet flow in diagram 7.7 could be considered as saturated with a wetness fraction χ_{out}. If the condensed portion of the efflux has a specific enthalpy h_f and the gaseous portion h_g then the outlet flow has enthalpy

$$h_{out} = \chi_{out} h_f + (1 - \chi_{out})\, h_g. \tag{7.14}$$

The overall enthalpy balance gives the rate of production of liquid gas as

$$\chi_{out}\dot{m}_{out} = \frac{\dot{m}_{in}\,(h_{in} - h_g) - \sum_i m_{waste,i} h_{waste,i} + h_g \sum_i m_{waste,i}}{h_f - h_g}, \tag{7.15}$$

which should be maximised for optimal performance.

Cascades with the fewest numbers of stages give the greatest outlet mass flow rate. It would be anticipated therefore that best liquefaction performance would be obtained from those cascades that employ the least number of stages in order to reach liquefaction. In other words adding extra stages to a cascade that already produces liquefied gas would result in a decreased performance. The increased wetness fraction resulting from the greater enthalpy removal would most likely be more than offset by the reduction in

overall mass flow rate.

7.4.2 Simple Cascade

The simplest possible cascade design is to connect the cold outlet of one vortex tube to the inlet of the next and vent the hot outlets away. Figure 7.8 shows the arrangement diagrammatically.

For a cascade with N stages the relationship between the inlet and outlet mass flows is given by

$$\frac{\dot{m}_{in}}{\dot{m}_{out}} = \mu_c^N . \tag{7.16}$$

The overall cascade pressure ratio can be calculated from

$$\left(\frac{P_{in}}{P_{out}}\right)_{cascade} = \left[\left(\frac{P_{in}}{P_{out}}\right)_{stage}\right]^N \tag{7.17}$$

which can be inverted to calculate the stage pressure ratio given an available driving pressure. Calculation of the outlet enthalpy shows

$$\begin{aligned} \frac{h_{out}}{h_{in}} \quad = \quad & [1 - \Phi\,(1 - \chi_1)] \times \quad [1 - \Phi\,(1 - \chi_2)] \times \ldots \\ & \times [1 - \Phi\,(1 - \chi_i)] \times \ldots \times [1 - \Phi\,(1 - \chi_N)] \end{aligned} \tag{7.18}$$

although for a cascade that just gives liquefaction all the χ_i will be zero.

Figure 7.9 shows a series of 'design' curves for the simple cascade, giving the lowest achievable outlet enthalpy as a function the available pressure ratio and the number of stages in the cascade. At atmospheric pressure, saturated air vapour has a specific enthalpy of 205.4 kJ/kg (see Haywood [139]). Assuming an inlet temperature of 298 K, and an outlet pressure of atmospheric any cascade producing liquid gas must give a ratio of outlet to inlet enthalpies of approximately 0.26. The design curves show that this is not reasonably attainable from a simple cascade. The ratio of the outlet and inlet mass flow rates for a cascade operating at the minimum enthalpy ratio is shown in figure 7.10.

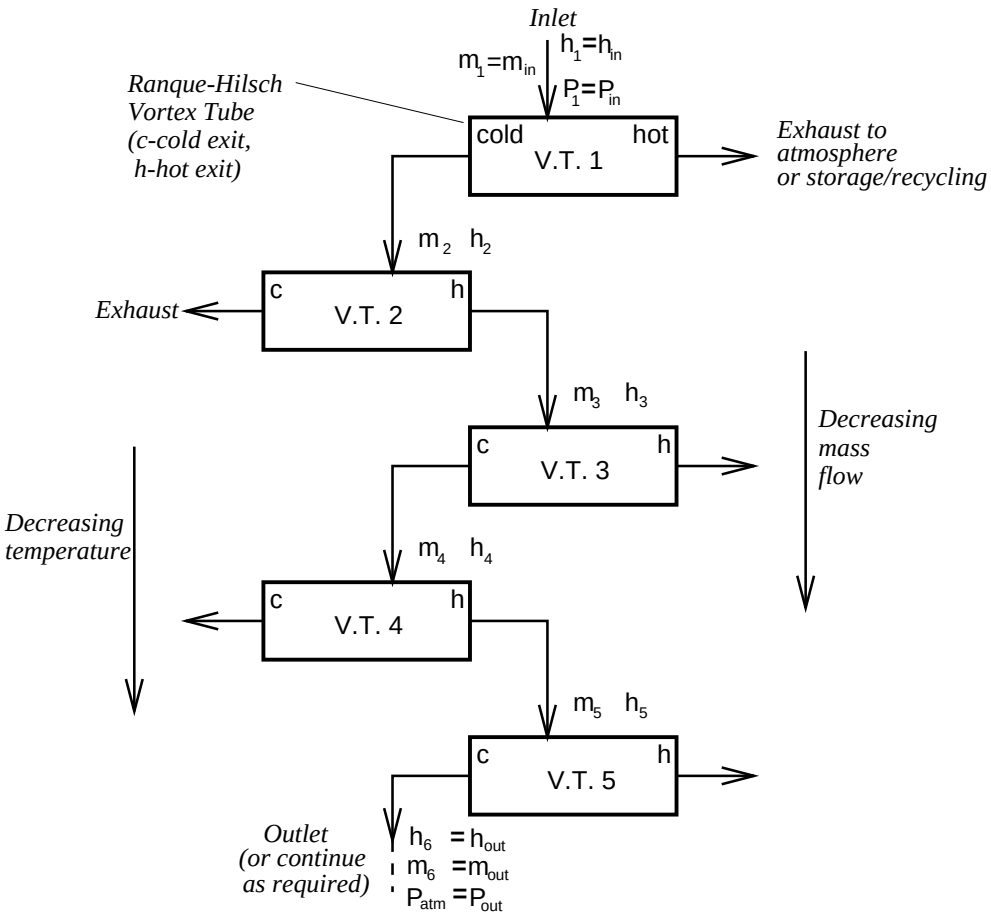

Figure 7.8: The simple cascade.

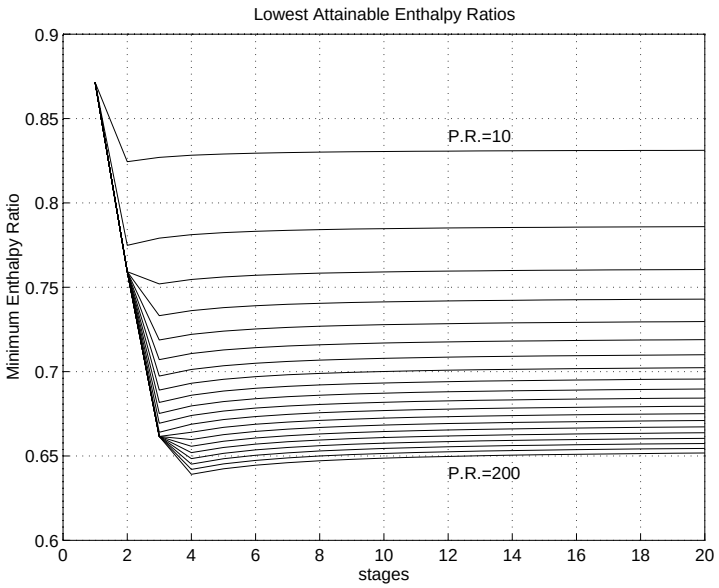

Figure 7.9: Design curves for the simple cascade. The solid lines give the minimum ratio of outlet enthalpy to inlet enthalpy as a function of the number of stages in the cascade, and the overall pressure ratio. The upper curve represents an overall ratio of 10, the lowest curve a ratio of 200. Other lines represent increments of 10 in the pressure ratio.

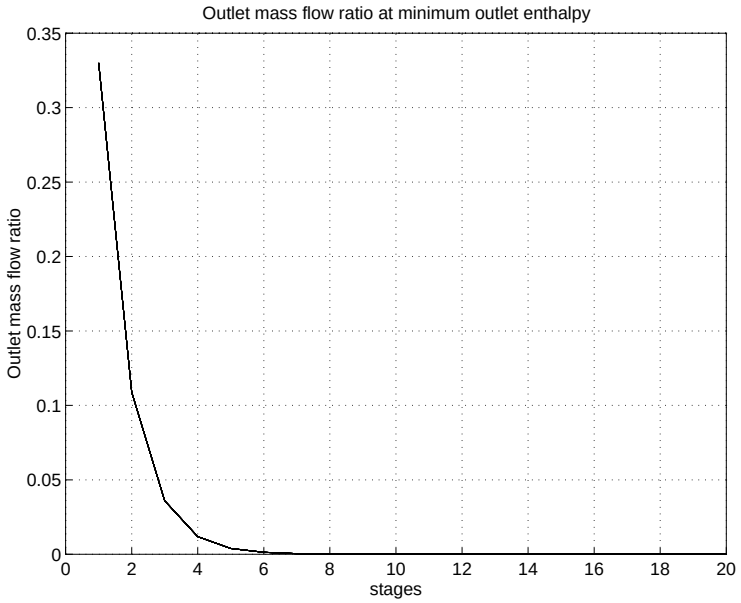

Figure 7.10: The ratio of outlet mass flow to inlet mass flow for a simple cascade operating at the minimum outlet enthalpy ratio, as a function of the number of stages. The relationship is independent of the pressure ratio.

As anticipated, the cascades give poor outlet enthalpies when few stages are present. In such cases the stage pressure ratios are very high and the vortex tubes saturate. An unexpected result is the rise in outlet enthalpy ratio at large stage numbers. When the number of stages is raised, the stage pressure ratio decreases along with the performance of each stage. We might expect the small decrease in stage performance to be offset by the additional thermal separation provided by the extra stages. The addition of extra stages, however, has the effect that more heat extraction is taking place at a lower temperature than without them. This destroys any advantage conferred by the extra stage, leading to a rise in outlet enthalpy with an increasing number of stages.

7.4.3 First Reflux Cascade

The simple cascade is wasteful in as much as some of the hot streams have a cooling potential compared to ambient conditions. Figure 7.11 represents an attempt to improve the performance by mixing hot flows with the inlet to the previous stage. The mixed flows should have similar enthalpies as the path from any inlet flow to the hot exit of the next stage represents one cooling and one heating.

The hot outlet from the first tube is not used as it has no direct cooling capacity[4]. The hot outlet of the second tube is also vented to the atmosphere as it is not significantly cooler than the flow it would be mixed with. Under certain conditions it can in fact be warmer than the flow it would mix with. Moreover it will be implicitly assumed in the following analysis that all mixing occurs with both streams at the same pressure. This could only be achieved by partially re-compressing the hot outlet flows. Any such compression is not likely to be isentropic and thence would reduce still further any cooling potential in the hot stream of the second stage. With this one exception, no account will

[4]It would be possible to expand the hot flow through further expansion engines and thereby produce some cooling. However this possibility will not be considered here as were vortex tubes employed at least three further stages of expansion would be needed to give useful cooling. With the numbers of stages employed here the additional cooling this could provide would be very small. In a cascade with a large number of stages however, this might provide some valuable extra cooling.

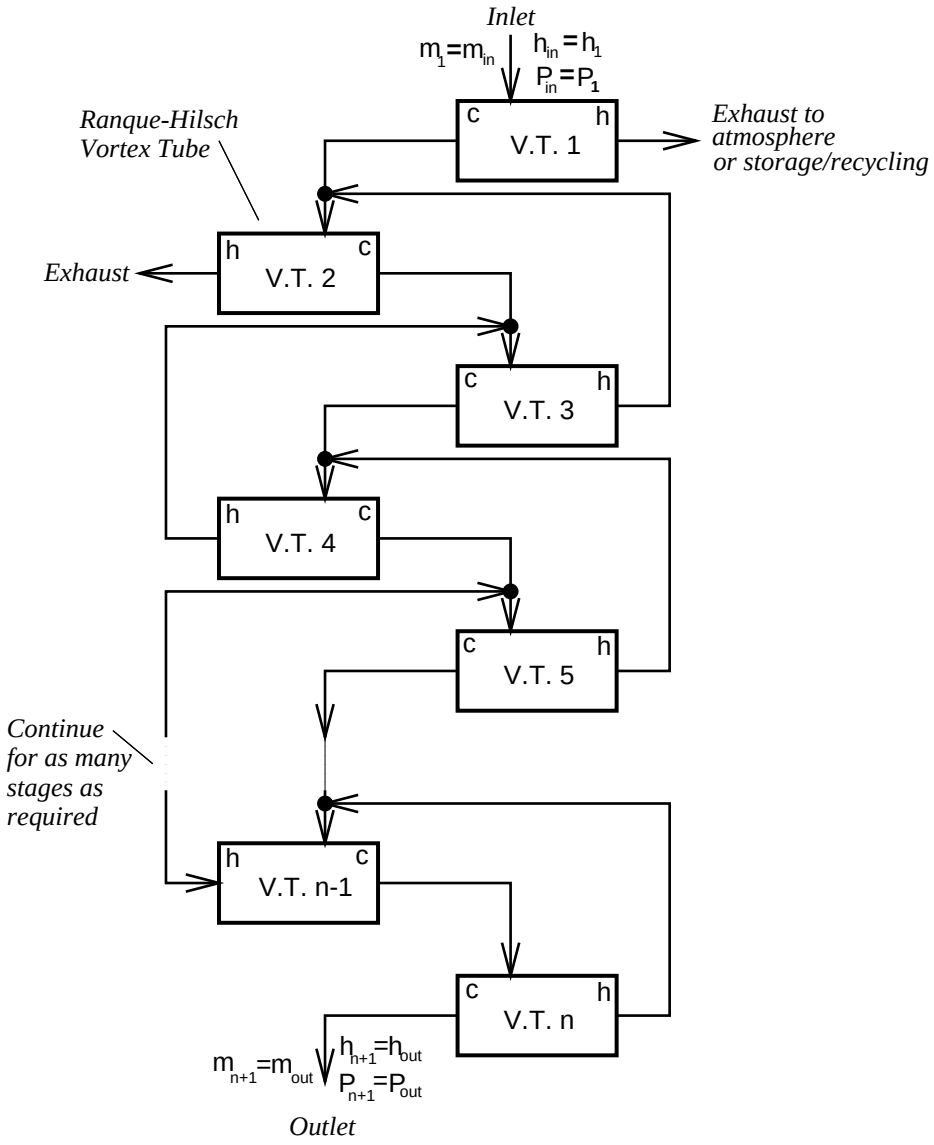

Figure 7.11: The first reflux cascade.

be taken of the thermodynamic effects of any re-compression required within the cascade.

Calculation of the mass flow rates within the cascade is complicated by the feed back. Simultaneous solution of mass flow balances for the mixers, the vortex tubes and the whole cascade with N stages gives

$$\frac{\dot{m}_{out}}{\dot{m}_{in}} = \frac{\mu_c}{1 + \frac{1-\mu_c}{\mu_c} \cdot f(\mu_c) + \frac{(1-\mu_c)^{N-1}}{\mu_c^N}} \tag{7.19}$$

where

$$f(\mu_c) = 1 + \frac{1-\mu_c}{\mu_c} + \frac{(1-\mu_c)^2}{\mu_c^2} + \ldots + \frac{(1-\mu_c)^{i-2}}{\mu_c^{i-2}} + \ldots + \frac{(1-\mu_c)^{N-3}}{\mu_c^{N-3}} \tag{7.20}$$

Assuming that the hot outlets are pumped up to the pressure of the stream they are mixed with then the pressure relationship is as for the simple cascade

$$\left(\frac{P_{in}}{P_{out}}\right)_{cascade} = \left[\left(\frac{P_{in}}{P_{out}}\right)_{stage}\right]^N. \tag{7.21}$$

Simultaneous solution of the enthalpy balance equations is difficult. A considerable amount of working gives

$$\frac{h_{out}}{h_{in}} = \frac{\dot{m}_{in}}{\dot{m}_{out}} \frac{1 - (1-\mu_c) f_{h1}}{1 + \frac{(1-\mu_c) f_{h2}}{\mu_c f_{c2}} \left(f_a + \frac{f_b}{\mu_c^2 f_{cN} f_{cN-1}}\right)} \tag{7.22}$$

where

$$f_a = 1 + \frac{(1-\mu_c) f_{h3}}{\mu_c f_{c2}} + \frac{(1-\mu_c)^2}{\mu_c^2} \frac{f_{h3} f_{h4}}{f_{c3} f_{c4}} + \ldots + \frac{(1-\mu_c)^{N-3}}{\mu_c^{N-4}} \frac{f_{h3} f_{h4} f_{h5} \ldots f_{hN-2}}{f_{c3} f_{c4} f_{c5} \ldots f_{cN-2}} \tag{7.23}$$

and

$$f_b = \frac{(1-\mu_c)^{N-3}}{\mu_c^{N-4}} \frac{f_{h3} f_{h4} f_{h5} \ldots f_{hN-1}}{f_{c3} f_{c4} f_{c5} \ldots f_{cN-2}} \tag{7.24}$$

having defined

$$f_{ci} = 1 - \Phi(1 - \chi_i) \tag{7.25}$$

$$f_{hi} = \frac{1 - \mu_c f_{ci}}{1 - \mu_c} \tag{7.26}$$

Design curves for the first reflux cascade are shown in figure 7.12 and 7.13, demonstrating again that the cascade is not reasonably capable of producing liquefied air.

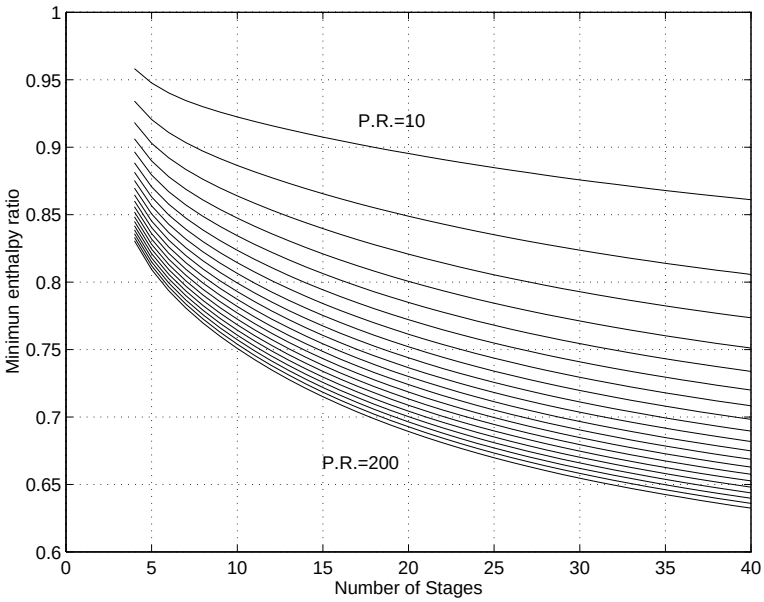

Figure 7.12: Design curves for the first reflux cascade. The upper curve represents an overall pressure ratio of 10, and the lowest curve an overall ratio of 200. Other lines represent increments of 10 in the pressure ratio.

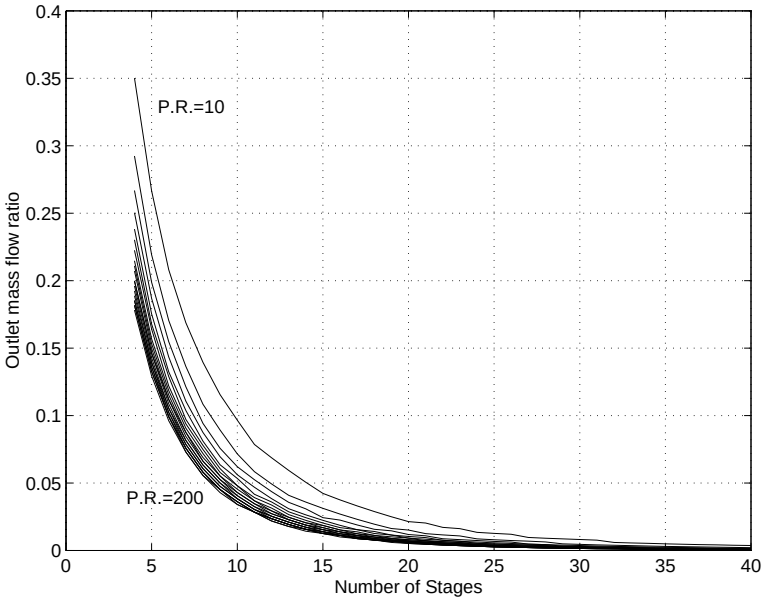

Figure 7.13: The ratio of outlet mass flow to inlet mass flow for a type 1 reflux cascade operating at the minimum outlet enthalpy ratio. The top curve represents an overall pressure ratio of 10, the bottom curve an overall ratio of 200, and intermediate curves are spaced at increments of 10 in the pressure ratio.

7.4.4 Second Reflux Cascade

Another scheme that attempts to improve on the simple cascade is shown in figure 7.14. In this case the lower stage hot flows are passed through heat exchangers to pre-cool the inlet flow in an effort to reduce the number of stages required for liquefaction and thereby increase the yield. Contrast this to the approach of the previous section, which attempted to improve the yield by reducing the mass flow loss at each stage. Note that as with the last design the hot outlets of the first two tubes are not used.

A cascade of N stages has an outlet mass flow rate the same as that of a simple cascade,

$$\frac{\dot{m}_{out}}{\dot{m}_{in}} = \mu_c^N \tag{7.27}$$

but at the expense of an increased overall pressure ratio, or a reduced stage pressure ratio. For the calculations presented here, the effect of the heat exchangers on the pressure drop was neglected, and thus pressure relationships are as for the simple cascade.

An overall expression for enthalpies was not derived in this case. Instead the cooling performance of the cascade was estimated numerically by chaining together recurrence expressions for the stage to stage cold flow enthalpies

$$\frac{h_{c,n}}{h_{c,n-1}} = \Delta C = 1 - \Phi\left(1 - \chi_{n-1}\right), \tag{7.28}$$

hot stream enthalpies

$$\frac{h_{h,n}}{h_{h,n-1}} = \Delta H = 1 + \frac{\mu_c}{1-\mu_c}\Phi\left(1 - \chi_{n-1}\right), \tag{7.29}$$

and for the enthalpies at the marked nodes in the heat exchanger network

$$\frac{h_{i,(n-1)}}{h_{i,n}} = \frac{1 - \mu_c^{n-1}\left(1-\mu_c\right)\Delta H\left(\Delta C\right)^{n-1}}{1 - \mu_c^{n-1}\left(1-\mu_c\right)}. \tag{7.30}$$

The design curves are computed numerically, and are shown in figure 7.15. There is a very small improvement in the performance of the cascade compared to the simple

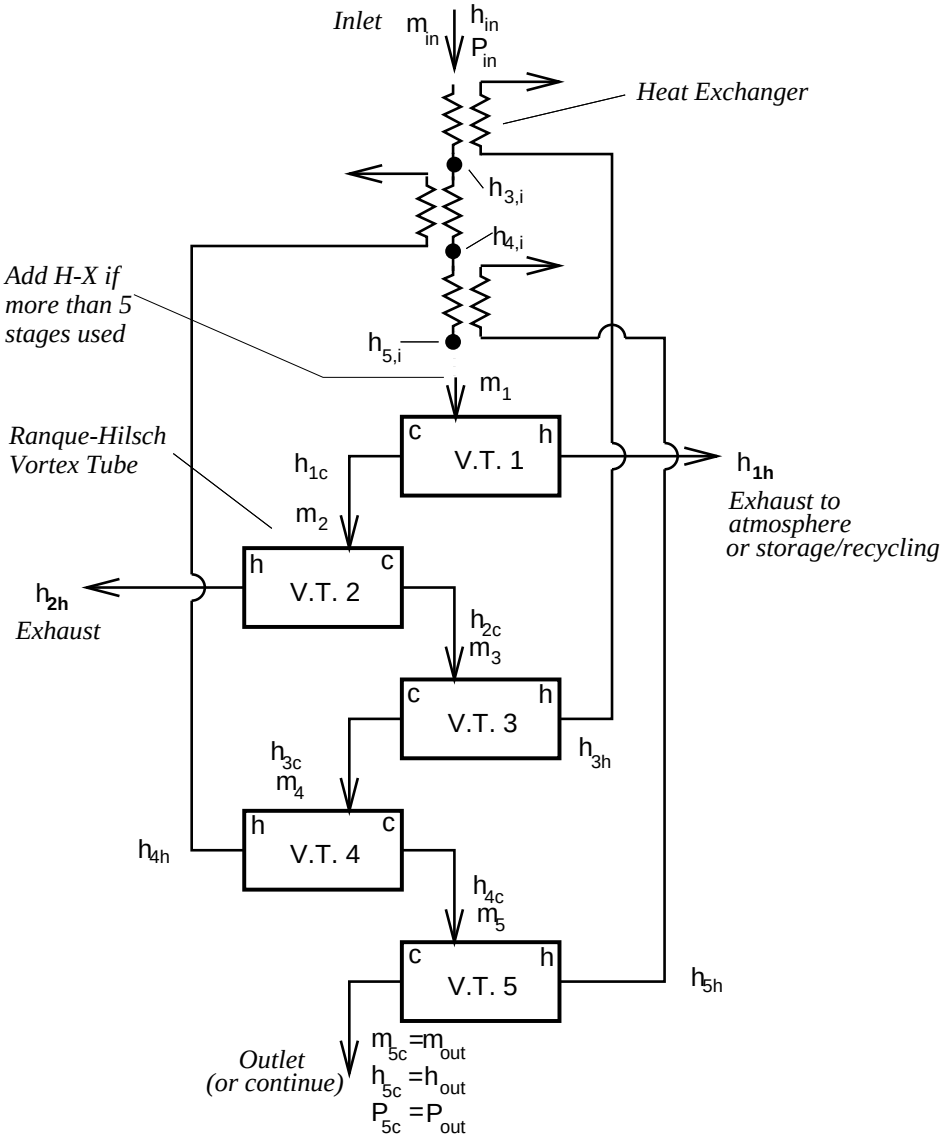

Figure 7.14: The second reflux cascade.

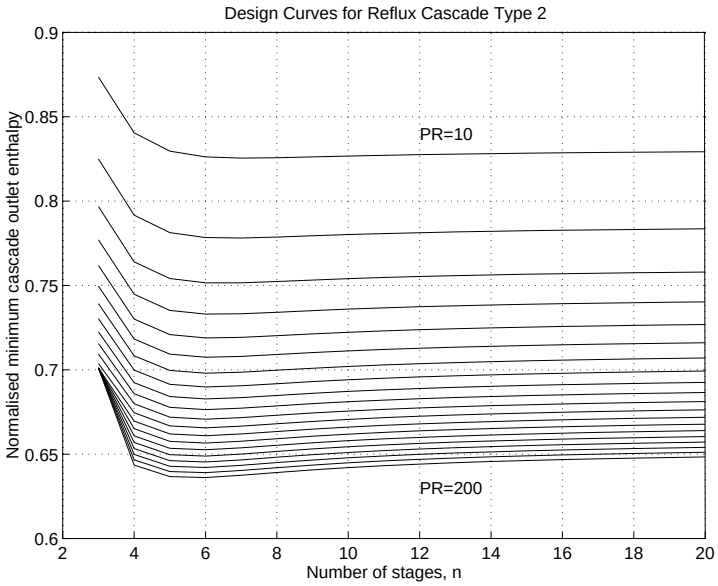

Figure 7.15: Design curves for the second reflux cascade. The upper curve represents an overall pressure ratio of 10, and the lowest curve an overall ratio of 200. Other lines represent increments of 10 in the pressure ratio.

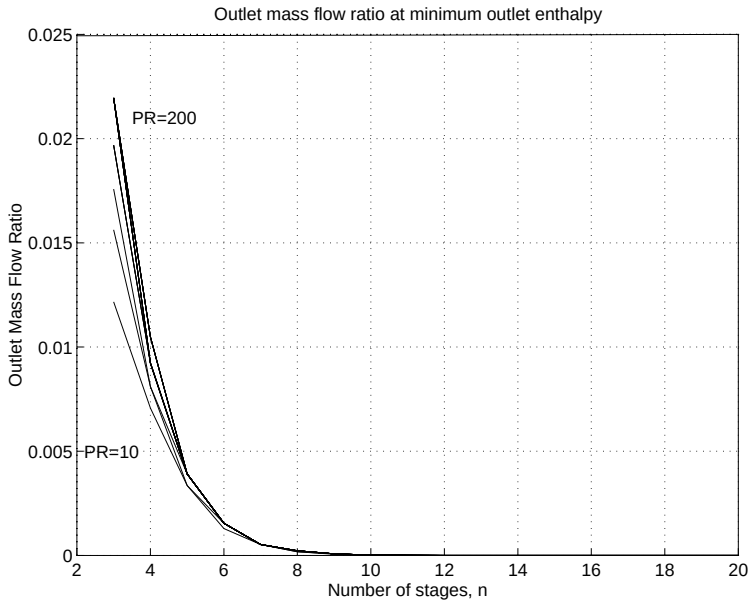

Figure 7.16: The ratio of outlet mass flow to inlet mass flow for a type 2 reflux cascade operating at the minimum outlet enthalpy ratio. The upper curve represents an overall pressure ratio of 10, and the lowest curve an overall ratio of 200. Other lines represent increments of 10 in the pressure ratio.

design. At any given pressure ratio the minimum outlet enthalpy is fractionally lower. The outlet mass flow fraction at minimum enthalpy, shown in figure 7.16 is also slightly improved, as the effect of the heat exchangers is to increase the cold mass flow fraction at which maximum cooling is obtained. In practice this design does not represent a significant improvement over the simple scheme. If the heat exchanger pressure drops were included in the calculations, the performance curves would be considerably worse than for the simple cascade.

7.4.5 Discussion of Performance

None of the cascades examined are capable of providing liquefied air under reasonable conditions. Even a drastic increase in the pressure ratio applied across a cascade would not provide a significant improvement in the liquefaction capabilities. The 'design curves'

show that a rule of diminishing returns operates as far as increases in pressure ratio are concerned. The cascades are however, able to appreciably reduce the temperature of the working gas, without the use of significant external power sources.

If cascades of vortex tubes are to be of use in liquefaction processes then one of two conditions must be satisfied. Either the working gas must be much more easily liquefied than air, or a means of improving the performance of the vortex tube, that is increasing the 'tube constant' k, must be found.

Cascades could perhaps liquefy the heavier gaseous hydrocarbons such as butane, which requires an outlet to inlet enthalpy ratio of approximately 0.91 when starting at room temperature, or propane at 0.85. The behaviour of Ranque-Hilsch tubes with gases other than air is difficult to model, as insufficient data is available in the literature for evaluation of a tube constant. Experiments by Collins and Lovelace [78] show, at least, that the Ranque-Hilsch effect is experienced by propane expanded through a vortex tube.

Given the difficulty of modelling vortex tube operation with gases other than air, we will proceed by assessing the level of vortex tube performance required to produce liquid air, given an overall pressure ratio of 200. Attempts will then be made to maximise the liquid production of the cascades at the new performance level.

7.4.6 Performance Required for Liquefaction

The curves of outlet enthalpy against number of stages for the first reflux cascade show a reduction in enthalpy as the number of stages is increased. In contrast, the other designs exhibit an optimum number of stages, with any further extensions of the cascade causing a rise in outlet enthalpy. It might be anticipated therefore, that the first reflux cascade was able to produce the lowest temperatures from the applied pressure ratio, and provide the easiest route to liquefaction. In *principle* this is true. Given a pressure ratio of 200, extension of the curves in figure 7.12 shows that the first reflux cascade can just produce liquid air from a vortex tube with a characteristic constant of approximately 22. Unfortunately this requires more than 120 separate stages and produces a negligible outflow.

The second design of reflux cascade is just capable of producing liquid air from a vortex tube with a constant of 27, using 4 separate stages. In this case the outlet mass flow (including both liquid and gaseous air) would be 0.012 of the inlet flow. Under the same conditions the first reflux tube could produce liquid air with 21 stages, and an outlet flow 7x10^{-4} times that at inlet .

Realistic use of a cascade of vortex tubes for the liquefaction of air requires development of a tube with at least three times the performance of the tubes encountered in this study. Existing tubes typically have a constant $k = 10$, whereas liquefaction requires $k \approx 30$. The analysis will proceed by investigating the optimal operating point of cascades built with such an improved tube.

7.4.7 Optimisation of a Liquefying Cascade

To provide a more realistic solution for the cascades, the presumed performance degradation with increasing wetness fraction was incorporated into the analysis. This was achieved by representing the dependence of the enthalpy of saturated liquid h_f and gaseous h_g air on pressure as a piecewise cubic polynomial in pressure. The values of the enthalpies employed are shown in figure 7.17, along with the piecewise polynomial. Data was obtained from Haywood [139].

Knowledge of the enthalpy and pressure of the working fluid at any point in a cascade allows evaluation of the wetness fraction using expression (7.14) to give

$$\chi = \frac{h - h_f}{h_g - h_f}, \tag{7.31}$$

having determined h_f and h_g from the pressure and the piecewise polynomial. The calculations were simplified by assuming that the wetness fraction remains constant within each tube, and thus wetness is only evaluated at the entrances to and exits from tubes.

With the reflux cascades an iterative approach is necessary. First the enthalpy at the outlet to each stage is calculated assuming that no liquefaction occurs. The values ob-

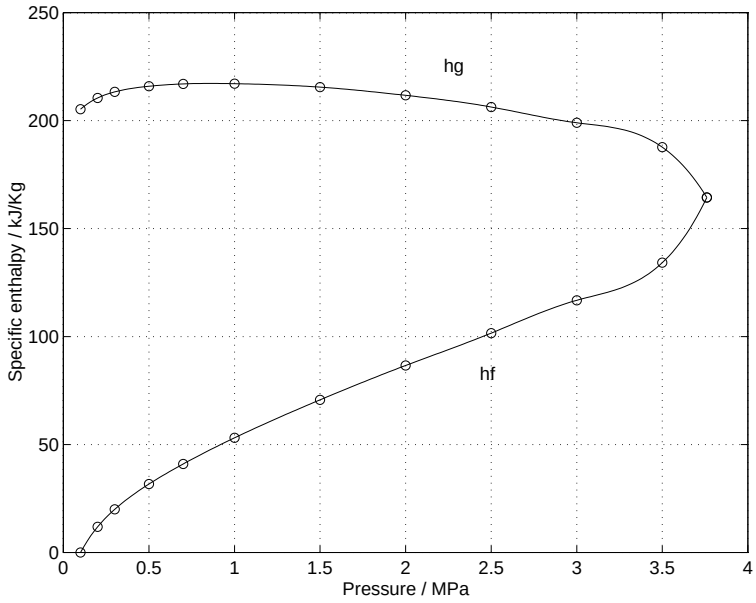

Figure 7.17: The enthalpy of saturated liquid and gaseous air as a function of pressure. The circles show the raw data points taken from Haywood [139], while the solid lines show the piecewise cubic polynomials used in the cascade calculations. Note that the arbitrary datum state for zero enthalpy is the enthalpy of saturated liquid air at a pressure of 0.1 MPa.

tained are used to provide an estimate of the wetness at each stage, and then recalculated. The process is repeated until the changes in the values from step to step become insignificant.

Performance of the cascades was assessed by looking for the maximum outflow of liquefied gas, $\chi_{out}\dot{m}_{out}$ under any set of conditions. Plots will be presented giving the maximum value of this parameter obtainable from both the reflux cascades operated at overall pressure ratios of 200, 250 and 300. As in previous calculations, it will be assumed that the cascade outlet is at atmospheric pressure, and the cascade inlet is at room temperature (298 K).

First Reflux Cascade

Figure 7.18 shows the maximum outlet flow of liquid air that could be obtained from a type 1 reflux cascade as a function of the number of stages in the cascade, and the overall pressure ratio. Figure 7.19 gives the vortex tube cold mass flow fraction μ_c at which maximum liquefaction occurs, so as to define the operating point of the optimal cascades. The maximum mass flow rate of liquid air shown is less than $8x10^{-4}$ times the inlet gas flow. This can be achieved in a cascade operated over a pressure ratio of 300, with 12 stages and each vortex tube set at a cold mass flow fraction of approximately 0.47.

Figure 7.20 shows that the performance of the cascade depends strongly on the cold mass flow fractions of the vortex tubes. To achieve optimal performance the cascade would have to be set up very carefully indeed.

Second Reflux Cascade

Under the range of conditions considered, the maximum mass flow rate of liquid air for the second type of reflux cascade is shown in figure 7.21 to be approximately $1.2x10^{-3}$ times the inlet flow of gas. This requires a cascade with 4 stages, operated at an overall pressure ratio of 300, and with each vortex tube set to a cold mass flow fraction of approximately 0.36, (see figure 7.22), and represents an improvement over the first design.

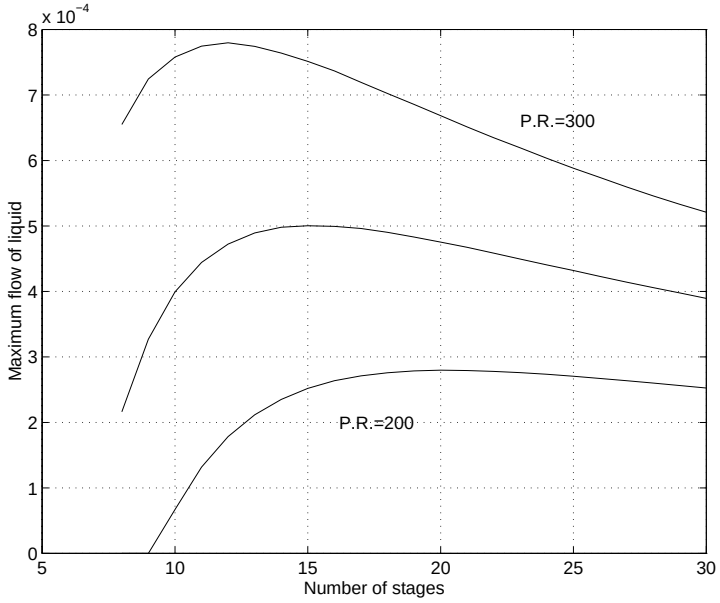

Figure 7.18: Maximum outlet flow of liquefied gas for the first reflux cascade operated at three pressure ratios, using air and vortex tubes with a tube constant of 30. The top line was calculated for an overall pressure ratio of 300, the middle line at 250, the bottom at 200. The outflow is at atmospheric pressure. The mass flow of liquid on the vertical axis is plotted as a fraction of the inlet mass flow rate.

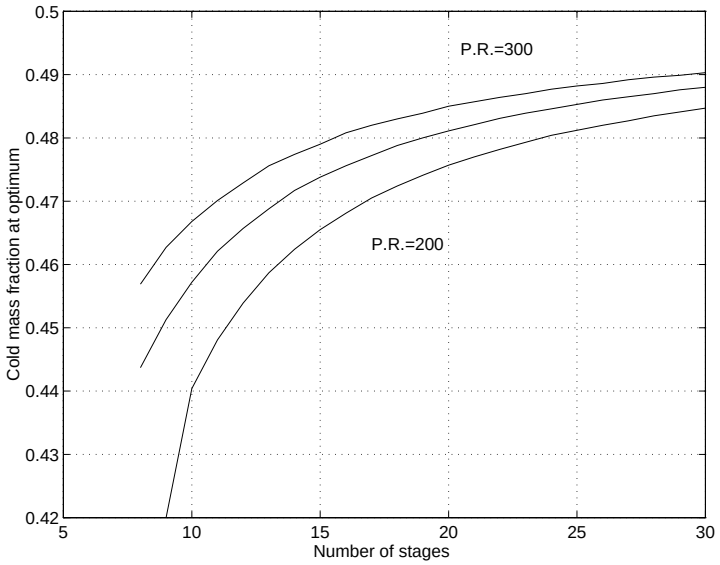

Figure 7.19: Vortex tube cold mass flow fraction for optimal operation of a type one reflux cascade for production of liquefied air. The top line was calculated for an overall pressure ratio of 300, the middle line at 250, the bottom at 200. The outflow is at atmospheric pressure.

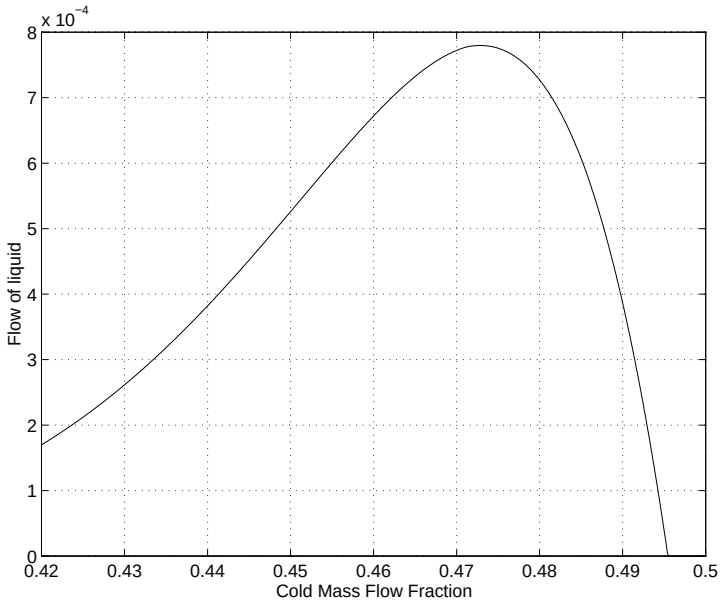

Figure 7.20: Relationship between the production of liquefied air and the vortex tube cold mass flow fraction for a type one reflux cascade operated at an overall pressure ratio of 300. The mass flow of liquid on the vertical axis has been normalised by dividing by the inlet mass flow rate of air.

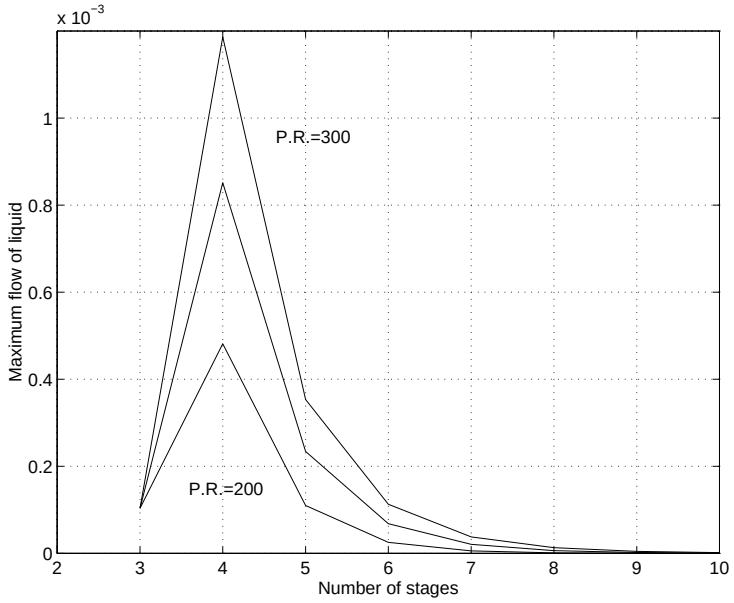

Figure 7.21: Maximum outlet flow of liquefied gas for the second reflux cascade operated at three pressure ratios, using air and vortex tubes with a tube constant of 30. The top line was calculated for an overall pressure ratio of 300, the middle line at 250, the bottom at 200. The outflow is at atmospheric pressure. The mass flow of liquid on the vertical axis is plotted as a fraction of the inlet mass flow rate.

In this case, accurate setting of the cold mass flow fraction is less important for optimal performance. Figure 7.23 shows the predicted variation of the liquid gas produced with the cold mass flow fraction. An error of $\pm$ 8% in the setting of the vortex tubes only produces a reduction in the liquefaction performance of approximately 15%. For the first design of cascade, such a setting error reduces the performance by at least 68%.

Conclusions

Both of the two cascades examined in detail have many disadvantages. When deciding which is the better design, the limitations of the calculations presented must be born in mind.

In estimating the performance of the first design of cascade, the power required to drive the internal pumps was neglected. While it might be possible to implement the

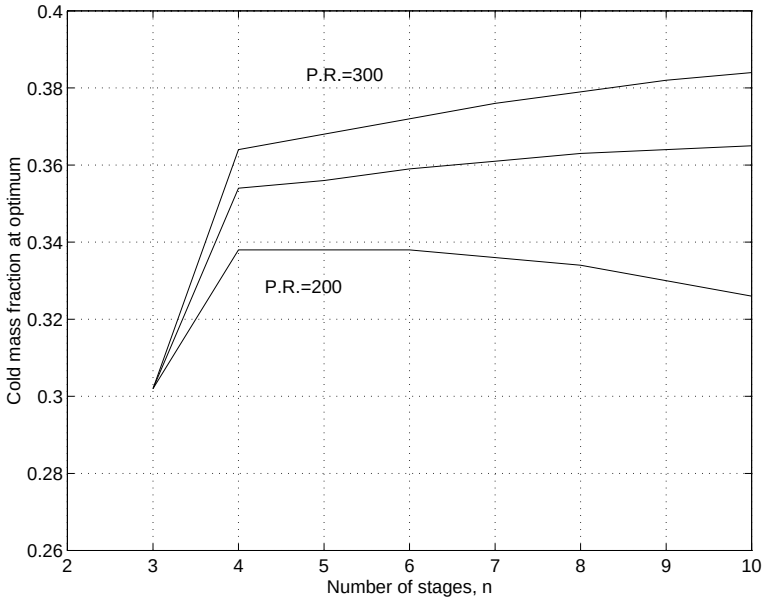

Figure 7.22: Vortex tube cold mass flow fraction for optimal operation of a type two reflux cascade for production of liquefied air. The top line was calculated for an overall pressure ratio of 300, the middle line at 250, the bottom at 200. The outflow is at atmospheric pressure.

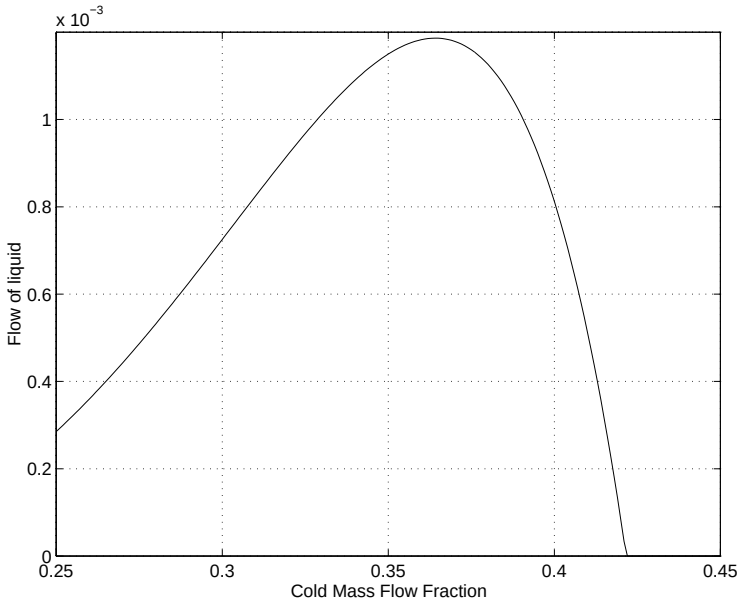

Figure 7.23: Relationship between the production of liquefied air and the vortex tube cold mass flow fraction for a type two reflux cascade operated at an overall pressure ratio of 300. The mass flow of liquid on the vertical axis has been normalised by dividing by the inlet mass flow rate of air.

cascade in such a manner that the mixing of the flow streams did not require pumps, it is clear that the actual performance would be significantly less than that predicted.

Calculations of the second cascade design took no account of the pressure losses imposed by the heat exchangers, which were also assumed to have unity effectiveness. Including these imperfections would substantially reduce the cascade performance, probably removing its small advantage over the first design.

The two cascades, then, have indistinguishable performance. In this case the second design is to be recommended over the first, thanks to its greater tolerance to errors in setting up the vortex tubes, and the fact that it requires many fewer stages making it cheaper to build.

One interesting feature of the optimal productions of liquid air shown in figures 7.18 and 7.21 is that increases in the overall pressure ratio produce substantial improvements in performance. This would not have been anticipated from the graphs of outlet enthalpy, where increases in the available pressure ratio above 200 did not have a noticeable effect on the result.

7.5 An Investigation of Mixture Separation in the Vortex Tube

A number of studies have investigated the mixture separation performance of the Ranque-Hilsch tube. In the following sections a simple model of the separative effect is developed on the assumption that centrifugation is responsible. The model is assessed by comparison to data available in the literature.

7.5.1 Proposed Mechanism and Model

Consider a binary mixture of gases. Let the component of interest have a mole fraction x and a molar mass m_x, leaving the other component with a mole fraction $y = (1 - x)$ and a molar mass m_y. We will work in cylindrical co-ordinates, account only for variations in

the radial direction and neglect the effect of any radial velocity. In these circumstances, Kerrebrock *et al.* [102] show that the radial flux of the interesting component in a laminar flow is given by an equation of the form

$$J_r = -D\rho \left[\frac{\partial x}{\partial r} - \left(\frac{\partial x}{\partial r} \right)_{press} \right] \tag{7.32}$$

where D is a diffusion co-efficient and $\left(\frac{\partial x}{\partial r}\right)_{press}$ represents the effect of any pressure gradient on the equilibrium concentration profile. At equilibrium, $J_r = 0$, we have

$$\frac{\partial x}{\partial r} = \left(\frac{\partial x}{\partial r} \right)_{press}. \tag{7.33}$$

Thus in laminar flow, any equilibrium concentration gradient is due entirely to pressure diffusion.

Following Benedict *et al.* [140] we can derive an expression for the equilibrium distribution of x in a rotating flow. The partial pressure of the two components is given by

$$P_x = xP \tag{7.34}$$

$$P_y = yP \tag{7.35}$$

where P is the local absolute pressure. Neglecting the effect of radial velocities the radial momentum equation for the vortex tube reduces to

$$\frac{1}{P}\frac{\partial P}{\partial r} = \frac{m}{\bar{R}T}\frac{v^2}{r} \tag{7.36}$$

where the density has been eliminated by substituting

$$\rho = \frac{Pm}{\bar{R}T}. \tag{7.37}$$

Applying equation (7.37) to the two components in turn gives

$$x(r) = [Px]_{cl} \, e^{\int_0^r \frac{m_x}{RT}\frac{v^2}{r_1}dr_1} \tag{7.38}$$

$$y(r) = [P(1-x)]_{cl} \, e^{\int_0^r \frac{m_y}{RT}\frac{v^2}{r_1}dr_1} \tag{7.39}$$

with $[Px]_{cl}$ representing the value of Px at the centre of the vortex. For any general swirl velocity and temperature distribution, this expression can be evaluated numerically. Writing

$$\frac{x/(1-x)}{x_{cl}/(1-x_{cl})} = e^{\frac{(m_x-m_y)}{\bar{R}}\int_0^r \frac{v^2}{r_1 T}dr_1} \tag{7.40}$$

clearly shows that any changes in mole fraction across the radius are due to the effects of swirl and the difference in molar mass of the components, i.e. centrifugation.

The flow in the vortex tube is turbulent as we have seen. Under these circumstances, Rosenzwieg *et al.* [103] suggest that equation (7.32) should be modified to

$$J_r = -D\rho\left[(1+\epsilon)\frac{\partial x}{\partial r} - \left(\frac{\partial x}{\partial r}\right)_{press}\right] \tag{7.41}$$

to account for the increased concentration diffusion that turbulence would produce, with ϵ representing the eddy diffusivity. The equilibrium solution is now given by integrating radially

$$\left(\frac{\partial x}{\partial r}\right)_{turbulent} = \frac{1}{1+\epsilon}\left(\frac{\partial x}{\partial r}\right)_{press} = \frac{1}{1+\epsilon}\left(\frac{\partial x}{\partial r}\right)_{laminar} \tag{7.42}$$

where $\left(\frac{\partial x}{\partial r}\right)_{laminar}$ is given by differentiating result (7.38).

These results of course represent equilibrium solutions, the concentration distribution that would eventually be reached by a two component mixture rotating for ever with a constant swirl velocity. Such conditions do not exist within the vortex tube, and so the model must be regarded as a gross approximation. However the axial flow patterns within the vortex tube mean that gas is retained for a long period in comparison to the rotational period of the vortex. Thus it would be anticipated that the concentration

distribution at the exit plane of the tube would approach equilibrium.

Accordingly evaluating expression (7.42) using swirl velocity and temperature profiles obtained near the exit plane of a vortex tube should give an estimate of the physical separation obtained assuming that centrifugation is indeed the major cause. In the case of a uniflow vortex tube, the exit plane is easily identified. For a counterflow tube, the profiles to be used are less obvious. Here it is probably better to calculate bounds on the separation. Mixture separation must occur in the recirculation region between the inlet valves and the stagnation point on the axis. Beyond the stagnation point no further useful separation is possible, the two streams already having been split. Thus, profiles taken part way along the tube near the stagnation point would give a lower bound on the separative effect, whereas profiles from near the inlet plane would produce an upper bound.

7.5.2 Comparison of Model with Experimental Data

In order to test the hypothesis of a centrifugation mechanism, expression (7.42) was evaluated numerically using some experimentally determined profiles, and the results compared to Linderstrom-Lang's experiments [98] on vortex tube mixture separation. Because of the small diameter (10 mm) and short length of Linderstrom-Lang's tubes (100 mm), suitable data is difficult to obtain. The experimental apparatus described in chapter 3 has much too large a value of L/D to have any hope of replicating the required conditions. Instead data taken by Lay in a tube with comparable L/D to that required, and operated at a similar pressure ratio $P_{in}/P_{out} \approx 3.5$ was employed. While far from perfect, this does at least satisfy the major requirements for similarity of integrated type parameters outlined in chapter 3. In all cases the working gas was air.

A major difficulty with the procedure is that Lay's data was taken in a uniflow tube, while Linderstrom-Lang worked with a setup that is reminiscent of a counterflow design. Since firstly, the best that can be hoped for such an elementary model as this is a qualitative comparison of results, and secondly that the influence of the axial flow on pattern on

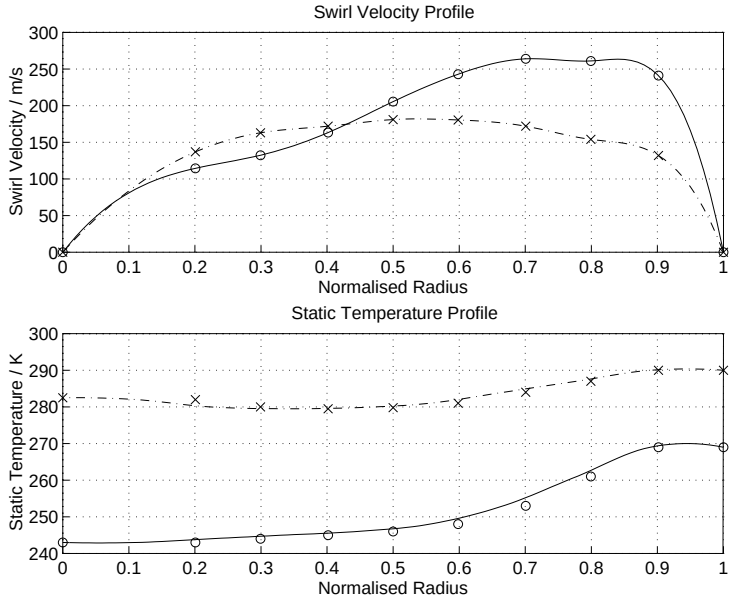

Figure 7.24: The velocity and temperature profiles used to evaluate the mixture separation. The circles represent experimental values measures by Lay near the entrance to a uniflow tube, and the crosses values taken near the exit. The solid and chained lines are interpolating splines. The values that the splines represent were used in the numerical calculations detailed in this section.

the swirl profiles is not great, it is reasonable to compare calculated bounds on the separation based on the inlet and outlet swirl profiles found by Lay with Linderstrom-Lang's results.

The scaled inlet and outlet profiles based on Lay's data are shown in figure 7.24. Corresponding radial oxygen content distributions calculated using the laminar expression (7.40) can be seen in figure 7.25. The working gas was air, assumed to be a binary mixture of oxygen and nitrogen with a natural composition as found in the atmosphere. It is clear that the decay of the swirl velocity near the periphery does not have a great effect on the predicted profile. This is consistent with Linderstrom-Lang's observation that the central regions of the flow are most involved in the mixture separation.

To estimate the turbulent oxygen concentration a value for the eddy diffusivity, ϵ is required. We will follow Rosenzweig *et al.* [103] and assume that the ratio of the turbu-

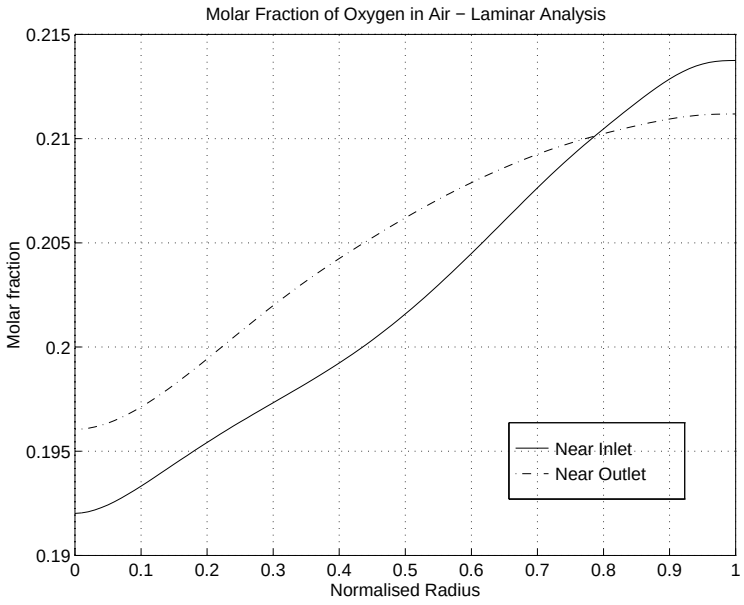

Figure 7.25: The radial oxygen concentration evaluated using the laminar expression. The solid line represents the calculation performed with the data taken by Lay near the inlet to a uniflow tube. The calculation for the broken line used data taken near the outlet.

lent and laminar diffusivities for concentration is the same as the ratio of the diffusivities for momentum. The required value of ϵ will be equal to the ratio of the turbulent and laminar viscosities

Keyes [101] investigates the values of eddy viscosity found in vortex tube like flows as a function of swirl Reynolds number measured near the tube wall and the inlet nozzles. For a vortex tube of 10 mm diameter with the near inlet velocity profile shown in figure 7.24 the swirl Reynolds number is $Re_{swirl} \approx 5 \times 10^5$. Examination of Keyes' data, which shows considerable scatter, suggests that the ratio of eddy viscosity to laminar viscosity at this Reynolds number lies between 70 and 162. Thence we shall assume $70 < \epsilon < 162$. Figure 7.26 shows the oxygen concentration profile evaluated using the turbulent expression with $\epsilon = 162$ for the velocity and temperature profiles taken near the inlet. Notice the enormous reduction in separation compared to the laminar case.

Using the calculated concentration profiles, bounds on the anticipated variation of

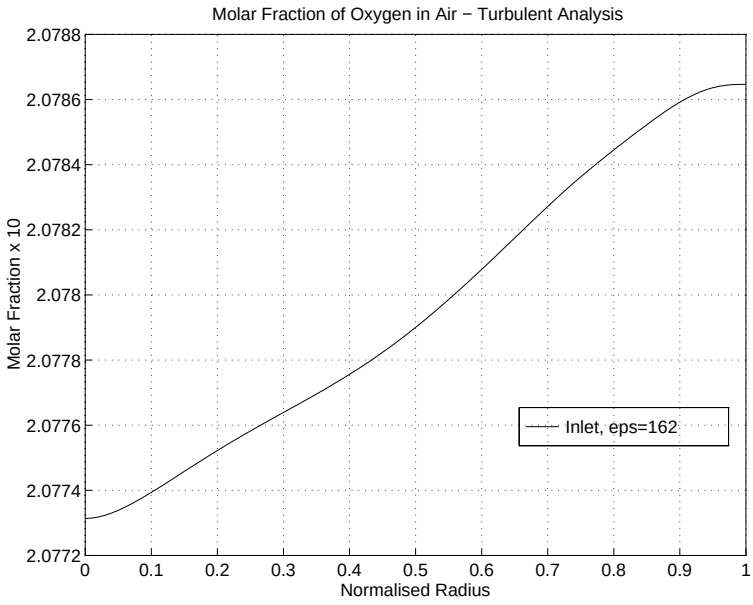

Figure 7.26: The radial oxygen concentration evaluated using the turbulent expression. The particular curve shown was calculated using the profiles taken by Lay near the tube inlet, and with a turbulent diffusivity of 162.

the *separation effect* defined by Linderstrom-Lang as the percentage molar oxygen content of the hot stream minus the percentage molar content of the cold stream may be calculated as a function of the hot mass flow fraction. To perform this, a 'cutting' radius is selected, and it is assumed that all the gas inside that radius represents the cold flow that exits near the centre of the tube, while that outside is the hot flow, exiting at the periphery. The hot flow fraction is calculated by integrating ρr over the space between the cutting radius and the outer wall, and then dividing by the same function integrated over the entire radius. Similarly the oxygen concentration in each stream is assumed to be the average mass weighted oxygen concentration over the appropriate portion of the radius.

The resulting characteristics are shown in figure 7.27 where they are compared to some of Linderstrom-Lang's data. The upper bound, shown by the upper solid curve has been estimated from the combination of variables that give greatest separation, spe-

cifically the inlet profiles with $\epsilon = 70$. Similarly the lower bound was calculated using the near exit profiles with $\epsilon = 162$. Note that not all of Linderstrom-Lang's data is recorded in the figure since the peculiar design of his device allows the central regions of the flow to exit at periphery and the outer regions towards the centre under certain conditions. Data sets where this phenomenon is evident[5] have been excluded. That the qualitative variation of the bounds and experimental data is similar, while the magnitudes are at least comparable indicates that centrifugation is indeed the mechanism responsible.

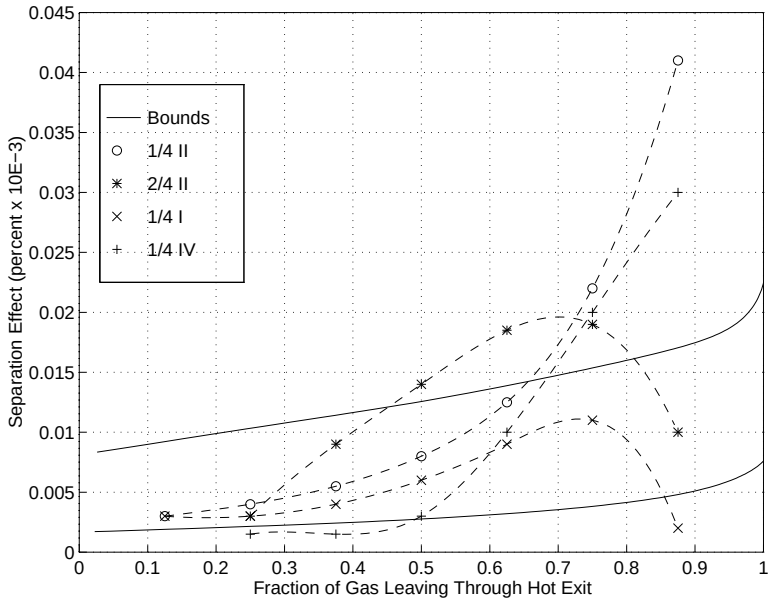

Figure 7.27: Predicted and experimental variation of separation effect with hot flow mass fraction. The solid lines are the calculated bounds on the separation effect. The symbols represent four data sets taken from Linderstrom-Lang [98], figure 4b, who used a 10 mm diameter counterflow tube, and the broken lines are the interpolating splines.

[5]Data sets that exhibit this flow inversion are readily identified since the usual separation effect with the heavier components towards the periphery of the tube appears to be reversed under high hot mass flow fractions. In other words, observation shows that gas leaving through the peripheral, hot exit is enriched in the lighter component, while that passing through the central, cold exit is depleted in the lighter component. Linderstrom-Lang advances a mechanism that is able to explain this peculiarity.

7.6 Application of the Vortex Tube to Uranium Enrichment

Now that the mechanism of mixture separation in the vortex tube has been attributed to centrifugation, the potential of the device to perform useful separation tasks can be better examined. Of particular interest are the abilities of the tube in separation of the uranium isotopes U-235 and U-238.

Most industrial scale enrichment processes work with uranium hexafluoride rather than elemental uranium. The principal advantage of the compound is that it sublimes at 330 K under atmospheric pressure, providing a gaseous form under reasonable conditions. As isotope separation techniques generally exploit the slight differences in mobility of molecules with small differences in atomic mass, a gaseous material is essential.

A number of centrifugal techniques for enrichment of uranium have been proposed. Currently the most popular is the *gas centrifuge*, wherein a rapidly spinning cylindrical container is supplied with gaseous UF_6. A stream enriched in the hexafluoride of U-235 is collected from the centre of the container, and material rich in the heavier U-238 is bled from the periphery. While a very successful technique, the gas centrifuge is a complex device requiring a high degree of precision in its manufacture. Additionally the rate of rotation, and hence the performance of the centrifuge is limited by the yield stress of the material from which it is made.

'Steady state' means of centrifugation, such as a jet driven vortex tube flow, represent an attractive alternative to 'proper' centrifuges thanks to their relative simplicity. That the gas container does not rotate also removes the constraint imposed on the rate of rotation by its mechanical strength. The physical properties of the working gas and design of the inlet nozzles, however, limit the maximum speed at which the gas can enter the vortex tube to the local sonic velocity. For a very heavy gas such as UF_6 this places a serious constraint on the rate of rotation[6], and thence the separation that could be obtained in a jet driven centrifuge.

[6] UF_6 has a molar mass of approximately 352 kg/kmol. The speed of sound in the material at 350 K is less than 100 m/s.

A solution adopted by many proponents of aerodynamically limited separation processes is to work with a dilute mixture of UF_6 in hydrogen (see for example, Geppert [141]). The sonic velocity in the resulting mixture is raised towards that in pure hydrogen. With a 0.04 mole fraction of UF_6, the sonic velocity would be 492 m/s at a temperature of 350 K. This is considerably less than the maximum peripheral speed achieved by a typical centrifuge, which can approach 700 m/s (Whitley [142]). In view of this, and the high levels of turbulence found within the vortex tube, it is unlikely that it could ever compete directly with a conventional centrifuge on the grounds of separation efficiency alone.

7.7 Conclusions

In this chapter we have looked at the utility of the Ranque-Hilsch tube for performing a number of tasks. While the device has a poor efficiency, its inherent simplicity can make it attractive where reliability and low-maintenance characteristics are important. Prospects for employment of the tube in gas-liquefaction are less promising, unless the cooling performance can be drastically improved.

Finally, the nature of the reported mixture separation properties of the vortex tube was investigated. A simple model suggested that 'straightforward' centrifugation was the mechanism responsible. Application of this deduction to the problem of uranium enrichment hinted that there may be some use for vortex tubes in the nuclear industry. While the isotope separation performance of a vortex tube is unlikely match that of a conventional ultra-centrifuge, the considerable reduction in complexity it represents is appealing.

Chapter 8

Conclusions and Recommendations for Further Work

8.1 Review

Discussion began with a literature review which highlighted some potentially important features of the Ranque-Hilsch vortex tube, and outlined a number of mechanisms postulated to explain its peculiar thermal properties. The lack of agreement between many investigations was clear.

A series of experiments characterised certain features of the Ranque-Hilsch vortex tube, and provided some general data on the internal flow. More specific work suggested that the acoustic effects found by some workers were not directly related to the thermal separation. Development of a Navier-Stokes solver demonstrated that flows in Ranque-Hilsch vortex tubes were amenable to calculation by conventional techniques. The results of the program also allowed a little further insight into the nature of the energy separation effect.

Based on some of the results of these investigations, a model of vortex tube performance was developed. This facilitated study of the potential of the vortex tube in a number of thermal engineering applications. The abilities of the vortex tube in nuclear engineer-

ing were also considered.

8.2 Conclusions

8.2.1 Energy Transfer in Vortex Tubes

Features

In essence the Ranque-Hilsch vortex tube is a means of converting potential energy, in the form of a pressure difference between the inlet and the outlets of the tube, into a radial temperature and energy separation. The warm peripheral fluid and the cool central fluid can be separated using an orifice. Operation with air can provide useful heating and cooling effects from the outlet streams.

The temperature difference between the outlet streams is dependent on a number of parameters, especially the fraction of the inlet gas leaving through the cold exit and the pressure ratio applied across the vortex tube. Other important factors influencing the performance include the diameter of the tube, the inlet temperature and physical properties of the fluid.

The most important feature of the flow is the formation of an approximately forced vortex when the fluid enters the tube. This forced vortex represents the 'interface' between the inlet gas flow and the flow within the vortex tube. As such it characterises the entire flow field and is responsible for many of its features. An approximately forced vortex is maintained over much of the vortex tube, although the profile decays as the fluid proceeds along the tube.

The stagnation and static temperature differences between the central and the peripheral flow are seen to grow as the gas proceeds along the initial regions of the tube. Some distance along, when the swirl has decayed significantly, the stagnation temperature difference starts to decline.

Flow within the vortex tube appears to be highly turbulent, especially near the inlet nozzles. On larger scales though, the flow is mostly steady and predictable. The only

exception to this is the bubble like vortex breakdown in the counterflow tube that marks the onset of the central region of reversed flow. Breakdown can occur in some uniflow tubes, producing a small region of recirculation. Apart from these regions there is little secondary flow in the radial direction, and hence fluid that remains at the periphery on inlet tends to stay there, and similarly for fluid that moves straight to the central regions.

Mechanisms

Two 'thermodynamic' separations can be identified in the vortex tube, a thermal separation in the sense that the peripheral fluid obtains a higher static temperature than the central fluid, and an energy separation in that the peripheral fluid also has a greater stagnation enthalpy than the central fluid. Of the two, the latter is the more interesting, since the thermal separation can in part be explained by the dissipation of the kinetic energy part of the stagnation enthalpy separation through the action of viscosity.

The primary feature of the vortex tube that produces the radial energy separation is the initial formation of a forced vortex. This immediately represents a radial separation of kinetic energy, with the fastest, high kinetic energy gas at the periphery, and the slow low energy gas at the centre. It appears that the inlet flow is not adiabatic, and thus the static temperature distribution is not that which would be associated with an isentropic expansion of the inlet gas into the inlet plane. Instead there is some evidence that there is a thermal temperature separation formed within the inlet plane, with the temperature increasing towards the periphery. This behaviour appears in part to be due to the proximity of the inlet nozzles to the orifice in the case of a counterflow tube, and to the closed end of the tube in a uniflow case. Details of the behaviour of the gas in the inlet plane warrant further investigation.

Dissipation of the kinetic energy of the forced vortex through viscous mechanisms is responsible for much of the thermal separation within the vortex tube. A substantial role is played by the action of turbulent eddies in the radial pressure gradient however. In regions where the radial pressure gradient is large, that is where the swirl is strongest, com-

pression of eddies as they move radially outwards through the pressure gradient permits the transport of heat radially outwards, even against the temperature gradient. This serves to supplement both the stagnation and static temperature separations by cooling the central gas and heating peripheral gas.

When combined with the effects of convection by the the mean flow in the axial direction, the turbulent heat transfer mechanism can account at least qualitatively for the observed behaviour of the stagnation enthalpy field in the vortex tube. In particular the turbulent heat transfer appears to be responsible for the region close to the inlet nozzles where the stagnation enthalpy separation increases as the flow progresses down the tube.

Beyond the region in which the stagnation enthalpy increases, the radial pressure gradient induced by the swirl is no longer sufficient to permit a thermal flux directed up the radial temperature gradient. The stagnation enthalpy separation now starts to decline, as turbulent conduction now transports heat down the temperature gradient and into the cooler central flow. Decline of the stagnation enthalpy separation occurs over a considerable length of tube however, as the radial pressure gradient is sufficient to reduce the propensity for thermal transport towards the centre until the swirl has decayed greatly.

The static temperature difference between the inner and the outer gas may continue to increase even beyond the region in which the heat flux is directed radially outwards. This is caused by the viscous dissipation taking place in the periphery of the flow, increasing the temperature of the peripheral flow faster than that at the centre. No further cooling of the central flow is possible in this flow regime however. Subject to the heat transfer condition at the wall of the tube, both the central and the peripheral gas become warmer through the action of turbulent heat transport and viscous dissipation as the swirl velocity decays until uniform temperature profiles are achieved. In practice, very few vortex tubes are long enough to achieve this.

8.2.2 Modelling of Vortex Tubes

A model relating the thermal separation performance of vortex tubes to the fraction of cold gas and to the applied pressure ratio has been developed. The precision of the model was not particularly good, but the result is sufficient for engineering purposes.

The flow internal to the vortex tube can be modelled adequately using the conventional techniques of computational fluid dynamics. Some aspects of the energy separation are also captured, but accurate modelling will require further careful study of the turbulent transport process at work within the tube.

8.2.3 Applications of Vortex Tubes

Ranque-Hilsch vortex tubes have potential for gas-liquefaction applications. Without improvements in the performance of the device, the potential is limited to providing cooling assistance in conventional techniques. With increased performance, then for air at least, liquefaction schemes consisting of cascades of vortex tubes and heat exchangers become feasible.

The mechanism behind the radial separation of components of the inlet gas of differing masses has been established as 'simple' centrifugation. This information allowed numerical investigation of the utility of the vortex tube in the separation of uranium isotopes. It can concluded that the vortex tube is capable of providing useful isotopic separation, and is worthy of further development.

8.3 Recommendations for Further Work

8.3.1 Energy Separation

Flow Measurements

The application of modern non-intrusive measurement techniques to the Ranque-Hilsch vortex tube would provide useful information regarding flow patterns within the tube,

the existence of any organised disturbances within the tube that cannot be detected acoustically, and the nature of the turbulence in the flow. This latter aspect would be of considerably wider interest, since developments in the modelling of turbulent rotating flows are partially restrained by the lack of experimental information with which to make comparisons. The extra information would also allow a better quantitative estimate of the contributions to the temperature separation made by the various mechanisms highlighted in this thesis.

As noted in earlier chapters, the use of optical techniques in cylindrical geometries is not without problems. The difficulties are definitely surmountable, but might turn such measurements into a substantial project by themselves requiring commitment of a number of expensive resources.

One region of particular interest not examined experimentally in this study, is the interaction of the flow from the inlet nozzles with the gas already in the vortex tube. The inlet region appears to be of fundamental importance in the energy separation produced by the tube, so a clearer understanding of the behaviour of the working gas in this region would be extremely useful. Moreover the mixing of the inlet streams with the body of the gas seems to be the largest source of entropy generation in the tube, manifesting itself as a loss of stagnation pressure. Reduction of the mixing losses might well assist in providing the increase in performance that would make many applications of the tube viable.

Empirical Modelling

Three aspects of the empirical model would benefit from attention. Firstly, the form of the function $f_2(\mu_c)$ given by equation (6.7) could be reformulated either as an expression derived more directly from an understanding of the energy separation mechanisms, or as an empirical function that accommodates the asymmetry introduced by 'non-ideal' vortex tubes. Secondly the choking apparently experienced by vortex tubes at high pressure ratios should be better defined and accommodated within the expressions for the thermal separation 'potential' of the inlet gas. Finally, the relationship between the 'tube

constant' and the tube radius suggested by the analysis, expression (6.23) should be given greater experimental attention.

8.3.2 CFD

The finite volume Navier-Stokes solver developed for outline numerical investigation of the vortex tube could be improved in numerous ways. Two particular aspects are the provision of a turbulence model more suited to swirling flows, such as a Reynolds' stress model, and the addition of 'full' compressibility. To dwell on the code's many deficiencies, however, is to miss the point of the work. The code provides a minimally adequate tool for investigation and the basic design of vortex tubes. A more more useful extension would be to employ the code in an extensive numerical investigation of various influences on vortex tube performance.

A more sophisticated numerical study of the significance of the turbulent heat transport mechanism outlined in chapter 5, using the finite volume code, would be useful in assessment of its importance. The heat transfer against the temperature gradient could be simulated in principle by allowing a spatially variable Prandtl number computed locally from values of the pressure and temperature gradients. Any contra-gradient transport would be represented by a negative Prandtl number. To ensure that the results of any calculations were quantitatively correct, there would have to be careful correlation of the calculated turbulence parameters with those found experimentally.

8.3.3 Gas Liquefaction

Further study of the potential of vortex tube cascades for gas liquefaction would be worthwhile if the efficiency of vortex tubes can be increased. Otherwise, there is scope for additional work on the incorporation of vortex tubes in existing liquefaction techniques.

8.3.4 Mixture Separation

Any development of the vortex tube as a mixture or isotope separation device requires a detailed investigation of the internal concentration distributions. As with the flow measurements, it is difficult to see how intrusive techniques could provide more reliable information than is currently available. Furthermore 'on-line' composition analysis, such as would be required in order to traverse the radius of a vortex tube, presents considerable difficulties.

For these reasons, an optical method of concentration measurement has been devised. An outline proposal is discussed in appendix D, which overcomes both of the disadvantages of intrusive methods. Fortunately optical concentration measurement does not have the same problems with vortex tube flows that beset optical velocity investigations.

A more complete numerical study of mixture separation within the tube, performed by discretising the governing equations of mass transport, equation (based on the mass flux expression 7.41) and incorporating them within the Navier-Stokes solver would be interesting.

Appendix A

Heat Transfer From the Cylindrical Wall

A.1 Introduction

This appendix investigates the magnitude of the heat exchange by natural convection between the uninsulated hot and cold tubes of the CUED installation and the surrounding atmosphere. The effect of any heat exchange on measurements of the wall temperature is assessed. Numerical results are given for installation A only, as this is the tube most affected by any errors induced through convection. The extension to the other tubes is straightforward.

Wall temperature data presented in the main part of the thesis were corrected using the result of this analysis (equation A.4).

A.2 Analysis

If the outer edge of the cylindrical wall of the vortex tube is at a temperature T_w and is surrounded by a still atmosphere at a temperature T_{atm}, then the heat flux from the wall is given by

$$q = Q_1/A = h\,(T_w - T_{atm}) \tag{A.1}$$

where h is the empirically determined heat transfer coefficient, and the area of the outer wall of a section of tube of length l is $A = 2\pi r_{outer} l$. Applying the Fourier law

$$q = -\lambda \nabla T \tag{A.2}$$

to the heat flux by conduction through the wall shows that the rate of conduction through a section of wall of length l, inner radius r_i and outer radius r_{outer} is

$$Q_2 = \frac{-2\pi l \lambda \left(T_w - T_{inner}\right)}{ln\left(r_{outer}/r_i\right)}. \tag{A.3}$$

T_{inner} is the temperature of the inside of the cylindrical wall, which is assumed to be identical to that of the gas in contact with it.

At steady state, $Q_1 = Q_2$ and thence

$$T_{inner} = T_w + \frac{hr_o}{\lambda}\left(T_w - T_{atm}\right) ln\left(r_{outer}/r_i\right), \tag{A.4}$$

or

$$\frac{T_{inner} - T_w}{T_w} = \frac{Nu}{2}\left(1 - \frac{T_{atm}}{T_w}\right) ln\left(\frac{r_{outer}}{r_i}\right). \tag{A.5}$$

A.3 Evaluation

From Holman [143], the heat transfer coefficient for a horizontal cylinder cooled by natural convection is given by

$$\bar{Nu}_f = f\left(Gr_f, Pr_f\right) \tag{A.6}$$

where $_f$ denotes a parameter evaluated at the film temperature. For the 26 mm vortex tube we have

$$\begin{array}{ll} \text{Prandtl number} & Pr_f = 0.7 \\ \text{Grashoff number} & Gr_f = 0.04\,, \end{array}$$

and thence from the graph of values in Holman, the Nusselt number is $Nu = 0.708$. Typically, T_{atm} = 292 K and T_w = 313 K, giving T_{inner} = 314.3 K, and a percentage error of less than 0.5% in using T_w as a measure of the gas temperature at the wall.

Appendix B

Assessment of Errors and Calibration of the Intrusive Measurement Probes

B.1 Basic Principles

The results of the flow field mapping in the main text include detailed estimates of the likely uncertainty field in each case. In order to calculate such estimates, it is necessary to have a clear, quantitative picture of the abilities of the equipment employed. This appendix gives the estimates of uncertainty used in the calculations, outlines how they were obtained, and assesses their correlation.

In general it is very difficult to account for the systematic errors in any experimental work. The aerodynamic probes employed to map the flow field, however, were extremely prone to systematic errors, thanks to their necessarily 'fiddley' construction. A simple calibration procedure was used to determine their systematic errors, and the appendix begins by outlining it.

B.2 Procedure and Results for Probes

B.2.1 Equipment

The probes were calibrated in the flow in a vertical square duct of cross sectional area 40000 mm^2. Flow was induced in the duct by means of a suction fan at its top. This had the advantage of ensuring that the stagnation temperature and pressure at the centre of the duct remained constant at atmospheric temperature and pressure under all flow conditions, since effectively the atmosphere was acting as the high pressure reservoir for the flow. A throttle at the exhaust from the fan allowed the flow velocity to be varied, and a static pressure tapping in the wall of the duct enabled its numerical evaluation. Axial flow speeds could be varied from 0 m/s to 60 m/s. While the velocities found in the vortex tubes were outside this range, it was considered that, providing careful consideration was given to the inaccuracies involved, the equipment could provide a useful assessment of the deficiencies of the probes.

Two aspects of the behaviour of the probes were investigated. Firstly, the variation of the reading given as a function of the angle of yaw between the probe and the flow. With the stagnation pressure and temperature probes, the maximum reading should be obtained when the probes face directly into the flow, and with the static temperature probe, a minimum reading. By using a sensitive manometer and plotting the readings of the measured quantity as a function of the indicated angle of the probe, any offset between the actual and indicated zero yaw position, due to manufacturing errors can be estimated. The flatness of the graph around zero yaw can also be used to estimate the likely precision of the probe in service, and an estimate of the error in the offset.

Secondly the variation of the calibration parameters with flow velocity was measured. In most cases this was not found substantial, and the particular parameters employed are described in the individual sections that follow.

B.2.2 Combination of Repeated Readings in the Evaluation of Systematic Errors

Estimates of random error are determined in general by highly subjective means. As such, there is little point in taking a number of estimates of the value, and then attempting to achieve a 'better' result by averaging.

Determinations of systematic error are usually much more 'scientific'. It is conventional, as here, to perform an experiment with the apparatus under test subjected to a well known input, and measure the difference between the response of the apparatus and the well known value. In such cases it is worthwhile to attempt to improve knowledge of the systematic error by repeating measurements.

Since all experiments are subject to random error, repeated measurements of systematic error will rarely agree. This raises the issue of how to combine such discrepant repeated measurements[1].

The best approach seems to be to adopt a Bayesian philosophy. Essentially we begin by using our experience of the situation to set some likely, all encompassing limits on the systematic error. In the case above, determining the angular offset of a stagnation pressure probe, I might be sufficiently confident of my skill in drilling to state that there was no misalignment greater than $\pm\ 10^{o}$. This estimate is used to establish a *prior error probability*, which is a probabilistic statement of the initial error estimate. For our stagnation

[1] or in other words, how to evaluate the error in the error.

pressure probe, the prior probability would be a rectangular[2] distribution thus:

$$\begin{aligned} p_a(\theta) &= \tfrac{1}{20} \quad -10 < \theta < 10 \\ &= 0 \qquad otherwise. \end{aligned} \tag{B.1}$$

When a measurement of the systematic error is taken, say θ_1 with error σ_1, it is combined with the prior information using Bayes' theorem,

$$p(\theta \mid \theta_1) = p_1(\theta) = \frac{p(\theta_1 \mid \theta)\, p_a(\theta)}{\int\limits_{all\ \theta} p(\theta_1 \mid \theta)\, p_a(\theta)\, d\theta}. \tag{B.2}$$

A little explanation is in order. The new information is encapsulated in $p(\theta_1 \mid \theta)$, which represents the probability of obtaining the new reading, θ_1 on the basis of the prior probability and the error estimate. It is termed the *likelihood* and often given the symbol $L(\theta_1 \mid \theta)$. The new, composite, probabilistic understanding of the parameter is represented by the subject of the Bayes' theorem expression, namely $p(\theta \mid \theta_1)$.

If further readings are taken, the newly calculated distribution becomes the prior. Thus for the second reading, (θ_2, σ_2),

$$p(\theta \mid \theta_1, \theta_2) = p_2(\theta) = \frac{p(\theta_2 \mid \theta)\, p_1(\theta)}{\int\limits_{all\ \theta} p(\theta_2 \mid \theta)\, p_1(\theta)\, d\theta}, \tag{B.3}$$

[2]Under the Bayesian interpretation, probability density functions represent the *degrees of belief* we have that the parameter in question adopts any particular value. As such, there is no requirement that p.d.f.s are formulated on the basis of a statistically sound frequency measurement experiment, and in effect, we are allowed to invent p.d.f.s arbitrarily. In any case, whatever distribution we hypothesise will eventually be overwhelmed by the effect of repeat readings. Clearly, though, it is preferable to adopt a density function that offers minimum bias towards the final result, especially in any experiment that has a limited number of readings. In this capacity, the selection of a rectangular distribution as the prior, is far from arbitrary, and is usually referred to as *Bayes' Equal Likelihood Postulate*. Shannon's theory of information entropy demonstrates that, with only range information available, a rectangular distribution has the least bias towards the final outcome of all possible distributions. Where more information is available, for example, a mean and standard deviation, other distributions become appropriate. See Smith [144] for more information, and details of the distributions applicable in other cases.

and so on, giving the general expression

$$p_n(\theta) = p(\theta \mid \theta_1, \theta_2, \ldots, \theta_n) = \frac{1}{C}\left[\prod_{j=1}^{j=n} L(\theta_j \mid \theta)\right] p_a(\theta). \tag{B.4}$$

where C is a normalisation constant to ensure that the sum of the probabilities is unity.

Using the final p.d.f., a new estimate of the value of the systematic error parameter, θ, and the uncertainty in its value can be calculated as the mean, $< \theta >$ and standard deviation, σ_θ respectively, where

$$< \theta >= \int_{-\infty}^{\infty} \theta \; p_n(\theta) \; d\theta, \tag{B.5}$$

and

$$\sigma_\theta = \sqrt{\int_{-\infty}^{\infty} (\theta - < \theta >)^2 \; p_n(\theta) \; d\theta}. \tag{B.6}$$

Returning to the investigation of the offset of the stagnation pressure probe, Shannon's information entropy methodology shows that the correct form of likelihood distribution to represent measurements of a location parameter θ_i, and its error σ_i is normal. When performing the calibration of the probe, we employ

$$L(\theta \mid \theta_i) = \frac{1}{\sigma_i\sqrt{2\pi}} e^{-\frac{1}{2}\left(\frac{\theta-\theta_i}{\sigma_i}\right)^2}. \tag{B.7}$$

This methodology provides a consistent and rigourous means of combining repeated estimates of the yaw offset in the aerodynamic probes, yielding both a value for the offset, which can be easily corrected for in the vortex tube readings, and an estimate of the uncertainty in this offset which must be accounted for in any overall error assessment. In practice, the effort involved was only beneficial in calibration of the stagnation pressure probe. Since this probe was used to determine the direction of the flow, a good knowledge of its errors was desirable to provide uncertainty information with regard to the flow angle. With the other two probes, knowledge of their offsets was only required for

their subsequent alignment with the flow. As neither probe was particularly sensitive to direction, a single measurement of their offsets was satisfactory, and there was no need to estimate uncertainty.

Such a procedure, can of course be applied to an attempt to evaluate a location parameter. It would have been possible to apply the Bayesian technique to every reading taken during the vortex tube flow mapping. This would be a complicated operation, with a very small additional benefit in comparison with the technique employed in the main text.

B.2.3 Stagnation Pressure Probe

The stagnation pressure probe was found to give essentially accurate measurements of the stagnation pressure at all flow velocities, so long as it was aligned with the flow. Precision of the stagnation pressure readings was thence entirely dependent on the manometer connected to the probe.

In the worst cases, for large pressure differences, a vertical mercury filled manometer with a millimetre scale was used. This would give an uncertainty in the readings of approximately $\pm$ 70 Pa. For small differences an alcohol manometer at a shallow angle was used. In principle this should give a much more accurate result, but often the liquid column would fluctuate, raising the absolute error to around $\pm$ 20 Pa.

Combining the results of the Bayesian offset measurement, with the limitations of the protractor employed, suggested that angular measurements were accurate to $\pm\ 3^o$.

B.2.4 Stagnation Temperature Probe

The stagnation temperature probe had a recovery factor of $R_T = 0.6$, with an estimated error of $\pm$ 10. There was no detectable variation of this parameter for flow speeds greater than 10 m/s, or over the amazingly wide angular range of $\pm 30^o$.

Considering the observed fluctuation of readings, and the specification of the thermocouple, the precision of the temperature readings was estimated to be ± 0.5 K.

B.2.5 Static Pressure Probe

The static pressure probe was found to give an accurate value for the static pressure across the range of flow velocities. In this case the precision of the readings is dictated by the manometer used. The comments made for the stagnation pressure probe apply here.

The probe was found to be insensitive to yaw angles of $\pm 10^{o}$, essentially eliminating any errors due to misalignment. This was unsurprising, as the probe had been specifically designed to be tolerant to angular misplacement.

B.3 Estimates of Other Errors

There are two other sources of uncertainty in the experiment not yet considered. Firstly fluctuations in the reservoir conditions could have caused errors. However, there was no evidence of rapid fluctuations in the supply, and no means by which to measure them, had they been present. Slow (period $>$ 10 minutes) fluctuations were observed, but steps were taken to correct for them.

A second source of uncertainty are errors in the spatial positioning of the probes. The axial position of the holes through which the probes were inserted was measured with a metre rule, giving an uncertainty of $\pm$ 0.5 mm. Radial positioning was dictated by the traverse equipment, which allowing for setting up errors also had an uncertainty of $\pm$ 0.5 mm.

It would be quite possible to convert the positional errors into errors in the measured variables, namely the stagnation pressure, stagnation temperature, static pressure and flow angle. Such a step has not been taken here, as it is a relatively simple matter to maintain both the positional and measurement error fields concurrently. When, for example, fitting a curve to data relating the stagnation temperature variation to the radial position, the two fields can be accommodated by specifying the (known) uncertainty in both co-ordinates. To attempt reduce the two error fields to one here would only serve

Description	Symbol	Value
Mach Number Calculation		
Static and stagnation pressure	$K_{p_o,p}$	0.5
Stag. Temperature Calculation		
Mach no. and recovery temp.	K_{M,T_R}	0.1
Mach no. and recovery factor	$K_{M,R}$	0.5
Recovery factor and recovery temperature	$K_{T_R,R}$	0.5

Table B.1: The correlation coefficients between the uncertainty estimates.

to complicate matters unnecessarily.

B.4 Correlation Coefficients

The error analysis employed in the main text requires estimates of the correlations of the uncertainties in the measures variables. Table B.1 gives the numerical values of the correlations used in the calculations of the flow Mach number and the stagnation temperature. Both these quantities are calculated directly from measured data. Other quantities of interest, in particular the static temperature, the flow velocity, and the density, depend to some extent on previously derived values. In these cases, the correlation coefficients between the variables cannot be given explicitly, as they vary with the values involved. Instead these correlation coefficients have to be calculated according to the standard expression for the correlation of two random variables, a, and b

$$\rho_{a,b} = \frac{cov\,(a,b)}{\sqrt{var\,(a)\;\;var\,(b)}}. \tag{B.8}$$

In all the cases considered, the error in each variable can be divided into two parts, one fully correlated with the other variable V, and one completely independent I. As such the correlation coefficient expression can be reformulated as

$$K_{x_{ij}} = \frac{Product\ of\ fully\ correlated\ errors}{Product\ of\ total\ errors} \tag{B.9}$$

or

$$K_{x_{ij}} = \frac{V_i V_j}{E_i E_j} \tag{B.10}$$

where

$$\sigma_{xi}^2 = V_i^2 + I_i^2 \tag{B.11}$$

$$\sigma_{xj}^2 = V_j^2 + I_j^2 \tag{B.12}$$

recalling that σ_{xi} represents the absolute error in the i^{th} component of the observables vector $\mathbf{x}$, and $K_{x_{ij}}$ is the correlation coefficient relating the i^{th} and j^{th} components. The following expressions for the remaining correlation coefficients are obtained:

Mach number, M, and stagnation temperature, T_0

$$K_{M,T_0} = \frac{\left(\frac{\partial T_0}{\partial M}\right)_{\mathbf{x}} \sigma_M \cdot \sigma_M}{\sigma_M \sigma_{T_0}} \tag{B.13}$$

Mach number, M, and static temperature, T

$$K_{M,T} = \frac{\left(\frac{\partial T_0}{\partial M}\right)_{\mathbf{x}} \sigma_M \cdot \sigma_M}{\sigma_M \sigma_T} \tag{B.14}$$

Pressure, P, and static temperature, T

$$K_{P,T} = \frac{\left(\frac{\partial T}{\partial M}\right)_{\mathbf{x}} \left(\frac{\partial M}{\partial P}\right)_{\mathbf{x}} \sigma_P \cdot \sigma_P}{\sigma_P \sigma_T}. \tag{B.15}$$

The differential terms are obtained as the results of the linearisation process described in section 3.5.3. The $_{\mathbf{x}}$ appended to each implies that the expression are to be evaluated at the current value of the observables matrix $\mathbf{x}$.

Appendix C

The Numerical Tests Carried Out on the Code

C.1 Introduction

In this appendix the numerical tests used to asses the vorticity-streamfunction solver are discussed in more detail than was possible in the main text. In all cases some quantitative indication of the results is given.

C.2 The Driven Cavity Laminar Benchmark

The basics of the vorticity-streamfunction solver were tested using the driven cavity problem. This problem is commonly used as a benchmark for numerical routines, and is quite well suited to the vorticity-streamfunction technique. It is a two dimensional laminar problem, in Cartesian co-ordinates, and thus tests only the vorticity and streamfunction solutions. Although the other solutions presented in this thesis are in cylindrical co-ordinates, a generalised orthogonal co-ordinate system was employed for the discretisation of the vorticity and streamfunction equations. The result of this is that the code is able to solve the vorticity and streamfunction equations in Cartesian co-ordinates, and

thus deal with the benchmark. Note that none of the other variables solved for were dealt with using the generalised system, as it was often advantageous to take advantage of the particular symmetry of the cylindrical co-ordinates system.

The driven cavity problem consists of the solution of the flow field within a two dimensional square cavity with a moving wall, as shown in figure C.1. To provide the boundary conditions, the streamfunction ψ is constant on all walls and is generally taken as zero. The vorticity at each wall was computed from a second order condition (see for example Gosman [50]).

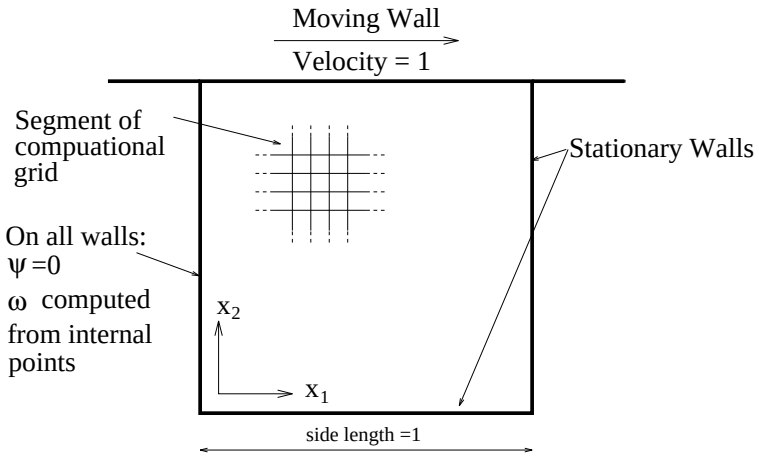

Figure C.1: Computational domain for the driven cavity problem.

A solution for the driven cavity problem at a Reynolds number Re of 1000 computed by the vorticity-streamfunction solver on a regular 21x21 grid is given in figure C.2. The contours represent streamfunction values. Comparison with a solution computed by Gosman [50] on a 13x13 irregularly spaced grid shown in figure C.3 is reasonable. The differences can probably be attributed to the inadequacies of the contouring techniques used in each case[1].

In order to test the degree of dependence of the solutions obtained on the grid em-

[1]Gosman estimated contours by hand. The contours for the vorticity-streamfunction solution were estimated using the Matlab package. The contouring technique it employs is not described in detail.

Figure C.2: Result using the vorticity-streamfunction solver to solve the square cavity benchmark problem on a 21x21 grid.

Figure C.3: Benchmark solution to the square cavity problem. Computed on an irregularly spaced 13x13 grid.

ployed, a further computation of exactly the same benchmark was performed on a grid of 91x91 points. The result is given in figure C.4, and has a reasonable correspondence to the previous solution. Again uncertainties about the contouring routine make comparison difficult.

Figure C.4: Result using the vorticity-streamfunction solver to solve the square cavity benchmark problem on a 91x91 grid.

C.3 The Rotating Pipe Flow Laminar Benchmark

To test the combined performance of the swirl and vorticity-streamfunction solvers, a benchmark comprising the solution of a strongly swirling flow in axisymmetric cylindrical co-ordinates was computed. Figure C.5 defines the problem. Further details are given in Silvester *et al.* [2], from where the benchmark solution in figure C.6 is taken. Two characteristic features are presented. Firstly the variation of axial velocity on the centre-line of the tube as a function of the axial distance from the origin of co-ordinates, and secondly the profiles of axial velocity at stations near to the origin. Computed solutions will be presented in a similar format, although discrepancies in the positions of the grid nodes mean that it will not always be possible to give the velocity profiles at exactly the same axial positions used by Silvester. In these cases a series of profiles near the origin will be given, and the reader left to judge the results qualitatively.

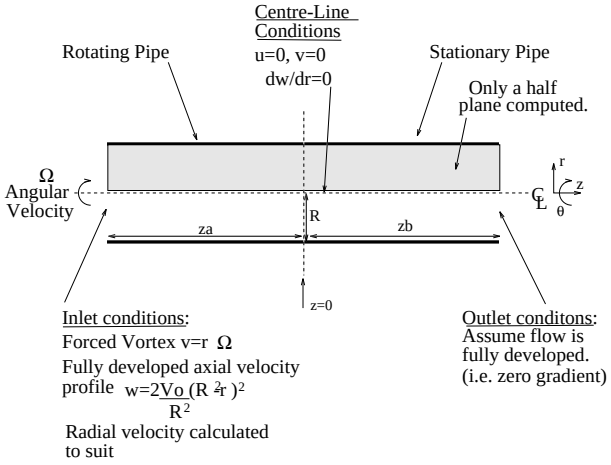

Figure C.5: Definition of the laminar swirling benchmark problem.

Figure C.6: Benchmark solution of the laminar swirling flow problem. Taken from Silvester *et al.* [2].

A solution of the benchmark problem provided by the vorticity-streamfunction solver using a 91x91 regularly spaced grid, is presented in figure C.7. Comparison with the benchmark solution shows a good qualitative similarity and a fair quantitative one. The area of recirculation caused by the decay of the swirl is resolved quite well. Results using a 31x31 grid (figure C.8) also stand comparison.

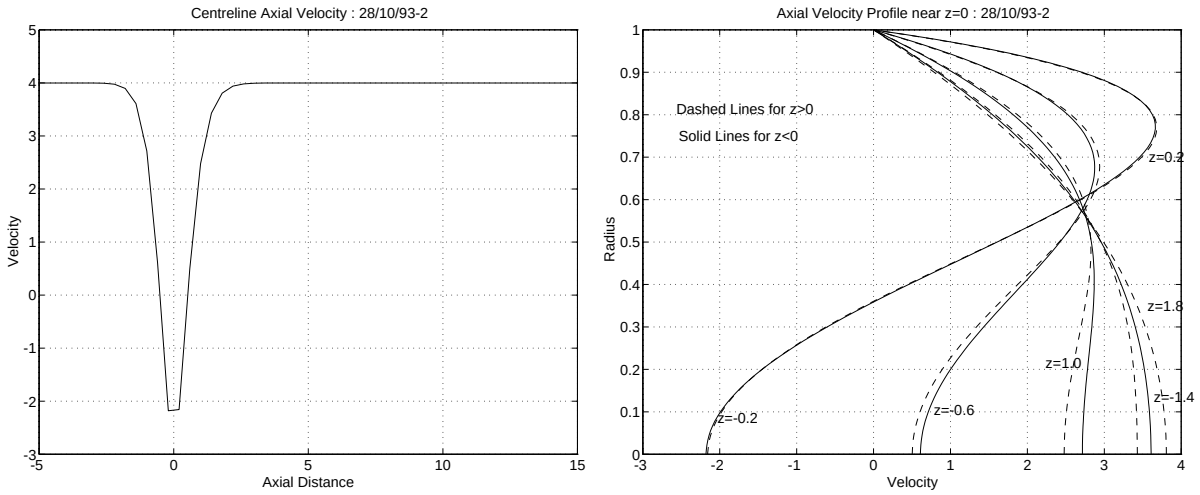

Figure C.7: Calculated solution of the laminar swirling flow problem using a 91x91 regular grid.

Further calculations were performed using a 31x31 irregularly spaced grid, with a concentration of nodes in the region where recirculation is present. The results are shown in figure C.9. As with the preceding calculations, the qualitative comparison is respectable, but the magnitude of the axial velocity reversal on the centre-line is over estimated.

To assess the mass conservation properties of the vorticity-streamfunction solver, the axial mass flow rate at each of the stations shown in figure C.9 was calculated. The outcome is given in figure C.10, where the normalised axial mass flow rate is plotted against axial distance from the origin of co-ordinates. The variation in mass flow rate was found to be of the order of 2.9 percent, a fairly small error, and adequate for the purposes of this work.

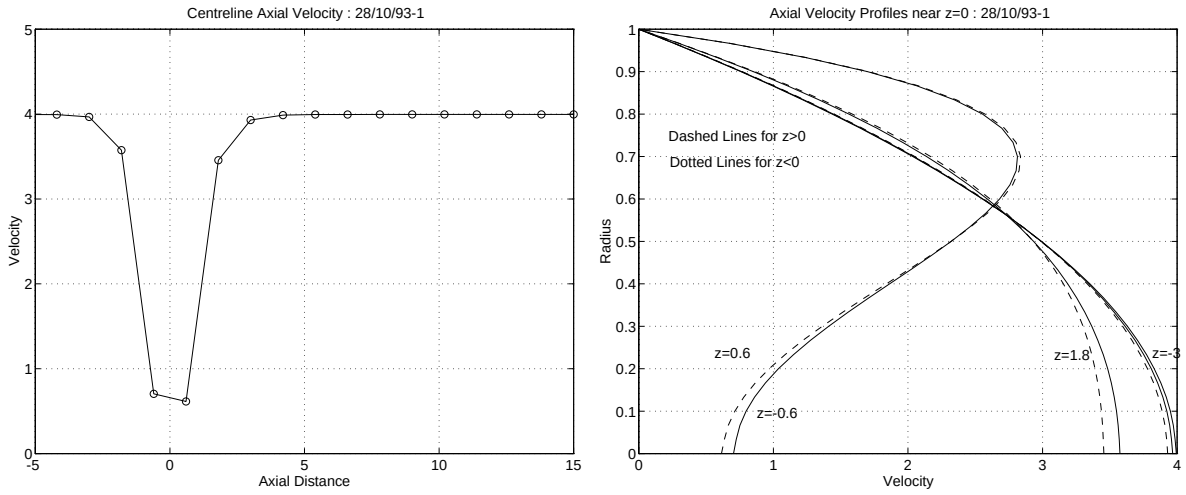

Figure C.8: Calculated solution of the laminar swirling flow problem using a 31x31 regular grid.

C.4 The Turbulent Pipe Flow Benchmark

Assessment of the implementation of the two-equation turbulence model was achieved though calculation of a turbulent pipe flow, without any swirl. The benchmark solution was taken as the results of Nikuradse's quasi-analytical solution (see Schlicting [125]).

The numerical problem considered is defined well by Elkaim *et al.* [52]. A fluid enters a circular channel with a uniform velocity profile and a Reynolds number based on the channel diameter of 1.1×10^5. At the exit, the flow is fully developed, and it is this velocity profile that is considered. Under such conditions Nikuradse gives the axial velocity profile as

$$\frac{w}{W} = \left(\frac{R-r}{R}\right)^{\frac{1}{7}} \tag{C.1}$$

where R is the maximum radius and W the maximum axial velocity.

Figure C.11 gives the numerical results and the analytic solution. The comparison is quite good, and verifies the performance of the turbulence model.

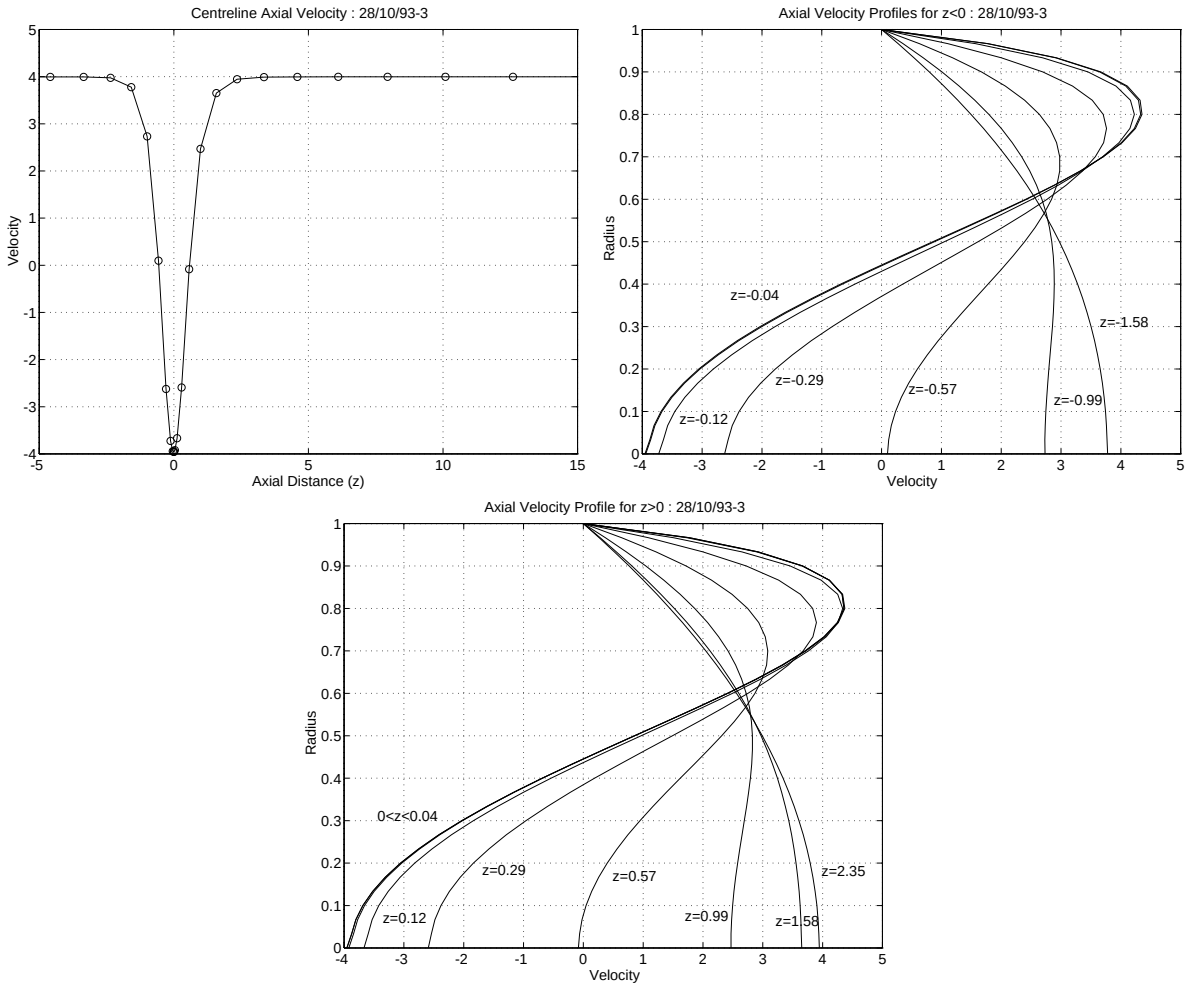

Figure C.9: Calculated solution of the laminar swirling flow problem using a 31x31 irregular grid.

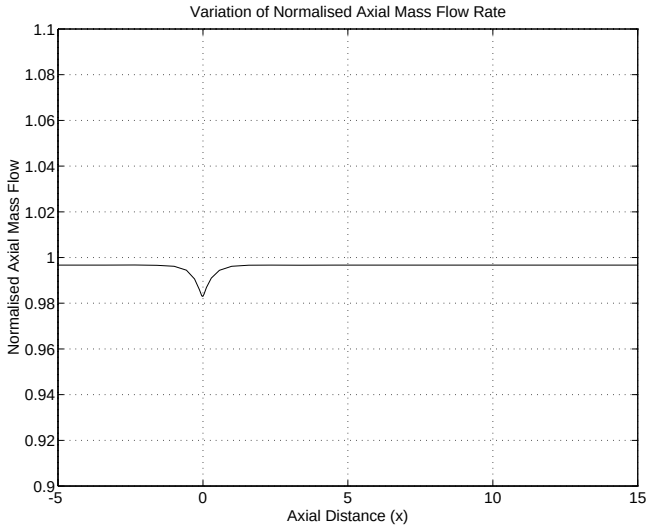

Figure C.10: Variation of calculated axial mass flow rate.

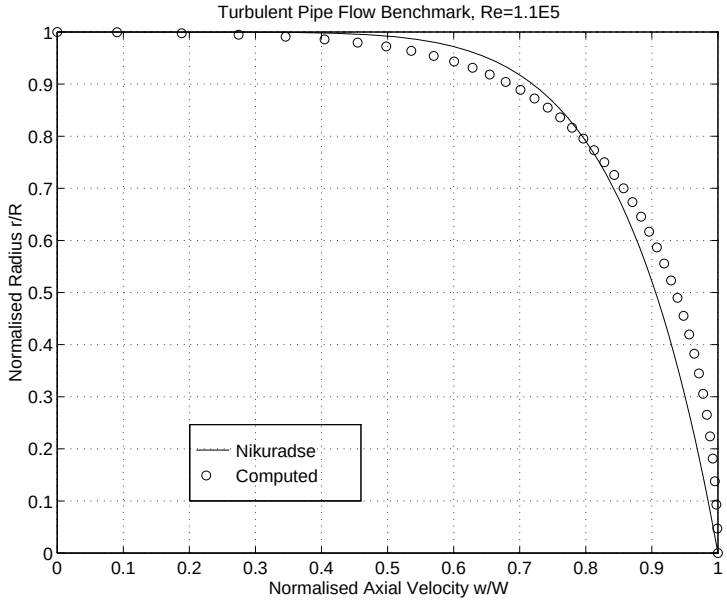

Figure C.11: Comparison of the axial velocity profile provided by the vorticity-streamfunction solver with the solution of Nikuradse [125] for a turbulent pipe flow. The points show the numerical solution, while the solid line gives Nikuradse's result.

C.5 Conclusions

The basic function of the numerical solution of the vorticity-streamfunction method employed in the main text has been validated. Calculations of a driven cavity problem, and of the swirling flow in a pipe gave fair comparisons with benchmark solutions.

The turbulence model was assessed through a calculation of the fully developed velocity profile in a turbulent pipe flow. Results compared well with classical solutions.

Appendix D

Outline of a Proposed Experiment for Further Investigation of Centrifugation Effects within the Vortex Tube

D.1 Introduction

This appendix outlines a possible experimental procedure that could be used for further investigations of the isotope separation abilities of the vortex tube. Only basic ideas are given, and certainly there would be much development work necessary in order to produce a working system. Successful implementation could provide the foundation for a comprehensive experimental study of isotope separation within the vortex tube.

D.2 Concept

The procedure envisaged employs optical means to deduce concentrations of components, using the phenomenon of fluorescence. When a molecule is irradiated by light of a suitable frequency, it absorbs a portion of the incident energy. A fraction of this is subsequently re-emitted in all directions as fluorescence.

If particular regions of a multicomponent gas are illuminated so as to cause one of its components to fluoresce, the intensity of the fluorescence in any particular region will be related to the concentration of that component there. This can be applied to a flowing gas in a transparent vortex tube to obtain some indication of the component concentrations at various points within the tube. The best approach would appear to involve illuminating whole cross-sections of the vortex tube with sheets of light and view them from a perpendicular direction as indicated in figure D.1. Illumination could be provided by a laser with a cylindrical lens or possibly by an illuminated slit, although care would have to be taken to ensure that the beam was not too divergent axially and illuminated a narrow plane.

A permanent record could be made photographically or with a high speed video camera. In the latter case a frame grabber could be used to digitise the picture and allow its analysis by computer. Since the fluorescence frequency differs from the illumination frequency, a filter designed to pass only the fluorescence frequency inserted between the observing device and the vortex tube would greatly improve the quality of the images.

The method will produce a concentration 'map' of the particular component within each cross-section. To make quantitative deductions it is necessary to understand the factors that influence molecular fluorescence.

The frequency of the radiations is affected by a number of parameters, including the flow conditions. This is not the primary concern here, but it is worth noting that it allows the measurement of certain flow properties, including pressure and temperature by fluorescence.

Of particular interest is the intensity of the emissions, which is dependent only on the number density of molecules, and the intensity of the incident radiation. The intensity of the fluorescence of a group of molecules varies in a complicated manner with increasing illumination intensity until a saturation value is reached. Above this level, the fluorescence intensity is independent of the illumination intensity. In such cases, the intensity of the fluorescence is directly proportional to the concentration (number density of molecules) of the component concerned, which is clearly beneficial. It is thus important to

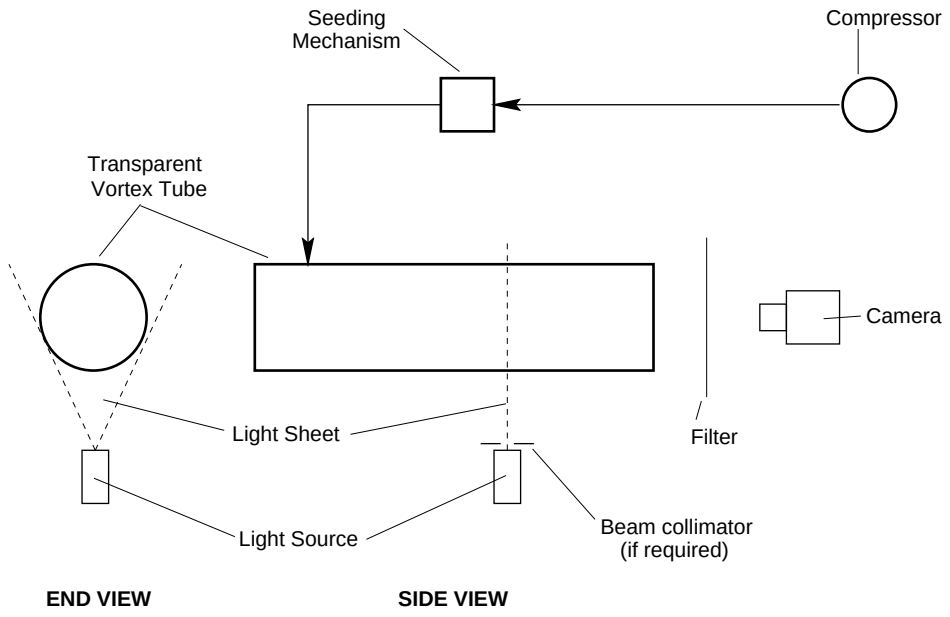

Figure D.1: The illumination arrangement for concentration measurements.

ensure that the illumination over the entire field of interest is greater than the saturation value. Account must be taken of the fact that the illumination intensity falls as the light passes through the flow field and is absorbed. Means of doing this are discussed by Huller and Hanson [145].

A further matter for consideration is which component of the flow through the vortex tube is the best to attempt to fluoresce. Unfortunately none of the components of air will fluoresce within the visible spectrum, rendering most optical recording techniques impractical. It is preferable to introduce a tracer gas which will fluoresce visibly. This has the added advantage that it would be possible to control the inlet concentration of the tracer to provide the greatest contrast between the low and high number density sites.

A good choice for the tracer is 2-3 butanedione, commonly known as biacetyl. It can be excited relatively easily, has a fairly wide fluorescence spectrum, is non-toxic and relatively inexpensive (see Epstein [146]). The only disadvantage is that it is an inefficient fluorescer, and may be difficult to capture on film. An alternative is iodine which provides a much greater light output, but imposes operational difficulties thanks to its mild tox-

icity. Its use in an open circuit arrangement, as is common with vortex tubes, would probably be impractical.

Appendix E

A Novel Method for Estimating the Velocity Distribution Across the Radius of a Vortex Tube

E.1 Background

Good experimental measurements of the flow parameters, particularly the fluid velocity, are difficult to obtain in a vortex tube for two reasons. Firstly inserting any probe into the tube substantially alters the flow pattern. Secondly the high levels of turbulence cause large and rapid fluctuations in several of the flow parameters simultaneously. Standard intrusive techniques have been developed to levels of sophistication that can overcome the second problem, but can be cumbersome and difficult to implement. Velocity measurement using a hot-wire, as an example, requires the use of two probes for accurate results: one to measure velocity fluctuations and a second to compensate for temperature fluctuations. This makes for a bulky arrangement causing considerable disruption to the flow. Additionally, inaccuracy is introduced thanks to the inevitable distance between the probes, and the whole assembly proves inconvenient.

Arguably the easiest flow parameter to measure in the vortex tube is the stagnation

pressure. This requires only a very small pressure probe, aligned such that its 'measuring hole' faces directly into the flow and connected to a manometer. There is comparatively little flow disruption, and as a bonus, the variation of the measured stagnation pressure as the probe is rotated can be used to deduce the approximate flow direction. The probe is quick and easy to use.

A method has been developed which allows velocity information to be deduced from radial traverses of the stagnation pressure in the vortex tube. While the accuracy of the method is not high, it does seem to provide a valid quantitative picture of the flow in the vortex tube. The stagnation pressure based method is quick and easy to use, making it convenient for rough investigations.

E.2 Theory

Assume that the swirl velocity across the radius of a vortex tube varies according to the relation

$$v = kr^n \tag{E.1}$$

where v is the swirl velocity, k and n are unknown constants to be determined, and r is the radial distance from the centre-line. This may seem a rash assumption, but examination of swirl velocity profiles available in the literature suggests that the departure from this simple analytical expression is small outside of the boundary layer on the curved wall. Holmann and Moore [18] in particular are able to model the vortex in a tube very well with a comparable expression.

Now assume that the flow is in *simple radial equilibrium*, such that the centripetal force required for circular motion is provided exclusively by the radial pressure gradient. Thus a force balance gives

$$\frac{\partial P}{\partial r} = \frac{\rho v^2}{r} \tag{E.2}$$

with P the static pressure, and ρ the density. This is a reasonable assumption, as is discussed in the main text, so long as the swirl velocity is the major component of the velo-

city vector and the effects of the axial and radial velocities can be neglected.

Eliminating v gives

$$\frac{\partial P}{\partial r} = \rho k^2 r^{(2n-1)}. \tag{E.3}$$

So long as $n \neq 0$, i.e. $2n - 1 \neq -1$

$$\int_{P_{cl}}^{P} dP' = \int_{0}^{r} \rho k^2 r'^{(2n-1)}\, dr' \tag{E.4}$$

which yields

$$P - P_{cl} = \frac{\rho k^2}{2n}\left(r^{2n}\right) \tag{E.5}$$

where P_{cl} is the static pressure at the centre-line.

Stagnation pressure for incompressible[1] flow is defined as

$$P_0 = P + \frac{1}{2}\rho v_{tot}^2 \tag{E.6}$$

where P_0 is the stagnation pressure and v_{tot} is the absolute fluid velocity. If α is the angle between the direction of flow and the axis of the vortex tube, and w is the axial component of velocity, then by simple geometry

$$tan(\alpha) = \frac{v}{w} \tag{E.7}$$

and thence

$$P_0 = P_{cl} + \frac{1}{2}\rho v^2 \left(1 + \frac{1}{tan(\alpha)}\right). \tag{E.8}$$

Using equation (E.5) gives

$$P_0 = P_{cl} + \frac{\rho k^2}{2}\left\{\frac{r^{2n}}{n} + r^{2n}\left(1 + \frac{1}{tan(\alpha)}\right)\right\}. \tag{E.9}$$

[1]The approximate method assumes that the flow is incompressible. As such, its success or otherwise could be regarded as an indication of the importance of compressibility in the fluid mechanics of the vortex tube.

We can use this expression to deduce the swirl velocity distribution from the information produced by a stagnation pressure probe in a number of ways. The most general will be described, but note that all the techniques are based around determining the value of n in equation (E.9).

The stagnation pressure probe tells us the radial variation of stagnation pressure P_0 and flow angle α. Let us assume for this calculation that the static and stagnation pressures on the centre-line of the tube are both equal to atmospheric pressure P_{atm}. This need not be the case - the 'exact' values can be determined fairly easily from experiments - but it makes the argument easier.

Putting

$$\Delta P = P_0 - P_{cl} \tag{E.10}$$

equation (E.9) can be written

$$ln(\Delta P) - ln\left\{\frac{1}{n} + 1 + \frac{1}{tan(\alpha)}\right\} = ln\left(\frac{\rho k^2}{2}\right) + 2n\ ln(r). \tag{E.11}$$

We have to use an iterative method to determine n. Let our initial estimate be n_1, so

$$ln(\Delta P) - ln\left\{\frac{1}{n_1} + 1 + \frac{1}{tan(\alpha)}\right\} = ln\left(\frac{\rho k^2}{2}\right) + 2n\ ln(r). \tag{E.12}$$

Plotting $ln(\Delta P) - ln\left\{\frac{1}{n_1} + 1 + \frac{1}{tan(\alpha)}\right\}$ against $ln(r)$ should yield a straight line with intercept $ln\left(\frac{\rho k^2}{2}\right)$ and gradient $2n$. We can take this value of the gradient to be a new estimate for n, which we can term n_2. Using this n_2 we can recompute our values and gain a new estimate n_3, continuing to convergence.

With a 'good' value for n we can estimate the swirl velocity distribution using equation (E.1), and then get the axial velocity with relationship (E.7).

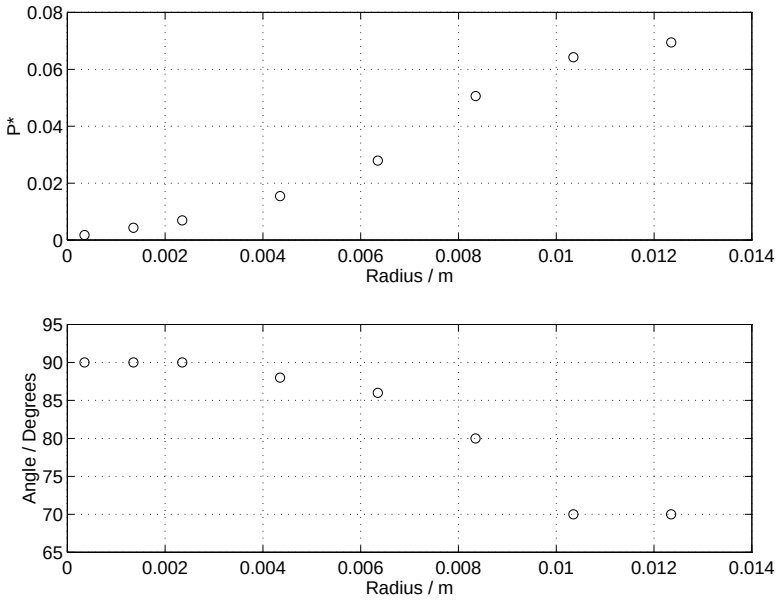

Figure E.1: Measured variation of stagnation pressure and flow angle across the radius of the 26 mm diameter vortex tube. P^* represents a normalised stagnation pressure.

E.3 Method and Results

To estimate the velocity distribution across the vortex tube radius, it is first traversed with a stagnation pressure probe, recording values of stagnation pressure and flow direction at a number of points. The flow direction is determined by rotating the probe in its holder and looking for the maximum reading, indicating that the probe is then pointing directly upstream.

The theory outlined above is unable to estimate the velocity distribution across the boundary layer on the cylindrical wall. Thus there is no need to perform a detailed traverse of this boundary layer. Figure E.1 shows a typical result for the variation of stagnation pressure and flow angle across a vortex tube radius, taken near to the inlets of the 26 mm diameter tube operated at a relatively low pressure.

To deduce the velocity distribution, n in equation (E.9) must first be determined. The iterative method outlined above is used, taking an initial guessed value for n to evaluate

the right and left hand sides. Plotting the values gives a straight line, the gradient of which gives a better estimation of n, and the process is repeated until convergence.

The method was applied to the data of figure E.1. Five iterations were required to produce converged values for the parameters n and k, the progression of which is given in table E.1. The result of the first iteration is given in figure E.2, with the upper diagram showing the function fitted to the raw data, and the lower diagram the corresponding estimated swirl velocity distribution. Figure E.3 gives the final result.

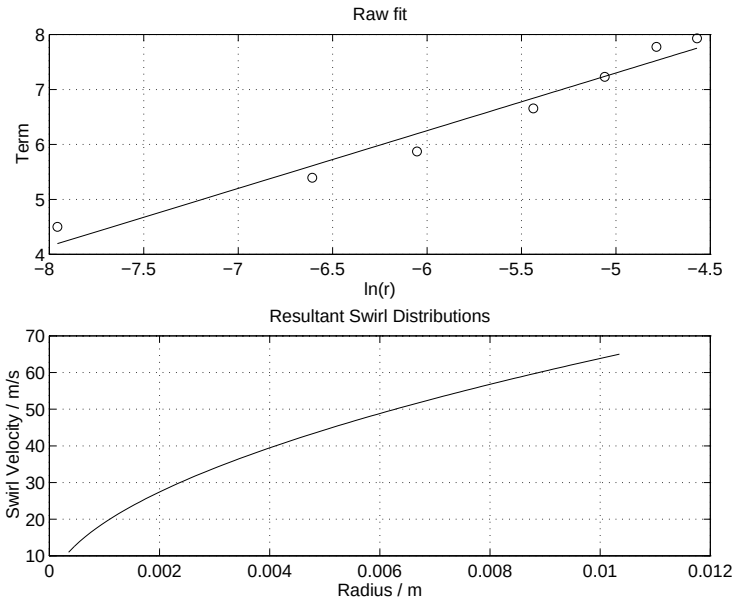

Figure E.2: First fit to the pressure/angle derived data discussed in the text. The upper diagram shows the fitted function compared to the raw data represented by the circles. Note that the vertical axis, labelled 'Term' represents values of $ln\,(\Delta P) - ln\left\{\frac{1}{n} + 1 + \frac{1}{tan(\alpha)}\right\}$. The lower diagram gives the corresponding swirl velocity distribution.

Iteration	1	2	3	4	5
n	1	0.5251	0.5306	0.5305	0.5305
k	9 662	716.7	618.0	619.7	619.7

Table E.1: Development of the vortex parameters with iteration.

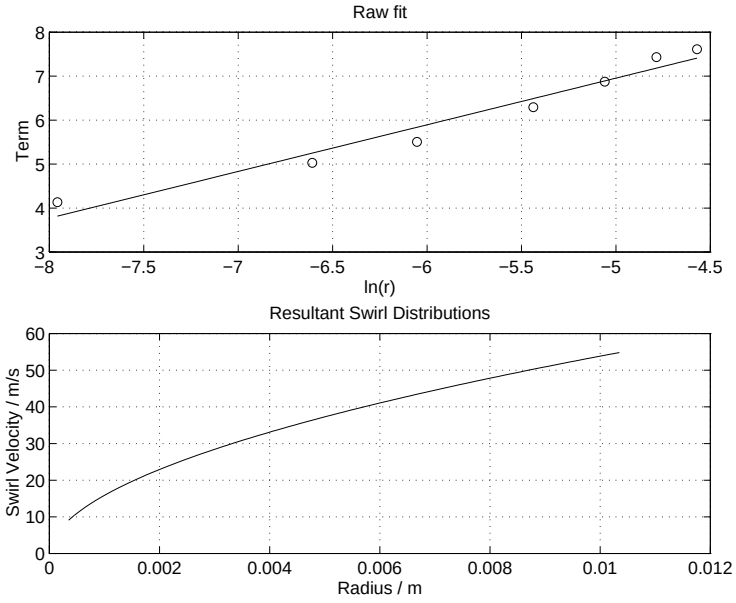

Figure E.3: Fifth and final fit to the pressure/angle derived data discussed in the text. The upper diagram shows the fitted function compared to the raw data represented by the circles. Note that the vertical axis, labelled 'Term' represents values of $ln\left(\Delta P\right) - ln\left\{\frac{1}{n} + 1 + \frac{1}{tan(\alpha)}\right\}$. The lower diagram gives the corresponding swirl velocity distribution.

E.4 Further Evaluation of the Technique

To test the reliability of the method further, it was used to estimate swirl velocity distributions using stagnation pressure and angle data available in the literature for already known swirl velocity distributions. Calculations were performed using two sets of data taken by Lay [74], who investigated the flow within a uniflow vortex tube of approximately 25 mm diameter. Results will be presented for data taken near the inlets, where the swirl velocity is comparable to a forced vortex, and near the valve where the swirl has decayed greatly to produce a much 'flatter' distribution.

E.4.1 Data From Near the Inlet

Figure E.4 shows the resultant fitted function and swirl velocity distribution based only on data taken inside a radius of 18 mm and therefore well outside the cylindrical wall boundary layer. Five iterations were performed, and the comparison in the lower diagram between the estimated function, given by the solid line, and the experimental values calculated by Lay, given by the circles, is very good.

If the approximate solution is extended to include all the data points taken by Lay, as given in figure E.5 then the result is less good, although still useful. The reduced performance in this case is a result of the fact that the data now extends into the cylindrical boundary layer. The simple analytic expression for the swirl velocity cannot cope with this region.

E.4.2 Data From Near the Valve

Comparison between the approximate solution for the swirl velocity and the true experimental values for data taken near to the outlet of Lay's uniflow tube is made in the lower diagram of figure E.6. Even though the fitted function in the upper diagram matches the data well, the method produces a very poor result for the swirl velocity. This is due to the fact that the velocity distribution differs greatly from a forced vortex, and cannot be

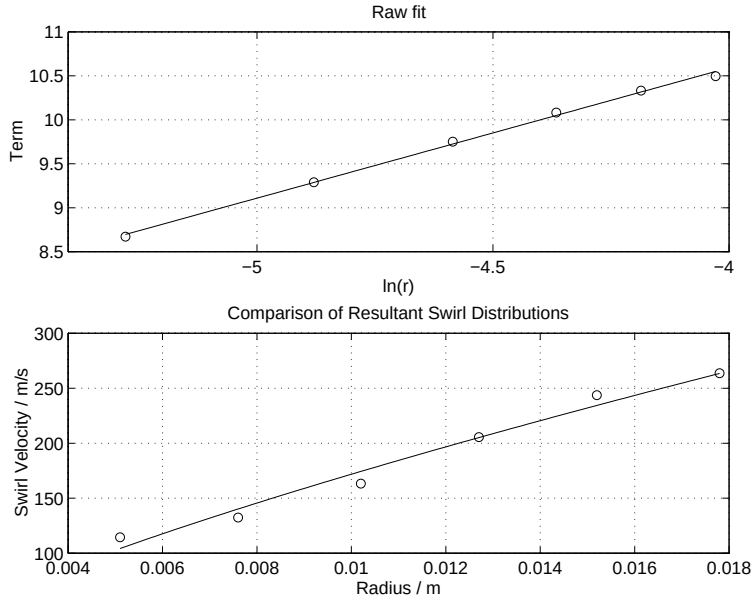

Figure E.4: Resultant fit after five iterations, for data from Lay [74], table 2, station 1, using only the data inside a radius of 0.018 m and outside the boundary layer on the cylindrical wall. The circles represent Lay's data points, and the solid lines give the fitted functions. The upper diagram shows the fitted function compared to the raw data represented by the circles. Note that the vertical axis, labelled 'Term' represents values of $ln\left(\Delta P\right) - ln\left\{\frac{1}{n} + 1 + \frac{1}{tan(\alpha)}\right\}$. The lower diagram gives the corresponding swirl velocity distributions.

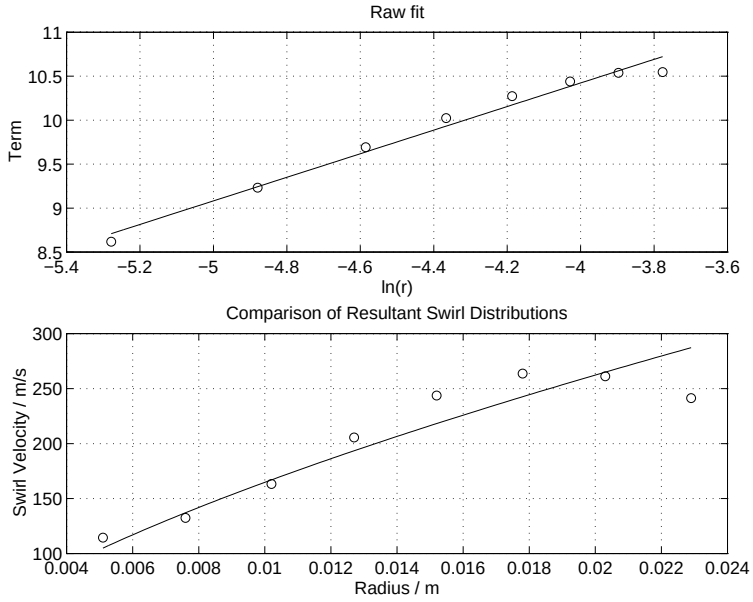

Figure E.5: Resultant fit after five iterations, for data from Lay [74], table 2, station 1, using all data up to the cylindrical wall. The circles represent Lay's data points, and the solid lines give the fitted functions. The upper diagram shows the fitted function compared to the raw data represented by the circles. Note that the vertical axis, labelled 'Term' represents values of $ln\left(\Delta P\right) - ln\left\{\frac{1}{n} + 1 + \frac{1}{tan(\alpha)}\right\}$. The lower diagram gives the corresponding swirl velocity distributions.

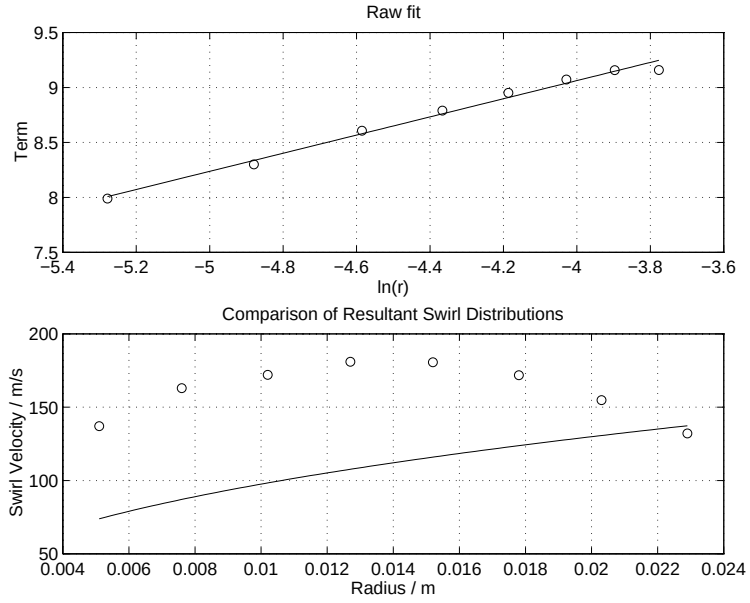

Figure E.6: Resultant fit after five iterations, for data from Lay [74], table 2, station 6, using all data up to the cylindrical wall. The circles represent Lay's data points, and the solid lines give the fitted functions. The upper diagram shows the fitted function compared to the raw data represented by the circles. Note that the vertical axis, labelled 'Term' represents values of $ln\left(\Delta P\right) - ln\left\{\frac{1}{n} + 1 + \frac{1}{tan(\alpha)}\right\}$. The lower diagram gives the corresponding swirl velocity distributions.

modelled by the simple expression. Essentially the boundary layer on the cylindrical wall extends almost all the way to the centre of the tube here.

E.5 Conclusion

The novel method of estimating the velocity distribution across the radius of a vortex tube based only on information from a stagnation pressure probe is a useful means of quickly investigating the flow.

There are two major limitations. Firstly the method assumes an analytic form for the swirl velocity distribution. Secondly, the method cannot calculate velocity distributions within the boundary layer on the cylindrical wall. Both problems can be addressed to

some extent. It is essential to assume an analytic expression for the swirl velocity distribution, but the form of that expression is not limited to the simple form,

$$v = kr^n \tag{E.13}$$

used here. More complex expressions can be incorporated into the theory, and this is an area worthy of investigation. There is also potential for extending the technique to deal with the flow within the boundary layer, by making use of the commonly used assumption that the static pressure is constant across that layer. Again this requires further work – while in principle possible, the difficulties involved in measuring the stagnation pressure in the boundary layer may make the results too inaccurate to be useful.

Bibliography

[1] J J Van Deemter. On the theory of the Ranque–Hilsch cooling effect. *Applied Scientific Research (Series A)*, 3:pp. 174–196, 1952.

[2] D J Silvester, R W Thatcher, and J C Duthrie. The specification and numerical solution of a benchmark swirling laminar flow problem. *Computers and Fluids*, 12(4):pp. 281–292, 1984.

[3] G Ranque. Expériences sur la détente giratoire avec productions simultanées d'un énchappement d'air chaud et d'un énchappement d'air froid. *Journal de Physique et de la Radium*, 4:pp. 1125–1155, 1933.

[4] R Hilsch. The use of the expansion of gases in a centrifugal field as a cooling process. *The Review of Scientific Instruments*, 18(2):p. 108ff, February 1947.

[5] M W Zemansky and R H Dittman. *Heat and Thermodynamics*. McGraw-Hill International, sixth edition. p. 299.

[6] James Clerk Maxwell. *Theory of Heat*. Longman, tenth edition, 1891. pp. 338-339.

[7] R Deissler and M Perlmutter. Analysis of the flow and energy separation in a turbulent vortex. *International Journal of Heat and Mass Transfer*, 1:pp. 173–191, 1960.

[8] M Kurosaka. Acoustic streaming in swirling flow. *Journal of Fluid Mechanics*, page p. 139ff, November 1982.

[9] R Westley. Bibliography and survey of the vortex tube. Cranfield Notes 9, Cranfield College of Aeronautics, 1954.

[10] G F C Rogers and Y R Mayhew. *Engineering Thermodynamics Work and Heat Transfer*. Longman Scientific and Technical, third edition, 1980.

[11] G K Batchelor. *An Introduction to Fluid Dynamics*. Cambridge University Press, 1970.

[12] D J Tritton. *Physical Fluid Dynamics*. Van Nostrand Reinhold (UK) Co. Ltd., 1984.

[13] M Escudier. Confined vortices in flow machinery. *Annual Review of Fluid Mechanics*, 19:pp. 27–52, 1987.

[14] H P Greenspan. *The Theory of Rotating Fluids*. Cambridge University Press, 1968. Chapter 2 introduces Ekman Layers etc.

[15] W S Lewellen. A review of confined vortex flows. Contractor Report CR-1772, NASA, 1971.

[16] F Chang and V K Dhir. Turbulent flow field in tangentially injected swirl flows in tubes. *International Journal of Heat and Fluid Flow*, 15(5):pp. 346–356, October 1994.

[17] G Gyarmathy. Optical measurements of mass density in a high-speed, confined, gaseous vortex. *AIAA Journal*, 7(10):pp. 1838–1845, October 1969.

[18] J P Holman and G D Moore. An experimental study of vortex chamber flow. *Transactions of the ASME*, pages 632–636, December 1961.

[19] M P Escudier, J Bornstein, and N Zehnder. Observations and LDA measurements of confined turbulent vortex flow. *Journal of Fluid Mechanics*, 98(1):pp. 49–63, 1980.

[20] J M Burgers. A mathematical model illustrating the theory of turbulence. *Advances in Applied Mechanics*, pages 197–9, 1948.

[21] C W Oseen. *Ark. f. Math. Astron. och. Fys.*, 9, 1911.

[22] C W Oseen. *Hydromechanik*. Leipzig, 1927.

[23] H Schlichting. *Boundary Layer Theory*. McGraw-Hill Book Company, sixth edition, 1968. p. 81.

[24] G H Vatistas. Tangential velocity and static pressure distributions in vortex chambers. *AIAA Journal*, 25(8):pp. 1139–1140, October 1987.

[25] A S Nejad and S A Ahmed. Flow field characteristics of an axisymmetric sudden-expansion pipe flow with different initial swirl distribution. *International Journal of Heat and Fluid Flow*, 13(4):pp. 314–321, December 1992.

[26] S Gilham, P C Ivey, and J M Owen. Self-induced flow and heat transfer in a rotating tube. *International Journal of Heat and Fluid Flow*, 14(1):pp. 27–36, March 1993.

[27] O Kitoh. Experimental study of turbulent swirling flow in a straight pipe. *Journal of Fluid Mechanics*, 225:pp. 445–479, 1991.

[28] M P Escudier and J J Keller. Vortex breakdown : A two stage transition. Current Papers 342, AGARD, 1983.

[29] M P Escudier and J J Keller. Recirculation in swirling flow : A manifestation of vortex breakdown. *Journal of the American Institute of Aeronautics and Astronautics*, 23:pp. 111–116, 1985.

[30] J H Faler and S Leibovich. Disrupted states of vortex flow and vortex breakdown. *The Physics of Fluids*, 20(8):pp. 1385–1400, 1977.

[31] J H Faler and S Leibovich. An experimental map of the internal structure of a vortex breakdown. *Journal of Fluid Mechanics*, 86:p. 313ff, 1978.

[32] T B Benjamin. Theory of the vortex breakdown phenomenon. *Journal of Fluid Mechanics*, 14:pp. 593–682, 1962.

[33] H B Squire. Analysis of the vortex breakdown phenomenon, part 1. *Miszellanen der Angewandten Mechanik*, pages 306–312, 1962.

[34] B Vonnegut. A vortex whistle. *Journal of the Acoustical Society of America*, 26:pp. 18–20, 1954.

[35] R C Chanuad. Experiments concerning the vortex whistle. *Journal of the Acoustical Society of America*, 35:pp. 953–960, 1963.

[36] R C Chanaud. Observations of oscilliatory motion in certain swirling flows. *Journal of Fluid Mechanics*, 21:p. 111ff, 1965.

[37] C A J Fletcher. *Computational Techniques for Fluid Dynamics : Volume 1*. Springer Series in Computational Physics. Springer-Verlag, second edition, 1991.

[38] O L Anderson. Theoretical effect of Mach number and temperature gradient on primary and secondary flows in a jet driven vortex. Technical Report RTD-TDR-63-1098, UAC Research Laboratory, 1962.

[39] M L Rosenzweig, W S Lewellewn, and D H Ros. Confined vortex flows with boundary layer interaction. Technical Report ATN-64(9227)-2 AD 431844, 1963.

[40] C U Linderstrom-Lang. The three-dimensional distributions of tangential velocity and total-temperature in vortex tubes. *Journal of Fluid Mechanics*, 45(1):pp. 161–187, 1971.

[41] A Favre. *J. Mech.*, 4:pp. 361–390, 1965.

[42] T Cebeci and A M O Smith. *Analysis of Turbulent Boundary Layers*. Academic Press, New York, 1974.

[43] W P Jones and B E Launder. The predicition of laminarization with a two-equation model of turbulence. *International Journal of Heat and Mass Transfer*, 15:pp. 301–314, 1972.

[44] Z Y Yang, G H Priestman, and H F Boysan. Internal flow modelling of vortex throttles. *Proceedings of the Institution of Mechanical Engineers Part C : Journal of Mechanical Engineering Science*, 205:pp. 405–413, 1991.

[45] M A Leschziner and W Rodi. Computation of strongly swirling axisymmetric free jets. *Journal of the AIAA*, (22):pp. 1742–1747, 1984.

[46] K Y Kim and M Y Chung. New eddy viscosity model for computation of swirling turbulent flows. *AIAA Journal*, 25(7):pp. 1020–1022, July 1987.

[47] R G Ragsdale. Applicability of mixing length theory to a turbulent vortex system. Technical Notes TN D-1051, NASA.

[48] S W Armfield and C A J Fletcher. Comparison of $k - \epsilon$ and algebraic Reynolds stress models for swirling diffuser flow. *International Journal for Numerical Methods in Fluids*, 9:pp. 987–1009, 1989.

[49] M J Warfield and B Lakshiminarayana. Computation of rotating turbulent flow with an algebraic Reynolds stress model. *AIAA Jounal*, 25(27):pp. 957–963, July 1987. Presented as paper 86-0214 at the AIAA 24th Aerospace Sciences Meeting, Reno, NV, 6-9 January 1986.

[50] A D Gosman, W M Pun, A K Runchal, D B Spalding, and M Wolfshtein. *Heat and Mass Transfer in Recirculating Flow*. Academic Press, Department of Mechanical Engineering, Imperial College of Science and Technology, London, 1969.

[51] I Kubo and F C Gouldin. Numerical calculations of turbulent swirling flow. *Transactions of the ASME : Journal of Fluids Engineering*, pages 310–315, September 1975. Also presented at the Joint Fluids Conference (Combustion Symposium), Monteal, Canada, May 13-15, 1974.

[52] D Elkaim, M Reggio, and R Camarero. Simulating two dimensional turbulent flow by using the $k - \epsilon$ model and the vorticity-streamfunction formulation. *International Journal for Numerical Methods in Fluids*, 14:pp. 961–980, 1992.

[53] A D Gosman and W M Pun. Calculation of recirculating flows. Technical Report HTS/74/2, Mechanical Engineering Department, Imperial College, London, 1974.

[54] I Harada. Computation of strongly compressible rotating flows. *Journal of Computational Physics*, 38:pp. 335–356, 1980.

[55] A I Borisenko, V A Safonov, and A I Yakovlev. The effect of geometric parameters on the characteristics of a conical vortex cooling unit. *Inzhenerno-Fizicheskii Zhurnal*, 15(6):pp. 988–993, December 1968. Original in Russian. Translation appears in Journal of Engineering Physics.

[56] A I Gulyaev. Investigation of conical vortex tubes. *Inzhenerno-Fizicheskii Zhurnal*, 10(3):pp. 326–331, 1966. Original in Russian. Translation appears in Journal of Engineering Physics.

[57] Khark Aviation Institute. Vortex pipe with nozzle inlet – has diaphragm and conical hot and cold ends. USSR Patent Number SU-455229. WPI Acc. No: 75-N5281W/51, May 1975.

[58] V S Martynovskii and V P Alekseev. Investigation of the vortex thermal separation effect for gases and vapors. *Soviet Physics : Technical Physics*, 26(2):pp. 2233–2243, 1957.

[59] Y D Raiskii and L E Tunkel. Influence of vortex tube configuration and length on the process of energetic gas separation. *Inzhenerno-Fizicheskii Zhurnal*, 27(6):pp. 1128–1133, December 1974. Original in Russian. Translation appears in Journal of Engineering Physics.

[60] Mentenin. Investigation of vortex temperature type compressed gas separators. *Soviet Physics : Technical Physics*, 5:pp. 1025–1032, February 1961. Translation of Russian original.

[61] B B Parulekar. The short vortex tube. *The Journal of Refrigeration*, July and August 1961.

[62] A M Arkharov, V L Bondarenko, and V P Yushin. Vortex pipe for gas separaton. has sound radiator at inlet nozzle connection zone to separation chamber. USSR Patent no. SU-1048264, October 1983. WPI Acc. No : 84-169119/27.

[63] A J Reynolds. A note on vortex tube flows. *Journal of Fluid Mechanics*, 14:p. 18ff, 1962.

[64] N W H Armstrong. *Planar Flowfield Measurements in Premixed Turbulent Combustion*. PhD thesis, Department of Engineering, University of Cambridge, August 1992.

[65] R J Adrian. Multipoint optical measurements of simultaneous vectors in unsteady flow - a review. *International Journal of Heat and Fluid Flow*, 7(2):pp. 127–145, 1986.

[66] F Durst, A Melling, and J H Whitelaw. *Principles and Practice of Laser-Doppler Anemometry*. Academic, New York, 1976.

[67] G I Taylor. Distribution of velocity and temperature between concentric rotating cylinders. page 494ff.

[68] J P Hartnet and E R G Eckert. Experimental study of the velocity and temperature distribution in a high velocity vortex type flow. Technical report, Heat Transfer and Fluid Mechanics Institute, 1956.

[69] J P Hartnett and E R G Eckert. Experimental study of the velocity and temperature distribution in a high-velocity vortex-type flow. *Transactions of the ASME*, pages pp. 751–758, May 1957.

[70] H H Bruun. Experimental investigation of the energy separation in vortex tubes. *Journal of Mechanical Engineering Science*, 11(6):pp. 567–582, 1969.

[71] H Takahama. Studies on vortex tubes. *Bulletin of the JSME*, 8(31):pp. 433–330, 1965.

[72] H Takahama and N Soga. Studies on vortex tubes (second report). *Bulletin of JSME*, 9(33):pp. 121–130, 1966.

[73] H Takahama and H Yokosawa. Energy separation in vortex tubes with a divergent chamber. *Transactions of the ASME: Journal of Heat Transfer*, 103:pp. 196–203, May 1981.

[74] J E Lay. An experimental and analytical study of vortex-flow temperature separation by superposition of spiral and axial flows part 1. *Transactions of the ASME*, pages 202–212, August 1959.

[75] P I Starostin and M S Itkin. Operation of a vortex tube on high pressure superheated steam. *Teploenergetika*, 15(8):pp. 31–35, 1968.

[76] H Takahama, H Kawamura, S Kato, and H Yokosawa. Performance characteristics of energy separation in a steam-operated vortex tube. *International Journal of Engineering Science*, 17:pp. 735–744, 1979.

[77] A Williams. The cooling of methane with vortex tubes. *Journal of Mechanical Engineering Science*, 13(6):pp. 369–375, 1971.

[78] R L Collins and R B Lovelace. Experimental study of two-phase propane expanded through the Ranque-Hilsch tube. *Transactions of the ASME : Journal of Heat Transfer*, 101:pp. 300–305, May 1979.

[79] Vortec Corporation catalogue. Company Catalogue, 10125 Carver Road, Cincinnati, Ohio 45242-9976, USA, 1992. UK Distributor: MEECH VORTEC, Burford House, 15 Thorney Leys Business Park, Witney, Oxford, OX8 7GE.

[80] R T Balmer. Pressure-driven Ranque-Hilsch temperature separation in liquids. *Transactions of the ASME : Journal of Fluids Engineering*, 110:pp. 161–164, June 1988.

[81] R Kassner and E Knoernschild. Friction laws and energy transfer in circular flow. Technical Report F-TR-2198-ND, Wright-Patterson Air Force Base, 1948.

[82] C D Fulton. Comments on the vortex tube. *Refrigerating Engineering*, 59:p. 984, 1951.

[83] G W Scheper. Flow patterns and a heat transfer theory for the vortex heating and refrigerating tube. Master's thesis, Union College, Schenectady, USA, Year Unknown.

[84] W A Scheller and G M Brown. 1957. *Ind. Eng. Chem.*, 49:p. 1013ff, 1957.

[85] O Hinze. *Turbulence*. McGraw-Hill Series in Mechanical Engineering. McGraw-Hill, second edition, 1975. Pages 473ff deal explicity with the Ranque-Hilsch Vortex Tube.

[86] Merwin Sibulkin. Unsteady, viscous, circular flow. Part 3: Application to the Ranque–Hilsch vortex tube. *Journal of Fluid Mechanics*, 12:pp. 269–293, 1962.

[87] Merwin Sibulkin. Unsteady, viscous, circular flow. Part 1: The line impulse of angular momentum. *Journal of Fluid Mechanics*, 11:pp. 291–308, 1961.

[88] Merwin Sibulkin. Unsteady, viscous, circular flow. Part 2 : The cylinder of finite radius. *Journal of Fluid Mechanics*, 12:pp. 148–158, 1961.

[89] W S Lewellen. A solution for three dimensional vortex flows with strong circulation. *Journal of Fluid Mechanics*, 14(1):p. 420ff, 1962.

[90] K Cohen. *The Theory of Isotope Separation*. McGraw-Hill, New York, 1951.

[91] A I Gulyaev. Vortex tubes and the vortex effect. *Soviet Physics : Technical Physics*, 10(10):p. 1441ff, April 1966.

[92] J E Lay. An experimental and analytical study of vortex-flow temperature separation by superposition of spiral and axial flows part 2. *Transactions of the ASME*, pages 213–222, August 1959.

[93] E E Khalil and H M W Assaf. Computer modelling of turbulent recirculating flows in engineering applications. In *Proceedings of the Second International Conference on Numerical Methods in Laminar and Turbulent Flow, Venice*, 1981.

[94] W G Stone and T A Love. An experimental study of the Hilsch Tube and its possible application to isotope separation. Technical Report ORNL-282, Oak Ridge National Laboratory, 1950.

[95] K Elser and M Hoch. Das verhaltn verschiedener gase und die trennung von gasgemischen in einem wirbelrohr. *Z. Naturf*, 6a(25), 1951.

[96] P S Baker and W R Rothkamp. Investigation on the Ranque-Hilsch vortex tube. Technical Report ORNL-1659, Oak Ridge National Laboratory, 1954.

[97] N S Torochesnikov and Zh A Koval. Experimental study of the eddy effect in small-diameter tubes. *Nauch. Dokl. Vysshi Shkoly, Khim. Tekhnol*, (3):p. 603ff, 1958.

[98] C U Linderstrom-Lang. Gas separation in the Ranque–Hilsch vortex tube. *International Journal of Heat and Mass Transfer*, 7:pp. 1195–1206, 1964.

[99] J Marshall. Effect of operating conditions, physical size and fluid characteristics on the gas separation performance of a Linderstrom–Lang vortex tube. *International Journal of Heat and Mass Transfer*, 20:pp. 227–231, 1977.

[100] R F Schlenker. Method for separating isotopes. USA Patent PCT/US78/00004, January 1980. Application filed : 5 June 1978. International Publication Number WO 80/00010.

[101] J J Keyes. Experimental study of flow and energy separation in vortex tubes with applications to gaseous fission heating. *Journal of the American Rocket Society*, 31:p. 1204ff, 1961.

[102] J L Kerrebrock and R V Meghrablain. Vortex containment for the gaseous fission rocket. *Journal of Aero/Space Science*, 28:pp. 710–724, 1961.

[103] M L Rosenzweig, W S Lewellwn, and J L Kerrebrock. Feasibility of turbulent vortex containment in the gaseous fission rocket. *Journal of the American Rocket Society*, 31:p. 292ff, 961.

[104] E R G Eckert. Energy separation in fluid streams. *International Communications in Heat and Mass Transfer*, 13, 1986.

[105] A J Reynolds. On energy separation by aerodynamic processes. *Journal of Aero/space Sciences*, 28, March 1961.

[106] Kurosaka, Gertz, Graham, Goodman, Sundaram, Riner, Kuroda, and Hankey. Energy separation in a vortex street. *Journal of Fluid Mechanics*, 178:pp. 1–29, 1987.

[107] D J Mullan and Q Q Chen. Acoustic heating of the chromosphere and cool corona in the F-star Alpha-Canis-Minoris (Procyon). *Astrophysical Journal*, 435(1):pp. 435–448, 1994.

[108] K Stephan, S Lin, M Durst, F Huang, and D Seher. A similarity relation for energy separation in a vortex tube. *International Journal of Heat and Mass Transfer*, 27(6):pp. 911–920, 1984.

[109] R Westley. Optimum design of a vortex tube for acheiving large temperature drop ratios. Cranfield Notes 30, Cranfield College of Aeronautics, 1955.

[110] K Stephan, S Lin, M Durst, F Huang, and D Seher. An investigation of energy separation in a vortex tube. *International Journal of Heat and Mass Transfer*, 26(3):pp. 341–388, June 1983.

[111] R Westley. Vortex tube performance data sheets. Cranfield Notes 67, Cranfield College of Aeronautics, 1957.

[112] A J Walker. The Ranque–Hilsch effect : A demonstration model. Project Report, Engineering Tripos Part II, Cambridge University Engineering Department, 1988.

[113] Y Soni and W J Thompson. Optimal design of the Ranque–Hilsch vortex tube. *Transactions of the ASME : Journal of Heat Transfer*, pages 317–317, May 1975.

[114] E Ower and R C Pankhurst. *The Measurement of Airflow*. Pergamon Press, fifth edition, 1977.

[115] R D Benedict. *Fundamentals of Temperature, Pressure and Flow Measurement*. Wiley, 1969.

[116] H W Leipmann and A Roshko. *Elements of Gas Dynamics*. Galcit Aeronautical Series. Wiley, California Instituite of Technology, 1957.

[117] Van Dyke. *Perturbation Methods in Fluid Mechanics*. Parabolic Press.

[118] N G McDuffie. Resonance in the Ranque-Hilsch vortex tube. pages 1–4.

[119] K W Arthur. *SoundBuilder 1.0.1*. 2204, Wheeler St., Kalamazoo, MI 49001, U.S.A, May 1993.

[120] Gabel and Roberts. *Signals and Linear Systems*, pages 327–328. John Wiley and Sons, Inc., second edition, 1980.

[121] W H Press, S A Teukolsky, William A Vetterling, and B P Flannery. *Numerical Recipies in Fortran. The Art of Scientific Computing*, pages 494–495. Cambridge University Press, second edition, 1992.

[122] S V Patankar. *Numerical Heat Transfer and Fluid Flow*. Hemisphere, 1980.

[123] B E Launder, C H Priddin, and B I Sharma. The calculation of turbulent boundary layers on spinning and curved surfaces. *Transactions of the ASME : Journal of Fluids Engineering*, pages 231–239, March 1977.

[124] W H Press, S A Teukolsky, W T Vetterling, and B P Flannery. *Numerical Recipies in Fortran : The Art of Scientific Computing*. Cambridge University Press, second edition, 1992. p. 859.

[125] H Schlichting. *Boundary Layer Theory*. McGraw-Hill Book Company, sixth edition, 1968. Chapter XX deals with turbulent flow through smooth pipes, and detail Nikuradse's results.

[126] R G Deissler. Analysis of fully developed turbulent heat transfer at low peclet numbers in smooth tubes with applications to liquid metals. Technical Report NACA RM E52F03, NACA, 1952.

[127] F Schultz-Grunow. *Forsch. Gebiete Ingenierw*, 17(65), 1951.

[128] A Bejan. *Convection Heat Transfer*. John Wiley and Sons, first edition, 1984.

[129] B Ahlborn, J U Keller, R Staudt, G Treitz, and E Rebhen. Limits of temperature separation in a vortex tube. *Journal of Physics, D: Applied Physics*, 27:pp. 480–488, 1994.

[130] A J Bull. Private communication. BNFL Risley, UK.

[131] B Vonnegut. Vortex thermometer for measuring true air temperature and true air speeds in flight. *Review of Scientific Instruments*, 121:pp. 136–141, 1950.

[132] T J Bruno. Laboratory applications of the vortex tube. *Canadian Journal of Chemical Education*, 64:pp. 987–988, 1987.

[133] K Landecker. A two stage refrigeration and power producing arrangement consisting of a vortex cooling tube and a thermoelectric stage. *Energy Conservation*, 17:pp. 119–122.

[134] A Baz and D Uhler. A compressed gas powered heating system for underwater divers. *Ocean Engineering*, 13(3):pp. 273–290, 1986.

[135] A Baz, J Gilheany, and A Kalvitas. Feasability of vortex tube asssited environmental control of an underwater research habitat. *Ocean Engineering*, 15(1):pp. 34–54, 1987.

[136] A Baz, R Johnston, and D Uhler. Dynamics of vortex tube assisted hyperbaric chambers. *Ocean Engineering*, 13(4):pp. 387–408, 1986.

[137] R W Haywood. *Analysis of Engineering Cycles*. Pergamon Press, fourth edition, 1991.

[138] V E Fin'ko. Cooling and condensation of gas in a vortex flow. *Soviet Physics : Technical Physics*, 28(9):p. 1089ff, September 1983.

[139] R W Haywood. *Thermodynamic Tables in SI (metric) Units*. Cambridge University Press, second edition, 1972.

[140] M Benedict, T H Pigford, and H W Levi. *Nuclear Chemical Engineering*. McGraw-Hill Series in Nuclear Engineering. McGraw-Hill, second edition, 1981. p. 857ff.

[141] H Geppert. The industrial implementation of the separation nozzle process. In *Proceedings of the International Conference on Uranium Isotope Separation*, British Nuclear Energy Society, London, March 1975.

[142] S Whitley. Isotope enrichment by diffusion and by the centrifuge. *Nuclear Energy*, 27(6):pp. 349–360, December 1988.

[143] J P Holman. *Heat Transfer*. McGraw-Hill, SI metric edition, 1989.

[144] D L Smith. *Probability, Statistics, and Data Uncertainties in Nuclear Science and Technology*. Neutron Physics and Nuclear Data in Science and Technology. American Nuclear Society, LaGrange Park, Illinois, USA, 1991. ISBN 0-89448-036-7.

[145] B Hiller and R K Hanson. Properties of the iodine molecule relevant to laser-induced fluoresence experiments in gas flows. *Experiments in Fluids*, 10:pp. 1–11, 1990.

[146] A H Epstein. Quantitative density visualisation in a transonic compressor rotor. *Transactions of the ASME : Journal of Engineering for Power*, pages 461–475, July 1977.